Magneto-Optical Effects in Hybrid Plasmonic Nanostructures

Dissertation

submitted in partial fulfillment of
the requirements for the degree of

Dr. rer. nat.

to the Faculty of Physics
TU Dortmund University, Germany

by

Lars Klompmaker

Dortmund, 2023

technische universität dortmund

Fakultät Physik

Accepted by the Department of Physics, TU Dortmund University, Germany

Date of submission: 08.07.2023

Date of the oral examination: 28.09.2023

Examination board:

Prof. Dr. Ilya A. Akimov
Prof. Dr. Heinz Hövel
Prof. Dr. H. Jelger Risselada
Dr. Jens Weingarten

Contents

Part I

Introduction

Chapter 1

Introduction and Motivation

Magneto-optical effects have played a significant role in basic research and in a wide range of applications since their discovery almost 180 years ago [1]. They describe the connection between magnetism and light, or more specifically, the phenomena that result from the interaction of light with matter that is subjected to a magnetic field. The first magneto-optical effect discovered is also the best-known, the Faraday effect. Michael Faraday discovered in 1845 that the polarization plane of linearly polarized light gets rotated when transmitted through glass with a magnetic field parallel to the propagation direction [2]. This was the first demonstrated connection between magnetism and light, and it sparked the emergence of magnetooptics as a large field of interest [1]. Fittingly, this geometry of parallel magnetic fields and light propagation is called the Faraday geometry and it is the basis for many magneto-optical effects. Another well-known class of magneto-optical effects are the magneto-optical Kerr effects (MOKEs). They are named after John Kerr, who discovered the polar MOKE (PMOKE) in 1877 as an influence on the polarization of light reflected from a magnetized medium in the Faraday geometry [3]. The transverse MOKE (TMOKE), on the other hand, occurs with the magnetic field perpendicular to the plane of light incidence. It is not defined by polarization changes but is mainly an intensity effect, describing the magnetic-field-dependent changes of the reflected light intensity [1]. This enables applications in the control of light at the nanoscale due to its sensitivity to the interface [4]. MOKEs in general are frequently used to observe and visualize magnetic domains in materials [5], which has been used for magneto-optical data-storage for many years already [6] and is a common tool in time-resolved spin-dynamics measurements with a high spatial resolution [7]. Overall, the field of magnetooptics is wide and recent advancements have led, e.g., to the first imaging of the magnetic domains of an antiferromagnetic metal using MOKEs [8], or applications like magneto-optical filters [9, 10] and isolation systems [11]. [1, 12]

However, the relative light intensity change of the non-resonant TMOKE from a homogeneous flat interface is below 10^{-3}, which limits its general applicability and warrants a search for enhanced magneto-optical effects [13]. In recent years, this search was mainly focussed on magneto-optical effects at the nanoscale, which are enabled by advancements of nanotechnology and the possibility to build arbitrary nanoscale structures. A recent example uses extreme anti-reflection layers to suppress non-magneto-optical reflection via destructive interference and, thus, enhance the MOKE signal [14]. Another prominent example are nanostructured periodic metal films close to the magnetic materials with periods below the light wavelength, which enables the excitation of surface plasmon polaritons (SPPs) at the metal/dielectric interface. SPPs describe the resonant coupling of light with collective oscillations of the electron plasma in the metal. They are evanescent electromagnetic waves that propagate along the interface and concentrate large electromagnetic

energy into nanoscale volumes [15]. In magnetoplasmonic structures, this can be used to enhance magneto-optical effects like the TMOKE significantly [16], e.g., up to 13 % in plasmonic bismuth iron garnet structures [17]. This enhancement also enables the use of the TMOKE for many (bio)sensing application that detect refractive index changes of the incidence medium as shifts in the resonantly enhanced TMOKE signal. Here, geometries range from periodic nanohole arrays [18, 19] and gratings [20] to randomly distributed metal nanoparticles [21], among others [22], with significantly higher resolutions than the shifts of the non-magnetic reflectance curves. Furthermore, SPPs can be used in magnetoplasmonic nonreciprocal waveguides for nanoscale optical systems, for example as a high bandwidth active optical phase shifter [23] and as integrated isolator for semiconductor lasers [24], and one-way guided plasmons can even be stopped with a vanishing group velocity [25]. Recently, plasmonics were also used to enable the switching of the optical chirality using magnetic fields, which could enable tunable chiral metasurfaces for integrated polarization control and sensing [26, 27], and for an enhanced optically induced magnetization in plasmonic gold nanoparticles [28]. These few examples already highlight the wide range of applications that are enabled or enhanced by the presence of plasmonic structures, which can be applied to a wide range of well-known or novel materials, like for the wide-band enhancement of the second harmonic generation in the recently popular monolayer materials [29]. [12]

Another magneto-optical intensity effect that is resonantly enhanced by SPPs is the transverse magnetic routing of light emission (TMRLE) [30], which is one of the main topics of this thesis. It takes place in the same geometry as the TMOKE but for emitted light, which is routed along a nearby surface perpendicular to the external magnetic field, and emitted directionally into the far-field. This is achieved by magnetically modifying the selection rules of the light source (excitons) so that it has a non-zero transverse spin $\boldsymbol{S} \parallel x \perp \boldsymbol{k}$ along the magnetic field in the xy-QW plane. By placing the light source near a surface, it can couple to subwavelength evanescent optical fields, like SPPs, with a strong transverse spin and spin-momentum locking, which translates the spin of the emitter into a routed wave along the surface. A good analogy for this is a bicycle wheel, which moves on a surface and where the spokes represent the electric field vector, as shown in Ref. [31]. Depending on the rotation direction (spin) of the wheel, it moves into opposite directions, just like the subwavelength surface waves. In contrast, light in free space behaves similar to the rotor blades of an aircraft, where the electric field vector spins around the propagation axis [31]. If this routed surface wave is able to emit into the far-field, e.g., using a periodic grating structure instead of a planar surface, directional emission is achieved via the TMRLE [30]. These interesting characteristics of a photonic wheel-like transverse spin and the spin-momentum locking are not limited to SPPs, though. The locking of the transverse spin to the momentum of the wave, which is important for the routing effects, is an inherent feature of all evanescent waves [32]. The transverse spin, on the other hand, is also present in evanescent waves [31], being identified early for SPPs [33], waveguides [34] and whispering-gallery-mode resonators [35], but can also be achieved, e.g., in tightly focussed light beams [36], but without the spin-momentum locking. These features promise interesting applications in on-chip optical circuits and quantum computing, where the spin can be used to route the emission of a light source for information transmission and processing in on-chip devices like integrated photonic or optoelectronic circuits [31]. The chirality of an emitter can generally be used as a parameter for emission routing, acting as an additional degree of freedom [37]. This has been shown, e.g., for asymmetric photonic crystal waveguides where the asymmetry of the confining nanophotonic holes leads to emission directionality due to non-transversal local electric-field components [38], and also in symmetric nanophotonic waveguides, where the emitter

is placed off-center [39], or for orthogonal crossed waveguides around a quantum dot emitter [40]. The spin-momentum locking of surface waves has also been used to translate circularly polarized light from the far-field into directional propagating waves [41, 42], or to optically orient exciton spins via plasmons excited with linearly polarized light [43].

One of the main goals of this thesis is a better understanding of the TMRLE magneto-optical effect regarding both components of the hybrid plasmonic-semiconductor model system used to demonstrate the effect recently in Ref. [30]: First, the diluted magnetic semiconductor (DMS) quantum well (QW) system that is used as light source to achieve strong magnetic routing but also exhibits a large temperature-dependence of its magnetic properties, and second, the plasmonic nanogratings used for the significantly enhanced routing effect and directional emission into the far-field, which depends strongly on the geometric grating parameters. In the process, interesting contributions to the emission directionality from both the light-holes and the weak coupling between the QW excitons and the SPPs are uncovered. Furthermore, the enhancement of the TMOKE through mode hybridization is studied in reflection and transmission from synthesized magnetite-based plasmonic waveguide structures.

This thesis is structured as follows: First, Chapter 2 introduces DMSs, which are used in the hybrid QW structures as magnetic-field modifiable light source for the TMRLE due to their large exchange interaction enabled Zeeman splitting. It also focusses on the large temperature-dependence of the splitting, and on the anisotropic Zeeman splitting in a DMS QW structure and the resulting transversal circular polarization of the optical transitions in the Voigt geometry, which is a key factor for the TMRLE. Next, Chapter 3 introduces the theory of surface plasmon polaritons (SPPs), focussing on their inherent spin-momentum locking and on enabling their interaction with the far-field using periodic metal gratings for the enhanced directional emission of the TMRLE. Chapter 4 focusses on magneto-optical effects, mainly the Faraday effect and how it can be used to probe the magnetic properties of a structure, and the TMOKE and how it is enhanced at optical resonances like SPPs or waveguide modes. Both effects are used in the experimental part of this thesis. Lastly, Chapter 5 explains the TMRLE, the main magneto-optical effect investigated in this thesis, and the different near- and far-field contributions to the overall emission directionality seen in the experiments.

Next, Chapter 6 presents the various plasmonic structures used in the experiments, namely (Cd,Mn)Te-based hybrid plasmonic-semiconductor QW structures for the TMRLE and magnetite-based waveguide structures for the TMOKE measurements. Then, Chapter 7 explains the Fourier plane imaging technique and its practical realization in a Fourier imaging spectroscopy setup. It enables the simultaneous measurement of the spectral and angular intensity distribution of the light emitted, reflected, or transmitted from and through the experimental structures to quantify the induced light intensity changes of the TMOKE and TMRLE.

Chapter 8 is the first experimental chapter and presents introductory measurements for the TMRLE from the (Cd,Mn)Te-based hybrid structures. This includes emission and reflection spectra to determine the important optical resonances, magneto-PL measurements to quantify the giant Zeeman splitting, and the emission directionality from the main hybrid structure as an example of a typical TMRLE measurement with larger routing magnitudes than previously achieved.
Then, Chapter 9 focusses on the temperature dependence of the TMRLE, which is mainly governed by the semiconductor part of the hybrid structure. It is confirmed that the routing magnitude from a DMS QW structure decreases in unison with the magnetization of the QW for increasing

temperatures. Furthermore, the directionality contribution of the light-hole emission is highlighted, which emerges at higher temperatures and is routed in the opposite direction to the main heavy-hole emission, and the influence of a different plasmonic grating period and of modulation doping near the QW on the temperature dependence is shown. Lastly, a non-magnetic (In,Ga)As-based QW structure is discussed as possible platform for a temperature-independent TMRLE, based on the intrinsic Zeeman splitting with a large hole g-factor instead of the exchange interaction in DMSs.

Next, Chapter 10 focusses on the other component of the hybrid structures, the periodic plasmonic grating. Its geometric parameters have a large impact on the TMRLE spectra, because they directly influence the dispersion relation of the SPPs that facilitate the large emission routing magnitude. For this, the directionality contributions of the different plasmonic branches and other optical modes and how they enhance or compensate each other are shown for various grating periods and slit widths. Most importantly, though, it is shown that the TMRLE can be used to probe the weak coupling between the QW excitons as light sources and the directionality-enhancing SPPs with high sensitivity, which is hard to detect otherwise.

Chapter 11 is the last experimental chapter and shifts the focus from the TMRLE to the similar transverse magneto-optical Kerr effect (TMOKE). It is used to investigate magnetite-based plasmonic waveguide structures in reflection and transmission, highlighting the enhanced TMOKE magnitude in the plasmonic structures compared to a bare magnetite film and how the TMOKE can be used to extract rich information about the various optical resonances of the structure. Furthermore, the importance of mode hybridization for the TMOKE enhancement is discussed, and how the position of the plasmonic grating can be used for a selective mode excitation.

Finally, Chapter 12 summarizes the results of the previous chapters and gives an outlook into possible future directions of research and application of the effects and structures investigated in this thesis.

Part II

Theoretical Background

Chapter 2

Diluted Magnetic Semiconductors (DMS)

Diluted magnetic semiconductors (DMS) are ternary alloys, in which a non-magnetic host semiconductor like cadmium telluride (CdTe) is doped with a magnetic transition metal like manganse (Mn), replacing a fraction x of the cations (Cd). The resulting substitutional alloy $Cd_{1-x}Mn_xTe$ combines the semiconductor properties of the CdTe host with magnetic effects due to the magnetic Mn ions. In general, DMSs are an excellent model system for magneto-optical effects because their magneto-optical properties and the exciton energy structure are well established. Furthermore, DMSs exhibit a giant Zeeman splitting of the band states due to the exchange interaction between the s and p electrons of the valence and conduction band and the d electrons of the magnetic Mn ions. This leads to a pronounced magneto-optical activity around the bandgap, like a giant Faraday rotation [44]. Due to the ternary nature of the alloys, they can be used flexibly in heterostructures like quantum wells and quantum dots, and for various other applications as their band parameters and lattice constants can be engineered in a wide range by changing the fraction x of the dopant or by switching to a different host material [45]. The samples used for the transverse magnetic routing of light emission (TMRLE) in the experimental part of this thesis are quantum well (QW) structures based on the DMS (Cd,Mn)Te. It is an attractive system for the TMRLE because the large Zeeman splitting of the QW excitons is essential for this routing effect and the (Cd,Mn)Te QW is a well-understood system. [44, 45]
First, Section 2.1 gives an introduction to the (magnetic) properties of DMSs based on the example of (Cd,Mn)Te. Then, Section 2.2 introduces the sp-d exchange interaction and the resulting giant Zeeman splitting of the band states. Section 2.3 focuses on the Zeeman splitting in DMS quantum wells (QWs), where the confinement in one direction results in the anisotropy of the band splitting with respect to the magnetic field direction. It also introduces the concept of the transverse circular polarization degree in the Voigt geometry, which enables the TMRLE, see Chapter 5.

The topic of DMSs is extensively covered in several publications, for example by Furdyna for the $A^{II}_{1-x}Mn_xB^{VI}$-type DMS [45] or by Kossut and Gaj [44] in greater detail and by Kuhn-Heinrich for DMS QWs [46]. These three publications are the main sources of this chapter (if not cited otherwise), so most of the information presented here can be found in greater detail there.

2.1 Magnetic Properties

While there are many different DMSs, (Cd,Mn)Te is a particularly good model system to introduce the properties of DMSs, as pointed out in Ref. [44]. For one, II-VI semiconductors (like CdTe) are well studied, and most transition metal ions form neutral centers in the background crystal lattice, whereas they are typically charged in III-V hosts. CdTe, in particular, forms in the simple zinc-blende lattice structure and has an intermediate bandgap. Its conduction and valence bands are formed by s and p electrons, respectively, and the zinc-blende structure comprises tetrahedral sp^3-hybridized bonds. When incorporated into the CdTe host, the manganese (Mn) $4s^2$ valence electrons contribute to the sp^3 bonds, while the 5 electrons in the half-filled outer $3d^5$-shell determine its magnetic properties: Following Hund's rule, all 5 electron spins are aligned in parallel. This leads to a vanishing orbital momentum L but the maximum possible spin value of $S = 5/2$ and, therefore, to a large magnetic moment μ of the individual ion. The band structure of the $A^{II}_{1-x}Mn_xB^{VI}$ DMS closely resembles that of the $A^{II}B^{VI}$ host with the same crystal structure, and the two electronic systems of delocalized sp-band electrons and localized d electrons of Mn can be considered independently due to their generally weak interaction.

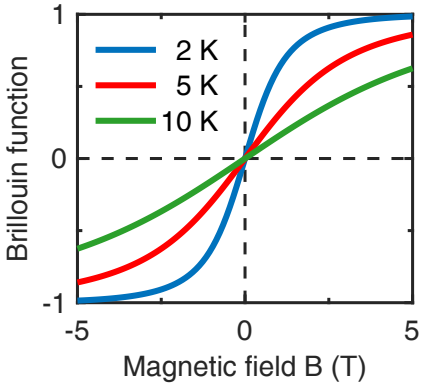

Figure 2.1 Brillouin function $B_{5/2}$ for different temperatures T.

An important property of DMSs is their giant Zeeman splitting of the electronic (and excitonic) levels, which can reach magnitudes in the order of 100 meV for a few Tesla at liquid helium temperatures. It originates from the alignment of the Mn^{2+} magnetic moments in (Cd,Mn)Te because the CdTe host material itself is diamagnetic. The magnetization of the Mn system grows linearly with small magnetic fields and saturates for higher fields. For low Mn content ($x < 0.01$), the magnetization can be characterized by a Brillouin function, which describes a system of non-interacting spins [44, 45]:

$$B_S(\xi) = \frac{2S+1}{2S}\coth\left(\frac{2S+1}{2S}\xi\right) - \frac{1}{2S}\coth\left(\frac{1}{2S}\xi\right) \tag{2.1a}$$

$$\xi = \frac{g_{\mathrm{Mn}}\mu_{\mathrm{B}}SB}{k_{\mathrm{B}}T}. \tag{2.1b}$$

Here, $S = 5/2$ is the spin of the Mn ions, $g_{\mathrm{Mn}} = 2$ their g-factor, μ_{B} the Bohr magneton, k_{B} the Boltzmann constant, and B the external magnetic field that aligns the magnetic moments. The Brillouin function $B_{5/2}$ is plotted in Figure 2.1 for three different temperatures. It shows the linear and then saturated dependence on the magnetic field and the lower magnetization at larger temperatures. For larger fractions x or temperatures T above that of pumped liquid helium, the magnetization needs to be described empirically by replacing the spin S and temperature T with the effective spin saturation value S_{eff} and the effective temperature $T_{\mathrm{eff}} = T + T_0$ with the temperature correction $T_0 > 0$. This results in the description of the magnetization as the mean spin value per Mn ion $\langle S_z^{\mathrm{Mn}}\rangle$ with the modified Brillouin function [44, 45]:

$$\left\langle S_z^{\mathrm{Mn}}\right\rangle = S_{\mathrm{eff}}B_{5/2}\left(\frac{5}{2}\frac{g_{\mathrm{Mn}}\mu_{\mathrm{B}}B}{k_{\mathrm{B}}(T+T_0)}\right) \tag{2.2}$$

Both S_{eff} and T_0 are functions of the Mn fraction x due to the ion-ion interaction of the d-shells of two Mn ions and can be used as fitting parameters for the experimental data. They take into account that the obtainable magnetization is reduced for $x > 1\,\%$ because of the emerging antiferromagnetic exchange interaction between the spins of neighboring Mn ions once they are no longer spatially well separated [44, 45]. The magnetization M and $\left\langle S_z^{\text{Mn}} \right\rangle$ are connected via $M = -xN_0 g_{\text{Mn}} \mu_{\text{B}} \left\langle S_z^{\text{Mn}} \right\rangle$ with the number of cations per unit volume N_0 [45].

2.2 Exchange Interaction and Giant Zeeman Splitting

With the knowledge of how the Mn spins react to an external magnetic field, the next step is to establish the interaction of these localized magnetic ions with the s- and p-type charge carriers of the bulk host material. They form the conduction and valence bands and are responsible for physical phenomena like the (giant) Zeeman splitting. As indistinguishable particles, the electrons (and holes) are subjected to the exchange interaction, a purely quantum mechanical effect that is also responsible for ferromagnetism [47]. The system can be described by a Hamiltonian $\hat{H} = \hat{H}_0 + \hat{H}_{\text{ex}}$, where $\hat{H}_0$ describes the non-magnetic semiconductor host and its band structure and $\hat{H}_{\text{ex}}$ the sp-d exchange interaction in the form of a Heisenberg Hamiltonian of interacting spins [44, 45]:

$$\hat{H}_{\text{ex}} = -\sum_i \boldsymbol{J}(\boldsymbol{r} - \boldsymbol{R}_i)\boldsymbol{\sigma} \cdot \boldsymbol{S}_i, \tag{2.3}$$

with the spin operators $\boldsymbol{\sigma}$ and $\boldsymbol{S}_i$ of the interacting carriers and Mn^{2+} ions, respectively, and the magnetic ion location $\boldsymbol{R}_i$. The sum only counts the lattice sites occupied by Mn^{2+}, and J is the sp-d exchange coupling constant. Assuming negligibly small Landau quantization and intrinsic spin splitting compared to the exchange splitting, the Zeeman splitting of the electrons and holes can be described using the exchange interaction alone [44]. Because each delocalized carrier interacts with many localized Mn^{2+} ions, we can assume that the magnetic ions affect the carriers but not vice versa. Therefore, the interaction originates solely from the magnetic ions, which align with the external magnetic field B_z and interact with the carriers via ion-carrier interaction. Now, the *mean field approximation* replaces the Mn spin operator $\boldsymbol{S}_i$ with the thermal average $\left\langle S_z^{\text{Mn}} \right\rangle$ of all Mn^{2+} ions, which we already know from Eq. (2.2). Furthermore, the periodicity of the crystal can be restored using the *virtual crystal approximation*, which replaces the random distribution of Mn^{2+} ions with an artificial periodic structure of cations with combined properties of the Cd and Mn ions. This lets us replace $\sum_i \boldsymbol{J}(\boldsymbol{r} - \boldsymbol{R}_i)$ with $x \sum_{\boldsymbol{R}} \boldsymbol{J}(\boldsymbol{r} - \boldsymbol{R})$ over all cation sites $\boldsymbol{R}$, and we obtain [45]

$$\hat{H}_{\text{ex}} = \sigma_z \left\langle S_z^{\text{Mn}} \right\rangle x \sum_{\boldsymbol{R}} \boldsymbol{J}(\boldsymbol{r} - \boldsymbol{R}), \tag{2.4}$$

which can be solved with the same bases as $\hat{H}_0$. Diagonalizing $\hat{H}_{\text{ex}}$ for the conduction band (CB) and the valence band (VB) at $k = 0$ leads to the matrix form [45]

$$\hat{H}_{\text{ex}}^{\text{CB}} = \begin{pmatrix} 3A & \\ & -3A \end{pmatrix} \quad \text{and} \quad \hat{H}_{\text{ex}}^{\text{VB}} = \begin{pmatrix} 3C & & & \\ & C & & \\ & & -C & \\ & & & -3C \end{pmatrix} \tag{2.5}$$

with $A = 1/6\, xN_0\alpha\left\langle S_z^{\mathrm{Mn}}\right\rangle$ and $C = 1/6\, xN_0\beta\left\langle S_z^{\mathrm{Mn}}\right\rangle$. The exchange integrals $\alpha = \langle S|J|S\rangle$ for the conduction- and $\beta = \langle X|J|X\rangle$ for the valence-band electrons multiplied with N_0 are material constants and independent of x, e.g. $N_0\alpha = 0.22\,\mathrm{eV}$ and $N_0\beta = -0.88\,\mathrm{eV}$ for (Cd,Mn)Te [44].

With only the exchange interaction taken into account, a magnetic field splits the conduction band (c) into two components with opposite spins separated by $6A$ and the valence band into four components with a splitting $6C$ between the outermost heavy-hole levels (h) and $2C$ for inner light holes (l):

$$\Delta E_{\mathrm{c}} = xN_0\alpha\left\langle S_z^{\mathrm{Mn}}\right\rangle \tag{2.6a}$$

$$\Delta E_{\mathrm{h}} = xN_0\beta\left\langle S_z^{\mathrm{Mn}}\right\rangle \tag{2.6b}$$

$$\Delta E_{\mathrm{l}} = xN_0\beta/3\left\langle S_z^{\mathrm{Mn}}\right\rangle \tag{2.6c}$$

Figure 2.2 schematically shows the splitting and the dipole-allowed transitions as arrows for the two opposite circular polarizations $\sigma^{\pm}$ that rotate transverse to the external magnetic field, and for the linearly polarized π transitions parallel to the field. Note that the Zeeman splitting depends only on the magnetization of the Mn ions $\left\langle S_z^{\mathrm{Mn}}\right\rangle$, which is temperature dependent according to Eq. (2.2). The exchange splitting is, however, the same as the ordinary splitting regarding the multiplicity, symmetry, and selection rules, but the magnitude is determined entirely by the exchange contribution of the Mn ions.

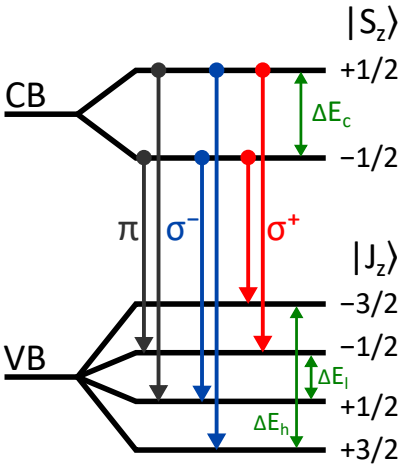

Figure 2.2 Schematic presentation of the Zeeman splitting of the conduction (CB) and valence band (VB) for a bulk $\mathrm{A}^{\mathrm{II}}_{1-x}\mathrm{Mn}_x\mathrm{B}^{\mathrm{VI}}$ alloy with dipole-allowed transitions shown as arrows. Adapted from Ref. [45].

2.3 Zeeman Splitting in DMS Quantum Wells

With the general properties of DMSs and the Zeeman splitting in a bulk DMS described in Section 2.1, this section will focus on DMS quantum well (QW) structures like those investigated in this thesis. First, the comparatively easy Faraday geometry will be discussed, followed by the more complex Voigt geometry used for the transverse magnetic routing of light emission (TMRLE). The main source of this section is the publication of Kuhn-Heinrich [46], along with our publications [30, 48].

The charge carriers in a QW are confined to its two dimensions. Therefore, the Zeeman splitting becomes anisotropic and depends strongly on the direction of the magnetic field relative to the

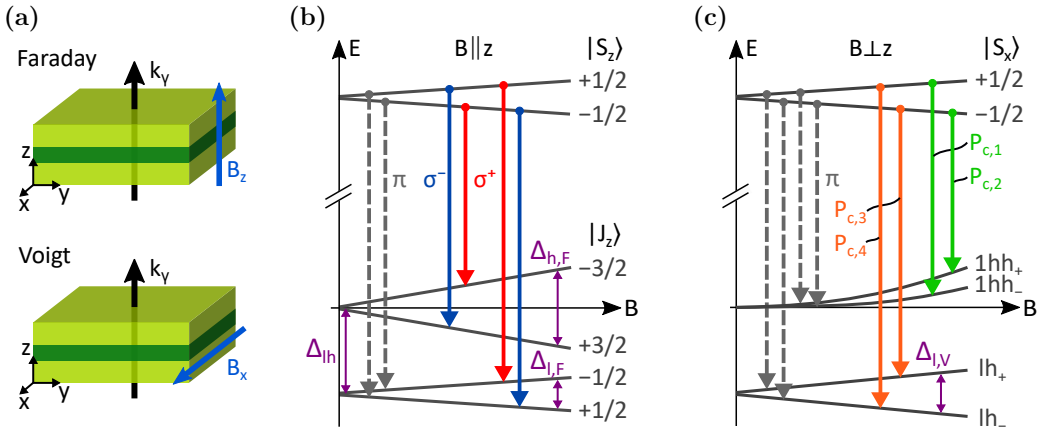

Figure 2.3 (a) Faraday and Voigt geometry. **(b),(c)** Zeeman splitting of the conduction and valence band states of a QW in a (b) longitudinal ($\boldsymbol{B} \parallel z$) and (c) transverse ($\boldsymbol{B} \perp z$) magnetic field. Optical transitions are shown as arrows, E is the energy. **(b)** Labels $\sigma^{\pm}$ and π indicate the polarization of the transition, $\Delta_{\mathrm{h,F}}$ and $\Delta_{\mathrm{l,F}}$ are the Zeeman splitting of heavy and light holes in Faraday geometry, respectively, and Δ_{lh} is the energy splitting between heavy and light holes at $B = 0$. **(c)** $P_{\mathrm{c},i}$ is the degree of circular polarization according to Eq. (2.10) and $\Delta_{\mathrm{l,V}}$ the Zeeman splitting of the light holes. Adapted from [48].

confinement axis. The field can be applied either parallel to the confinement axis ($\boldsymbol{B} \parallel z$) (perpendicular to the plane of the QW), which in our case is the Faraday geometry, or in the QW plane ($\boldsymbol{B} \perp z$), which is the Voigt geometry. Both geometries are shown in Figure 2.3, along with a schematic presentation of the Zeeman splitting of the conduction and valence bands for the two geometries with only the lowest levels of quantization considered. Compared to the bulk, the heavy hole and light hole bands are split by Δ_{lh} at the Γ-point even without a magnetic field B due to the confinement and strain from the lattice mismatch between the QW and barrier materials. For our 10 nm thin (Cd,Mn)Te/(Cd,Mg)Te QW structure, the splitting between the upper heavy-hole states with $|J_z\rangle = \pm 3/2$ and the lower light-hole states with $|J_z\rangle = \pm 1/2$ is $\Delta_{\mathrm{lh}} \approx 20$ meV. Following Ref. [46], the bulk model established in Section 2.1 can also be used for the quantum well, with the diagonalized matrix forms $\hat{H}_{\mathrm{ex}}^{\mathrm{CB}}$ and $\hat{H}_{\mathrm{ex}}^{\mathrm{VB}}$ for the conduction and valence bands shown in Eq. (2.5). The Zeeman splitting of the conduction band is not changed by the quantization and is still isotropic with the same splitting of $6A = xN_0\alpha\left\langle S_z^{\mathrm{Mn}}\right\rangle$ [46], see Figure 2.3. The splitting of the valence band states, however, depends on the orientation of the magnetic field $\boldsymbol{B}$ relative to the quantization axis z or wave vector $\boldsymbol{k}$ of the holes.

2.3.1 Faraday Geometry

In the Faraday geometry, $\boldsymbol{B}$ is perpendicular to the QW plane but parallel to the confinement axis, $\boldsymbol{B} \parallel z$. Therefore, the electron and hole states can be characterized by their total angular momentum projection on the z-axis, $S_z = \pm 1/2$ for electrons and $J_z = \pm 3/2,\ \pm 1/2$ for the heavy and light holes, respectively. In an external magnetic field in Faraday (F) geometry, the heavy hole levels are split by $\Delta_{\mathrm{h,F}} = 6C$ and the light hole levels by $\Delta_{\mathrm{l,F}} = 2C = \Delta_{\mathrm{h,F}}/3$, with $C = 1/6\, xN_0\beta\left\langle S_z^{\mathrm{Mn}}\right\rangle$. The conduction band splitting is $6A$, as mentioned above. Including the intrinsic splitting, the Zeeman

splitting of the holes can be written as

$$\Delta_{k,\mathrm{F}} = 2J_z g_\mathrm{h} \mu_\mathrm{B} B + \frac{2}{3} J_z x N_0 \beta \left\langle S_z^\mathrm{Mn} \right\rangle, \tag{2.7}$$

with $k = \mathrm{l}$ and $J_z = \pm 1/2$ for light holes and $k = \mathrm{h}$ and $J_z = \pm 3/2$ for heavy holes. The first term describes the intrinsic splitting of the valence band states with the Landé g-factor of the holes g_h, which is negligible at low temperatures compared to the second term of the exchange contribution. However, the exchange contribution is strongly temperature dependent through the average alignment of the Mn spins $\left\langle S_z^\mathrm{Mn} \right\rangle$ and quickly decreases for increasing temperatures, see Eq. (2.2). The intrinsic splitting, on the other hand, depends only on g_h, making it largely temperature independent. Both terms are proportional to J_z and the splitting of the heavy holes $\Delta_{\mathrm{h,F}}$ is, thus, three times larger than that of the light holes $\Delta_{\mathrm{l,F}}$, independent of its origin. Figure 2.3(b) shows a schematic presentation of the magnetic field dependent Zeeman splitting and the resulting optical transitions and their polarization. The electron and hole splittings are linear in B in small fields and match those of the bulk with the additional splitting between the heavy and light holes Δ_lh. In the exciton picture, their angular momentum projection is along the z confinement axis with $J_z = \pm 1$, which corresponds to circularly polarized dipoles rotating in the xy-plane of the QW, either clockwise or anticlockwise. They are fully circularly polarized, $d_x \boldsymbol{e}_x \mp i d_y \boldsymbol{e}_y$ with $d_x = d_y$, which does not depend on the applied magnetic field because the polarization is strictly given by the optical selection rules [30]. The electric field $\tilde{\boldsymbol{E}}$ of the linearly polarized π transitions is normal to the QW plane, $\tilde{\boldsymbol{E}} \parallel \boldsymbol{B} \parallel z$.

2.3.2 Voigt Geometry: Transversal Circular Polarization

The Voigt geometry is used for the transverse routing of light emission (TMRLE) and, thus, is more important for our experiments. Here, the magnetic field B is applied in the QW plane and perpendicular to the quantization axis $\boldsymbol{B} \perp (z \parallel k)$, which leads to a more complex splitting and coupling of the hole wave functions. The Zeeman splitting of the bands is shown schematically in Figure 2.3(c). Due to its isotropy, the conduction band splits the same as in the Faraday geometry. For the holes, the exchange Hamiltonian splits into two subspaces $\hat{H}^{\uparrow\downarrow}$ in the Luttinger form with projections $J_{\mathrm{h},x} = [3/2, -1/2]$ ($\uparrow$) and $J_{\mathrm{h},x} = [-3/2, 1/2]$ ($\downarrow$) of the total angular momentum J_h on the magnetic field direction B_x [30, 46]:

$$\hat{H}^{\uparrow\downarrow} = \begin{pmatrix} -(\gamma_1 + \gamma_2)k_z^2 \pm 3C & \sqrt{3}\gamma_2 k_z^2 \\ \sqrt{3}\gamma_2 k_z^2 & -(\gamma_1 - \gamma_2)k_z^2 \mp C \end{pmatrix}. \tag{2.8}$$

Here, $k_z \approx \pi/d$ is the effective hole wave vector in the z-direction with the QW width d and assuming infinite barrier height. γ_i are the Luttinger parameters and $C = 1/6\, x N_0 \beta \left\langle S_z^\mathrm{Mn} \right\rangle$ like in the Faraday geometry. The Hamiltonian in Eq. (2.8) shows the competition between the Zeeman splitting in the B_x field and the confinement along the z-axis. The splitting of the heavy holes $\Delta_{\mathrm{h,V}}$ is suppressed in the Voigt geometry and requires an admixture of light-hole states, resulting in a cubic dependence on B. In zero magnetic field, the total angular momentum J_h is projected along the quantization axis z with $\pm 3/2$ for heavy holes and $\pm 1/2$ for light holes, like in the Faraday geometry. At low magnetic fields, the heavy holes show no spin splitting, while the light holes split linearly in the magnetic field with $4C$, i.e. twice as much as in the Faraday geometry:

$$\Delta_{\mathrm{l,V}} = 2\Delta_{\mathrm{l,F}}. \tag{2.9}$$

Larger magnetic fields lead to a reorientation of the hole angular momentum along the magnetic field axis. This induces a non-zero circular polarization $P_{c,i}$ of the electric field in the yz-plane (perpendicular to the QW) for the four optical transitions $i = 1, 2, 3, 4$ that are shown as orange and green arrows in Figure 2.3(c). Effectively, the transitions become elliptically polarized in the yz-plane, which corresponds to dipoles with $\mathbf{d}_X^{\pm} = d_y \boldsymbol{e}_y \mp i d_z \boldsymbol{e}_z$ and $d_y > d_z$ for small magnetic fields [30]. This partial circular polarization in the yz-plane is the origin of the TMRLE, in which surface plasmon polaritons with effective transverse spin in the same plane couple to the QW transitions, and the magnetic field induced helicity of the optical transition is translated into routed emission. This is discussed in detail in Chapter 5 and Refs. [30, 48]. Note that the transitions are not fully circularly polarized in the yz-plane perpendicular to the QW, with $P_c = \pm 2 d_y d_z / (d_y^2 + d_z^2) \leq 1$ [30]. Instead, P_c depends strongly on B and is governed by the competition of the QW quantization and the magnetic field. Here, the former aligns the hole angular momentum along the z-axis with the electric field in the QW plane, whereas the magnetic field B_x aligns it along the x-axis and mixes the light- and heavy-hole states. Consequently, $P_c = 0$ for $B = 0$ and increases with B, which can be seen in Figure 2.4. This magnetic field dependence of the circular polarization is in contrast to the Faraday geometry, where the optical transitions are fully circularly polarized in the xy QW plane according to the selection rules and independent of the magnetic field strength. According to our theory, $P_{c,i}$ for the optical transitions $i = 1, 2, 3, 4$ is given by [30, 48]

$$
\begin{aligned}
P_{c,1} = -P_{c,3} &= \frac{-4\,Z^2 + 4(Z_- + 1)Z - 2\,Z_- + 2}{4\,Z^2 - 4(Z_- + 1)Z + 2\,Z_- + 7}, \\
P_{c,2} = -P_{c,4} &= \frac{4\,Z^2 + 4\left(Z_+ + 1\right)Z + 2\,Z_+ - 2}{4\,Z^2 + 4\left(Z_+ + 1\right)Z + 2\,Z_+ + 7}, \\
Z = \frac{\Delta_{l,V}}{\Delta_{lh}}, &\quad Z_\pm = \sqrt{Z^2 \pm Z + 1}\,,
\end{aligned}
\tag{2.10}
$$

where $\Delta_{l,V}$ is the Zeeman splitting of the light holes in the Voigt geometry. It is the main parameter used to describe $P_{c,i}$ for both the light-hole transitions and the energetically lower heavy-hole transitions through the mixing of the hole states. The electric field of the linearly polarized π transitions stays oriented along the x-axis, and they are thus not relevant for the TMRLE.

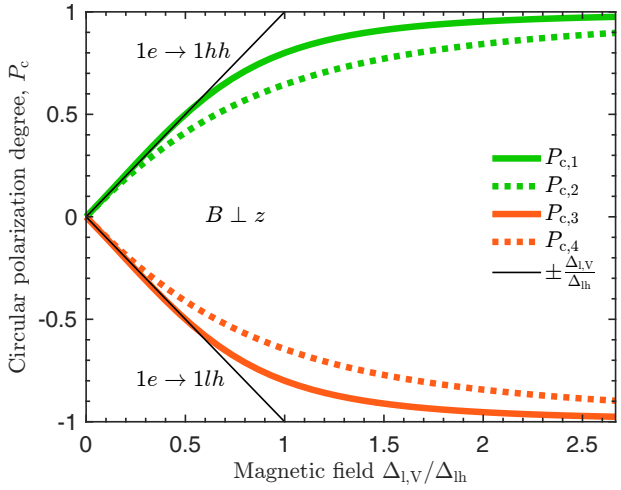

Figure 2.4 Dependence of P_c on the magnetic field (expressed as $\Delta_{l,V}/\Delta_{lh}$) for the optical heavy-hole transitions $1e - 1hh$ (green, upper lines) and light-hole transitions $1e - 1lh$ (orange, lower lines), as indicated in Figure 2.3(c). Bold curves are calculated from Eq. (2.10), the thin black lines corresponds to the approximation Eq. (2.11). Reproduced from [48].

Figure 2.4 shows the dependence of P_c on the magnetic field (expressed as $\Delta_{l,V}/\Delta_{lh}$). The upper

green curves show P_c for the two $1e-1hh$ heavy-hole transitions and the lower orange lines for the two $1e-1lh$ light-hole transitions according to Eq. (2.10). All transitions are linear for small magnetic fields and asymptotically approach $P_c = \pm 1$ for large fields. Interestingly, the heavy-holy transitions $i = 1, 2$ have pairwise opposite polarization degrees to the light-hole transitions 3 and 4, i.e. $P_{c,1} = -P_{c,3}$ and $P_{c,2} = -P_{c,4}$, even though their Zeeman splittings differ significantly. The reason for this is that the polarization of the heavy-hole transition is not directly determined by the Zeeman splitting but rather by the mixing with the light holes. Qualitatively, the polarization perpendicular to the QW plane can best be understood in the limit of large magnetic fields, where the induced Zeeman splitting greatly exceeds the splitting between the heavy- and light-hole subbands Δ_{lh}: In this limit, the valence band states can be characterized by the angular momentum projection $J_x = \pm 3/2, \pm 1/2$ on the x-axis, i.e. fully along the magnetic field. Then, the selection rules enforce the angular momentum conservation along x, and the transitions are fully circularly polarized with $P_{c,1} = P_{c,2} = \pm 1$ and $P_{c,3} = P_{c,4} = \mp 1$ for the heavy and light holes, respectively. For small magnetic fields ($P_c \ll 1$ due to $\Delta_{l,V} \ll \Delta_{lh}$), Eq. (2.10) can be simplified to [30, 48]

$$P_{c,1/2} = -P_{c,3/4} \approx \pm \frac{\Delta_{l,V}}{\Delta_{lh}}, \tag{2.11}$$

so that P_c grows linearly with B via the Zeeman-splitting of the light holes $\Delta_{l,V}$. This approximation is shown in Figure 2.4 as thin black lines, which closely follow the more complex curves of Eq. (2.10) at small fields. Additionally, P_c depends inversely on the energy gap between the heavy- and light-hole subbands Δ_{lh}, with a smaller gap promoting the heavy-light-hole mixing. The two lowest transitions are both into weakly split heavy-hole states with the same population and, crucially, the same sign of P_c so that they do not cancel each other in their contribution to the TMRLE.

Thus far, we used the electron-hole picture to describe the polarization of the optical transitions in the DMS quantum well structure, where the light-hole splitting $\Delta_{l,V}$ alone describes P_c in the approximation of Eq. (2.11). At low temperatures, below the binding energy of excitons, the emission from the QW is given by the exciton emission and not the radiative recombination of the photo-excited electrons and holes. The selection rules and the polarization of the transitions are the same for our purposes, neglecting e.g. the exciton fine structure, and both descriptions are assumed to be equal for the TMRLE.

2.4 Summary

Diluted magnetic semiconductors (DMSs) exhibit large magneto-optical activity due to the exchange interaction of the host band electrons and holes with the magnetic transition metal ions (e.g. Mn), which leads to giant Zeeman splitting. The magnetization of the system is described via the thermal average of the Mn^{2+} spin projection $\langle S_z^{Mn} \rangle$ along the external magnetic field, which can be described using a modified Brillouin function as shown in Eq. (2.2). The exchange interaction can be described using a Heisenberg Hamiltonian of interacting spins (Eq. (2.3)), which can be simplified using the mean field approximation and the virtual crystal approximation. This results in the description of the giant Zeeman splitting using only material properties and $\langle S_z^{Mn} \rangle$, see Eq. (2.6), with the same selection rules and multiplicity as the host material but amplified.

In a quantum well, the Zeeman splitting becomes anisotropic regarding the magnetic field direction due to the quantization of the carriers in one axis (z). For the Faraday geometry with $B \parallel z$, the electrons and holes have the same linear splitting in B as in bulk, but the heavy and light holes are energetically separated by Δ_{lh} due to the confinement and strain. The intrinsic splitting is negligible at low temperatures compared to the large exchange interaction. However, it is also independent of the temperature, which is in contrast to the exchange contribution. The latter decreases quickly for increasing temperatures due to the decreasing average spin orientation $\left\langle S_z^{\mathrm{Mn}} \right\rangle$, see Eq. (2.2). This reveals the possibility of temperature-independent applications, which will be explored in Section 9.5.

Most important for this thesis, however, is the Voigt geometry with $B \perp z$. Here, the Zeeman splitting of the holes is more complex. The light-hole splitting is twice as large as in the Faraday geometry, but the heavy holes split only with an admixture of the light-hole states, and their splitting is small and cubic in B. In this geometry, there is a competition between the confinement along the z-axis and the reorientation along the magnetic field in x-direction, see the Luttinger Hamiltonian in Eq. (2.8). In the magnetic field, the degree of circular polarization of the optical transitions P_{c} perpendicular to the QW plane becomes non-zero. This effect is the origin of the TMRLE, which is one of the main topics of this thesis, as the reoriented exciton transitions can directionally couple to surface plasmon polaritons, which enable and enhance the transverse routing. P_{c} can be described using only the light-hole splitting in the Voigt geometry $\Delta_{\mathrm{l,V}}$ and the heavy-light-hole splitting Δ_{lh}, as shown in Eq. (2.10) and approximated in Eq. (2.11) for small magnetic fields.

Chapter 3

Surface Plasmon Polaritons

Surface plasmon polaritons (SPPs) describe a localized electromagnetic excitation at the interface between a dielectric and a metal that propagates along the interface and is evanescently confined perpendicular to the interface [49]. It combines the description of the oscillations of electromagnetic fields (*polariton*) and of the electron plasma in the metal (*surface plasmon*). For this thesis, SPPs at a magnetic interface are used to significantly enhance the transverse magneto-optical Kerr effect (TMOKE, see Sections 4.3 and 4.4 and Chapter 11). Furthermore, they are an integral part of enhancing the transverse magnetic routing of light emission (TMRLE), see Chapters 5 and 8 to 10.

This chapter is based on the book about SPPs by Maier [49] and the short but comprehensive summary by Belotelov [13]. First, Section 3.1 describes the dielectric function of metals with the Drude model and the dispersion relation of SPPs at a planar metal/dielectric interface. Then, Section 3.2 explains how to enable the interaction of SPPs with light in the far field by substituting the metal film with a periodic metallic grating. Finally, Section 3.3 describes the spin-momentum locking of SPPs, which is a key feature needed for the TMRLE.

3.1 Dispersion Relation

The theory behind SPPs is based on the interaction between metals and electromagnetic fields and can be described in a classical framework using the macroscopic Maxwell equations. A detailed description of these interactions and the derivation of the SPP dispersion relation and other properties is given in Ref. [49], whereas this chapter will only summarize the relevant results.

The optical properties of a metal can be described in a wide frequency range by a model of a free electron gas that moves against a fixed background of positive ion cores. This simple model ultimately results in

$$\varepsilon(\omega) = \varepsilon_\mathrm{b}(\omega) - \frac{\omega_\mathrm{p}^2}{\omega^2 + i\gamma\omega}, \quad \text{with} \quad \omega_\mathrm{p}^2 = \frac{ne^2}{\varepsilon_0 m}, \tag{3.1}$$

which describes the dielectric function $\varepsilon(\omega)$ of noble metals well for energies below the threshold of transitions between electronic bands. Here, ω_p is the plasma frequency, which is the frequency of the collective oscillation of the free electron plasma. ε_b is an additional dielectric constant that accounts for the residual polarization at $\omega > \omega_\mathrm{p}$ due to the positive background of the ion cores compared to the ideal free-electron metal. [49]

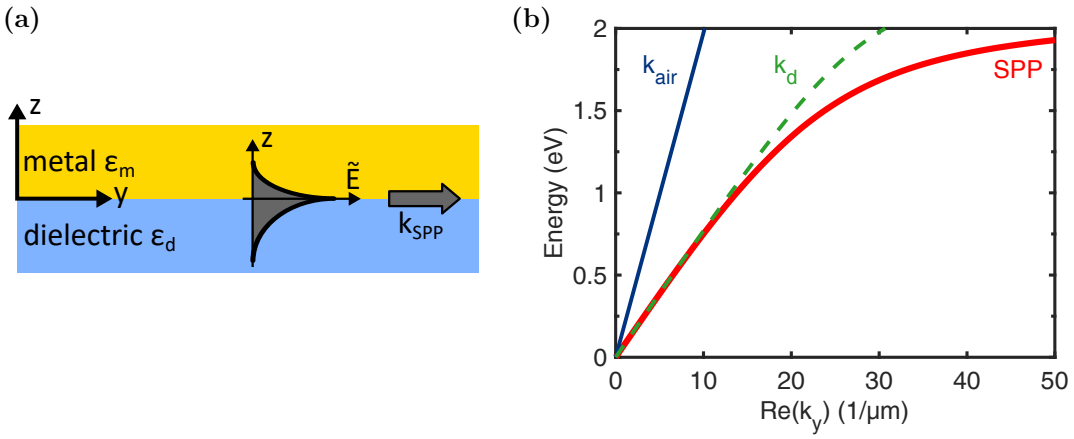

Figure 3.1 (a) Schematic presentation of the metal/dielectric interface supporting SPPs with electrical field $\tilde{E}(z)$, adapted from [13]. **(b)** Dispersion relations $E(k_y)$ of light in air k_{air}, light in the dielectric (Cd,Mg)Te k_d with $\varepsilon_d > \varepsilon_{air}$ and of the SPP at the planar gold/(Cd,Mg)Te interface according to Eq. (3.3).

The simplest geometry supporting SPPs is a flat interface between a conducting metal containing the electron plasma and a dielectric, non-conducting material, see Figure 3.1(a). Let the dielectric be described by a positive ε_d and the conductor by $\varepsilon_m(\omega)$ with $\mathrm{Re}(\varepsilon_m) < 0$ for the metallic character, which holds true below the bulk plasmon frequency ω_p. Solving the wave equation in this geometry with the conditions of a propagating wave solution that is confined to the interface and, therefore, evanescently decaying into the z-direction perpendicular to the interface leads to a set of non-zero E_i and H_i components of the wave. Continuity at the interface of the two media requires

$$\frac{k_d}{k_m} = -\frac{\varepsilon_d}{\varepsilon_m} \tag{3.2}$$

for a TM wave, which confirms the requirement of $\varepsilon_d > 0$ and $\mathrm{Re}(\varepsilon_m) < 0$. Ultimately, the dispersion relation of the SPP wave propagating along the flat interface is

$$k_{SPP} = k_0 \sqrt{\frac{\varepsilon_m \varepsilon_d}{\varepsilon_m + \varepsilon_d}}, \tag{3.3}$$

where $k_0 = \frac{\omega}{c}$ is the vacuum wave number of light with the frequency ω and speed of light c. k_{SPP} is complex, and its imaginary part defines the propagation length along the interface $l_y = 1/\mathrm{Im}(k_{SPP})$ due to damping. Perpendicular to the interface, the electromagnetic field decays exponentially with the rate

$$\gamma_i = k_0 \sqrt{\frac{-\varepsilon_i^2}{\varepsilon_d + \varepsilon_m}}, \tag{3.4}$$

which is shown schematically in Figure 3.1(a) for the electric field $\tilde{E}(z)$. The corresponding attenuation length in the normal direction is $l_{zi} = 1/\gamma_i$. For a TE mode, on the other hand, the continuity at the interface leads to $A(k_m + k_d) = 0$, which is only valid for the wave amplitudes $A = 0$ because $\mathrm{Re}(k_i) > 0$. Therefore, SPPs exist only in TM polarization. [49]

As an example, the dispersion relation of the SPP (3.3) at the interface of gold and the dielectric $Cd_{.75}Mg_{.25}Te$ is shown in Figure 3.1(b) (red curve). This material combination is used in our

experimental studies on the transverse magnetic routing of light emission (TMRLE). The dielectric function of the dielectric is taken from [50] and that of gold from [51]. The experimental data for gold is extended at low energies using the Drude model (3.1) with the constants $\varepsilon_b = 9.9$, $\hbar\omega_p = 9\,\text{eV}$, and $\hbar\omega = 77\,\text{meV}$ from fits to the higher energy data in Ref. [52]. In addition, the light lines in air $k_{y,\text{air}} = k_0\sqrt{\varepsilon_{\text{air}}}$ (blue curve) and $Cd_{.75}Mg_{.25}Te$ $k_{y,\text{d}} = k_0\sqrt{\varepsilon_{\text{d}}}$ (dashed green curve) are shown, assuming light incidence parallel to the interface, i.e. $k_y = k_0 \sin(\theta = 90°)$. The dispersion of the SPP as a bound wave always lies to the right of the air line in the dielectric or air. This wave-vector mismatch prevents direct coupling of light from the air or the dielectric into the SPP mode, and thus SPPs can not be excited optically for a simple planar interface like in Figure 3.1(a).

3.2 Enabling Optical Excitation

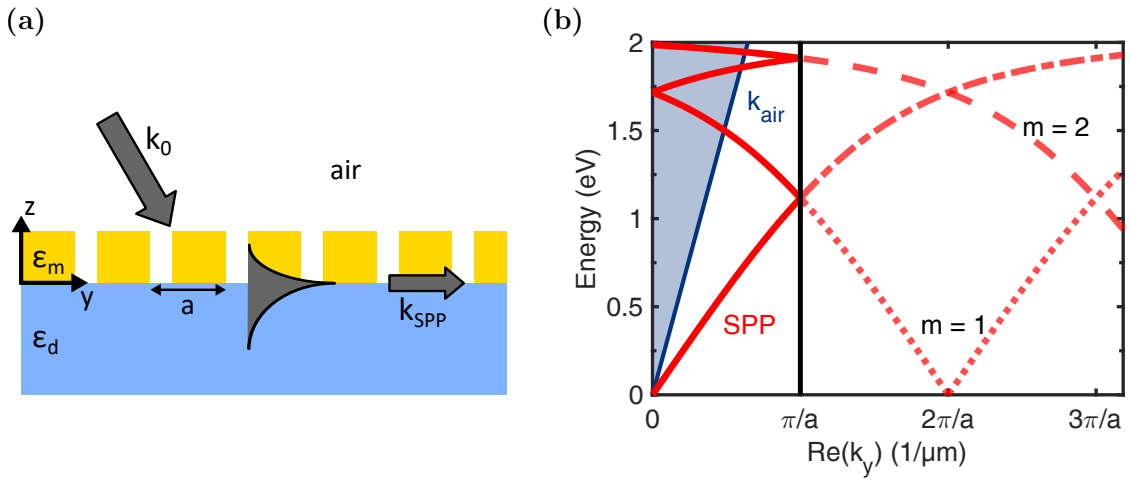

Figure 3.2 (a) Schematic presentation of the metallic grating with period a to enable the interaction between SPPs and light from the far-field with k_0. Adapted from [13]. **(b)** Dispersion relations $E(k_y)$ of light in air k_{air} and of the SPP at the interface of a periodic gold grating with period $a = 200\,\text{nm}$ and $Cd_{.75}Mg_{.25}Te$ according to Eq. (3.5). Blue area contains all light lines between $\theta = 0°$ and $90°$, π/a marks the border of the reduced zone scheme and dotted ($m = 1$) and dashed ($m = 2$) curves are the higher order SPP branches.

The mismatch between the wave vector k_{SPP} of the SPP along the $z = 0$ interface with the in-plane momentum of the impinging photons $k_y = k_0 \sin\theta$ can be overcome in several ways. One of them is using a dielectric prism with large ε_{pr}, where the total internal reflection in the prism leads to an evanescent wave towards the interface and the momentum conservation law can be satisfied along the interface with $k_{\text{SPP}} = k_0\sqrt{\varepsilon_{\text{pr}}}\sin\theta$ [13]. Another method of wave vector matching, which is used for this thesis, utilizes the diffraction effects of periodic structures. As shown schematically in Figure 3.2(a), the planar metal film is substituted with a one-dimensional metal grating with a period a. This provides additional in-plane wave vector components $m2\pi/a$, i.e. multiples of the reciprocal grating vector. The phase-matching between the light with $k_0 = \omega/c$ and the SPPs now takes place under the condition [49]

$$k_{\text{SPP}} = k_0 \sin\theta \pm m\frac{2\pi}{a}, \qquad m = 1, 2, \ldots \tag{3.5}$$

This manifests as additional branches of the SPP dispersion (3.3) in the dispersion diagram originating from $k_y = \pm 2\pi/a, \pm 4\pi/a, \ldots$, which have intersection points with the light line. Similar to the reduced zone scheme of the first Brillouin zone for the phonon dispersion, the SPP dispersion can be drawn up to $k_y = \pi/a$, where it is folded back towards the center. Figure 3.2(b) shows this for a grating with a $a = 200$ nm period. In the reduced scheme, the SPP dispersion $E(k_y)$ (bold red) increases up to $k_y = \pi/a$ before it is folded back towards the center, where it intercepts the blue dispersion line for light in air k_{air}. This corresponds to the $m = 1$ SPP branch originating from $2\pi/a$ and is shown as a red dotted line. It is folded back once more at $k_y = 0$, corresponding to the opposite branch originating from $-2\pi/a$, and again at the zone border, which now corresponds to the $m = 2$ branch from $4\pi/a$ (dashed line). The light dispersion $k_y = k_0 \sin\theta$ with $\theta = 90°$ is shown as a blue line, and lower angles of incidence θ are represented by the shaded area. The interaction of the light and SPP is possible at all these points. In general, the dispersion relation of the SPP at the grating interface differs from that of a plain film, but for narrow holes or slits Eq. (3.3) is still valid. Note, however, that the real dispersion curve splits at the zone borders $k_y = m\pi/a$ and a bandgap appears. The excitation of SPPs is detected as a minimum in the reflected light intensity, and the reverse process of SPPs emitting as light into the far-field is also possible. [13, 49]

3.3 Spin-Momentum Locking

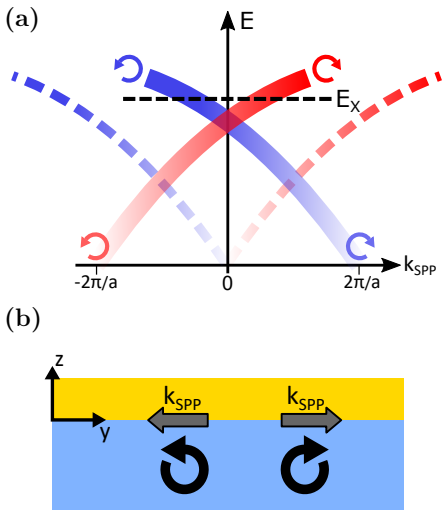

Figure 3.3 (a) Opposite SPP wave vectors k_{SPP} (red, blue) and opposite elliptical polarizations (circular arrows) due to spin-momentum locking. Exciton at energy E_X with same spin can couple directionally. Reproduced from [48]. **(b)** Spin-momentum locking for circular dipole emission close to metal interface via SPPs.

Collimated light in free space has a purely transverse electric field E_0 perpendicular to the propagation direction, and the polarization and propagation direction are independent. This is the easiest solution of the Helmholtz equation

$$(\nabla^2 + \omega^2/c^2)\boldsymbol{E}(\boldsymbol{r}) = 0 \tag{3.6}$$

and $\nabla \cdot \boldsymbol{E} = 0$, which results in perpendicular propagation directions $\boldsymbol{k}$ and electric fields $\boldsymbol{k} \cdot \boldsymbol{E_0} = 0$. However, light can also have longitudinal components of the electric field and even be elliptically polarized in the propagation plane (e.g. yz-plane for light in z-direction) if it is tightly focussed by a large numerical aperture and the transversal and longitudinal components have a phase of $\pi/2$ [31]. Other sources of circular polarization in the propagation plane are evanescent waves at an interface, like SPPs at a metal/dielectric interface. TM-polarized SPPs (and similar photonic modes along the interface) are also a solution of Eq. (3.6), which results in transverse and longitudinal field components E_z and E_y

$$\begin{aligned} E_z(\boldsymbol{r}) &\propto \exp\left(-k_z z + i k_y y\right) \\ E_y(\boldsymbol{r}) &\propto -i(k_z/k_y)\exp\left(-k_z z + i k_y y\right) \end{aligned} \tag{3.7}$$

with a $\pi/2$ phase between them due to the evanescent field in the z-direction and the corresponding imaginary factor i [31]. Therefore, the electric field of the evanescent SPP wave is elliptically polarized in the yz-plane containing its wave vector k_{SPP} and the surface normal z. See Figure 3.3(b) for the geometry. [31]

Interestingly, the propagation direction and polarization of these waves are also no longer independent because all fast-decaying evanescent waves exhibit spin-momentum locking. This property links their propagation direction $\pm\boldsymbol{y}$ along the surface to their transverse spin $\pm\boldsymbol{S}$, i.e.

$$\boldsymbol{k} \propto \boldsymbol{S} \times \boldsymbol{e}_z \,, \tag{3.8}$$

with the surface normal $\boldsymbol{e}_z$ [32]. An analogy for this is a bicycle wheel, which propagates along a defined surface and where the spokes represent the electric field vectors. When the propagation direction is reversed, so is the rotation direction (spin) of the wheel and spokes [31]. Figure 3.3(a) shows the spin-momentum locking in the dispersion diagram of SPPs with opposite wave vector k_{SPP} (red and blue) and circular polarization (circular arrows) due to the spin-momentum locking. The dashed curves represent the SPP dispersion at a homogeneous metal film, and the solid curves that of a grating with period a. The transverse spin of SPPs can be expressed as [42]

$$S_x = \frac{\mathrm{Re}(k_{\mathrm{SPP}}) \times \mathrm{Im}(k_{\mathrm{SPP}})}{[\mathrm{Re}(k_{\mathrm{SPP}})]^2}. \tag{3.9}$$

The real part of k_{SPP} determines the propagation direction. In contrast, the imaginary part is oriented perpendicular to the surface and describes the exponential decay of the evanescent SPP away from the interface.

This inherent feature of SPPs and other evanescent waves is the basis of many interesting applications, like the conversion of circularly polarized light from the far-field into directional propagating SPP waves [41, 42], plasmon-to-exciton spin conversion [43], or many other chiral routing effects [38, 39]. In this thesis, we use the spin-momentum locking of SPPs for the transverse emission routing from excitons (TMRLE, see Chapter 5). Without going into too much detail here, the basis is a circularly polarized dipole emitter with the electric field of its emission in the yz-plane so that it spins around the x-axis. This is shown in Figure 3.3(b) as black circular arrows. In free space (not shown), the emission is equal in all lateral directions and, therefore, independent of the dipole rotation direction. If the transversely spinning dipole is placed close to a metal interface, instead, it couples to evanescent waves (SPPs and arbitrary photonic modes) which propagate along the interface. The coupling efficiency between the dipole emitter and the respective wave depends on the overlap of the spinning dipole moment and the rotating electric field of the evanescent surface wave. Therefore, clockwise rotating dipoles preferentially couple to either left- or right-going waves and vice versa for anticlockwise rotation. This results in a translation of the dipole emitter polarization into routed emission along the interface via spin-momentum locking of the evanescent wave. Figure 3.3(b) shows this schematically with the two oppositely rotating dipole emitters (circular arrows) close to the metal interface that couple to SPPs with opposite k_{SPP} (straight arrows). In the SPP dispersion relation in Figure 3.3(a), the excitons as dipole emitter are represented by the black dashed line at the constant energy E_{X}. They can couple to either blue or red SPP modes of the same energy with opposite circular polarization and propagation direction. For further details, check the thesis of Felix Spitzer [52], the supplement of [30], or Ref. [31] for a more general overview of the transverse spin of light.

Chapter 4

Magneto-Optical Effects

The field of magnetooptics or magneto-optical effects describes the interaction between light and magnetized matter in a magnetic field. The magnetic field alters the optical properties of the medium, influencing the intensity and polarization of reflected or transmitted light. Well-known examples of magneto-optical effects are the Faraday effect, which describes the rotation of the polarization plane of linearly polarized light transmitted through a magnetized medium, or the magneto-optical Kerr effects (MOKEs), which are usually considered for light reflected from the surface of a magnetized medium and influence the reflected intensity and polarization characteristics of the light [1]. Therefore, magneto-optical effects can be used as a sensitive probing tool of the magnetic properties of a structure, for example in time-resolved pump-probe measurements for optically oriented electron spins [43], to detect spin waves via magnetization changes in magnetic garnet films [53–55] or for reading high-density data from magneto-optical data storage [56]. The other way around, magneto-optical effects can also be used to actively modify the characteristics of the reflected or transmitted light in a variety of applications, for example in ultrafast optical switches, where short optical pulses quickly change the magnetization of the magnetic medium [57], or to control light at the nanoscale through the increased magneto-optical effects at optical resonances [15, 17, 58–60]. For this thesis, the Faraday effect is used to obtain the magneto-optical parameters of a thin magnetite film (Section 11.1) and the transverse MOKE to observe optical resonances with greater contrast than non-magnetic measurements in Chapter 11 [4].

First, Section 4.1 will introduce the dielectric permittivity tensor $\hat{\boldsymbol{\varepsilon}}$ and the gyration g that are used for the macroscopic description of magneto-optical effects. The Faraday effect is explained in Section 4.2, which is used in the experimental part of this thesis to obtain magneto-optical parameters of the investigated structures for further theoretical analysis and simulation. Then, Section 4.3 introduces the transverse magneto-optical Kerr effect (TMOKE), a special case of the magneto-optical Kerr effects, which manifests as changes in the reflected intensity of light. The TMOKE is a comparatively weak effect but can be enhanced significantly in the vicinity of optical resonance, which is described in Section 4.4. Experimental data of the TMOKE from magnetite structures near optical resonances is presented later in Chapter 11.

4.1 Macroscopic Description

The description of magneto-optical effects is usually based on the influence of the magnetic field on the dielectric permittivity ε of the magnetized material, which is expressed as $\hat{\boldsymbol{\varepsilon}}$-tensor with elements ε_{ij}, $i, j = (x, y, z)$. In the magnetized state, the tensor depends on the magnetization M of the medium or antiferromagnetic sublattices, which is induced by an external magnetic field B in our experiments. For the case of an optically isotropic medium, $\varepsilon_{xx} = \varepsilon_{yy} = \varepsilon_{zz} \equiv \varepsilon$, and the tensor can be written as [1, 4]

$$\hat{\boldsymbol{\varepsilon}} = \begin{pmatrix} \varepsilon & 0 & 0 \\ 0 & \varepsilon & 0 \\ 0 & 0 & \varepsilon \end{pmatrix} + \begin{pmatrix} 0 & -ig_z & ig_y \\ ig_z & 0 & -ig_x \\ -ig_y & ig_x & 0 \end{pmatrix} . \tag{4.1}$$

Here, the first part only contains the dielectric permittivity ε of the non-magnetized material, and the second part describes the changes induced by the magnetic field via the off-diagonal elements comprising the gyration vector $\boldsymbol{g}$. The gyration is proportional to the magnetization $\boldsymbol{g} = \alpha \boldsymbol{M}$ in the isotropic medium. α is assumed to be equal for all directions of M and thus $g_x = g_y = g_z = g$. Therefore, only the respective elements remain nonzero in Eq. (4.1) for magnetization along either x, y, or z. ε and g become complex functions of the frequency if absorption takes place. The second part of Eq. (4.1) results, for example, in different refractive indices $n_\pm$ for left- and right-circularly polarized light, which manifests as the Faraday effect for transmitted light. In all cases relevant to this thesis, the magnetic permeability tensor $\hat{\boldsymbol{\mu}}$ is assumed to be unity. [1]

4.2 Faraday Effect

The Faraday effect is probably the best known of the magneto-optical effects and can be used to obtain magneto-optical properties of a structure. The effect was discovered in 1845 by Michael Faraday and was the first demonstration of the connection between magnetism and light [2]. It describes the rotation of the polarization plane of linearly polarized light that propagates through a magnetized medium in a magnetic field B parallel to the direction of light propagation [1]. This is schematically shown in Figure 4.1, and the geometry of the light propagation with respect to the magnetic field is fittingly called the Faraday geometry, see also Section 2.3. The rotation of the polarization can be explained by different refractive indices $n_\pm$ for the left- and right-circularly polarized light ($\sigma^\pm$) in the magnetized medium, which are the eigenmodes of the system. The incident linearly polarized light can be decomposed into these two circular eigenmodes $\boldsymbol{e}_\pm$, where their relative phase defines the polarization plane of the linear polarization. Then, the two components acquire a phase difference traveling in the medium with different velocities $c/n_\pm$, which leads to the rotation angle ϑ of the recomposed components

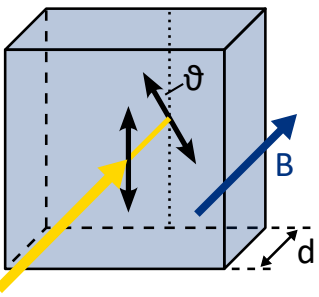

Figure 4.1 Geometry and polarization rotation of the Faraday effect in a magnetic field B. Adapted from Ref. [44].

$$\vartheta(\omega) = \frac{\omega}{2c} d \left(n_+(\omega) - n_-(\omega) \right) , \tag{4.2}$$

which is half the acquired phase shift through the medium with thickness d. Here, ω and c are the angular frequency and the speed of light, respectively. [1, 44]

Sources for large differences between n_+ and n_- are optical transitions that correspond to light absorption at a certain frequency affected by a magnetic field [44]. An easy example of this is the magnetic-field-induced Larmor precession of electron orbits. As explained in Ref. [1], two eigenfrequencies $\omega_\pm$ arise, which correspond to left and right circular oscillations. This leads to the splitting of the absorption line and, consequently, to a relative displacement of the two curves $n_\pm(\omega)$. Other examples are the interband transitions in a diluted magnetic semiconductor (DMS), which exhibit a giant Zeeman splitting and, thus, an equally large Faraday rotation that exceeds $1\,^\circ/(\mathrm{mm\,mT})$ close to the exciton resonance for (Cd,Mn)Te at 4.2 K [61]. Note that the rotation is two orders of magnitude smaller at room temperature due to the large temperature dependence of the Zeeman splitting in DMS, see Chapter 2.

The Faraday rotation can be used to probe the magnetic properties of a sample. For a transparent medium without absorption, the transmitted light remains linearly polarized with the acquired rotation angle ϑ due to the magnetic circular birefringence $n_+ \neq n_-$, i.e. the Faraday effect. For a medium exhibiting absorption, the absorption coefficients for left- and right-circular light also become different in a magnetic field, which is called magnetic circular dichroism (MCD). If linearly polarized light is transmitted through such a medium, the light becomes elliptically polarized due to the MCD, and the major axis of the polarization ellipse is rotated by the angle ϑ due to the magnetic circular birefringence. For materials with cubic symmetry or crystals where the light wave vector and magnetization are oriented along a symmetry axis, the rotation ϑ and ellipticity ψ are connected to the complex gyration $g = g' + ig''$ via [1]

$$\vartheta = -\frac{g'\pi}{\lambda n_0} d \qquad \text{and} \tag{4.3}$$

$$\psi = -\frac{g''\pi}{\lambda n_0} d, \tag{4.4}$$

where $\lambda = 2\pi c/\omega$ is the light wavelength, d the thickness of the magnetic film and n_0 its refractive index. Measuring the rotation angle ϑ and the ellipticity ψ can, therefore, be used to experimentally acquire the real and imaginary parts of the gyration $g = g' + ig''$, respectively. This will be used in Chapter 11 to characterize the magneto-optical properties of the thin magnetite (Fe_3O_4) film for theoretical simulations of that structure and its magneto-optical response presented in Ref. [4]. This comparatively easy model works well for the plain magnetite film because it does not exhibit optical resonances in the measured spectral range.

4.3 Transverse Magneto-Optical Kerr Effect (TMOKE)

The magneto-optical Kerr effect (MOKE) is another well-known magneto-optical effect, which describes the changes to light reflected from the surface of a magnetized medium due to optical anisotropy. It is named after John Kerr, who discovered the effect in 1877 for light reflected from the polished pole of an electromagnet [1, 3]. Depending on the orientation of the external magnetic field B (or the magnetization M) with respect to the surface and the incidence plane of the light, the effect is split into three geometries: For the *polar* and the *longitudinal* MOKE, the magnetic field

is oriented in the plane of incidence and normal or parallel to the reflecting surface, respectively. Their influence manifests in the rotation of the polarization plane and the appearance of ellipticity for the reflected linearly polarized light. The *transverse* magneto-optical Kerr effect (TMOKE), on the other hand, is mainly an intensity effect and describes the magnetic-field-dependent change of the intensity of linearly p-polarized light reflected at an angle θ. The geometry is shown in Figure 4.2, where the black arrows indicate the p-polarization of the light (yellow). In this geometry, the magnetic field B_x is oriented parallel to the surface but perpendicular to the yz incidence plane of the light so that the projection of the light wave vector k onto B is zero. The TMOKE is measured by comparing the reflected (or transmitted) light intensities I at opposite magnetic field directions $\pm B$:

$$\delta = 2\,\frac{I(+B) - I(-B)}{I(+B) + I(-B)}\,. \tag{4.5}$$

The factor 2 originates from the normalization with the average intensity $1/2\,(I(+B) + I(-B))$ instead of the intensity at zero field $I(0)$ found in some literature. It is an odd effect in the magnetization and generally has a small magnitude with relative intensity changes δ in the order of 10^{-3}. [1] While usually used in the reflection geometry, the TMOKE can also be measured for transmitted light. This requires structures with a lack of mirror symmetry regarding the opposite boundary layers of the magnetic film, e.g. with different materials on either side of the magnetic film or by adding a periodic grating structure at the surface [4, 13, 17].

For a theoretical description of the TMOKE, we use the macroscopic $\hat{\varepsilon}$-tensor with the additional off-diagonal elements containing the gyromagnetic vector g due to the magnetization of the material, see Eq. (4.1) with $g_y = g_z = 0$ for $B = B_x$. The magnetic permeability is assumed $\mu = 1$, and n_1 is the refractive indices of the medium containing the incident wave and $n_2 = \sqrt{\varepsilon}$ that of the reflecting medium. The full derivation can be found in [1]. Assume a plane wave incident onto the magnetized medium at the angle θ with the electric field vector in the incidence plane (p-polarization), which is reflected at the same angle (see Figure 4.2), but also excites a wave in the magnetized medium that propagates from the interface into the medium. In an unmagnetized medium, the electric field $\boldsymbol{E}$ of that wave contains only the standard transverse components of light. However, in a magnetized medium, the electric field is elliptically polarized in the yz incidence plane due to an additional longitudinal component oriented along the wave vector and proportional to the magnetization, which is expressed via the magneto-optical parameter $Q = g/\varepsilon$. This additional component in the field vector is the cause of the magneto-optical effect. Matching the tangential components of $\boldsymbol{E}$ and $\boldsymbol{H}$ at the interface for the incoming, reflected, and transmitted waves leads to magnetization-dependent transmission and reflection coefficients with corrections to the conventional Fresnel coefficients that are linear in Q [1, p. 44]. This results in the relative change of the reflected light intensity [1, p. 47]

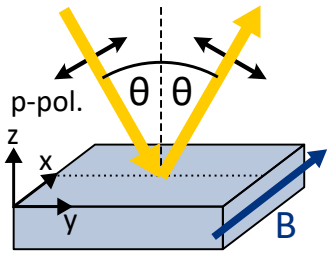

Figure 4.2 Geometry of the TMOKE with B parallel to the surface and perpendicular to the plane of incidence.

$$\delta = -\,\mathrm{Im}\left(\frac{8\eta^2 \tan\theta}{(\eta^2 - 1)(\eta^2 - \tan^2\theta)}Q\right) \tag{4.6}$$

with $\eta = n_2/n_1$ and $n_1 = 1$ for air. Equation (4.6) also shows that the TMOKE requires an absorbing medium with $\mathrm{Im}(n_2) \neq 0$, as otherwise $\delta = 0$. For s-polarized incident light (electric field vector

perpendicular to incidence plane), the TMOKE vanishes because the reflected and transmitted waves are also fully s-polarized, without longitudinal components proportional to Q. [1]

4.4 TMOKE Enhancement at Optical Resonances

The reflection (or transmission) spectra of plain magnetic films are usually monotonic and featureless, and the TMOKE magnitude is small at around $\delta = 10^{-3}$, even for ferromagnets. This limits its applicability [15]. It can, however, be significantly enhanced in the vicinity of an optical resonance [1, 15]. These include, but are not limited to, surface plasmon resonances [15, 17, 62–64], waveguide modes [65], excitons [60], and other optical resonances [58, 59, 66–68]. For example, Belotelov et al. achieved $\delta = 1.5\times10^{-2}$ from a nanostructured gold grating on top of a ferromagnetic iron garnet film for transmitted light in the vicinity of plasmonic resonances and up to 13 % in bismuth-substituted iron garnets (BIGs) covered with gold gratings [17]. Farther spaced-out gold nanowires on BIG still lead to large TMOKE magnitudes of 1.5 % for coupled particle plasmons and waveguide modes while maintaining a high transparency of the system. For the narrow excitonic resonance in a plain (Cd,Mn)Te QW, $\delta = 1\,\%$ was achieved with different contributions for the confinement-split heavy- and light-hole excitons [60].

The general mechanism behind the enhanced magneto-optical effects near resonances are magnetic-field-induced changes to the resonance frequency through the dielectric permittivity ε. For example, the dispersion relation of the surface plasmon polariton (SPP) at the interface of a plain metal film and a dielectric without an external magnetic field $k_{\mathrm{SPP},0}$ can be approximated by Eq. (3.3). This SPP resonance appears as a pronounced dip in a reflection spectrum, contrasting the monotonic spectrum of plain films. In a magnetic field, this wave number k_{SPP} of the SPP resonance changes. For the interfaced plain dielectric and metal films, the influence of the magnetic field can be described via the gyration $g \propto M$ [15, 69]

$$k_{\mathrm{SPP}} = \underbrace{k_0\sqrt{\frac{\varepsilon_\mathrm{m}\varepsilon_\mathrm{d}}{\varepsilon_\mathrm{m}+\varepsilon_\mathrm{d}}}}_{=k_{\mathrm{SPP},0}}(1+\alpha g), \tag{4.7}$$

with $\alpha = (-\varepsilon_\mathrm{m}\varepsilon_\mathrm{d})^{-1/2}(1-\varepsilon_\mathrm{m}^2/\varepsilon_\mathrm{d}^2)^{-1}$. Here, $k_0 = \frac{\omega}{c}$ is the vacuum wave number of light with the frequency ω and speed of light c, and ε_m and ε_d are the dielectric constants of the unmagnetized metal and dielectric, respectively. Equation (4.7) holds as long as the thickness of the metal film exceeds several tens of nm and the SPPs at the two metal interfaces are independent. Therefore, the wave vector k_{SPP} differs for opposite magnetic fields, and the associated intensity dip shifts to larger or smaller energies depending on the magnetic field direction. This magneto-optical non-reciprocity significantly enhances the TMOKE signal δ in the otherwise monotonic reflection spectrum. Equation (4.7) is also valid for a perforated metal film, e.g. a one-dimensional gold grating, as long as the grating slits are much smaller than the SPP wavelength. Metallic gratings with period a are one way of enabling the optical excitation of SPPs by adding the multiples m of the reciprocal grating vector $2\pi/a$ to the incoming light, see Chapter 3. In combination with Eq. (4.7), this leads to the magnetic-field-induced shift $\Delta\lambda$ of the SPP resonance wavelength λ_0 with $k_{\mathrm{SPP},0}$ according to Eq. (3.3) [69]:

$$\frac{\Delta\lambda}{\lambda_0} = \frac{k_{\mathrm{SPP},0}\,\alpha}{mG}g. \tag{4.8}$$

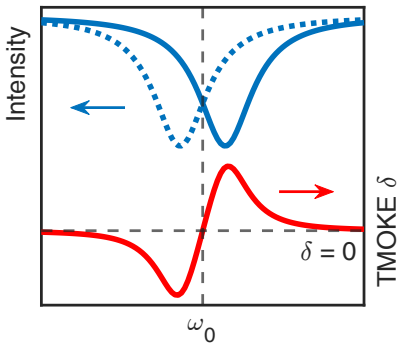

Figure 4.3 Top: Arbitrary Lorentzian resonances at $\omega_0 \pm \Delta\omega$. Bottom: Resulting S-shaped TMOKE signal δ.

Similarly, it can be shown that the dispersion relation of guided modes κ in a thin magnetic layer also shows magneto-optical non-reciprocity, so that κ becomes magnetic-field dependent and, crucially, that this dependence is odd in the magnetic field direction $\pm B$ [13]. This also leads to a shift to lower or higher energies in the reflection or transmission spectra and, thus, an enhanced TMOKE response of the structure compared to a plain film. With a periodic structure, they have the same general resonance condition $\kappa = k_0 \sin\theta \pm 2\pi m/a$ for light in the far-field. It should be noted that the eigenmodes of the system (waveguide, SPP) become leaky due to the periodic grating structure. Therefore, the guided modes should rather be called quasi-guided modes, and their resonances in the reflection and transmission spectra have a typical shape of a minimum followed by a maximum or vice versa. This type of resonance is called a Fano resonance. They appear when a resonant process (eigenmode excitation via grating diffraction) and a non-resonant one (wave propagation through the structure) are connected [13, 70]. Different modes can also interact and form hybridized modes, for example particle plasmons and waveguide modes [63] or waveguide modes in a magnetic medium and the SPP resonance at the spatially close non-magnetic metal/air interface [4].

The TMOKE signal created by a shifting resonance usually has an S-shape with a sign-change of δ. This can be shown easily for a resonance at the frequency ω_0 with a Lorentzian shape in the form

$$L_0(\omega) = \frac{I_0 \gamma^2}{(\omega - \omega_0)^2 + \gamma^2}, \tag{4.9}$$

with the parameters I_0 and γ. If the resonance frequency shifts from ω_0 to $\omega_0 \pm \Delta\omega$ and $0 < \Delta\omega \ll \gamma$, the two resulting Lorentzian peaks $L_{1,2}$ can be approximated as [4]

$$L_{1,2}(\omega) \approx L_0(\omega)\left[1 \mp \frac{2\Delta\omega(\omega - \omega_0)L_0(\omega)}{I_0\gamma^2}\right]. \tag{4.10}$$

The resulting TMOKE signal for this arbitrary resonance is

$$\delta = 2\,\frac{L_2(\omega) - L_1(\omega)}{L_2(\omega) + L_1(\omega)} = \frac{4\Delta\omega(\omega - \omega_0)L_0(\omega)}{I_0\gamma^2}, \tag{4.11}$$

which is zero at the non-shifted resonance position ω_0 and has opposite signs on either side of it. This is visualized in Figure 4.3, which schematically shows two Lorentzian resonances shifted from their non-magnetic resonance frequency ω_0 in the upper part (blue) and the resulting S-shaped TMOKE signal around $\delta = 0$ according to Eq. (4.5) at the bottom (red). The sign change of the resonant TMOKE signal can provide better contrast for resonance observation than the standard transmission and reflection spectra with broad or non-visible optical resonances. [4]

Chapter 5

Transverse Magnetic Routing of Light Emission (TMRLE)

Most magneto-optical effects, like the Faraday effect and the magneto-optical Kerr effects presented in Chapter 4, either modify the properties of light transmitted through a magnetized medium or reflected from its surface. The Faraday effect, for example, rotates linearly polarized light during transmission. In contrast, the transverse magneto-optical Kerr effect (TMOKE) influences the intensity of reflected (or transmitted) light depending on the magnetic field. They have in common that most of them can be enhanced significantly in the vicinity of optical resonances, for example surface plasmon polaritons (SPPs) for the TMOKE (Section 4.4). A less common class of magneto-optical effects takes place for light emitted from a magnetized structure. One of them is the transverse magnetic routing of light emission (TMRLE), which was first reported in Ref. [30] for the routing of the light emitted from excitons in a diluted magnetic semiconductor quantum well structure. The magnitude of the emission routing by the transverse magnetic field was significantly increased by introducing a plasmonic interface close to the quantum well, which utilizes the strong spin-momentum locking of the SPPs (see Section 3.3).

Routing the emission of a nanoscale light source and controlling its emission properties is important for the information transmission and processing in on-chip devices like integrated photonic or optoelectronic circuits [37, 71]. Two-dimensional transition metal dichalcogenides (TMDCs) are interesting candidates for such nanoscale light sources, but their low quantum efficiency and poor emission directionality need to be improved for meaningful applications [37, 71, 72]. Therefore, one direction of current research focuses on TMDCs [72–74] and other quantum emitters [71, 75, 76] combined with passive structures like nanoantennas or nanoresonators to both decrease the emission lifetime and route the emission into a specific direction that is mostly defined by the structures geometry and does not depend on, e.g., the emitters polarization. Other examples for such passive routing structures are fluorescence molecules surrounded by a circular plasmonic antenna [77] or a plasmonic nanoantenna routing its own emission [78]. The chirality of the emitter can also be used as a parameter to route the emission into different directions, so that it can be used as an additional degree of freedom [37]. This has been shown, e.g., for asymmetric photonic crystal waveguides [38], symmetric nanophotonic waveguides with an off-center emitter [39], or for orthogonal waveguides around a quantum dot emitter [40]. In those cases, the emitter polarization is controlled via a magnetic field in Faraday geometry, contrary to the TMRLE in Voigt geometry. Theoretically predicted to route the emission of a chiral emitter via spin-momentum locking is, e.g., the gap plasmon between a nanorod and a nanowire [37], and Ref. [79] explores the symmetry mechanisms in emitter-waveguide systems, while Ref. [80] shows that nanophotonic slabs can be

used for chiral routing applications. The other way around, the spin-momentum locking of surface waves like plasmons can also be used to translate circularly polarized light from the far-field into directional propagating waves [41, 42], or to optically orient exciton spins via plasmons excited with linearly polarized light [43].
In contrast to most of these effects, the TMRLE is a transverse effect with the magnetic field in Voigt geometry controlling the emitter polarization and consequently the emission direction perpendicular to the magnetic field. We use a diluted magnetic semiconductor quantum well as a well-understood model system, but the TMRLE is a general concept that is transferable to any system fulfilling its two key requirements, see below. Furthermore, Chapter 10 will demonstrate the TMRLE as a sensitive tool to probe the weak coupling between the excitons as light source and the plasmons resonantly enhancing the routing effect.

This chapter will summarize the concepts behind the TMRLE based on the model system of a diluted magnetic semiconductor (Cd,Mn)Te/(Cd,Mg)Te quantum well structure in the vicinity of a metal/dielectric interface that supports SPPs and is based on Refs. [30, 48]. It builds on several aspects discussed in the previous chapters, like the giant Zeeman splitting of exciton levels in DMS (Chapter 2) and the spin-momentum locking of SPPs (Section 3.3).

5.1 General Description of the TMRLE

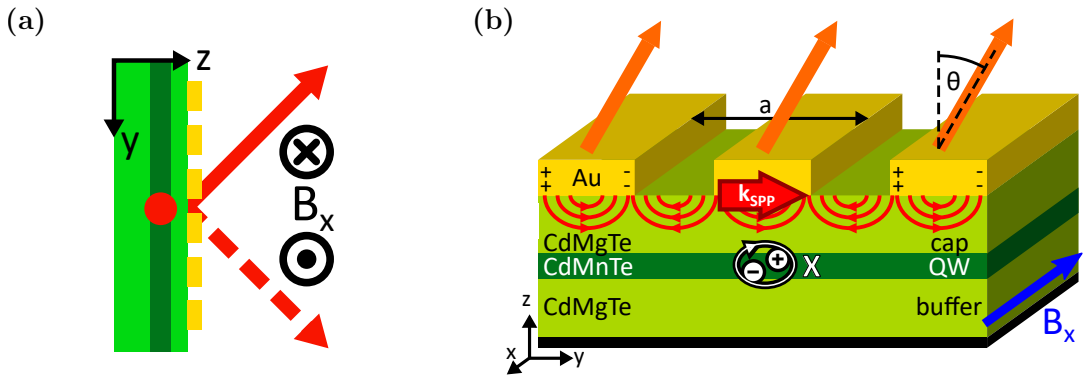

Figure 5.1 (a) Scheme of TMRLE geometry. **(b)** Schematic presentation of the enhanced TMRLE in hybrid plasmonic-semiconductor quantum well structures, where the exciton (X) transitions in the QW become elliptically polarized in the yz-plane due to the magnetic field B_x and directionally couple to SPPs (red) at the gold/semiconductor interface. The metal grating enables their detection as directional emission in the far-field. Reproduced from [48].

The TMRLE describes the magnetic routing of the emission from a light source in the direction perpendicular to the applied magnetic field, with the light source located close to the surface of the emitting structure. It manifests as a change in the angular distribution of the far-field emission intensity $I(\theta)$ induced by the external magnetic field B. The geometry of the effect is shown in Figure 5.1(a), where an external magnetic field B in x-direction leads to directional emission into the far-field in the yz-plane. Inverting the magnetic field direction $B \rightarrow -B$ also shifts the emission towards the opposite direction $-\theta$.

Generally, the TMRLE has two key requirements: First, the selection rules of the light source transitions in the structure need to be modifiable by a magnetic field, and second, the emitted light needs to have non-zero transverse spin $\boldsymbol{S} \parallel x \perp \boldsymbol{k}$ with $\boldsymbol{k} \propto \boldsymbol{B} \times \boldsymbol{e}_z$ pointing in the routing direction y. In our case, the light source is an exciton in a magnetic quantum well (QW) with the diluted magnetic semiconductor (Cd,Mn)Te as well medium that exhibits giant Zeeman splitting. The barriers are comprised of non-magnetic (Cd,Mg)Te. Without a magnetic field, the excitons have the angular momentum projection $J_z = \pm 1$, which is oriented along the QW confinement axis that points toward the surface. This corresponds to circular dipoles that rotate in the xy QW plane $d_x \boldsymbol{e}_x \mp i d_y \boldsymbol{e}_y$ with $d_x = d_y$. By applying a magnetic field B_x in the QW plane, the optical selection rules are modified and the transitions become elliptically polarized in the yz-plane, perpendicular to the QW plane and the confinement direction. This corresponds to a dipole $d_y \boldsymbol{e}_y \mp i d_z \boldsymbol{e}_z$ with $d_y > d_z$ and is shown schematically in Figure 5.1(b) for the exciton $\boldsymbol{X}$ in the QW, where the elliptical polarization rotates in the yz-plane. Important for the TMRLE is the degree of circular polarization in the xy-plane P_c, which is defined as $P_\mathrm{c} = \pm 2 d_y d_z / (d_y^2 + d_z^2)$. Therefore, $P_\mathrm{c} = 1$ for a fully circular dipole in the yz-plane ($d_y = d_z$), which would be the case for large magnetic fields, and otherwise $P_\mathrm{c} < 1$ for elliptical polarization. P_c can also be expressed as

$$P_\mathrm{c} \approx \frac{\Delta_{\mathrm{l,V}}}{\Delta_{\mathrm{lh}}}, \tag{5.1}$$

according to Eq. (2.11), which is more relevant to the experimental studies and holds true for small splittings $\Delta_{\mathrm{l,V}} \ll \Delta_{\mathrm{lh}}$. Here, $\Delta_{\mathrm{l,V}}$ is the Zeeman splitting of the light holes in the Voigt geometry, which depends on the applied magnetic field, and Δ_{lh} is the energy splitting between the heavy- and light-hole subbands due to confinement and strain. For details, see Section 2.3 on the Zeeman splitting in DMS QWs. The directionality of the emission is expected to be weak in bulk material because the propagation direction of a conventional electromagnetic wave does not depend on its polarization. [30, 48]

The routing is increased if the emitter is located close to the surface of the emitting structure, which breaks the mirror symmetry in the z-direction. There, the exciton emitter can couple to photonic modes, which exhibit spin-momentum locking, i.e. their spin is linked to their propagation direction (Section 3.3). This translates the magnetic-field-induced polarization of the emitter P_c into a preferred propagation direction along the interface, and stronger emission routing is established. The largest directional emission was obtained in Ref. [30] by coupling the emitter with surface plasmon polaritons (SPPs) at a nearby gold/dielectric interface, which are also elliptically polarized in the yz-plane, as shown in Figure 5.1(b) and discussed in Section 3.3. Now, the excitons X couple predominantly to SPPs (shown in red) with the same polarization helicity. SPPs possess a strong spin-momentum locking, so their spin $\pm S_x$ is linked to their propagation direction along the interface $\pm k_\mathrm{SPP}$. Furthermore, the spatial localization at the nanoscale and the corresponding increased electric field of the SPPs enhance the TMRLE further [30]. If the gold layer at the surface is perforated into a one-dimensional grating, the guided evanescent SPPs can couple out as directional photon emission into the far-field, which is accessible in the experiments (see Chapter 3 about SPPs for details). Therefore, to quickly summarize the effect, the propagation and emission direction of the SPPs is now linked to the direction of the magnetic field via the direction and circularity of the dipole rotation $\pm P_\mathrm{c}$ in the QW, and strong emission routing transverse to the magnetic field is established.

To quantify the TMRLE in experiments, it is convenient to measure the emitted intensity $I(E,\theta)$ for the two opposite magnetic field directions $\pm B$ and compare them. The relative change of the emission intensity induced by the magnetic field can be quantified as

$$\rho = \frac{I(+B) - I(-B)}{I(+B) + I(-B)}, \tag{5.2}$$

which compares the emitted intensities I at opposite magnetic field directions and normalizes the difference with the sum of the intensities. Therefore, positive values of ρ indicate a higher light intensity emitted for positive than negative magnetic field at a certain angle and photon energy, and negative values vice versa, with a maximum of $|\rho| = 100\,\%$ if the whole emission is routed by the magnetic field. This equation is similar to Eq. (4.5) describing the TMOKE δ. Since the intensity change due to the TMRLE is an odd function of the emission angle θ [30], i.e. $\rho(\theta) = -\rho(-\theta)$, the magnetic-field-induced directionality of the emission C can be expressed as the antisymmetric part of ρ regarding the emission angle

$$C = [\rho(\theta) - \rho(-\theta)]\,, \tag{5.3}$$

which removes all omnidirectional, symmetric changes of the emission intensity from the measured data.

5.2 Near- and Far-Field Contributions

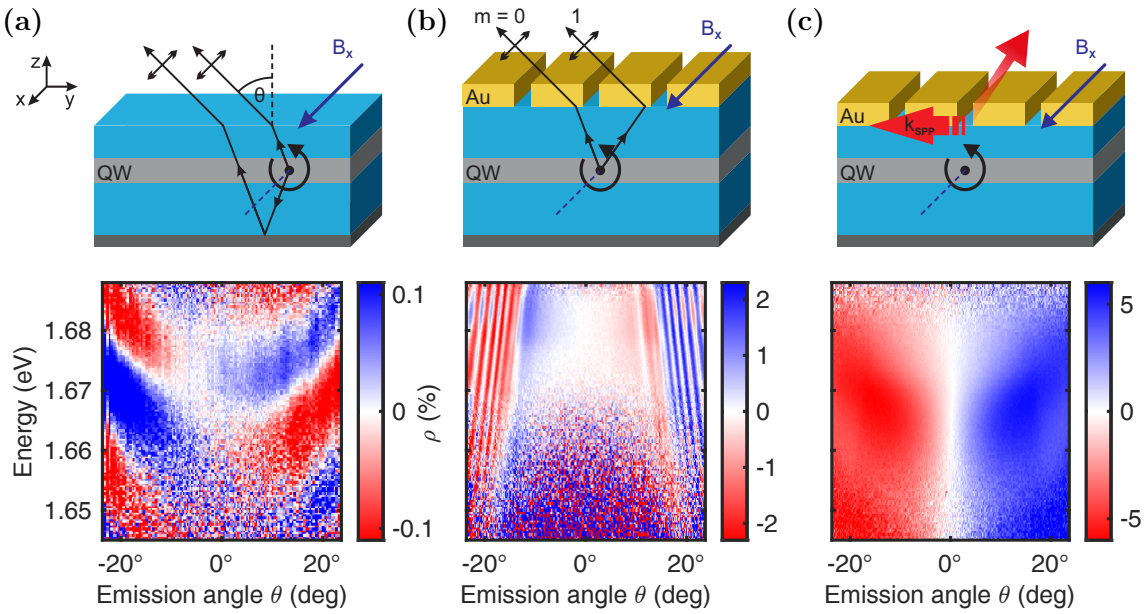

Figure 5.2 Main contributions to the TMRLE with a schematic presentation of the contribution (top) and the corresponding $\rho(E,\theta)$ data (bottom). **(a)** Bare QW structure: Interference between directly emitted and backside-reflected light outside the sample. **(b)** Hybrid structure with thick cap layer (250 nm): Interference between different diffraction orders ($m = 0, 1$). **(c)** Hybrid structure with thin cap layer (32 nm): Near-field effect of QW excitons emitting into SPP modes at the nearby metal/semiconductor interface. Adapted from [30].

With the basic concept of the TMRLE covered, this section will summarize the primary contributions to the TMRLE directionality signal from a real structure, as they were presented in Ref. [30]. A total of three different samples were used, which are based on two different bare (Cd,Mn)Te/(Cd,Mg)Te semiconductor QW structures. They are shown schematically in Figure 5.2 and described in detail in Refs. [30, 52]. Briefly summarized, the two semiconductor structures feature a 10 nm thin magnetic QW layer of (Cd,Mn)Te sandwiched between two layers of (Cd,Mg)Te as the barrier material. The buffer layer towards the substrate at the bottom is a few µm thick and not highly relevant. However, the cap layers towards the top of the respective samples are only 32 nm and 250 nm thin, so that the QW is located close to the surface. To highlight the importance of subwavelength optical fields for the TMRLE, both semiconductor samples are partially covered with gold gratings that support SPPs, forming hybrid plasmonic-semiconductor structures. The periodic gratings with a 250 nm period allow the detection of the routed optical spin fluxes by coupling them out of the structure as directional emission into the far-field. This ultimately results in the three prominent cases shown in Figure 5.2: A bare QW structure without a plasmonic grating and two structures with the same plasmonic grating but different cap layer thicknesses between the grating and the QW. The thicker cap layer spatially separates the QW and the SPP interface to disable the near-field interaction between the SPPs and the QW due to the evanescent nature of the former. The measurements were performed using the same Fourier imaging setup described in Chapter 7 in reflection geometry and for p-polarized emission. The samples were cooled to around 10 K using liquid helium, excited with 2.25 eV continuous-wave laser light, and magnetic fields of 520 mT were applied in the Voigt geometry using an electromagnet. The maximum QW emission from the hybrid structures (i.e. from below the plasmonic grating) was centered around 1.67 eV [30, 52]. The structures used in those studies are similar to the sample used in the experimental part of this thesis on the TMRLE, see Section 6.1. Therefore, the same contributions to the overall signal are expected.

From those three structures, three main contributions to the overall routing of the QW emission with varying angular and spectral distribution $\rho(E, \theta)$ were revealed. They are summarized in Figure 5.2, with a schematic representation of the contribution from each structure in the top row and the respective signal $\rho(E, \theta)$ according to Eq. (5.2) below. Figure 5.2(a) shows the bare QW structure (i.e. without plasmonic grating) with the small cap layer, (b) the hybrid structure with a gold grating and a large cap layer, and (c) the hybrid structure with a gold grating and a small cap layer. The colors red and blue represent a negative or positive sign of ρ, respectively, and the color saturation indicates the magnitude of ρ. White corresponds to $\rho = 0$. The contributions need to be divided into **far-field effects** like the interference of different light beams from the structure outside of the sample in (a) and (b), and the **near-field effect** as the strongest contribution in (c), where excitons emit directly into evanescent optical modes (SPPs and photonic modes) that exhibit spin-momentum locking.

(a) Bare QW, Far-Field Figure 5.2(a) shows the first far-field effect measured from the bare QW structure without a gold grating on top. Here, the emission was barely influenced by the magnetic field with $|\rho| < 0.1\,\%$, and the routing shows a strong energy dependence, periodically oscillating around $\rho = 0$ (white lines). This small contribution originates from the interference of directly emitted light beams from the QW with those reflected at the backside of the structure (substrate). The far-field interference pattern changes for opposite magnetic fields because the flipped direction of dipole rotation $\pm P_c$ leads to a different phase between the two interfering beams. [30]

(b) Hybrid Structure, Far-Field Figure 5.2(b) shows the second far-field contribution, which was measured from the hybrid structure with the thicker 250 nm cap layer between the QW and the gold grating on top of the structure. Here, despite the presence of the plasmonic grating, no direct interaction occurs between the QW and the SPPs due to the exponential decay of the evanescent SPP wave towards the distant QW layer. There is, however, a small routing effect for small emission angles θ, and a step-like increase of the directional emission at an angle θ_c with the onset of interference fringes for larger angles, and ρ reaches a maximum of around 2 %. The step-like increase correlates with the appearance of the first-order diffracted beam from the grating structure for the emitted light, and the weaker interference patterns at larger angles appear due to the additional emission beam reflected on the sample backside. The weak routing effect for small emission angles (that is present despite the absence of an SPP contribution) originates from the near-field coupling to non-resonant, evanescent photon modes that are bound to the gold/semiconductor interface and emitted via the grating, just like SPPs. [30]

(c) Hybrid Structure, Near-Field The final and strongest contribution to the emission routing is the near-field effect of directly interacting QW excitons and SPPs, which is shown in Figure 5.2(c). Here, the 250 nm plasmonic gold grating and the emitting QW are separated by a 30 nm thin cap layer, which enables the interaction between the SPPs and the QW. This leads to a significant increase of the routing magnitude with up to $\rho = 4\,\%$, as the magnetic field induced polarization degree $\pm P_c$ of the exciton optical transitions is translated into left- or right-propagating SPP waves due to their strong spin-momentum locking. Through the grating structure, this ultimately leads to the directional emission of the SPPs into the far-field. There is no strong spectral and angular dependence of ρ because the SPP resonance is broad compared to the other contributions (50 meV) and covers the whole measured range. The two far-field effects seen in (a) and (b) are also present in this case, but they are weaker and mostly suppressed: Along the energy axis, a weak oscillation of ρ occurs with a period of about 30 meV corresponding to the bare QW case of interference with light reflected at the sample backside (a). The inference patterns for high emission angles seen for the larger cap layer (b) are also present but only visible in cross-sections for specific energies. [30]

In all three cases (a)-(c), ρ is an odd function of the emission angle, i.e. $\rho(E, \theta) = -\rho(E, -\theta)$, and therefore $\rho = C$ holds true (see Eq. (5.3)). The small deviation in the case of the bare QW (a) originates from an offset in those measurements in combination with the small routing magnitude. All contributions can be reproduced in simulations using the scattering matrix method, where the excitons are modeled as uncorrelated point dipoles with a fixed polarization based on the external magnetic field direction and P_c as parameter to influence the TMRLE magnitude. These results are shown in Figure 5.3 for comparison with the experimental data in Figure 5.2. The case most relevant for this thesis is the near-field effect in (c). It shows the largest routing magnitude, and the structure used for the experiments in this thesis closely resembles the hybrid structure with the thin cap layer. See Section 6.1 for the sample description and Section 8.3 for a comparison of the directionality signals from the two samples. For more details about these simulations, see Refs. [30, 48].

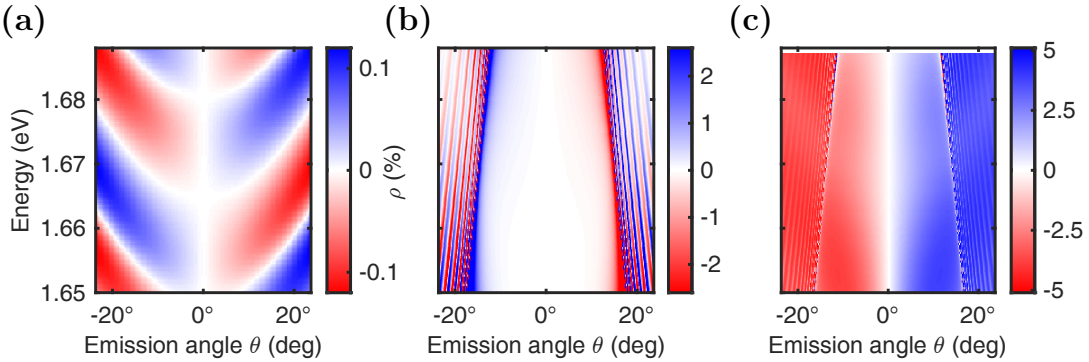

Figure 5.3 Simulations of $\rho(E,\theta)$ for the structures shown in Figure 5.2 using the scattering matrix method. Adapted from [30].

5.3 Temperature Dependence

In the hybrid system of a semiconductor quantum well (QW) structure and a plasmonic gold grating, where the former acts as the magnetic-field sensitive light source for the TMRLE and the latter enhances the TMRLE magnitude through spin-momentum locking of the SPPs, the temperature dependence of the routing is defined by the temperature dependence of the exciton Zeeman splitting in the QW. The influence of the grating, on the other hand, is largely temperature independent. The main parameter for the TMRLE magnitude ρ is the degree of circular polarization P_c of the exciton optical transitions in the QW, which in turn depends on the Zeeman splitting of the light holes $\Delta_{l,V}$ according to Eq. (5.1). For the diluted magnetic semiconductor (DMS) QW structures discussed thus far, the giant Zeeman splitting, which originates from the sp-d exchange interaction of the free carriers with the magnetic Mn^{2+} ions, is highly temperature dependent. It is ultimately described by the alignment of the Mn spins $\langle S_z^{Mn} \rangle$ along the magnetic field via a modified Brillouin function, see Chapter 2 and Eqs. (2.1) and (2.2). Experimental data on the TMRLE temperature dependence for the DMS QW structure will be shown later in Chapter 9. For non-magnetic QWs, the Zeeman splitting depends on the intrinsic g-factor of the holes, instead. It is generally weaker but largely temperature independent, see Eq. (2.7). This will be discussed in detail in Section 9.5 based on the example of an (In,Ga)As/(In,Al)As QW structure.

5.4 Grating Parameter Dependence

The magnitude and the spectral and angular dependence of the TMRLE $\rho(E,\theta)$ also depend on the geometric parameters of the plasmonic gold grating, i.e., the grating period and width of the slits. Ultimately, the overlap of the three interacting systems is important, as shown in Figure 3.2: First, the excitons as light source at a constant energy E_X. Second, the SPPs with their more complex dispersion relation (3.3) in red, which additionally is folded back into the first Brillouin zone due to the periodic grating structure according to Eq. (3.5). These two together lead to the magnetic-field-induced spin fluxes along the interface of the gold grating. The third system is the directional photon emission into the far-field, which we can measure in the experiment. It depends on the overlap of the folded SPP dispersion with the light line in air, shown in blue. The SPP

dispersion (3.5) is most directly influenced by the grating period, which shifts the folded dispersion in the dispersion diagram and, thus, the SPP resonance to different energies and angles. The influence of the slit width is less direct. It shifts the folded dispersion by increasing or decreasing the gap between the upper and lower dispersion lines at the Brillouin zone borders, similar to the phonon dispersion (not shown). Ultimately, the overlap between the three systems changes, and so does the TMRLE spectrum $\rho(E, \theta)$. This will be discussed in Chapter 10.

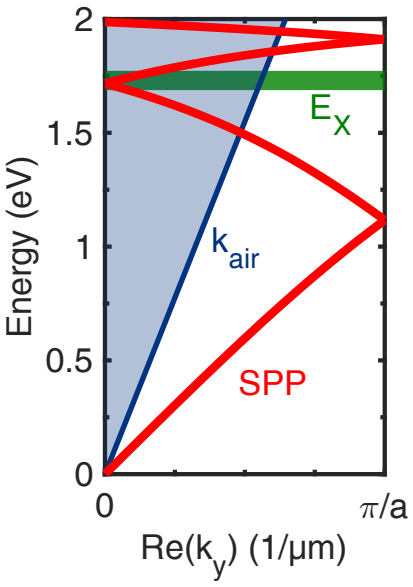

Figure 5.4 Schematic dispersion relations of the systems involved in the TMRLE in the reduced SPP zone scheme: Excitons E_X as light source (green), SPPs (red) with spin-momentum locking and the emission into the far-field k_{air} (blue).

Part III

Experimental Methods

Chapter 6

Samples

The following chapter will focus on the samples used in the experimental parts of this thesis and explain their composition. A large part of this thesis focuses on investigating the transverse magnetic routing of light emission (TMRLE) from hybrid plasmonic-semiconductor structures comprising a (Cd,Mn)Te/(Cd,Mg)Te-based quantum well structure and plasmonic gold nanogratings. Those structures are described in Section 6.1. The other main subject are several hybrid plasmonic-waveguide structures comprising thin synthesized magnetite films (Fe_3O_4) and various plasmonic gold nanogratings that are either placed on top of the magnetite film or embedded into it. This is described in Section 6.2.

6.1 (Cd,Mn)Te/(Cd,Mg)Te

The first system investigated in the thesis is a hybrid plasmonic-semiconductor nanostructure, which combines a diluted magnetic semiconductor (Cd,Mn)Te/(Cd,Mg)Te quantum well and a one-dimensional plasmonic gold grating. The two systems are in close proximity of each other to enable their near-field interaction. Such hybrid structures are a model system for the TMRLE. A similar sample was used to demonstrate the TMRLE in Refs. [30, 52], and for the demonstration of the optical orientation of electron spins via plasmon-to-exciton spin conversion in Ref. [43]. The excitons in the diluted magnetic semiconductor (DMS) quantum well (QW) are the light source whose emission gets routed in the TMRLE by an external magnetic field. The DMS QW is a particularly good system for the TMRLE due to its giant Zeeman splitting and the subsequent large influence of a magnetic field on the exciton light source and its polarization, see Chapters 2 and 5. The additional plasmonic grating in close proximity greatly enhances the TMRLE due to the strong spin-momentum locking of the SPPs, see Section 3.3, and enables their directional emission into the far-field (Section 3.2). Here, we focus on a deeper understanding of the TMRLE and how it can be used to probe the dielectric environment close to the interface. This thesis presents data on TMRLE from two similar samples: The **main sample** was used for all major measurements and will be described in detail now. A second, **alternative** hybrid structure with a slightly different composition of the semiconductor part was used to verify some results and for comparison. It is the older QW structure that was used in Refs. [30, 52], but with a different set of gold gratings on top. The differences to the main sample will be discussed at the end of this section.

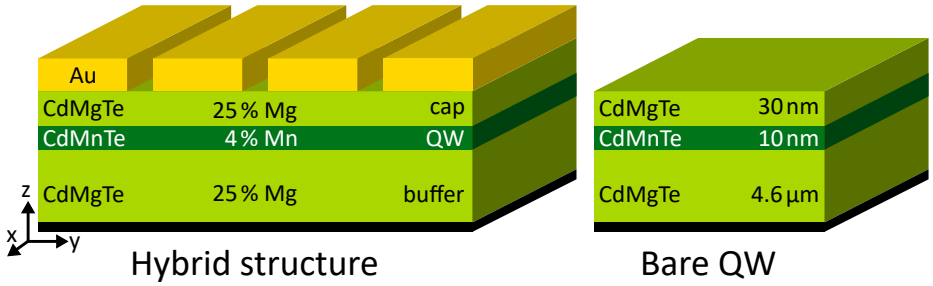

Figure 6.1 Left: Schematic presentation of the main hybrid plasmonic-semiconductor QW structure used in the experiments on the TMRLE, comprising a (Cd,Mn)Te/(Cd,Mg)Te QW and a plasmonic gold grating in close proximity. The QW structure comprises a 10 nm DMS $Cd_{0.96}Mn_{0.04}Te$ layer sandwiched between a 30 nm cap and a 4.6 µm buffer layer of $Cd_{0.75}Mg_{0.25}Te$. **Right:** The semiconductor part without the plasmonic grating (called bare QW) is used to verify the plasmonic influence on the TMRLE.

6.1.1 Main sample

A schematic presentation of the main sample is shown in Figure 6.1, highlighting the different semiconductor layers and their composition, as well as the plasmonic gold grating (Au), which combined comprise the **hybrid structure** (left). The **semiconductor part** (called 022818A) of the hybrid structure is a (Cd,Mn)Te/(Cd,Mg)Te quantum well structure that was grown on a semi-insulating (100) GaAs substrate using molecular beam epitaxy (MBE). MBE is an epitaxial process used to grow thin films of different materials with atomic layer precision, like the compound semiconductors used here. In an ultra-high vacuum, localized beams of the constituents impinge on a heated crystal or substrate at a moderate rate in the order of 1 ML/s, forming a crystalline layer. The elevated temperature allows for lateral movement of the atoms reaching the surface. The slow growth rate, combined with shutters in the beam paths, makes it possible to change the composition of single layers, e.g. the doping of semiconductor layers, which enables the production of quantum wells, superlattices, and other nanostructures. [81]

The **quantum well** (QW) consists of a 10 nm thin layer of the diluted magnetic semiconductor (DMS) $Cd_{0.96}Mn_{0.04}Te$ that is sandwiched between two layers of non-magnetic $Cd_{0.75}Mg_{0.25}Te$ (i.e. without magnetic ions), which serves as potential barriers for the electrons and holes in the QW. As shown in Figure 6.1, this is a 4.6 µm thick buffer layer towards the GaAs substrate and a thin 30 nm cap layer on top of the QW that acts as a spacer between the QW and the surface. The resulting QW structure has a type-I band alignment (straddling gap), which confines the electrons and holes within the magnetic (Cd,Mn)Te layer. The DMS (Cd,Mn)Te shows giant Zeeman splitting of the hole spin levels due to the strong *p-d* exchange interaction between valence band holes and the magnetic Mn^{2+} ions, which makes it a good model system to study the TMRLE, see Chapter 5. (Cd,Mg)Te as the non-magnetic barrier material is similar to (Cd,Mn)Te with a wider bandgap and an adjustable lattice constant to minimize strain in the QW. At temperatures of $5-10$ K, the QW has its emission maximum at 1.687 eV and the barriers at 2.075 eV. Additional weak emission around 1.495 eV can be attributed to the GaAs substrate. The QW Mn content of 4 % was determined from magneto-PL measurements based on the Zeeman splitting of the QW emission for various magnetic fields, as shown in Section 8.2. The Mg content of the non-magnetic barriers of about 25 % is instead estimated from the photoluminescence maximum and the bandgap data in Ref. [82].

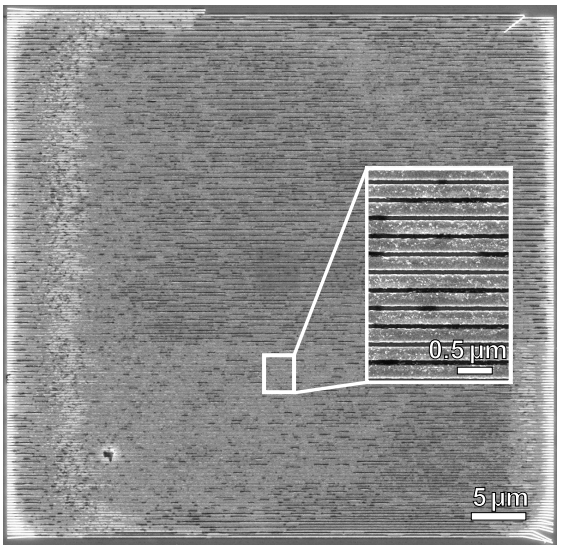

Figure 6.2 SEM image of the whole $50\times50\,\mu m^2$ grating with 250 nm period, 55 nm slit width, and a close-up of the grating center (inset). Adapted from [48].

To create the **hybrid structure**, one-dimensional gold nanogratings that support surface plasmon polaritons (SPPs) were patterned on top of the cap layer of the semiconductor using electron beam lithography and subsequent lift-off processing: First, a 250 nm thick layer of the positive polymer resists PMMA[1] is applied on top of the spacer, into which the grating pattern is written by a tightly focused electron beam (exposure) by Raith [83]. A solvent (MIBK:IPA[2]) removes the exposed regions afterward (development). This leaves the non-exposed regions of the resist intact as an inverse mask of the grating. Next, gold is deposited onto the sample by thermal evaporation. It attaches either directly to the semiconductor surface in the exposed regions or on top of the remaining resist. Then, the remaining resist with gold on top is removed, leaving only the gold on the surface behind. No metal was used in this step to support the adhesion of the gold layer to the surface, but the sample was subjected to a short plasma treatment to descum the surface right before the gold deposition. The gratings support SPPs, which enhance the TMRLE magnitude due to their strong spin-momentum locking, and the periodicity of the grating enables their directional emission into the far-field to detect the spin fluxes along the interface.

Each gold grating has an area of $50 \times 50\,\mu m^2$ and a thickness of 45 nm. The grating period and the width of the slits vary between gratings because they directly influence the SPP dispersion and, thus, the emission characteristics into the far-field (Section 3.2). The periods range from 200 nm to 400 nm in 10 nm steps and from 400 nm to 800 nm in 20 nm steps. Every grating period is patterned five times, each with a different slit width between about 40 nm and 60 nm, for a total of 205 different gratings. The gratings are arranged in a grid-like structure with the period increasing from left to right and the slit width from top to bottom. Most used for this thesis is the 250 nm grating period and its neighbors because they showed the largest enhancement of the TMRLE. In practice, the grating periods are created with high accuracy because a laser interferometer is used for positioning during the electron beam lithography process. The real slit width also depends on the subsequent lift-off processing and needs to be determined from scanning electron microscopy (SEM) measurements. For example, Figure 6.2 shows an SEM image of the whole $50\times50\,\mu m^2$ grating with a 250 nm period and an intended slit width of 50 nm, and a close-up from the grating center. For this specific grating, the mean slit width was measured to be 55 nm with a standard deviation of 2.5 nm, while the mean period corresponds to 249.8 nm with a 1.3 nm standard deviation. Only 14 periods were averaged for this, and a larger accuracy is usually achieved by including more periods. The slit widths were measured for all five gratings with a 250 nm period. The results are presented in Table 6.1. Gratings with different periods are expected to have similar deviations of the slit width from the expected values.

[1] Polymethylmethacrylate
[2] Methylisobutylketone:Isopropanol

Table 6.1 Expected slit widths, measured mean values and standard deviation (Std.) for the gratings with 250 nm period with a sample size of 14 slits each.

Expected (nm)	Mean (nm)	Std. (nm)
40	42.8	3.6
45	47.5	2.5
50	54.9	2.5
55	60.4	3.6
60	67.9	2.4

The SEM image in Figure 6.2 shows the high quality of the patterned structure with no missing gold stripes or defects (except right at the edges) without using an adhesion layer at the gold-semiconductor interface. The black horizontal lines in the main figure are organic residue trapped in the slits due to an imperfect lift-off procedure, not defects of the grating itself. Large areas around each gold grating are left uncovered, which allows us to compare signals from the hybrid structure to those without gratings, i.e. just the semiconductor part. In contrast to the **hybrid structure**, these bare parts are called **bare QW** in the following sections.

6.1.2 Alternative sample

The older, alternative sample is similar to the main sample of this thesis and was used in the studies on the TMRLE in Refs. [30, 52]. A different set of gratings was used in this thesis for comparative measurements. It also comprises a 10 nm (Cd,Mn)Te QW with (Cd,Mg)Te barriers and gold gratings with similar parameters to create the hybrid structure. The cap layer is slightly thicker at 32 nm instead of 30 nm, and the buffer layer toward the GaAs substrate measures 3 µm instead of 4.6 µm. The Mn content for the alternative sample was estimated to be 2.6 % in Refs. [30, 52]. However, because the effective spin S_{eff} was assumed to be 5/2, this is the effective Mn content of the Mn^{2+} ions that have not formed antiferromagnetic pairs (i.e. that contribute to the magnetization, see Chapter 2). Following Ref. [84], the actual Mn content x_{Mn} of the sample can be approximated to around 3.5 %, which is still lower than the approximately 4 % determined similarly for the main sample (see Section 8.2). The PL emission energy of 1.67 eV at 4 K is also lower compared to 1.68 eV from the main sample. This supports the lower Mn content because the bandgap energy increases with x [85]. Most importantly, though, the alternative sample features a 2D electron gas close to the QW in both the cap and buffer layer, which provides additional free carriers. This likely increases the cooling of the Mn spin system but also seems to negatively impact the magnitude of at least the TMOKE and possibly the TMRLE (see Section 8.3). The main parameters of both samples are summarized in Table 6.2.

Table 6.2 Sample comparison: Thickness of layers (nm/µm), Mn content of the QW x_{Mn}, PL emission maximum from bare QW (eV), and doping with 2D electron gas (yes/no).

Sample:	Main (022818A)	Alternative (110614A)
Cap	30 nm	32 nm
QW	10 nm	10 nm
Buffer	4.6 µm	3.0 µm
x_{Mn}	4.0 %	3.5 %
QW PL	1.68 eV	1.67 eV
2D gas	✗	✓

6.2 Magnetite Fe_3O_4

The second hybrid plasmonic system investigated combines a thin film of the magnetic mineral magnetite (Fe_3O_4) with one-dimensional plasmonic gold nanogratings that are either placed on top of the magnetite film (i.e. exposed to air) or embedded into the film, as shown schematically in Figure 6.3. This type of system with a periodically structured metal film that interfaces with dielectric materials is called a plasmonic crystal, based on the similar concept of photonic crystals. The local enhancement of the electric field in a plasmonic crystal can, for example, be used to trigger non-linear effects at low excitation powers or improve the efficiency of photonic components like LEDs, photodetectors, and solar cells. The sensitivity of the plasmonic modes to their environment can also be used for precise sensing of changes in the refractive index, for example, to detect molecules on the surface or close to it [86]. Our structure, in particular, is called a magneto-plasmonic crystal due to the presence of magnetite as the dielectric [15]. Magneto-plasmonic crystals are well known for enhancing magneto-optical effects compared to the plain magnetic materials, especially the otherwise very small TMOKE investigated here, see Section 4.4. Magnetite is a ferrimagnet and the most magnetic naturally occurring mineral on earth [87], making it a promising candidate for the magnetic constituent in a magneto-plasmonic crystal. Due to its finite transparency, magnetite is a promising material for SPP-enhanced TMOKE measurements in transmission geometry, in addition to the more common reflection geometry. The added gold gratings on one side of the structure provide the necessary lack of mirror symmetry for the TMOKE in transmission [4, 63].

A schematic presentation of the different sample architectures is shown in Figure 6.3. Both structures are based on a quartz (SiO_2) substrate with a 100 nm thin magnetic film on top that contains Fe_3O_4/α-Fe nanoparticle complexes. One-dimensional gold nanogratings of $200 \times 200\,\mu m^2$ area were patterned either on top of the magnetite film or are located in the film. They support the excitation of surface plasmon polaritons (SPPs) at the interfaces of the gold as well as guided modes in the magnetite film excited by incoming light. The gratings cover only a small area of the sample, so the majority is just the bare magnetite film on top of the substrate. These areas can be used for comparative measurements to highlight the influence of the grating on the transmitted or reflected light.

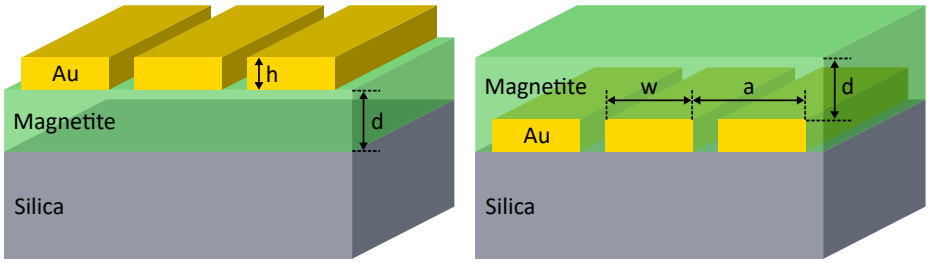

Figure 6.3 Schematic presentation of the two magnetite samples, both comprising a thin magnetite film and one-dimensional gold gratings either exposed on top of the magnetite film or embedded into the film. The magnetite films on top of the silica substrate are $d = 100\,\text{nm}$ thick. The $h = 40\,\text{nm}$ high gold gratings have a period of $a = 580\,\text{nm}$ and the gold stripes are $w = 400\,\text{nm}$ wide.

The planar magnetite films were grown onto the SiO_2 substrate using the laser electrodispersion technique with subsequent annealing, explained in detail for similar magnetite films in Ref. [88] and in Ref. [4] for the samples used here: A pulsed laser melts the surface of a single crystal Fe_3O_4 target in a vacuum, creating liquid micrometer- and sub-micrometer-sized droplets that get charged in the laser torch plasma. In a process called cascade fission, the droplets break apart into smaller droplets whenever the Coulomb repulsion force due to the increasing electrical charge exceeds the surface tension force, ending in nanometer-sized droplets. The superheated droplets lose oxygen, though, creating nanometer-sized FeO droplets that cool rapidly and solidify, leading to FeO (wüstite) nanocrystals on the substrate along with additional amorphous parts. The metastable FeO is converted into Fe_3O_4 + α-Fe nanoparticles by annealing the sample at 300 °C in a vacuum for 1 h. The individual nanoparticles have the crystal structure of magnetite and an average size of about $6 - 10\,\text{nm}$ according to X-ray diffraction and electron microscopy measurements and seem to form larger clusters of about 45 nm [88]. As determined from optical measurements in Ref. [4], the dielectric permittivity ε and gyration g_z of the magnetic films are close to literature data for monocrystalline and epitaxial films, even though they are non-uniform and comprise not pure Fe_3O_4 but additional α-Fe parts. The complex permittivity ε is shown below in Figure 6.5 and the gyration g_z is shown later in Figure 11.3. Compared to usual polycrystalline Fe_3O_4 films, synthesized nanostructured films like these showed a larger coercive force and saturation magnetization of up to 660 Oe and 520 emu/cm^3, respectively, which may result from the formation of the larger clusters with a considerable magnetic anisotropy and random orientation of the easy axis of magnetization. [4, 88]

The one-dimensional gold nanogratings of $200 \times 200\,\mu\text{m}^2$ area were patterned using electron beam lithography and subsequent lift-off processing, which is described in detail for the (Cd,Mn)Te/(Cd,Mg)Te structures in Section 6.1. This was done either before or after the magnetite film was grown, depending on the position of the gold grating. After the exposure and development, 40 nm of gold was deposited on top of a 5 nm titanium adhesive layer (not shown) via thermal evaporation, followed by the final lift-off process. The gratings on both samples are similar, with a grating period of 580 nm and a stripe width of 400 nm. The resulting gratings can be seen in Figure 6.4, which shows SEM images of both grating configurations side by side. The proportions of the gold grating embedded in magnetite (right) are distorted because of electron scattering in magnetite.

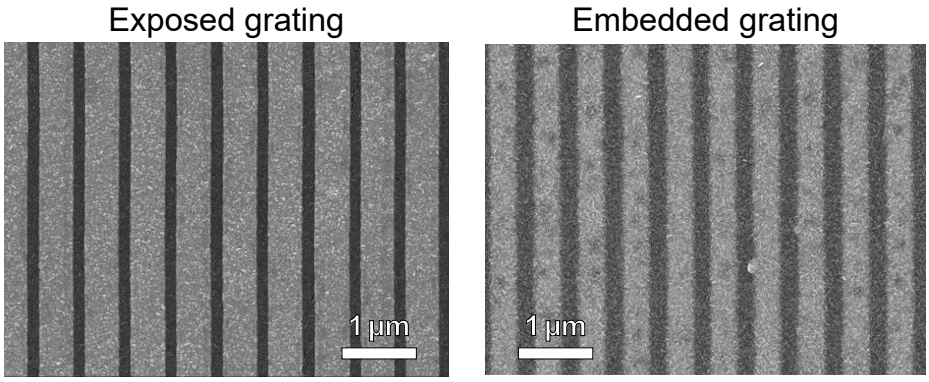

Figure 6.4 SEM images of the two gold grating configurations with 580 nm period, either on top of the magnetite film (left) or embedded into the film (right). The proportions of the grating embedded in magnetite is distorted due to electron scattering in the film.

The complex dielectric permittivity ε of the bare magnetite film, i.e. without a gold grating, was deduced from standard ellipsometry measurements that were done for Ref. [4]. The results are shown in Figure 6.5 as blue and orange dots for the real and imaginary parts $\mathrm{Re}(\varepsilon)$ and $\mathrm{Im}(\varepsilon)$, respectively. The real part reaches its maximum at 1.5 eV, while the imaginary part has a more complex spectral dependence with a minimum at 1.35 eV and a maximum at 2 eV, but without sharp features. The relatively large imaginary part measured in the visible range shows that magnetite has rather large internal optical losses for those energies. The experimental values are close to literature data for monocrystalline and epitaxial films, even though the magnetite films used here are non-uniform and comprise Fe_3O_4/α-Fe nanoparticle complexes [89, 90].

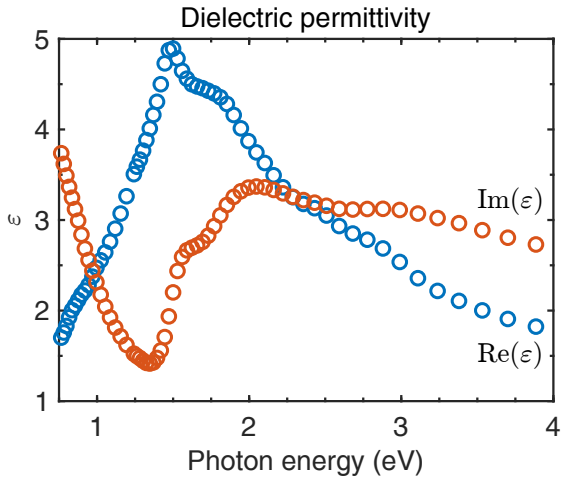

Figure 6.5 Real and imaginary parts of the dielectric permittivity ε of the magnetite film containing Fe_3O_4/α-Fe nanoparticle complexes, measured using the standard ellipsometry technique.

Chapter 7

Experimental Setup

Most measurements presented in this thesis were performed on a **Fourier imaging spectroscopy setup**. It gives direct access to the angular distribution of light intensity collected from a sample, i.e. the emission or reflection angle, and its wavelength or energy. This setup was also used by Felix Spitzer for Ref. [52]. The following Section 7.1 introduces the Fourier plane and the concept of Fourier imaging as a measurement technique. Then, Section 7.2 focuses on the practical realization of the concept for measurements in reflection and transmission geometry.

7.1 Fourier Plane Imaging

Whereas a normal imaging setup creates an image of the sample with information like the light intensity obtained in spatial coordinates, a Fourier imaging setup forms an image of the Fourier plane that is created by a microscope objective (MO). The Fourier plane is located at a distance of twice the focal length of the microscope objective f_{MO} from the sample. It contains the projections k_x and k_y of the light momentum $|\vec{k}|$ as proportional spatial offsets from the optical axis, with x and y spanning the plane of the sample surface and $k_x = k_y = 0$ on the optical axis. This is presented schematically in Figure 7.1, where k_i is replaced by the angle of the light $\theta_i \approx \sin\theta_i = k_i/|\vec{k}|$ for $i = x, y$. Two light rays that are emitted in the same direction θ_i (i.e. with the same k_i) but from different positions are mapped into the same point in the Fourier plane (shown by two lines in either red or green). Their offset from the optical axis $f_{\mathrm{MO}}\theta_i$ depends solely on the initial emission direction θ_i and the focal length of the objective [91]. A pixelated detector positioned in the Fourier plane, e.g. a charge-coupled device (CCD) image sensor, could then be used to measure this angular resolved light intensity $I(\varphi, \theta)$ in both the x- and y-direction, with θ for the y-direction and φ in the x-direction (not shown).

A real microscope objective is not a thin lens and the Fourier plane is usually located close to the objective, so that relay optics are needed to project an image of the Fourier plane onto the detector. For that purpose, two collecting lenses are used as a telescope, which can also be used to scale the image to match the size of the detector. To create an image of the Fourier plane, the first lens is placed at the distance of its focal length f_1 from the Fourier plane and the second lens is f_2 away from the detector. In our case, this is the entrance slit of an imaging spectrometer equipped with a CCD image sensor (see Figure 7.1). The two lenses are separated by the sum of their focal lengths $f_1 + f_2$ in the optimal case, though a small deviation from this distance does not significantly affect the image quality.

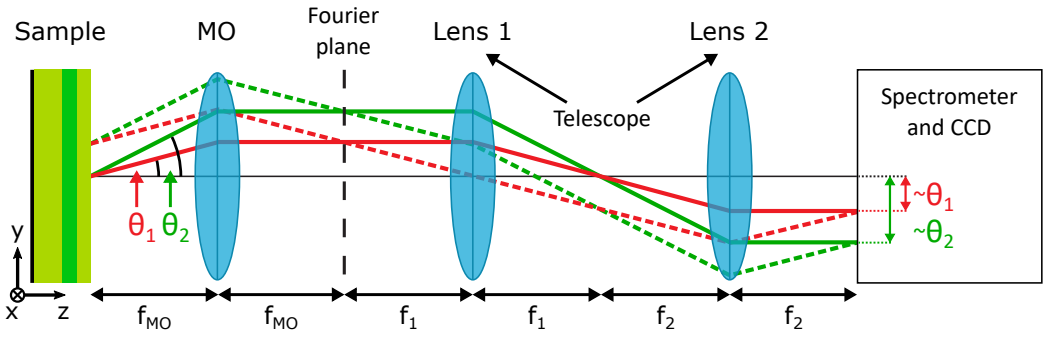

Figure 7.1 Schematic depiction of the Fourier imaging setup with the main optics and their influence on the path of the light. Light rays emitted (or reflected) from the sample at the same angle θ_i, but from different points, are mapped into the same spacial position in the Fourier plane. A telescope comprising two lenses with focal lengths f_i projects the Fourier plane onto the detector, in our case an imaging spectrometer. Adapted from [52].

The Fourier imaging setup can be described in a simple, one-dimensional model using ray transfer matrix analysis to highlight these features: A light ray that leaves the sample from position y_0 and (small) angle θ_0 relative to the optical axis reaches the Fourier plane behind the MO with a new offset from the optical axis and angle

$$\begin{aligned} y_{\mathrm{FP}} &= f_{\mathrm{MO}}\theta_0 \qquad \text{and} \\ \theta_{\mathrm{FP}} &= -y_0/f_{\mathrm{MO}}, \end{aligned} \tag{7.1}$$

so that the new spatial position y_{FP} depends solely on the initial angle θ_0. Adding the two lenses of the telescope with an arbitrary distance d between them, but placed f_1 from the Fourier plane and f_2 from the detector, results in

$$\begin{aligned} y_{\mathrm{end}} &= -\frac{f_{\mathrm{MO}} f_2}{f_1}\theta_0 \qquad \text{and} \\ \theta_{\mathrm{end}} &= \frac{f_1}{f_{\mathrm{MO}} f_2} y_0 - \frac{f_{\mathrm{MO}}}{f_1 f_2}(f_1 + f_2 - d)\theta_0 \end{aligned} \tag{7.2}$$

at the detector. Here, y_{end} is defined solely by the initial angle θ_0 and the three focal lengths f_i, but crucially not by the initial offset y_0 or the distance d between the two lenses. This is only true if the first lens is positioned correctly at a distance f_1 from the Fourier plane. The angles of the light rays θ_{end} reaching the detectors show a more complex form and depend on both the initial spatial offset y_0 and angle θ_0, but the latter dependence vanishes for $d = f_1 + f_2$ between the lenses. The focal length ratio f_2/f_1 of the telescope is used to resize the Fourier plane image to fit onto the detector, which is important because the edges of the light spot are used to define the angular axis.

In practice, the Fourier imaging spectroscopy setup is more complicated than shown in Figure 7.1. For example, the excitation of the sample via laser or whitelight has been omitted thus far, as well as additional optics in the detection and excitation like filters and polarization optics that manipulate the light but are not strictly needed for the Fourier imaging. Additionally, a cryostat is used to cool the sample, and an electromagnet is used to apply an external magnetic field at the sample position.

7.2 Fourier Imaging Spectroscopy Setup

The Fourier imaging spectroscopy setup used for this thesis is a realization of the concepts explained above for the detection of the spectrally and angular-resolved light intensity $I(E, \theta)$ emanating from a sample. The whole setup is shown in a schematic presentation in Figure 7.2 and can be split into three parts: First, the excitation part on the left with the light sources and optics used to illuminate the sample in the cryostat, and then the two parts of the detection, one for the reflection geometry with lenses f_1 and f_2 and the other for the transmission geometry behind the sample with lenses f_3 and f_4. Both geometries use the same spectrometer and CCD for the final detection of the light intensity.

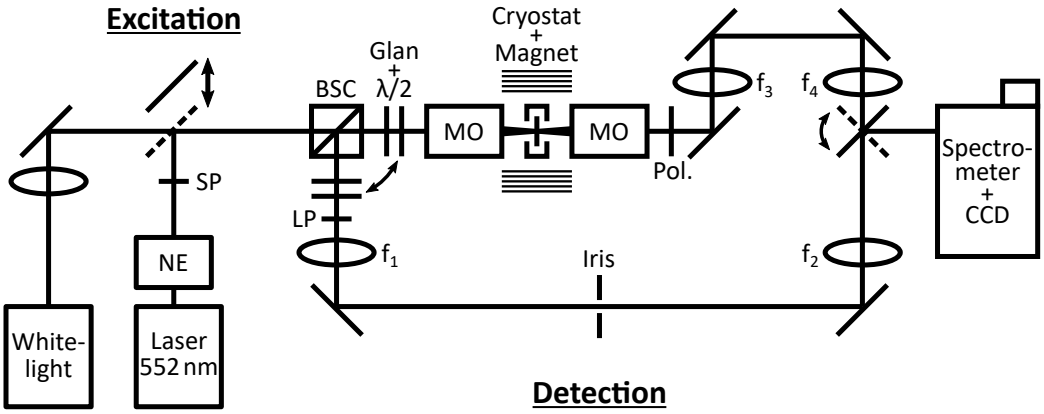

Figure 7.2 Schematic presentation of the Fourier imaging spectroscopy setup. **Excitation:** The light from a thermal whitelight source or a CW laser is focussed onto the sample in a flow cryostat by a 20× microscope objective (MO). Magnetic fields are applied in transversal direction via an electromagnet. **Detection:** The light from the sample is collected by the same MO in the reflection geometry or by an identical MO on the backside of the sample (transmission geometry) and mapped onto the imaging spectrometer by a different telescope comprising two lenses in each geometry.

7.2.1 Excitation

The excitation part of the setup is shown on the left side of Figure 7.2. Depending on the type of measurement, either a laser or a thermal white light source (WL) was used to illuminate the sample. The **white light source** was a tungsten halogen white light lamp (Spectral Products ASB-W-030) with a broad and flat emission spectrum between 300 nm and 2600 nm and a peak wavelength of 950 nm. It can be used for reflection and transmission measurements over a broad spectral range. From its metal housing, the light was coupled into an optical fiber. For the measurements on the magnetite-based samples and some (Cd,Mn)Te/(Cd,Mg)Te reflection and transmission measurements, the light was emitted towards the sample from the other end of the fiber using a fiber coupler (focal length 36 mm). For later measurements on the (Cd,Mn)Te/(Cd,Mg)Te samples with smaller gold gratings, the light was instead emitted divergently from the fiber and then collimated by a 400 mm achromatic lens. Using a lens with a large focal length allows for much better collimation and, consequently, better focusing into smaller spots on the sample.

The **laser**, on the other hand, was used to excite the sample non-resonantly with photon energies above the bandgap energy, which leads to the emission of photoluminescence light at lower energies. For the experiments in this thesis, an optically pumped semiconductor laser (Coherent OBIS LS 552 nm 60 mW) in continuous wave (CW) mode was used, which emits light at 2.25 eV. A noise eater (**NE**) was used to stabilize the laser power during long measurements and to lower the laser power easily, and a 600 nm shortpass filter (**SP**) was used to block unwanted laser emission at longer wavelengths.

The light of either source (chosen via a movable mirror) reaches a 50:50 non-polarizing beamsplitter cube (**BSC**) that is needed to separate the incoming light and the signal from the sample in the reflection geometry. The cube transmits about 50 % of the incoming light intensity and reflects the other half orthogonally to one side, independent of the light polarization. The transmitted light passes a polarizer (**Glan**-Taylor prism) and an achromatic half-wave plate ($\boldsymbol{\lambda/2}$), which are used to linearly polarize the incoming light and rotate the polarization plane without moving the beam position. For most measurements in this thesis, the p-polarization was the default setting since the investigated SPP-enhanced magneto-optical effects are absent for s-polarized light. Measurements in s-polarization can therefore be used to verify the expected effects in p-polarization.

The subsequent infinity-corrected microscope objective (**MO**, Mitutoyo M Plan Apo NIR 20x) focuses the collimated light onto the sample in its focal plane. It has a focal length of $f_{\mathrm{MO}} = 10\,\mathrm{mm}$, a 20× magnification factor, a numerical aperture of $NA = 0.4$, and is optimized for wavelengths between 480 nm and 1800 nm. The maximum angle at which the objective focuses the light onto the sample and is similarly able to collect the emitted or reflected light is $\theta_{\mathrm{max}} = \pm \arcsin(NA) \approx \pm 23.5°$. The laser spot had a diameter of about 7 µm on the sample, with a corresponding power density of approximately $400\,\mathrm{W/cm^2}$ if not stated otherwise. The whitelight spot was about $100 - 200\,\mu\mathrm{m}$ in diameter if emitted from the fiber via the fiber coupler or 20 µm after switching to the $f = 400\,\mathrm{mm}$ lens for collimation instead.

Cryostat and Magnet The sample was mounted in a liquid helium flow **cryostat** (Oxford Instruments MicrostatHe-R) with windows to cool it down to about 4 K to 10 K and allow optical measurements. It is not submerged in liquid helium but cooled indirectly through a constant flow of liquid helium from a storage vessel that evaporates on the other side of a heat exchanger. The sample is glued to a copper sample holder using silver conductive paint, and the sample holder is connected to the heat exchanger. A cryogenic temperature sensor (RhFe Resistor) close to the heat exchanger enables the monitoring of the temperature and cooling process. The sample is slightly warmer due to (local) heating from the excitation and the distance to the sensor. The temperature can be controlled by limiting the helium flow rate using a valve on the transfer tube, but this is a delicate process and not stable in the long term. Therefore, the cryostat is also equipped with an electrically powered resistive heating element close to the heat exchanger that can keep a constant temperature up to about 50 K. The heater is controlled via an external PID (proportional integral derivative) feedback controller. The sample was also mounted in the cryostat for measurements at room temperature (e.g. the magnetite samples) but not cooled down.

The cryostat is attached to a three-axis translation stage with micrometer precision, which is used to position the relevant portion of the sample surface into the narrow focus of the first MO. Magnetic fields of up to 500 mT at the sample position and perpendicular to the optical axis (Voigt geometry) are provided by a water-cooled resistive **electromagnet** featuring ferrite cores to maximize the magnetic field at the sample position. A remote-controlled bidirectional power supply (Kepco

BOP20-50MG) provides up to 40 A of constant electrical current through the magnet coils, limited by the 20 V voltage limit of the power supply and the available cooling.

7.2.2 Detection

The setup provides two detection geometries: the reflection and the transmission geometry. Both are implementations of the Fourier imaging technique described above and are thus similar in their composition. In both cases, the light is collected from the sample by a microscope objective, which defines the angular range accessible in the experiments. For the 20× MO with $NA = 0.4$, this is $\theta = \pm 23.5°$.

Reflection geometry In the reflection geometry, the signal emanating from the sample (reflected whitelight or emitted photoluminescence) is collected by the same microscope objective used for the excitation in backscattering geometry. By passing the same combination of half-wave plate ($\boldsymbol{\lambda/2}$) and polarizer (**Glan**) again, only the set linear polarization of the signal is transmitted and subsequently deflected to the side in the beamsplitter cube (**BSC**), separating it from the incoming excitation signal. For photoluminescence measurements, an additional longpass filter (**LP**, cut-on wavelength 600 nm) is used to suppress laser stray light from reaching the sensor. Here, before the first lens, a camera with a focussing lens can be used to align the sample into the focus of the MO (not shown). Next is a telescope comprising two achromatic lenses with focal lengths of $f_1 = 400$ mm and $f_2 = 300$ mm. It maps the Fourier plane onto the entrance slit of the spectrometer and resizes the spot to fit onto the CCD sensor. The correct position of the second lens (f_2) can be determined by removing the first lens and creating a sharp real-space image of the sample surface on the CCD while bypassing the spectrometer grid. For the first lens (f_1), the correct position was determined by measuring the distance towards the Fourier plane.

Transmission geometry A second Fourier imaging setup comprising another microscope objective (MO) and two lenses (f_3, f_4) is located on the backside of the sample to measure the light transmitted through the sample or light emitted from its backside. The MO is the same as in the excitation to cover the same angular range on both sides of the sample. Unlike the first objective, it is not strictly fixed in place but movable along the optical axis so that its narrow focal plane can be matched to the first MO for different samples. This can be checked using a second camera before the first lens f_3 (not shown). For transmission measurements, the sample is glued across a small hole in the sample holder. The two achromatic lenses have smaller focal lengths of $f_3 = 200$ mm and $f_4 = 150$ mm due to the smaller distance between the objective and the spectrometer, but their magnification factor f_4/f_3 is the same as in the reflection geometry. An optional longpass filter blocks the remaining laser light, and a linear film polarizer (**Pol.**) defines the linear polarization reaching the sensor. It can also be used to further block remaining laser light by crossing it with respect to the filter in the excitation.

Spectrometer The detector used for both geometries is a single-stage 0.5 m imaging **spectrometer** (Princeton Instruments Acton SP2500i) equipped with a charge-coupled device (**CCD**) image sensor (Princeton Instruments PIXIS: 256E). The optical grating used in all measurements has 300 grooves/mm, leading to a linear dispersion of 6.43 nm/mm. The CCD sensor has 1024 × 256 pixels, each $(26 \times 26)\,\mu m^2$ in size, resulting in a full sensor size of about $(26 \times 6.7)\,mm^2$. The spectral resolution is about 1 nm with the entrance slit of the spectrometer opened 150 µm wide, and the

CCD covers a spectral range of around 170 nm in one image. The CCD was cooled down to −70 °C via a Peltier cooler to reduce the dark current (noise) of each pixel. A low noise level is important since every pixel is read out individually to measure the spectral and angular dependence of the signal simultaneously.

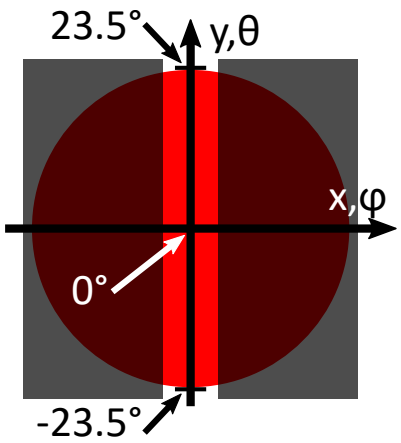

Figure 7.3 The light spot (red) contains the angle information for θ and φ as offset from the spot center. The spectrometer entrance slit (black overlay) blocks $\varphi \neq 0°$ but leaves θ intact.

Figure 7.3 shows a schematic presentation of the light spot (red circle) at the spectrometer entrance slit (black overlay). The light spot contains the information about the light angle in both the horizontal and vertical direction (φ and θ) as spatial offset from the center ($\theta = \varphi = 0°$). The vertical entrance slit blocks most of the horizontal portion of the light spot, leaving only a vertical slice to enter the spectrometer. This limits the light entering the spectrometer to around $\varphi = (0.0 \pm 0.8)°$ in the horizontal direction and θ between $\pm 23.5°$ in the vertical direction, which are defined by the angular range of the MO. Then, the imaging spectrometer separates the light into its spectral components in the horizontal plane but leaves the angular information in the vertical direction θ intact. The spectrally- and angle-resolved light intensity signal $I(E, \theta)$ is then detected by the CCD sensor, and each pixel is read out individually. As mentioned in Section 7.1, the angular axis is defined using the edges of the light spot because they correspond to the maximum positive and negative angle $\theta_{\text{max}} = \pm \arcsin(NA)$ that the MO collects from the sample. The spot size on the CCD can be adjusted by the telescope magnification factor f_2/f_1 (see Eq. (7.2)) to fit into the CCD detector height of 6.7 mm. The angular resolution of the setup is about 0.5°.

7.2.3 Measuring the TMOKE and TMRLE

Both the TMRLE ρ in Eq. (5.2) and the TMOKE δ in Eq. (4.5) are defined by the changes of the emitted or reflected/transmitted light intensities I induced by an external magnetic field in opposite directions $\pm B$. Both effects depend on the photon energy E and the angle of the light θ at which it departs the sample. Therefore, the Fourier imaging spectroscopy setup is a good tool to detect these magneto-optical intensity effects by measuring the angle- and spectrally-resolved intensity spectra $I(E, \theta)$ for the two opposite magnetic field directions $\pm B$, to deduce ρ or δ from the data. The signal-to-noise ratio of the deduced spectra is increased by illuminating each CCD pixel for a longer time. By repetitive switching of the magnetic field direction and subsequent averaging of the intensities, the influence of long-term instabilities or changes of the light source power can be lessened compared to the case of only one long illumination for each magnet field direction back to back. For a typical measurement, the magnetic field direction was switched back and forth at least 25 times, and each time around 16 spectra were taken with three seconds exposure time each. Combined with idle times after each change of the magnetic field direction for stability reasons and the initial CCD background measurement, each measurement takes at least one hour.

Part IV

Results

Chapter 8

Transverse Magnetic Routing of Light Emission

The first experimental part of this thesis focuses on the investigation of the transverse magnetic routing of light emission (TMRLE) from hybrid plasmonic-semiconductor structures comprising a diluted magnetic semiconductor (Cd,Mn)Te/(Cd,Mg)Te quantum well and plasmonic gold nanogratings. First, Section 8.1 presents reflection and emission spectra to characterize the main sample of this thesis and identify the optical resonances. Then, Section 8.2 quantifies the giant Zeeman splitting of the excitons in the quantum well (QW), which is an important quantity for the TMRLE. Next, Section 8.3 serves as an introduction to the typical TMRLE measurement from the hybrid structure, before Section 8.4 compares the main sample with the old alternative sample used in Refs. [30, 52]. Lastly, Section 8.5 compares the experimental TMRLE data with simulation results from the theoretical model. The following Chapters 9 and 10 will then focus on the temperature dependence of the TMRLE and the influence of the geometric grating parameters, like the grating period, on the directionality spectra.

8.1 Emission and Reflection Spectra

The samples used in the experiments are described in detail in Section 6.1. Briefly summarized, the main sample comprises a 10 nm layer of the diluted magnetic semiconductor (Cd,Mn)Te sandwiched between two non-magnetic (Cd,Mg)Te layers, namely a 4.6 µm thick buffer layer towards the substrate and a thin 30 nm cap layer on top. Together, they form a semiconductor QW structure with type-I band alignment so that the electrons and holes are confined within the magnetic (Cd,Mn)Te layer. One-dimensional plasmonic gold nanogratings were patterned on top of the thin cap layer that support surface plasmon polaritons (SPPs) and enable their interaction with the far-field. The thin cap layer enables the interaction of the evanescent SSPs confined to the gold interface with excitons in the QW. The directional coupling between the QW excitons and the SPPs substantially increases the magnitude of the TMRLE for the QW emission compared to the case of a bare QW without a plasmonic grating on top, see Chapter 5.

Photoluminescence As explained in Chapter 7, the Fourier imaging setup enables the simultaneous measurement of the angle- and spectrally-resolved intensity distribution $I(E, \theta)$ of light emitted or reflected from the sample. Figure 8.1 exemplarily shows two intensity spectra $I(E, \theta)$ of the photoluminescence (PL) from the (Cd,Mn)Te/(Cd,Mg)Te quantum well (QW) as color plots. The emission spectrum from the bare QW (i.e. with no gold grating on top) is shown on the left (a),

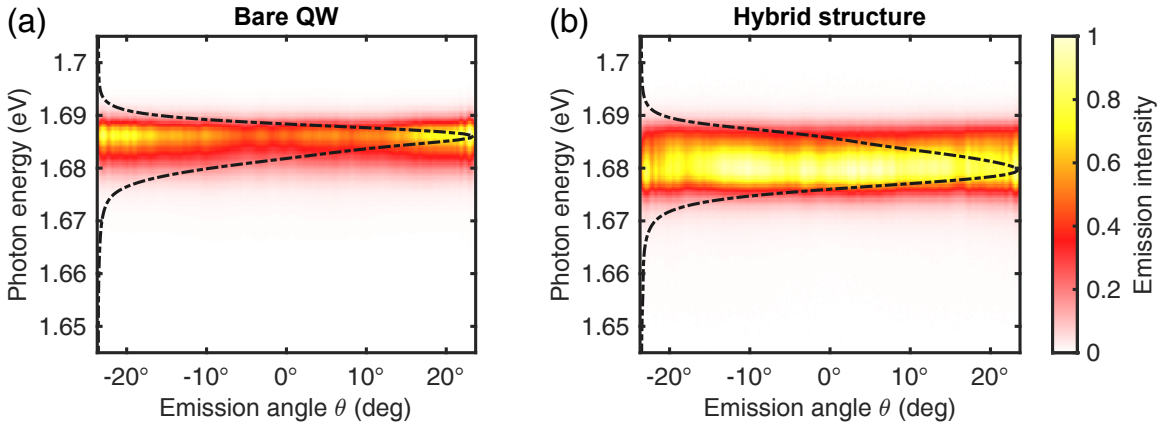

Figure 8.1 Intensity spectra $I(E, \theta)$ (normalized) of the PL emitted from the QW as a function of the photon energy E and the emission angle θ at about $T = 4\,\mathrm{K}$ for **(a)** the bare QW and **(b)** the hybrid structure with a 250 nm grating period. The respective angle-integrated intensity spectra $I(E)$ are shown as dash-dotted overlays with an arbitrary intensity axis increasing from left to right.

and from the QW below the gold grating with a grating period of 250 nm (hybrid structure) on the right (b). The normalized light intensities $I(E, \theta)$ are represented by colors ranging from white (no light intensity) to red and bright yellow for the maximum intensity. Both spectra were measured at cryogenic temperatures of about 4 K, and the sample was excited off-resonantly using a green continuous-wave laser (552 nm, 2.25 eV), which corresponds to an excitation above both the QW and barrier bandgaps. The emission originates from the recombination of heavy-hole excitons in the QW. Only p-polarized light was measured, i.e. light with the electric field vector in the incidence plane and thus partially perpendicular to the grating bars, which enables the interaction with SPPs. Angle-integrated spectra $I(E)$ are shown as dash-dotted overlays in both subfigures with an arbitrary intensity axis that increases from left to right to highlight the spectral shape.
The PL from the bare QW (a) is centered around 1.686 eV with a full width at half maximum (FWHM) of 7 meV, while the PL from the hybrid structure (b) is centered around 1.680 eV with a larger FWHM of 10 meV. This does not significantly change for different grating periods. The angular intensity distribution from both structures is flat with no sharp features. The lower emission energy of the hybrid structure is attributed to the formation of a Schottky barrier at the interface between the metal and the semiconductor. This leads to the bending of the semiconductor band structure, and the energy of the interband optical transitions in the QW is lowered due to the Stark effect. The increased spectral width could originate from differences in the band bending below the metal stripes and slits, leading to an inhomogeneous distribution of the electric field in the plane of the structure. Between different measurement series, the spectral position and FWHM change slightly (about 1 to 2 meV) due to changing experimental conditions like the sample temperature in the flow cryostat.

Whitelight Reflection Instead of using monochromatic laser light to excite the sample, white light with a broad spectrum can be used to measure the spectrum of the reflected light. Figure 8.2(a) shows the reflected p-polarized intensity (normalized) from the bare QW in a broad spectral range. It is dominated by a periodic modulation of the reflected intensity, which originates from the interference between the light reflected at the surface and the sample substrate (Fabry-Perot

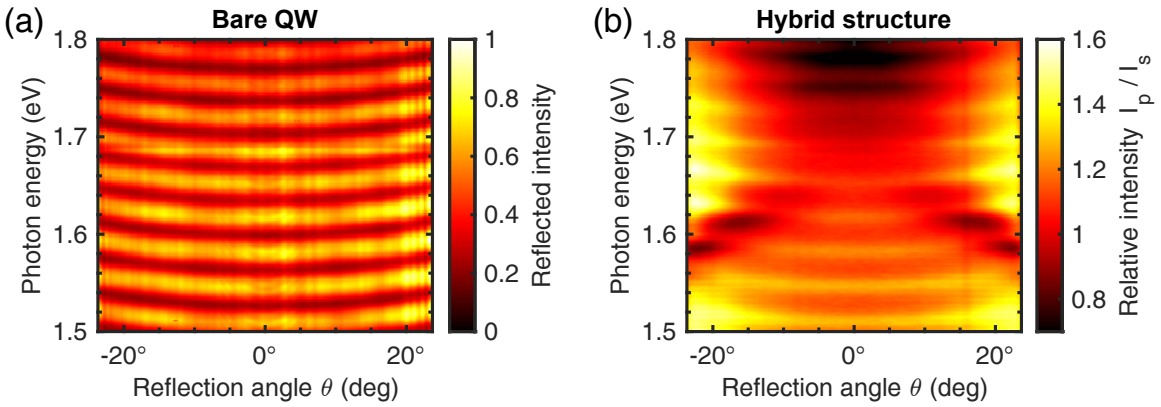

Figure 8.2 (a) Light intensity $I(E, \theta)$ (normalized) reflected from the bare QW structure. **(b)** Relative intensity between the reflected light in p- and s-polarization I_p/I_s from the hybrid structure with 250 nm grating period, which highlights the SPP dispersion intensity minima.

modes). The thin absorption line at 1.688 eV corresponds to the optical excitation of the quantum well. The s-polarized reflection looks almost identical (not shown here).
Figure 8.2(b) shows the relative intensity I_p/I_s of the reflected p- and s-polarized light from the hybrid structure with an additional periodic 250 nm grating on top of the bare QW surface. The periodic grating enables the optical excitation of SPPs by p-polarized light (see Section 3.2), and the normalization with the s-polarized light suppresses the interference pattern. The SPP at the interface between the gold grating and the (Cd,Mg)Te cap layer appears as the X-shaped intensity minimum starting at 1.6 eV and large reflection angles. The grating parameters have a large influence on SPP dispersion relation $E(k)$ and change its spectral position, see e.g. Eq. (3.5). Therefore, the spectral dependence of magneto-optical effects like the TMOKE and the TMRLE, which are enhanced significantly by the optical resonance, are also influenced by the grating parameters. This will be discussed in Chapter 10 for the TMRLE and TMOKE from this hybrid structure.

8.2 Giant Zeeman Splitting of the Excitons

The diluted magnetic semiconductor (DMS) quantum well (QW) structures investigated here are a model system for the investigation of the TMRLE. Their giant Zeeman splitting of the heavy- and light-hole energy levels leads to a large degree of circular polarization P_c of the QW emitters, which results in a large magnitude of directional emission, see Chapter 5. The Zeeman splitting of the heavy-hole excitons Δ_Z in the Faraday geometry can be determined by measuring the shifting spectral position of their emission peak in a magnetic field. Properties needed for theoretical models like the manganese concentration x and the effective temperature T_0 of the (Cd,Mn)Te QW can be derived from the magnetic field dependence of the Zeeman splitting. These measurements were first published in Ref. [48].

A schematic depiction of the experimental setup is shown in Figure 8.3. The bare QW structure was mounted in a pumped liquid helium bath cryostat with superconducting magnet coils, which cools the sample to $T = 1.5$ K and provides magnetic fields up to $B = \pm 5$ T in the Faraday geometry. The QW was excited non-resonantly with linearly polarized light from a Ti:Sa-laser centered at

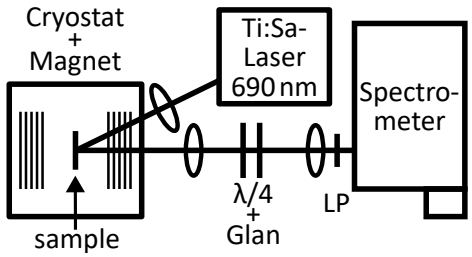

Figure 8.3 Schematic presentation of the experimental setup used to measure the Zeeman splitting of the QW emission. The laser excites the magnetized sample in the cryostat, the spectrometer measures the circularly polarized emission.

$\lambda = 690\,\text{nm}$, which was focussed onto the sample at a small angle using an $f = 200\,\text{mm}$ lens. The light emitted from the QW was collected and collimated using an $f = 400\,\text{mm}$ lens. Then, either σ^+ or σ^- circularly polarized light was selected using the combination of a quarter-wave plate ($\lambda/4$) and a Glan-Thompson prism, and measured by the subsequent spectrometer with a nitrogen-cooled CCD sensor. The light was focussed onto the spectrometer entrance slit by an additional lens, and remaining laser light was blocked by a longpass filter (LP). The spectrum of the light emitted from the QW was measured for external magnetic fields between $\pm 5\,\text{T}$ in steps of 250 mT for both polarizations at each step.

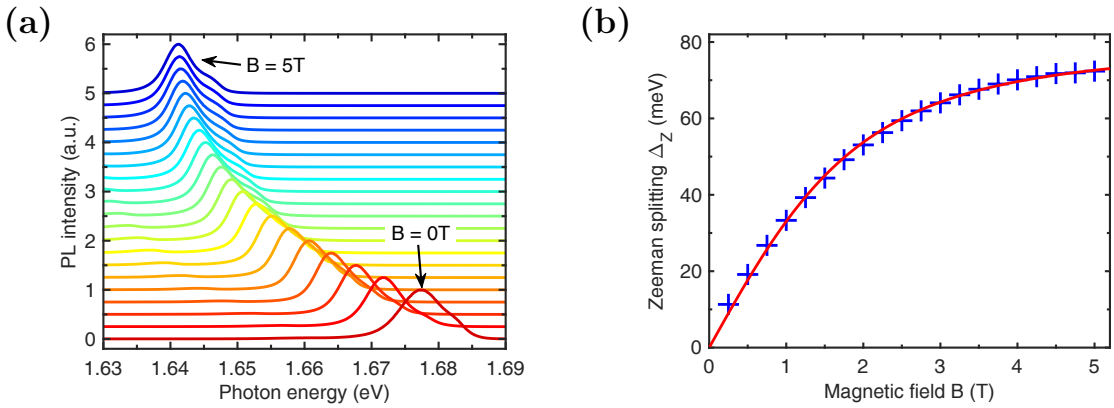

Figure 8.4 (a) Spectra of the σ^+-polarized PL from the QW (normalized) for magnetic fields B from 0 T (bottom, red) to 5 T (top, blue) in steps of 250 mT. **(b)** Magnetic field dependence of the the heavy-hole exciton Zeeman splitting Δ_Z and fit according to Eq. (8.2). Both adapted from [48].

Figure 8.4(a) shows the normalized spectra of the σ^+-polarized photoluminescence (PL) from the QW for increasing positive magnetic fields between $B = 0\,\text{T}$ at the bottom and 5 T at the top. The magnetic field of each spectrum can be determined as the interception of the respective line with the y-axis. The emission already becomes strongly polarized in small magnetic fields due to the giant Zeeman splitting in DMS materials. Therefore, only one emission polarization $\sigma^\pm$ is reliably detectable for each magnetic field direction $\pm B$, but the shift of the spectral line is the same in each case. The emission from the QW is centered at 1.677 eV for $B = 0\,\text{T}$ and shifts down to 1.641 eV for 5 T. The FWHM of the main emission peak decreases from 8.3 meV at 0 T to 5.3 meV at 5 T as the magnetic field aligns the Mn-spins and the inhomogeneous broadening decreases.
From this data, the Zeeman splitting of the heavy-hole exciton Δ_Z can be calculated as twice the difference of the emission energies at $B = 0\,\text{T}$ and $B > 0\,\text{T}$

$$\Delta_Z = 2\left[E_{\sigma^\pm}(B=0) - E_{\sigma^\pm}(B>0)\right], \tag{8.1}$$

because the emission is already strongly polarized at small magnetic fields. Figure 8.4(b) shows Δ_Z

for magnetic fields between 0 T and 5 T as crosses. At first, it increases linearly with B and then almost saturates at 5 T with a splitting of 73 meV. The giant Zeeman splitting of the excitons Δ_Z due to the exchange interaction between the carriers and magnetic Mn^{2+} ions in a DMS can be expressed as the difference between the valence and conduction band splittings [44, 92]:

$$\Delta_Z = xN_0(\alpha - \beta)\left\langle S_z^{Mn}\right\rangle, \tag{8.2}$$

see also Section 2.2. Here, x is the Mn concentration, $N_0\beta = -0.88\,\text{eV}$ and $N_0\alpha = 0.22\,\text{eV}$ are the exchange constants for the valence and conduction bands in (Cd,Mn)Te, and $\left\langle S_z^{Mn}\right\rangle$ is the thermal average of the Mn^{2+} spin projection along the external magnetic field direction. As discussed in Section 2.1, $\left\langle S_z^{Mn}(B)\right\rangle$ is well described by a modified Brillouin function $B_{5/2}$

$$\left\langle S_z^{Mn}(B)\right\rangle = S_{\text{eff}} B_{5/2}\left(\frac{5}{2}\frac{\mu_B g_{Mn} B}{k_B(T_{Mn} + T_0)}\right), \tag{8.3}$$

with the Boltzmann constant k_B, the applied magnetic field B, the g-factor of Mn^{2+} ions $g_{Mn} = 2$, the Mn-spin temperature T_{Mn}, and the effective temperature T_0 and effective spin S_{eff} as phenomenological parameters. In combination, Eqs. (8.2) and (8.3) can be used to fit the experimental data with the fit parameters T_0 and the combined xS_{eff} due to the lack of an accurate x value. Assuming that the Mn spin temperature is equal to the liquid helium temperature in the bath cryostat $T_{Mn} = T_{He} = 1.5\,\text{K}$, the fit yields $T_0 = (1.9 \pm 0.1)\,\text{K}$ and $xS_{\text{eff}} = 0.071 \pm 0.001$. The resulting curve is shown in red in Figure 8.4(b) and has a good agreement with the experimental data. The Mn content can be estimated to $x \approx 4\,\%$ using the experimental data from Ref. [92], which in turn corresponds to $S_{\text{eff}} \approx 1.7$. This matches similar values reported in Ref. [93] for a slightly larger Mn concentration of about 5 %.

The Zeeman splitting is lower for the TMRLE measurements in the Fourier imaging setup, where magnetic fields of 485 mT were applied. This corresponds to $\Delta_Z = 17\,\text{meV}$ at $T = 1.5\,\text{K}$ and about 10 meV at $T = 4\,\text{K}$. With the sample placed in a flow cryostat, the splitting is reduced further because the sample is not in direct contact with the liquid helium and, thus, warmer. For low amounts of Mn ions x, the continuous-wave laser photoexcitation can increase the Mn-spin temperature significantly due to slow spin-lattice relaxation [44], further reducing the Zeeman splitting for the same magnetic field. In the experiments on the temperature dependence of the TMRLE (see Chapter 9 and Ref. [48]), the relatively large laser excitation power density of $400\,\text{W/cm}^2$ leads to a temperature offset of $(19 \pm 3)\,\text{K}$ between the temperature measured by the sensor in the cryostat and the actual temperature of the Mn spins T_{Mn} obtained from fitting the experimental data. At those temperatures, the Zeeman splitting is estimated to around 2.4 meV. Since the TMRLE takes place in the Voigt geometry, the Zeeman splitting of the light holes in the Voigt geometry is used to define the the TMRLE parameter P_c in the corresponding theory in Chapter 5. The two splittings are connected via the heavy-hole splitting in Faraday geometry $\Delta_{h,F}$:

$$\Delta_{l,V} = \frac{2}{3}\Delta_{h,F} = \frac{2}{3}\underbrace{\frac{|\beta|}{|\alpha - \beta|}}_{=0.8}\Delta_Z. \tag{8.4}$$

8.3 TMRLE from the Main Hybrid Structure

As an introduction to the measurements of the TMRLE, this section first presents the TMRLE signal measured at 4 K from the main hybrid structure of this thesis with a 250 nm grating period, before later chapters will go into more detail on the temperature dependence of the routing effect and the dependence on the plasmonic grating parameters. This 250 nm hybrid structure is similar to the sample used in Refs. [30, 52] and shows an easy-to-understand spectral and angular dependence of the emission directionality. It features a 10 nm thin (Cd,Mn)Te QW and a plasmonic gold grating with a 250 nm period that supports SPPs and their outcoupling into the far-field. They are separated by a 30 nm thin (Cd,Mg)Te cap layer, which enables their near-field interaction for an enhanced TMRLE, see Section 5.2.

The TMRLE manifests as a change of the angular distribution of the far-field emission intensity $I(\theta)$ induced by the external magnetic field $\pm B$ in the Voigt geometry. The Fourier imaging spectroscopy setup is particularly suitable for TMRLE measurements because it enables the angle-resolved detection of the emission intensity for a large angular range θ in one image. From theory, we know that the change of the emission intensity due to the TMRLE is an odd function of the in-plane magnetic field B: If, for example, the emitted intensity $I(E,\theta)$ increases at a certain light energy E and emission angle θ for a positive B, it will decrease when the magnetic field is inverted ($B \to -B$). The relative change ρ of the emission intensity $I(E,\theta)$ induced by the opposite magnetic fields $\pm B$ can be deduced by measuring the emitted intensity at opposite magnetic fields and is quantified as

$$\rho = \frac{I(+B) - I(-B)}{I(+B) + I(-B)}, \tag{8.5}$$

see Eq. (5.2). Therefore, a positive ρ indicates a higher light intensity emitted for positive than negative magnetic field and vice versa for negative ρ, with a maximum of $|\rho| = 100\,\%$ if the whole emission is routed by the magnetic field. The quantity ρ is not limited to the intensity changes due to the TMRLE but includes all intensity changes induced by the inversion of the magnetic field direction. These include overall changes to the emission intensity for opposite B as a symmetric offset in ρ, or long-term intensity changes due to changing sample temperature or other experimental parameters, like changes of the sample position in the focal plane or the laser intensity that reaches the sample. Since the intensity change due to the TMRLE is an odd function of the emission angle θ, i.e. $\rho(\theta) = -\rho(-\theta)$, the magnetic-field-induced directionality of the emission C can be expressed as the antisymmetric part of ρ with respect to the emission angle

$$C = [\rho(\theta) - \rho(-\theta)], \tag{8.6}$$

see Eq. (5.3). This removes all omnidirectional, symmetric changes of the emission intensity from the measurements [30]. For all measurements presented in this thesis, $\rho = C$ holds true, and both quantifies will, therefore, be called directionality.

Starting with the emission from the QW, Figure 8.5(a) shows the normalized intensity of the QW emission $I(E,\theta)$ for the main hybrid structure with a 250 nm grating period, measured at $T = 4\,\mathrm{K}$. The emission is centered around 1.681 eV with a full width at half maximum (FWHM) of 11 meV, integrated over the whole angular range. The spectrum has a flat angular dependence with an intensity dip at $-22°$, which is caused by an obstruction in the optical path. Figure 8.5(b) shows the corresponding spectrum of emission intensity changes $\rho(E,\theta)$ induced by the magnetic field

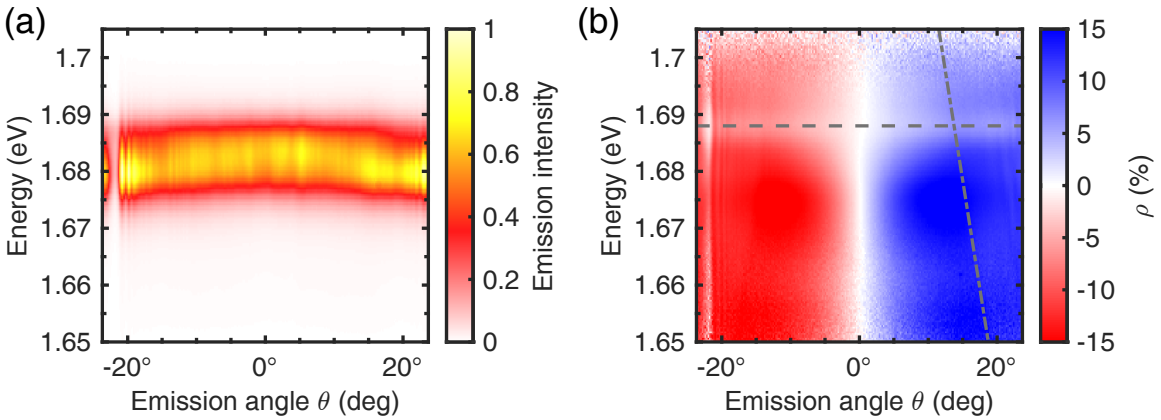

Figure 8.5 For the main hybrid structure with a 250 nm grating at $T = 4$ K: **(a)** Two dimensional plot of the intensity $I(E, \theta)$ emitted from the QW (normalized). An obstruction in the optical path blocked most light emitted at $-22°$. **(b)** Relative intensity change $\rho(E, \theta)$ induced by the magnetic field $B = \pm 485$ mT, reaching $\rho = 9\,\%$ at the PL maximum and up to 15 % for lower energies. Horizontal dashed line: Emission maximum of the bare QW. Dash-dotted line: Step-like change of ρ from the first-order diffracted beam.

$B = \pm 485$ mT according to Eq. (8.5). Blue and red represent different signs of ρ and their saturation visualizes its magnitude. Thus, blue indicates more light emitted for positive than for negative magnetic fields at the specific energy and emission angle, and vice versa for the color red. Like the signal from the similar old structure presented in Figure 5.2(c), the spectral and angular dependence $\rho(E, \theta)$ is fairly flat and uniform, with a negative sign (red) for negative angles and a positive sign (blue) for positive angles. It reaches around $\rho = 9\,\%$ at the emission maximum and up to 15 % for lower energies, but with an almost negligible emission intensity compared to the maximum. The large routing magnitude stems from the near-field interaction of the excitons in the magnetic QW with the SPPs at the nearby plasmonic grating, which possess strong spin-momentum locking and significantly enhance the TMRLE in a broad spectral range, see Section 5.2.
The two far-field effects that were discussed in Figure 5.2(a) and (b) also contribute to the directionality spectrum here: First, the weak oscillations of ρ along the energy axis with a period of about 30 meV are present but less pronounced compared to the stronger SPP-assisted routing. They are caused by the interference of directly emitted light beams with those first reflected at the backside of the sample, see Figure 5.2(a). The second far-field effect, the step-like change in emission routing at a critical angle, that correlates with the appearance of the first-order diffracted beam from the grating structure, is also present but barely visible. It manifests a slight change of ρ and is highlighted in the positive angular range by the dash-dotted line. At 1.688 eV, slightly above the emission maximum, the directionality shows a local minimum for all angles (highlighted by the dashed line). As will be seen later, it also appears at larger temperatures and for different grating periods (e.g., Figures 9.4 and 10.7). This line coincides with the emission maximum from the bare QW structure (without the gold grating), which has a higher emission energy than the hybrid structure because a Schottky barrier is formed at the metal/semiconductor interface of the hybrid structure, which bends the band structure (see Section 8.1). The feature can either be attributed to weak emission from outside the gratings, since the gratings show no defects or missing gold stripes in the SEM images that could cause this bare-QW-like emission, or it is connected to a local change of the dielectric permittivity ε by the excitons in the QW (see Chapter 10).

The spectral and angular dependence of the SPP-enhanced directionality $\rho(E, \theta)$ is mostly determined by the parameters of the plasmonic gold grating. They define the dispersion relation of the SPPs and, consequently, its overlap with the QW emission line and the emission characteristics into the far-field. Small changes to the QW emission spectrum $I(E, \theta)$ do not change the TMRLE spectrum $\rho(E, \theta)$ much, especially for the SPP-enhanced case, because the SPP resonances are spectrally broad in comparison. In other words, the QW emission is the light source that reveals the routing characteristics $\rho(E, \theta)$ of the grating in a broader spectral window of a few tens of meV so that small changes in the emission energy do not matter for the normalized quantity ρ.

8.4 Sample Comparison

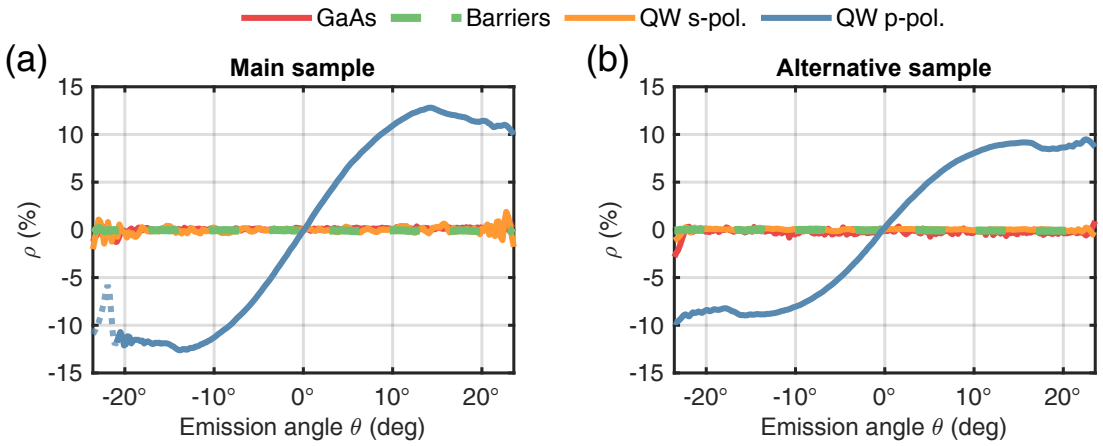

Figure 8.6 Directionality $\rho(\theta)$ of different emission types for **(a)** the main sample and **(b)** a similar alternative sample: The p-polarized emissions from the (Cd,Mn)Te QW (blue), GaAs substrate (red) and (Cd,Mg)Te barriers (green, dashed), and the s-polarized QW emission (orange), with all but the first showing $\rho = 0$, i.e. no magnetic field influence on the emission.

For a better qualitative picture of the routing effect, Figure 8.6 shows the angular dependence $\rho(\theta)$ for the emission from different semiconductor layers of the 250 nm hybrid structure. Those are the p-polarized emission from the (Cd,Mn)Te QW (blue), which shows the largest SPP-enhanced directionality of the emission, as well as the p-polarized emissions from the GaAs substrate (red) and the (Cd,Mg)Te barrier (green, dashed), and the s-polarized QW emission (orange), which are all expected to show no significant directionality. Furthermore, it compares those signals from the main structure of this thesis (a) to those from the similar alternative structure (b) used for the earlier TMRLE measurements in Refs. [30, 52], but with a different batch of gratings. The emitted intensity spectra $I(E, \theta)$ were measured in the Fourier imaging setup and afterward spectrally integrated in a 10 meV window around the respective emission maximum before calculating ρ according to Eq. (8.5), except for the (Cd,Mg)Te barrier emission in a 20 meV window due to its larger FWHM. The 10 meV spectral window is about the same size as the FWHM of the QW emission.

Starting with the p-polarized emission from the magnetic QW (blue lines), the directionality reached up to $\rho = 12.5\,\%$ on the main sample and 9 % on the alternative sample under comparable conditions and around their respective emission maxima of about 1.68 eV and 1.67 eV. The angular

dependence $\rho(\theta)$ is similar on both structures, rising monotonously from $\rho = 0\,\%$ at $\theta = 0°$ towards their respective maxima between 12° and 15° and slowly decreasing for further increasing emission angles. The angle of maximum emission routing θ_{max} corresponds approximately to the resonance condition where the energies of the SPP and the exciton resonance E_X match. It is given by $\sin\theta = k_{SPP}/k_0$ with the wave vector of the emitted light $k_0 = E_X/\hbar c$ and the reduced Planck constant $\hbar$. The obstructed signal around −22° is shown as a dotted line. As seen before, the angular dependence is the same for negative angles but with flipped signs $\rho(-\theta) = -\rho(\theta)$. In both cases, a step-like change of ρ connected to the appearance of the first-order diffracted beam occurs at an angle close to the maximum of ρ with small oscillations for larger angles. This was highlighted in Figure 8.5(b) by the dash-dotted line. Notably, the routing magnitude ρ achieved on both samples is significantly larger than those measured in Refs. [30, 52] with $\rho < 5\,\%$. Most likely, this is due to better experimental conditions, mainly a lower sample temperature due to less heating with the exciting laser or better thermal contact with the liquid helium.
These results can be verified with the emission directionality from the other semiconductor layers, namely from the (Cd,Mg)Te barriers at 2.075 eV (dashed green line in Figure 8.6) and from the GaAs substrate at 1.5 eV (red). Both layers are non-magnetic, and their emission is not influenced by the external magnetic field for both samples, i.e. $\rho = 0$. Similarly, the directionality of the s-polarized QW emission (orange line) does not show any significant routing effect because its polarization is perpendicular to that of the SPPs and the elliptically polarized QW emitters [30]. Additionally, the emission routing from the bare QW is negligible in comparison due to the absence of surface waves (e.g. SPPs) close to the QW layer, so only weak directional emission with $\rho < 0.5\,\%$ takes place, see Section 5.2. That data is shown later in Figure 8.7, which compares the experimental data with the theory model.

The different routing magnitudes of the two structures likely stem from their different compositions. For one, the cap layer on the main sample is a few nm thinner, which may increase the near-field interaction between the QW and the SPPs. Additionally, the barrier layers of the alternative sample are modulation-doped with a 2D electron gas in close proximity to the QW (7 and 10 ML of added Iodine). This increases the number of free carriers, which is expected lead to a better Mn-spin cooling [44]. On the other hand, it also seems to negatively impact the magnitude of magneto-optical effects like the TMOKE and possibly the TMRLE. This became apparent in preliminary TMOKE measurements on the bare structures for Ref. [60], where the TMOKE magnitude δ reached between 1 % to 1.3 % for undoped cap layers of different thicknesses, but did not exceed 0.08 % for the modulation-doped cap layer. The undoped main sample of this thesis also shows TMOKE $\delta > 1\,\%$ (see Chapter 10), which further solidifies the suspected influence of the cap-layer doping on the TMOKE and possibly the TMRLE.

8.5 Theoretic Simulations

The experimental results can be verified by theoretical calculations of the routing effect using the scattering matrix method, which is explained in detail in Ref. [30], where it was also used to reproduce the three routing cases presented in Section 5.2. In the model, the excitons are uncorrelated point dipoles with a fixed polarization $\pm P_c$ perpendicular to the QW plane, based on the external magnetic field direction $\pm B$. They are randomly distributed 30 nm below the plasmonic interface at the surface. The far-field emission is calculated for the two oppositely polarized circular

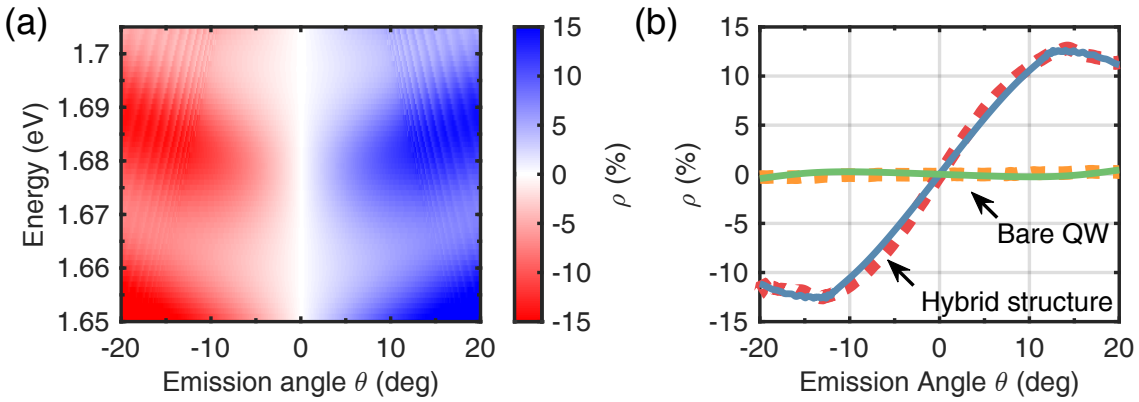

Figure 8.7 (a) Theoretical calculation of $\rho(E, \theta)$ for the main hybrid structure with 250 nm grating. **(b)** Angular dependence $\rho(\theta)$ at the emission maximum of the main hybrid structure (1.681 eV) and the bare QW (1.687 eV), comparing experimental data from Figure 8.6 (dotted lines) and simulations (solid lines). Adapted from [48].

emitters and compared according to Eq. (8.5) to deduce ρ. The magnitude of ρ can be changed by increasing or decreasing the parameter P_c. At the same time, the spectral and angular dependence is mostly controlled by the geometric and optical parameters of the modeled structure. The energy-dependent refractive indices for gold, (Cd,Mg)Te, and GaAs were taken from Refs. [50, 51, 94]. The contrast of the background refractive indices of the thin QW and the (Cd,Mg)Te cap layer was neglected.

Figure 8.7(a) shows $\rho(E, \theta)$ resulting from the model with $P_c = \pm 9\,\%$, which was chosen to reproduce the routing magnitude from the experimental data. This corresponds to a Zeeman splitting of the light holes in Voigt geometry $\Delta_{l,V} = 1.8$ meV, assuming $\Delta_{lh} = 20$ meV according to Eq. (5.1). The value of $\Delta_{l,V}$ is close to those obtained from the fit in Section 8.2 for temperatures $T_{Mn} > 4$ K and at 485 mT. The grating has a period of 250 nm with 55 nm slits, and the thickness of the semiconductor layers also matches the real sample. Overall, the data resulting from the model is in good agreement with the experimental data in Figure 8.5(b) with negative (positive) $\rho(E, \theta)$ for negative (positive) angles in the depicted spectral range and a magnitude up to 15 %. The oscillations along the energy axis and the interference fringes at large angles are also present, albeit slightly more pronounced than in the experimental data. The buffer thickness can influence the spectral position of the long-period oscillation maxima by changing the optical path difference of the interfering beams. Figure 8.7(b) shows a comparison of the calculated (solid lines) and the experimental data (dashed lines), for the emission from the hybrid structure and from the bare QW structure (without gold grating), with good agreement in both cases. The angular dependencies $\rho(\theta)$ were obtained by first averaging the emission intensity spectra $I(E, \theta)$ along the energy axis in a 10 meV window around the respective emission maximum, before calculating ρ according to Eq. (8.5). It is important to note that the model assumes uniform emission at all energies from optical transitions with $\pm P_c$ with an equal and independent contribution to the emitted intensity. Therefore, the simulated spectra were further multiplied with a Gaussian distribution in the shape of the experimental data to increase the comparability. As discussed in Figure 8.6, ρ reaches about 12.5 % from the hybrid structure due to the spin-momentum locking and directional emission of the SPPs. The signal from the bare QW reaches about 0.5 % in the absence of such surface waves, mainly due to interference

of directly emitted and backside reflected light beams, which is also reflected in the simulations. For the emission from the non-magnetic semiconductor layers, $P_c = 0$ can be assumed due to their negligible Zeeman splittings, which leads to $\rho = 0$ in the simulations.

Chapter 9

TMRLE at Elevated Temperatures

This chapter focusses on the temperature dependence of the TMRLE and its routing magnitude. All previous measurements were conducted at cryogenic temperatures of about 4 K using liquid helium for cooling. For a given hybrid structure, the routing magnitude is determined by the semiconductor quantum well (QW) and the Zeeman splitting of the excitons. The splitting at low temperatures is giant in the diluted magnetic semiconductor (Cd,Mn)Te structures due to their strong exchange interaction with the magnetic Mn^{2+}-ions. However, the alignment of the Mn^{2+}-ions in the magnetic field, i.e. their magnetization, is highly temperature dependent and, thus, the resulting Zeeman splitting and the TMRLE routing magnitude. The theory behind this is described in detail in Chapters 2 and 5 for the Zeeman splitting in DMSs and the TMRLE, respectively.

In this chapter, Section 9.1 will present temperature-dependent measurements of the TMRLE and compare them with the theory. It confirms the lower emission routing magnitude due to the temperature influence on the Mn-spin system. Next, Section 9.2 will show that the light-hole exciton emission becomes detectable at elevated temperatures due to an increased thermal occupation compared to the main heavy-hole bands, and that the emission from the heavy- and light-hole excitons is routed in opposite directions. Then, Sections 9.3 and 9.4 will present similar measurements for two slightly altered structures to show the influence of the grating structure and the semiconductor composition on the temperature dependence. In the final Section 9.5, an alternative structure will be considered theoretically, where the DMS QW is replaced by a nonmagnetic (In,Ga,Al)As QW structure (i.e., without magnetic ions). Its Zeeman splitting is not governed by the exchange interaction but by the intrinsically large hole g-factor. This promises a temperature-independent realization of the TMRLE for a wider temperature range up to 200 K for an improved applicability of the emission routing compared to DMS structures.

Most results presented in this chapter have already been published in Ref. [48]. Therefore, this chapter closely follows said publication, and its content and figures are reproduced and adapted for this thesis with permission.

9.1 Temperature Dependence of the TMRLE

To measure the temperature dependence of the TMRLE, the relative intensity change $\rho(E, \theta)$ of the QW emission induced by the external magnetic field was measured at various temperature steps T between 4 K and 45 K on the main hybrid structure with the 250 nm grating. For this, the sample in the cryostat was cooled down to 4 K using liquid helium. Then, the resistive heating

element in the cryostat was used to increase the temperature of the sample and locked using the external PID feedback controller. Additionally, the helium flow had to be reduced to reach the higher temperatures in this series. The emission spectra for opposite magnetic fields of ±485 mT were measured and compared according to Eq. (8.5) to deduce the routing magnitude ρ for each temperature step. The full spectrum $\rho(E, \theta)$ of the 250 nm grating at 4 K was already shown in Figure 8.5, and the spectra at higher temperatures do not look significantly different. Quickly summarized, the routing magnitude ρ decreases for increasing temperatures and the temperature dependence originates from the semiconductor QW of the hybrid structure, where the alignment of Mn-spins $\left\langle S_z^{\mathrm{Mn}} \right\rangle$ in the magnetic field decreases, as does the giant Zeeman splitting of the exciton levels from the sp-d exchange interaction and thus the routing. The overall shape of $\rho(E, \theta)$ stays the same, though, as it is determined by the parameters of the plasmonic grating. Additionally, the directional emission from the light-hole excitons becomes visible at $T > 35$ K due to increasing thermal occupation. Crucially, it is routed in the opposite direction compared to the main emission from the heavy-hole excitons. The theory behind the TMRLE is explained in Chapter 5, and Chapter 2 contains the temperature dependence of the giant Zeeman splitting in diluted magnetic semiconductors (DMSs), which also dictates the temperature dependence of the TMRLE. For an overview of a typical TMRLE measurement and how to analyze the results, see Chapter 8.

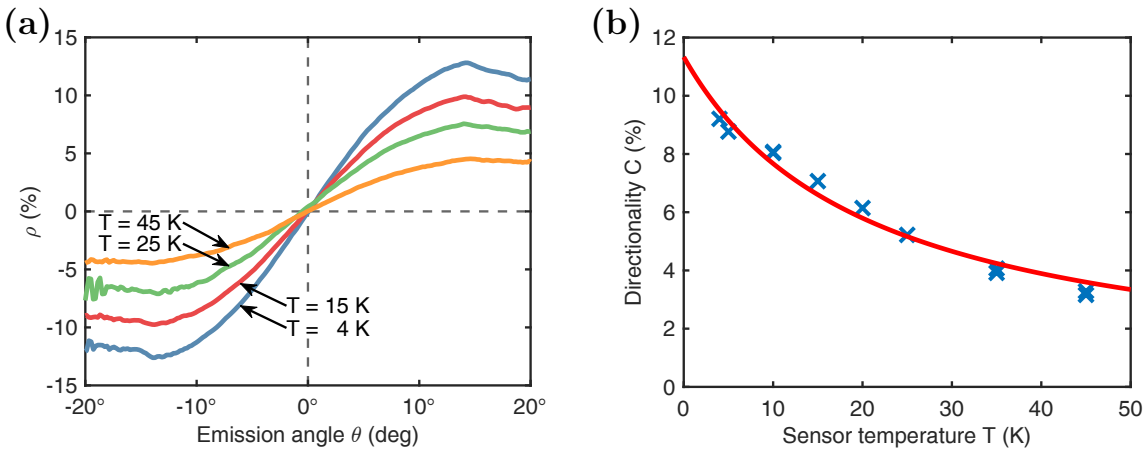

Figure 9.1 (a) Angular dependence $\rho(\theta)$ for the light emitted from the hybrid structure in a 10 meV window around the QW PL maximum at $E = 1.681$ eV for different temperatures T. The magnitude of the directional emission decreases with increasing temperature while the angular dependence does not change. **(b)** Temperature dependence of the directionality $C(T)$ for the PL emitted between $\theta = 0°$ and $\pm 20°$ and in the photon energy range of (a). Red line: Fit using a modified Brillouin function according to Eq. (9.1), yielding $T_{\mathrm{off}} = (19 \pm 3)$ K. Adapted from [48].

The data from the temperature series are summarized in Figure 9.1. Panel (a) shows the angular dependence of the relative intensity change $\rho(\theta)$ induced by the external magnetic field, i.e. the directionality, for four different temperatures $T = 4$ K, 15 K, 25 K and 45 K. Here, T is the temperature measured by the temperature sensor in the cryostat. As for Figure 8.6, the emitted light was integrated along the energy axis in a 10 meV window around the maximum of the QW emission at 1.681 eV before $\rho(\theta)$ was calculated according to Eq. (8.5). The 10 meV window is about the same size as the FWHM of the QW emission. The angular range is limited to $\pm 20°$ because dirt in the optical path blocked portions of the light emitted at $-22°$. It is apparent that the shape of the angular dependence $\rho(\theta)$ is the same for all temperatures, but the overall magnitude of the emission routing

decreases for increasing temperatures: For all temperatures, the routing magnitude increases from 0 % at 0° towards a maximum at 14°, where the interaction between the QW and the SPPs is best, and slowly decreases again for larger angles. This maximum decreases from 12.5 % at 4 K to 4.5 % at 45 K. Furthermore, $\rho(\theta)$ is fully antisymmetric regarding the angular axis, i.e. $\rho(\theta) = -\rho(-\theta)$. Therefore, the directionality C of the emission at all temperatures is fully determined by the TMRLE without other influences and $\rho = C$ holds true, see Eq. (8.6). This was also the case for all previous directionality measurements at 4 K, e.g. in Refs. [30, 52].

In order to quantify the temperature dependence of the directionality and compare it with the theory, it needs to be condensed into one value $C(T)$ for each temperature step T. Figure 9.1(b) shows the experimental data for $C(T)$ (blue crosses) for temperatures between 4 K and 45 K. The values shown are the mean directionality for all light emitted in the same 10 meV FWHM window around the emission maximum (like before) and in the two angular ranges between $\theta = 0°$ and $\pm 20°$. First, the measured intensities $I(\pm B)$ were integrated spectrally and in the two separate angular ranges. Then, ρ was calculated independently for the positive and negative angular range according to Eq. (8.5), and finally, the directionality C as the antisymmetric average of both angular ranges according to Eq. (8.6). Two measurements each were taken at $T = 10\,\mathrm{K},\ 35\,\mathrm{K}$ and 45 K to verify the previous measurements. The data show a monotonous decrease of the directionality for increasing temperatures from around $C = 11\,\%$ at 4 K to below 5 % at 45 K, with a larger gradient at low temperatures.

These results match the expected behavior for the hybrid structure with a DMS QW: The angular (and spectral) shape of ρ (and C) is mainly determined by the plasmonic grating and its parameters, which are not influenced by the temperature. Instead, the temperature dependence of the directionality C is solely determined by the degree of circular polarization P_c of the exciton optical transitions in the QW and is, therefore, a property of the magnetic semiconductor part of the hybrid structure. P_c is used for the theoretical description of the TMRLE and $C \propto P_\mathrm{c}$, see Chapter 5. It can be estimated at small magnetic fields using Eq. (5.1), which reads

$$P_\mathrm{c} \approx \frac{\Delta_\mathrm{l,V}}{\Delta_\mathrm{lh}}$$

and depends on two values: First, the splitting $\Delta_\mathrm{lh} \approx 20$ meV between the light- and heavy-hole subbands, which is determined by the structure of the QW and is temperature independent, and secondly, the Zeeman splitting $\Delta_\mathrm{l,V}$ of the light-hole levels in Voigt geometry. The giant Zeeman splitting of the levels in a diluted magnetic semiconductor (DMS) like (Cd,Mn)Te is solely determined by the strong exchange interaction between the carriers and magnetic Mn^{2+} ions. For light holes with $J_z = \pm 1/2$, it can be expressed as

$$\Delta_\mathrm{l,V} = \frac{2}{3} x N_0 \beta \left\langle S_z^\mathrm{Mn} \right\rangle .$$

Here, x is the Mn concentration and $N_0\beta = -0.88$ eV is the exchange constant for the valence bands in (Cd,Mn)Te. $\left\langle S_z^\mathrm{Mn} \right\rangle$ is the thermal average of the Mn^{2+} spin projection along the applied magnetic field B_z, i.e. the magnetization [92]. It is highly temperature dependent and quickly decreases for increasing temperatures according to Eqs. (2.1) and (2.2), and so is the corresponding Zeeman splitting.

With the link between experimental data and theory $C \propto P_c$ in mind, the temperature dependence $C(T)$ can be approximated as

$$C(T) = C_0 B_{5/2}\left(\frac{5}{2}\frac{\mu_B g_{Mn} B}{k_B(T + T_{off} + T_0)}\right). \tag{9.1}$$

where μ_B is the Bohr magneton, k_B is the Boltzmann constant, B is the applied magnetic field, and $g_{Mn} = 2$ is the g-factor of the Mn^{2+} ions. The temperature dependence would usually be described by $T_{Mn} + T_0$ (see Eq. (8.3)). However, for the analysis of these experimental data, the temperature of the Mn-spin system T_{Mn} is replaced by $T + T_{off}$. Here, T is the temperature measured by the sensor in the cryostat and T_{off} is the possible temperature difference towards the warmer Mn-spin system T_{Mn}. $T_0 = (1.9 \pm 0.1)\,\mathrm{K}$ was deduced from the measurements of the giant Zeeman splitting in Section 8.2. Using Eq. (9.1) to describe the data in Figure 9.1(b) with T_{off} and C_0 as fitting parameters yields $T_{off} = (19 \pm 3)\,\mathrm{K}$ and $C_0 = (312 \pm 23)\,\%$ (standard errors). The resulting curve, shown in red, is in good agreement with the experimental data, which confirms the validity of the model to describe the TMRLE temperature dependence. The offset $(19 \pm 3)\,\mathrm{K}$ between the sensor temperature T and the Mn-spin temperature T_{Mn} from the fit is notably large and mostly caused by the laser excitation. The Mn-spin temperature can be increased significantly compared to the colder lattice by continuous-wave photoexcitation because the main process of cooling the Mn-spin system, the spin-lattice relaxation, is slow for low amounts of Mn-ions x [44, Ch. 8]. The laser power density from the exciting continuous-wave laser in the experiments was high at $P_0 \approx 400\,\mathrm{W/cm^2}$. In addition, the sample is not in direct contact with the liquid helium in the flow cryostat and the temperature sensor is located at some distance from the sample in the cryostat, which leads to a further temperature offset. The amplitude C_0 of over 100 % stems from the large additional offset temperature T_{off} in Eq. (9.1) that shifts the curve, and from the linear approximation of P_c in Eq. (5.1) and the subsequent general assumption of $C \propto P_c$, which does not hold true at very low temperatures. Evaluating Eq. (9.1) with a lower temperature offset reduces the necessary amplitude to fit at low temperatures, but the resulting curve decreases too quickly for the larger temperatures. We assume a constant temperature offset T_{off} for all temperatures T, even though a temperature dependence is to be expected because the cooling of the Mn-spin system via spin-lattice relaxation becomes more effective for increasing (lattice) temperatures [44, Ch. 8]. This could explain the deviations between the fitted curve and the data in Figure 9.1(b).

Several things need to be mentioned to put the data into perspective: First, $400\,\mathrm{W/cm^2}$ is a relatively large power density and was chosen to increase the PL intensity and limit the duration of each measurement. It is only a rough estimate because the laser power was measured in front of the cryostat window and the spot size on the sample was estimated from comparisons with the known size of the gold gratings. Keller et al. used significantly lower excitation power densities in their studies on similar (Zn,Mn)Se/(Zn,Be)Se QW structures, where $13\,\mathrm{W/cm^2}$ already led to a heating of $T_{Mn} = 23\,\mathrm{K}$, though with a lower Mn concentration of $x = 0.012$ [44, 95]. The strong influence of the Mn concentration on the cooling can be seen in their comparative measurements, where around $10\,\mathrm{W/cm^2}$ excitation power density lead to a Mn-spin temperature of about 40 K for $x = 0.004$ but only around 3 K for $x = 0.06$. With $x = 0.04$, our sample should show a similar cooling because the spin-lattice relaxation of the Mn ions does not change much for different host materials [44]. Additionally, the semiconductor part of our sample is covered by a gold layer to create the hybrid structure, which reflects a portion of the incoming laser light and reduces the power density further. The excitation of SPPs by the laser would lead to a stronger heating of the sample, as was seen in

Ref. [43] for spectrally broad laser pulses, but the sharp laser energy and almost normal incidence angle do not excite a significant amount of SPPs in our case. One possibility to reduce the heating of the Mn system could be below-barrier excitation to excite carriers only in the QW because carriers in the barriers that diffuse into the QW layer heat the system with their excess energy. However, this would also reduce the emission intensity from the QW. Finally, the large temperature offset in our measurements can also partially stem from not optimal cooling of the lattice in the flow cryostat compared to a bath cryostat, which likely amounts to a few Kelvin of the offset alone.

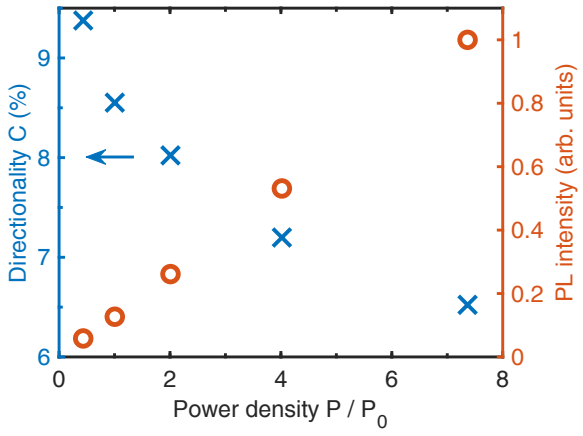

Figure 9.2 Blue crosses: Directionality C for different excitation power densities P/P_0 at $T = 4\,\mathrm{K}$, with $P_0 \approx 400\,\mathrm{W/cm^2}$, for light emitted in a 10 meV window around the QW PL maximum at 1.681 eV and between 0° to ±20°, from the hybrid structure. Orange circles: Emitted light intensity for the same photon energies and angles.

To confirm the influence of the excitation power density P on the Mn-spin temperature and thus the directionality C, Figure 9.2 shows C (blue crosses) for various relative power densities P/P_0 at the constant temperature $T = 4\,\mathrm{K}$. $P_0 = 400\,\mathrm{W/cm^2}$ is the excitation power used in all other experiments. The directionality was, again, determined for all light emitted in a 10 meV window around the emission maximum at 1.681 eV and between $\theta = 0°$ and ±20°. The directionality $C(P)$ shows the same dependence for increasing power densities as it did for increasing temperatures in Figure 9.1, decreasing quickly at first but slower for larger powers. At the same time, the emitted light intensity increases linearly with the power density, which is shown as orange dots in Figure 9.2. A higher emission intensity increases the signal-to-noise ratio in the measurements.

So far, we have shown that the temperature in general and, more specifically, the Mn-spin temperature has a large impact on the TMRLE magnitude in the DMS (Cd,Mn)Te/(Cd,Mg)Te QW structure. The TMRLE magnitude is proportional to the Zeeman splitting of the light-hole states, which in the DMS structure is given by the exchange interaction with the Mn ions and their temperature-dependent spin orientation. Evaluating the fit of Eq. (9.1) to the experimental data at higher temperatures of 200 K and 300 K and a still moderate magnetic field of 1 T yields $C = 2.2\,\%$ and 1.5 %, respectively. This should be interpreted as a lower estimate, though, because it does not consider the intrinsic g-factor of holes $g_\mathrm{h} \approx 0.5$ [96, 97]. Both contributions have the same sign, so a larger Zeeman splitting at high temperatures can be expected. Even though these routing magnitudes are small compared to those at lower temperatures, they are still not insignificant. However, this strong dependence of the routing magnitude on the temperature can be problematic for practical applications in not temperature-stabilized environments. Therefore, Section 9.5 will explore the usage of nonmagnetic semiconductor constituents (i.e. without magnetic ions) with intrinsically large hole g-factors as a temperature-independent alternative that still achieves noticeable routing, even without the giant Zeeman splitting from the exchange interaction.

9.2 Routing of the Light-Hole Emission

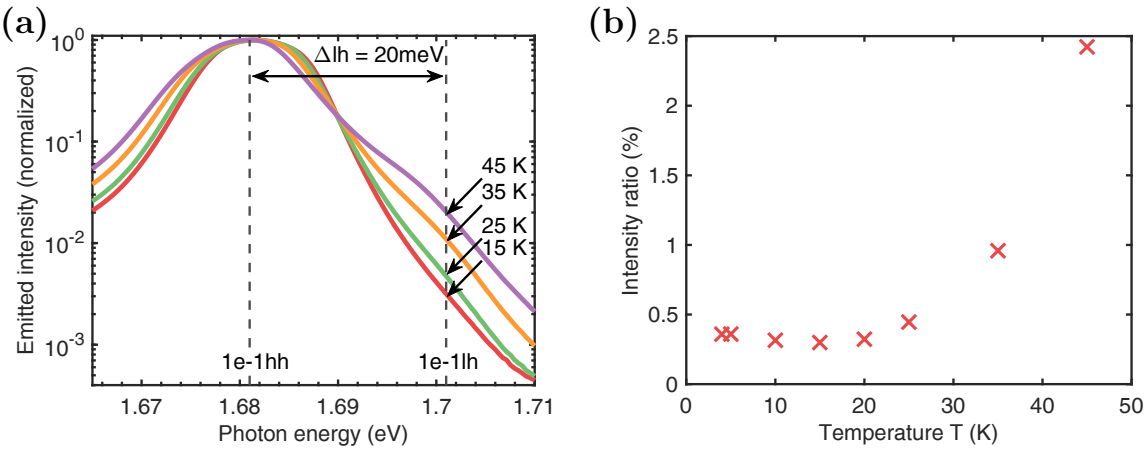

Figure 9.3 (a) Intensity spectra of the QW emission from the hybrid structure in a semi-logarithmic scale for $T = 15\,\mathrm{K}$, $25\,\mathrm{K}$, $35\,\mathrm{K}$ and $45\,\mathrm{K}$, normalized. The light-hole emission (1e−1lh) around 1.7 eV becomes more pronounced for increasing temperatures. Adapted from [48]. **(b)** Intensity ratio between the light-hole and heavy-hole emission for temperatures between $T = 4\,\mathrm{K}$ and $45\,\mathrm{K}$.

In the last sections, we have examined the TMRLE for the main emission from the QW, which originates from the recombination of heavy-hole excitons. In small magnetic fields, the two heavy-hole (1e−1hh) excitons are the lowest energy states, and their emission dominates the spectrum. Their emission is indistinguishable due to their low Zeeman splitting, and their emission is routed in the same direction because their optical transitions have the same sign of P_c, see Section 2.3.2. The light-hole (1e−1lh) excitons, on the other hand, are higher energy states and split from the heavy-hole excitons due to the confinement and strain of the QW, see Figure 2.3. With the large splitting $\Delta_{lh} \approx 20\,\mathrm{meV}$ for our (Cd,Mn)Te/(Cd,Mg)Te QW structure [60], the light-hole occupation is almost zero at low lattice temperatures $k_B T_c \ll \Delta_{lh}$ because most light-hole excitons relax into the lower energy heavy-hole exciton states within their lifetime. For increasing temperatures, though, the relative thermal occupation of the light-hole states increases $\propto \exp(-\Delta_{lh}/k_B T_c)$, and so does their contribution to the emission spectrum through recombination. This is evident in Figure 9.3(a), which shows the normalized QW emission spectra between $\theta = \pm 20°$ for the temperatures $T = 15\,\mathrm{K}$, $25\,\mathrm{K}$, $35\,\mathrm{K}$ and $45\,\mathrm{K}$ in a semi-logarithmic scale. For all four temperatures, the heavy-hole transition at 1.681 eV dominates the emission spectrum as the lowest energy state, and no light-hole emission is visible at low temperatures of, e.g., $4\,\mathrm{K}$ (not shown) or $15\,\mathrm{K}$, even in the logarithmic scale. At larger temperatures, though, an intensity shoulder of light-hole emission develops about 20 meV higher than the heavy-hole emission, which matches Δ_{lh}. Even at $45\,\mathrm{K}$, the light-hole emission is still weak, reaching around 2.5 % of the main heavy-hole emission. This can also be seen in Figure 9.3(b), which shows the temperature dependence of the intensity ratio between the heavy- and light-hole emissions. The relative intensity is roughly constant at 0.3 % from $4\,\mathrm{K}$ to $20\,\mathrm{K}$ and increases exponentially up to 2.5 % at $45\,\mathrm{K}$ due to the occupation of the light-hole states by thermal activation.

With their increasing emission intensity at higher temperatures, the light-hole excitons also contribute to the TMRLE spectrum. The two (1e−1lh) optical light-hole transitions also have

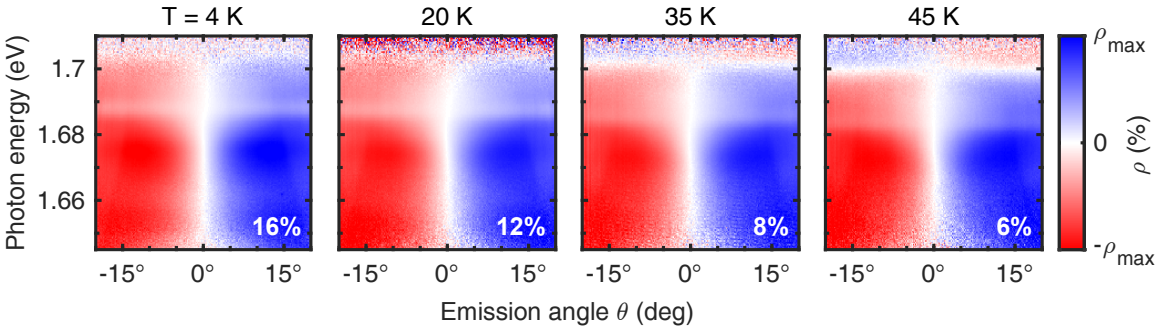

Figure 9.4 Relative intensity change $\rho(E,\theta)$ for $T = 4\,\mathrm{K},\ 20\,\mathrm{K},\ 35\,\mathrm{K}$ and $45\,\mathrm{K}$ according to Eq. (8.5). Each subplot has different colorbar limits $\pm\rho_{\mathrm{max}}$ that are shown in the respective bottom right corner.

the same sign of circular polarization in the yz-plane P_{c}. However, it is opposite to the heavy-hole transitions, i.e., the electrical dipole rotates in the opposite direction. This was already discussed in theory in Section 2.3 and can be seen in Figures 2.3 and 2.4. Consequently, the light-hole and heavy-hole emissions are routed in opposite directions, which leads to opposite directionalities ρ in the experimental data. This can be seen in Figure 9.4, which shows $\rho(E,\theta)$ for $T = 4\,\mathrm{K},\ 20\,\mathrm{K},\ 35\,\mathrm{K}$ and $45\,\mathrm{K}$ next to each other. The colors blue and red represent positive and negative values of ρ and their saturation the magnitude. Because ρ decreases in magnitude for increasing temperatures, each subplot has its own colorbar limit $\pm\rho_{\mathrm{max}}$, shown in the bottom right corner of each subplot. For energies lower than 1.7 eV, all measurements show the same spectral and angular dependence $\rho(E,\theta)$, and only the overall magnitude changes, as discussed in Section 9.1. At $T = 4\,\mathrm{K}$ and $20\,\mathrm{K}$, the TMRLE signal is noisy for energies above 1.7 eV and, on average, shows no directionality due to the absence of emission. The noise level for $20\,\mathrm{K}$ is larger due to a lower integration time. Compared to that, the expected sign change of ρ due to the emerging light-hole emission can be clearly seen for $T = 45\,\mathrm{K}$ around 1.7 eV as color change from blue to red or vice versa. The light-hole signal is still noisy due to the lower emitted intensity, but the two contributions do not overlap significantly and are easily distinguishable due to their large energy splitting. At $35\,\mathrm{K}$, the light-hole contribution is also visible but less pronounced and with more noise. This sign change of ρ confirms the predicted opposite routing direction of the TMRLE for heavy and light holes.

For a more detailed look at the spectral dependence of the directionality, Figure 9.5 shows $C(E)$ in the same spectral range as Figure Figure 9.3(a) for various temperatures T between $4\,\mathrm{K}$ and $45\,\mathrm{K}$. $\rho(E)$ was calculated using the averaged PL between 0° and ±20° (Eq. (8.5)) and then $C(E)$ as its antisymmetric part using Eq. (8.6). The emission maxima of the heavy-holy excitons (1e−1hh) at 1.681 eV and the light-hole excitons (1e−1lh) about 20 meV higher are shown as thin highlighted areas. As seen before, the directionality decreases for increasing temperatures, but the general shape of $C(E)$ stays the same. For all temperatures, the directionality has its maximum on the lower energy side of the heavy-hole emission maximum around 1.675 eV. This can be attributed to the additional far-field routing effect due to interference between directly emitted and backside-reflected emission, which was discussed in Section 5.2. The overlap between the narrow exciton energy and the wide SPP dispersion also influences this spectral dependence. A dip in the directionality occurs at larger energies between 1.68 eV and 1.69 eV. This was already seen in the $\rho(E,\theta)$ spectra as a

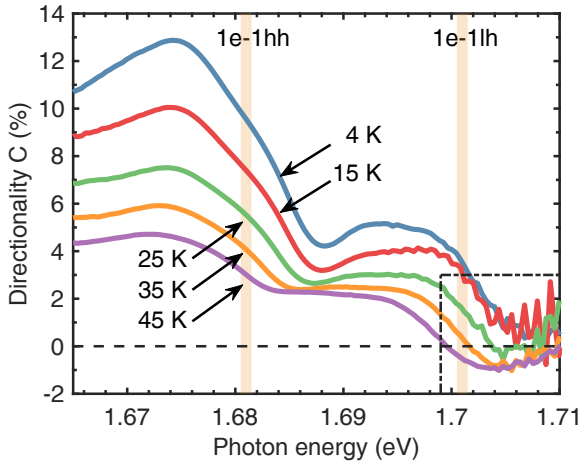

Figure 9.5 Spectral dependence of the directionality $C(E)$ for the QW emission from the hybrid structure for various T. Highlighted areas mark the maximum of the heavy- and light-hole emission, respectively. The dash-dotted box highlights the light-hole influence on $C(E)$: For 35 K and 45 K the sign of $C(E)$ changes above 1.7 eV due to the emerging light-hole emission with opposite P_c. Adapted from [48].

horizontal line with less saturated color, and it matches the maximum of the PL from the bare QW, which shows less directionality. The dip shifts towards lower energies for increasing temperatures, which matches the decreasing trend of the (Cd,Mn)Te bandgap for increasing temperatures [98]. At energies closer to the light-hole exciton emission at 1.7 eV − 1.71 eV, the light-hole influence on the directionality is evident for the larger temperatures, which is highlighted by a dash-dotted box. The directionality is still faintly positive for low temperatures of 4 K and 15 K, but the signal gets noisy because of the low emission intensity. The directionality becomes negative for 35 K and 45 K once the light-hole intensity with opposite P_c is large enough to contribute meaningfully. This was already seen in Figure 9.4 as color change. The influence of the light holes already appears at 25 K, where the directionality trends towards 0 more than for the lower temperatures. Furthermore, the sign change of the TMRLE moves to lower energies because of the larger relative light-hole emission intensity.

In theory, the light- and heavy-hole optical transitions have the same polarization degree P_c but with an opposite sign, despite the vastly different Zeeman splittings of the light and heavy holes in the Voigt geometry. This is because the polarization P_c of the heavy-hole transitions is not directly determined by their Zeeman splitting but solely by the mixing with the Zeeman-split light holes, see Eq. (5.1). This should lead to the same magnitude of directionality C for the heavy and light-hole emission. However, this is not the case in the experimental data, where only about $C = -1$ % is reached, compared to about 5 % for the heavy-hole emission at 45 K. While the theory accounts only for the ground states of the excitons and their emission, in reality, the excited states of the heavy-hole exciton with larger energies can mix with the light-hole ground state and lower its circular polarization degree P_c. The emission from the main heavy-hole peak can also negatively impact the directionality of the light hole if they overlap spectrally. Similar results were obtained by Weisbuch et al., who measured the energy-dependent emission polarization from a GaAs-$Al_xGa_{1-x}As$ multi-QW structure and saw a three to four times larger polarization of the dominant heavy-hole emission peak compared to the smaller light-hole peak [99]. The opposite sign of the heavy- and light-hole directionalities also confirms the importance of the close proximity between the QW and the SPPs at the surface for the routing effect: The heavy and light-hole emission can only show opposite directionality if the routing is caused by the near-field interaction between the QW and the SPPs, according to our theory. One could think that the TMOKE in transmission could also explain the directionality of the emission because the magnetic

(Cd,Mn)Te layer in the structure could influence the SPP dispersion, as discussed in Ref. [15]. This effect would also work if the light source is far away from the plasmonic grating. However, it would not show opposite directionality for the heavy- and light-hole emission, as both transitions would only contribute to p-polarized light in the far-field, independent of their initial circular polarization sign. [48]

Finally, since the increased light-hole emission at large temperatures leads to a decrease of the overall, spectrally integrated directionality, especially once the thermal energy becomes significantly larger than the splitting Δ_{lh}, one could think that an easy solution would be to increase Δ_{lh} through confinement or strain, unless spectral filtering of the two emission bands is feasible. This has the drawback of a lower TMRLE magnitude, though, since $C \propto 1/\Delta_{\mathrm{lh}}$, in addition to the already strong temperature dependence. Therefore, Section 9.5 will focus on alternative QW structures without magnetic ions, which are expected to have a weaker but temperature-independent TMRLE across a wide temperature range. First, though, Sections 9.3 and 9.4 will briefly show experimental data of the TMRLE temperature dependence from both a different grating period on the main sample and from the old alternative sample with the same 250 nm grating period but a slightly different semiconductor composition, which comprises an additional 2D electron gas through modulation doping.

9.3 Different Grating Period: 240nm

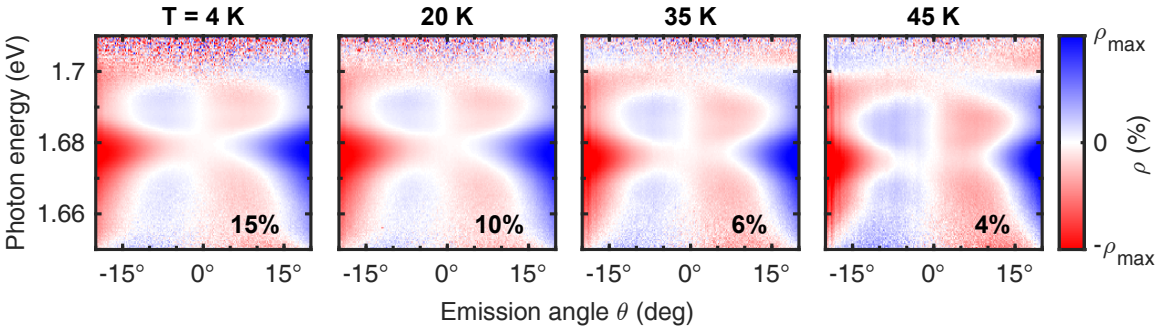

Figure 9.6 Relative intensity change $\rho(E,\theta)$ for $T = 4\,\mathrm{K}$, 20 K, 35 K and 45 K according to Eq. (8.5) for the main sample with 240 nm grating period. Each plot has different colorbar limits $\pm\rho_{\mathrm{max}}$, shown in the respective bottom right corner.

The temperature dependence of the TMRLE was also measured on the same sample but with a 240 nm grating period instead of the previous 250 nm grating. Again, the spectral and angular dependence $\rho(E,\theta)$ is expected to stay the same, and that only the TMRLE magnitude decreases for larger temperatures, in addition to the emerging light-hole emission. Figure 9.6 shows $\rho(E,\theta)$ for $T = 4\,\mathrm{K}$, 20 K, 35 K, and 45 K. Here, the spectral and angular dependence of ρ is more complicated than for the 250 nm grating shown in Figure 9.4. Most noticeable, the sign of ρ changes at around $\theta = \pm 15°$ and is not uniform over the whole angular range. This is represented by a color change with a white line in between. Put simply, the emission at e.g. 20° is oppositely influenced by the magnetic field compared to the emission of the same energy at 10°. Furthermore, this sign change moves to smaller angles close to the PL emission maximum at 1.68 eV, forming a hump-like feature

towards the center. These interesting features will be discussed in Chapter 10, which focuses on the dependence of the TMRLE on the grating parameters. For now, though, the temperature dependence is similar to the 250 nm grating. As predicted, $\rho(E, \theta)$ only changes in magnitude, but the spectral and angular distribution stays largely the same, because it is mainly governed by the semiconductor part of the hybrid structure and not by the grating structure and its parameters. Only for 45 K, the hump-like feature of ρ towards lower angles seems less pronounced, which hints at its origin from the semiconductor part of the hybrid structure and not the plasmonic grating. Most importantly, though, a contribution from the light hole becomes visible above 1.7 eV for 35 K (barely) and 45 K as another sign change. This validates the previous measurements on the 250 nm grating, which also showed the light-hole contribution.

9.4 Influence of Modulation Doping

The same measurements were also done on the older alternative (Cd,Mn)Te/(Cd,Mg)Te sample introduced in Section Section 6.1 to verify the previous results. As a quick reminder, it is similar to the main sample discussed above but has two differences that affect the cooling of the Mn-spin system: First, a lower Mn content in the QW of about 3.5 % compared to 4 % in the main sample, and secondly, it features a 2D electron gas in both the cap and buffer layer close to the QW, which provides additional free carriers. In general, the lower Mn content leads to a slower cooling of the Mn-spin system, so that the Mn-spin temperature would be higher in similar conditions. This leads to a lower magnetization and, consequently, a lower Zeeman splitting and TMRLE magnitude [44]. On the other hand, the 2D electron gas close to the QW likely improves the cooling of the Mn-system via spin-lattice relaxation by providing an additional energy transfer channel from the Mn spins into the phonon system via the free carriers [44, Ch. 8]. However, as was shown in Section 8.4, the alternative sample with the 2D electron gas shows less routing than the main sample, which could also be attributed to the presence of the electron gas, as it seems to influence magneto-optical effects negatively.

The results from the measurements are summarized in Figure 9.7, which shows a collection of plots from Sections 9.1 and 9.2 but for the alternative sample. Panel (a) shows the angular dependence $\rho(\theta)$ for the QW emission, spectrally integrated in a 10 meV window around the QW emission maximum at 1.669 eV, for select temperatures T. The angular dependence is almost identical to that of the main sample shown in Figure 9.1(a). At 4 K, it increases from 0 % at 0° towards the maximum of 9 % at 15° due to optimal exciton and SPP dispersion overlap. Like on the main sample, $\rho(\theta)$ is an odd function of the emission angle, so that $\rho = C$ and the emission directionality is solely due to the TMRLE. The angular dependence is also the same for different temperatures and only decreases in magnitude for increasing temperatures due to the lower magnetization of the Mn spins in the QW.

The angularly and spectrally integrated directionality $C(T)$ for all light emitted in the same energy range and for angles between $\theta = 0°$ and $\pm 20°$ is shown in Figure 9.7(b). The decrease of the directionality C is also well described by a fit using the modified Brillouin function from Eq. (9.1), which is shown as the red curve. The fit yields an offset $T_{\mathrm{off}} = (14 \pm 2)\,\mathrm{K}$ between the sensor temperature T and the Mn-spin temperature T_{Mn}, which is lower than the $(19 \pm 3)\,\mathrm{K}$ offset obtained for the new sample with higher Mn concentration and without the 2D electron gas. This seems

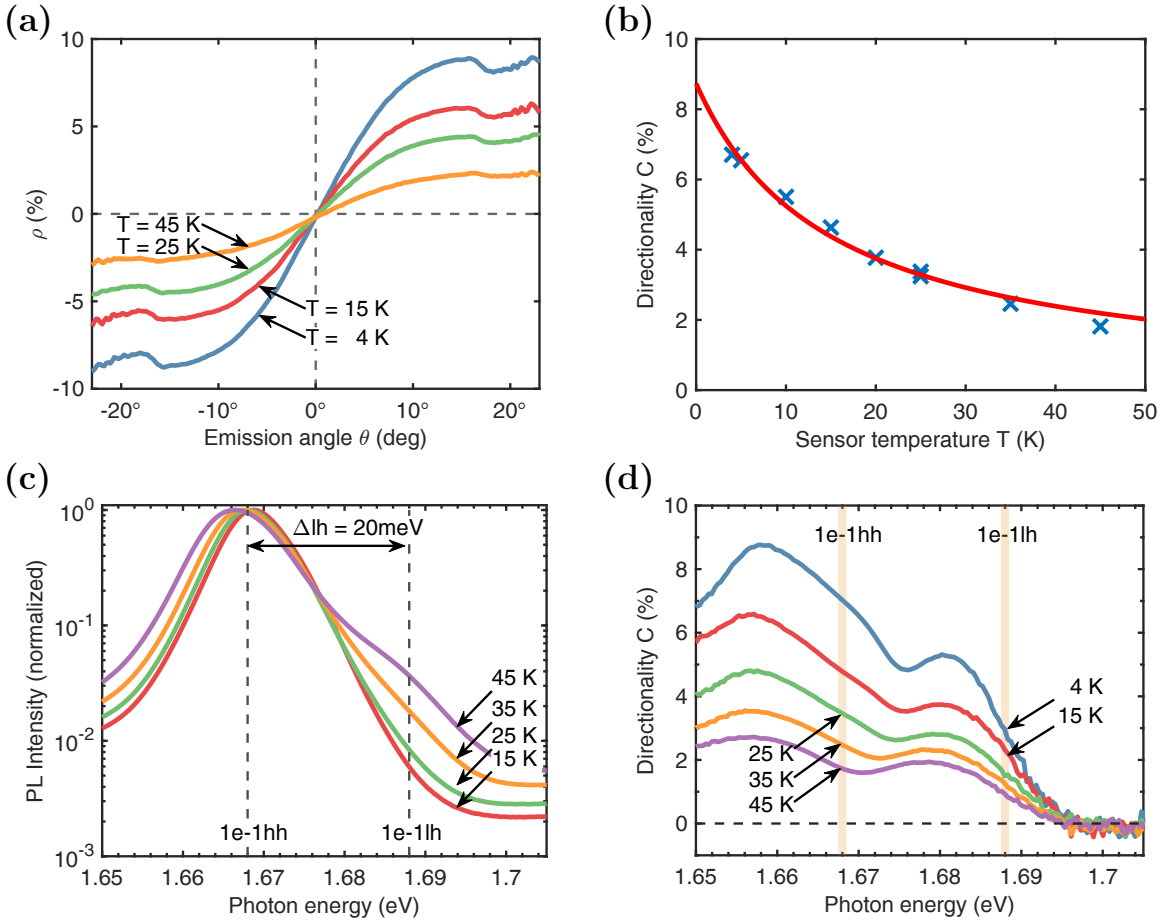

Figure 9.7 For the alternative hybrid (Cd,Mn)Te/(Cd,Mg)Te structure with 250 nm grating period: **(a)** Angular dependence $\rho(\theta)$ at the QW emission maximum (1.669 eV) for different T. **(b)** Temperature dependence of the directionality $C(T)$ and fit according to Eq. (9.1), yielding $T_{\text{off}} = (14 \pm 2)$ K (red). **(c)** Intensity spectra of QW emission in a semi-logarithmic scale with increasing light-hole emission (1e−1lh) for increasing T (normalized). **(d)** Spectral dependence of the directionality $C(E)$ for various T.

to confirm the more efficient cooling of the Mn-spin system due to the added free carriers of the electron gas, despite the lower Mn-content in the QW, possibly at the cost of the overall routing magnitude. However, for a more comprehensive picture of the influence of the electron gas on the Mn cooling and the routing magnitude, the two samples need to be equal in all properties except for the presence of the electron gas. The added differences of unequal Mn contents and slightly different cap layer thicknesses do not allow for a confident conclusion on the Mn-spin cooling properties from this comparison. However, it reveals an interesting path for further investigations on the tuning and optimization of the TMRLE magnitude.

Next, Figure 9.7(c) shows the spectrum of the QW emission $I(E)$ in a semi-logarithmic scale for varying temperatures. The intensities are normalized to the respective maximum of the heavy-hole emission. The maximum shifts towards lower energies for increasing temperatures, just like in Figure 9.3(a) for the main sample and in Ref. [98]. The emission of the 1e−1lh light-hole increases with the temperatures about 20 meV above the 1e−1hh heavy-hole emission peak and reaches about 4.6 % of the main peak at 45 K. This is almost twice the amount seen on the main sample, which reached an intensity ratio of 2.5 %. However, this increased light-hole emission does not result in a larger or more pronounced contribution to the directionality spectrum, as seen in Figure 9.7(d). It shows the spectral dependence of the directionality $C(E)$ for select temperatures and generally looks similar to the corresponding Figure 9.5. Again, the temperature only influences the magnitude of the directionality of the heavy-hole emission but not the spectral dependence. However, the sign of the directionality does not change at the light-hole emission energy (1e−1lh), even for $T = 45$ K. This behavior is unexpected since the electron gas does not seem to have a large influence on the heavy-hole emission directionality (aside from the magnitude), and an influence on the short-lived light holes seems unlikely. However, there could be some spin relaxation channel from the light holes into the electron gas, which would explain the light-hole emission not showing any directionality in the applied magnetic field. This is speculative, though, and needs to be investigated further.

9.5 TMRLE in Non-Magnetic QW Structures

Quantum well structures based on diluted magnetic semiconductors (DMSs) like (Cd,Mn)Te show strong TMRLE because of their giant Zeeman splitting. The giant splitting is enabled by the sp-d exchange interaction between the magnetic Mn-ions and the charge carriers that leads to a large degree of circular polarization of the optical transitions in the yz-plane P_c, see Eq. (5.1). However, DMSs have the disadvantage of a strong temperature dependence, and the TMRLE magnitude quickly diminishes for temperatures above those reachable with liquid helium (around 4 K), as was shown in the previous sections. This is caused by the decreased Mn spin polarization $\left\langle S_z^{\mathrm{Mn}} \right\rangle$ (i.e. their magnetization), which decreases the large exchange contribution to the Zeeman splitting. And even though significant routing is still achievable from these DMS structures at 200 K, their varying routing magnitude for different temperatures can be problematic in not temperature-controlled environments. In general, ferromagnet-based structures could also be of interest for routing applications, but they pose unresolved challenges, such as potential low-temperature ferromagnetic phases and the strong non-radiative decay of photoexcited carriers [48, 100, 101].

Another possible way to achieve routing with a noticeable magnitude at high temperatures is to use non-magnetic materials with an intrinsically large hole Landé g-factor g_h to achieve the required large Zeeman splitting of the light holes instead of via the temperature-dependent exchange interaction like in DMS. Without the magnetic ions, the light-hole splitting in Voigt geometry is (see Eqs. (2.7) and (2.9))

$$\Delta_{l,V} = 2 g_h \mu_B B \tag{9.2}$$

and, therefore, independent of the temperature. Well-studied materials with a large g-factor are narrow bandgap semiconductors like InAs. Therefore, we will (in theory only) model a hybrid structure comprising a lattice-matched (In,Ga)As/(In,Al)As QW with a plasmonic grating, similar to our hybrid (Cd,Mn)Te/(Cd,Mg)Te structures presented before. The structure is intended to emit photons with energies in the telecommunication spectral range (around 1600 nm or 0.78 eV), which is widely used in optical fiber based applications [102]. Other lattice-matched semiconductor heterostructures can also be viable candidates, e.g., the well-studied (In,Ga)As QW with InP barriers [103], though a large hole g-factor is always of importance. Using these ternary semiconductor alloys has the advantage that material properties like bandgaps and lattice constants can be easily adjusted in the growth process by changing the composition. This theoretic model for a temperature-independent hybrid structure for the TMRLE was first described in Ref. [48].

Exact values for the hole g-factor of an (In,Ga)As/(In,Al)As QW structure are not available, so estimates of g_h based on the effective energy bandgap have to be made. In our case, this is the energy of the 1e–1hh heavy hole optical QW transition. Belykh et al. directly measured the g-factor of the holes in InAs/$In_{0.53}Al_{0.24}Ga_{0.23}As$ self-assembled quantum dots (QDs) for various energies using time-resolved ellipticity measurements in transmission geometry, reaching an estimate of $3g_h \approx 4$ at 0.77 eV [104]. Terent'ev et al. reported even larger hole g-factors up to 15 in a 4 nm InAs QW with $In_{0.75}Al_{0.25}As$ barriers in the photon energy range between 0.58 eV and 0.72 eV, which they evaluated from magneto-PL data [105]. However, those structures would not be good candidates for emission routing because the lattice mismatch between their active region and the surrounding barrier materials produces strain. This increases the splitting between the heavy- and light-hole bands Δ_{lh}, which in turn reduces the achievable P_c for the TMRLE, see Eq. (5.1). Assuming the lower estimate of $3g_h = 4$ for an (In,Ga)As/(In,Al)As QW structure, the Zeeman splitting of the light-hole levels in Voigt geometry would reach around $\Delta_{l,V} = 0.15$ meV in a magnetic field of 1 T.

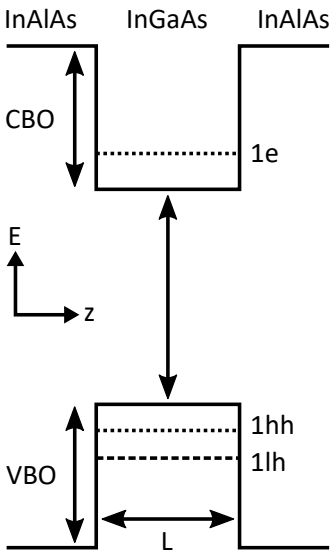

Figure 9.8 Schematic presentation of the 1D QW potential for electrons and holes used in the model.

Next, the material compositions of the (In,Ga)As/ (In,Al)As QW and its thickness L need to be optimized for emission around 1600 nm and a heavy-light-hole splitting Δ_{lh} in the order of the thermal energy $k_B T_c$ at the desired operating temperature. Additionally, the materials should be lattice-matched to minimize the strain in the QW. We model the structure using a simple one-dimensional QW potential with a finite barrier height, from which the ground state energy levels of the electrons in the conduction band (1e) and heavy and light holes in the valence band (1hh and 1lh) are calculated. Then, the PL emission energy and the heavy-light-hole splitting Δ_{lh} can be

deduced. A schematic presentation of such a one-dimensional QW potential is shown in Figure 9.8 with the QW width L and the conduction and valence band offsets *CBO* and *VBO* that define the finite depths of the QW potential for electrons and holes, respectively. z is the growth direction and E is the energy. The effective masses of electrons m_e/m_0 and holes (m_{hh}/m_0, m_{lh}/m_0), the bandgap energies E_g of both QW materials and their lattice constants can be linearly approximated from the known material properties of the binary constituents InAs, GaAs and AlAs. Note that the effective masses of electrons and holes are different in the barrier and well materials. The material properties of the binary constituents were taken from the recommended values in Ref. [103] and are summarized in Table 9.1. The effective hole masses of the binary constituents were calculated from the respective γ_i values. Additional bowing parameters for the interpolation were used if available [103]. Now, the QW thickness L and the composition of the two materials remain as variable parameters, expressed by the respective In-content x_i. The QW thickness can be used to optimize Δ_{lh}, but it also influences the emitted photon energy.

Table 9.1 Material properties of the binary constituents used in the (In,Ga)As/(In,Al)As QW calculations (recommended values from Ref. [103]) and resulting parameters for the ternary materials $In_{0.61}Ga_{0.39}As/In_{0.60}Al_{0.40}As$.

	E_g (eV)	γ_1	γ_2	m_{hh}/m_0	m_{lh}/m_0	m_e/m_0
InAs	0.417	20.0	8.5	0.333	0.027	0.026
GaAs	1.519	6.98	2.06	0.350	0.090	0.067
AlAs	3.099	3.76	0.82	0.472	0.185	0.150
(In,Ga)As	0.733	–	–	0.374	0.047	0.040
(In,Al)As	1.322	–	–	0.389	0.090	0.064

A good starting point for the calculations is the well-studied and lattice-matched heterojunction $In_{0.53}Ga_{0.47}As/In_{0.52}Al_{0.48}As$, which has nearly identical InAs fractions and the valence band and conduction band offsets $VBO = 520\,\text{meV}$ and $CBO = 190\,\text{meV}$ are known from experimental data [103]. An $L = 10\,\text{nm}$ thick QW results in the emission energy of about 0.872 eV (1420 nm) and a heavy-light-hole splitting $\Delta_{lh} = 23\,\text{meV}$, which is equivalent to the thermal energy $k_B T_c$ at about 260 K. The material compositions need to be changed slightly for emission closer to 1600 nm. Using $In_{0.61}Ga_{0.39}As/In_{0.60}Al_{0.40}As$ with an $L = 12\,\text{nm}$ thick QW leads to emission around 0.78 eV and a heavy-light-hole splitting of $\Delta_{lh} \approx 19\,\text{meV}$. This is still larger than the thermal energy 17 meV at 200 K, which is reachable with cooling via the Peltier effect. A slightly lower splitting Δ_{lh} would increase the achievable P_c for the TMRLE, but as a rule of thumb, it needs to be larger than the thermal energy. In this composition, the two materials are still lattice matched according to the approximated lattice constants [103]. The relative valence band and conduction band offsets are assumed to be the same as above, with VBO = 26.8 % and CBO = 73.2 %. The emission energy is approximated as the sum of the bandgap energy and the heavy-hole and electron ground-level energy.

Using the estimated light-hole Zeeman splitting $\Delta_{l,V} = 0.15\,\text{meV}$ at 1 T and $\Delta_{lh} = 19\,\text{meV}$ results in $P_c \approx 0.82\,\%$ according to Eq. (5.1). This can be used to predict the directionality in a hybrid plasmonic-semiconductor QW structure comprising the (In,Ga)As/(In,Al)As QW and a plasmonic gold grating similar to the previously investigated DMS structures. The theoretical model based on the scattering matrix method is described in Refs. [30, 48] and was also used to reproduce the

experimental directionality data $C(E,\theta)$ correctly in Sections 5.2 and 8.5. It calculates the far-field emission spectrum from QW emitters below the plasmonic grating with opposite polarization $\pm P_c$, which is the equivalent of opposite external magnetic field directions $\pm B$ in the experiment. Then, $\rho(E,\theta)$ is calculated according to Eq. (8.5) as the magnetic field induced change of the emission intensity, which is equal to the directionality $C = \rho$ in these calculations, see Eq. (8.6). The simulated plasmonic grating is similar to that in our experimental studies with a slightly larger grating period $a = 420\,\text{nm}$, slit width $w = 70\,\text{nm}$, and 40 nm thickness of the gold bars. The (In,Ga)As QW is separated from the grating by a 30 nm (In,Al)As cap layer and in the other direction from a GaAs substrate by a 5 µm thick (In,Al)As buffer layer. The buffer thickness is fairly arbitrary, but the cap layer thickness needs to be this small due to the evanescent nature of the SPPs towards the QW. The energy-dependent refractive indices of gold and GaAs are based on experimental data from Refs. [51, 94]. The refractive index for (In,Al)As was assumed as constant $n = 3.3$ in the considered energy range, based on similar compositions examined in Refs. [106, 107]. The contrast of the background refractive indices of the (In,Ga)As QW and the (In,Al)As cap layer was neglected.

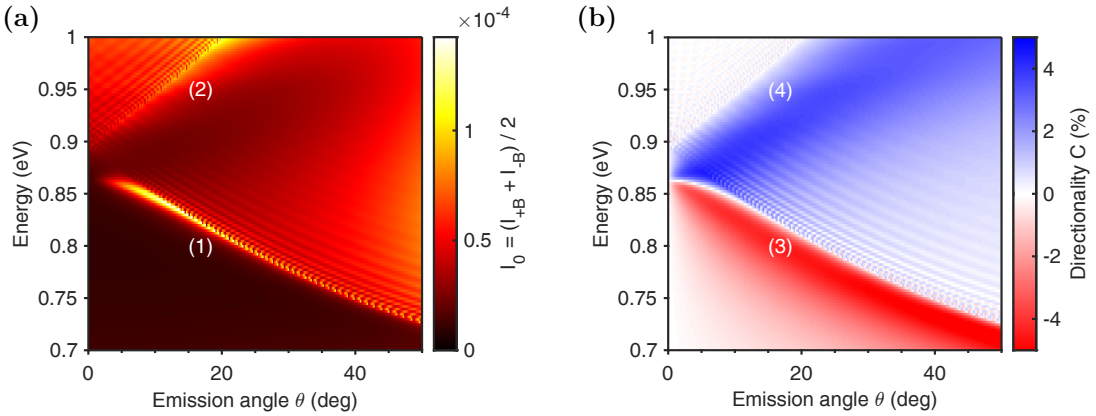

Figure 9.9 (a) Modeling of the intensity spectrum $I_0(E,\theta)$ of the light emitted from the hybrid (In,Ga)As/(In,Al)As QW structure via plasmonic gold grating. An evenly distributed light emission from interband optical transitions is assumed in this model for the depicted spectral range. The intensity I_0 is the average of the two oppositely elliptically polarized emitters in the QW $I_{\pm B}$ with $\pm P_c$. Areas of high intensity (1), (2) highlight plasmonic branches. **(b)** Directionality $C(E,\theta)$ of the light emitted from the QW with $P_c = \pm 0.82\,\%$. A white line ($\rho = 0$) from 0.86 eV at 0° to 0.73 eV at 50° separates two areas of positive (4) and negative (3) directionality. Reproduced from [48].

The results of the model calculation are shown in Figure 9.9, with the light intensity emitted from the hybrid structure $I_0(E,\theta)$ in (a) and its directionality $C(E,\theta)$ in (b), both spectrally and angular resolved. The intensity spectrum shown in Figure 9.9(a) is the average intensity for opposite magnetic fields or oppositely polarized emitters in the QW $I_0 = (I(+B) + I(-B))/2$, which is equivalent to $B = 0$. Unlike in the experiments, where the emission from the QW is a relatively sharp line with an FWHM of a few meV, the model assumes emission from optical transitions with $P_c = \pm 0.82\,\%$ in the full spectral range (0.7 eV − 1.0 eV) with an equal and independent contribution to the emitted intensity. The intensity spectrum should, therefore, be considered as a response of the hybrid structure to the uniform QW emission. It can be multiplied with the corresponding emission spectrum of the QW structure to achieve a spectrum closer to the experiment. All these assumptions are valid as long as the light hole contribution can be neglected, i.e. for $\Delta_{lh} \geq k_B T_c$. The lines of high emission intensity, highlighted by (1) and (2), follow the SPP dispersion branches

at the metal-semiconductor interface. The two branches differ in the sign of their group velocity $\partial\omega/\partial k$: If we consider only positive wave vectors, i.e. positive emission angles θ as shown here, the lower mode (1) corresponds to SPPs with negative group velocity while the SPPs at the higher energy mode (2) have a positive group velocity. For negative emission angles θ the situation is inverse. Due to spin-momentum locking, the two modes with different energies have opposite propagation directions and thus also opposite circular polarization in the yz-plane (see Figure 3.3), which is important for the coupling between the SPPs and the elliptically polarized emitters in the QW that are controlled using the external magnetic field. This can be seen in Figure 9.9(b), which shows the directionality of the emission $C(E, \theta)$ from the hybrid structure according to Eqs. (8.5) and (8.6) in the same energy and angular range. Features in the directionality spectrum clearly correlate with the SPP resonances in the emission spectrum on the left. When the photon energy is scanned from the low energy to the higher energy mode for a given angle θ, the sign of C changes, which is represented by a color change from red to white and blue. The directionality reaches its maximum $C \approx 5\,\%$ close to the SPP resonances (see (3) and (4)) with opposite signs for each branch due to the link between the SPP group velocity and the emitter polarization. For a given emitter polarization, it preferentially couples to SPPs with the same circular polarization, so that the coupling to the lower branch is strongest for one magnetic field direction and to the upper branch for the opposite direction.

The model calculations demonstrate that routing of $C = 5\,\%$ is possible in a temperature range up to 200 K, assuming $P_c = 0.82\,\%$ for the (In,Ga)As/(In,Al)As QW structure discussed above. This enables the application of the TMRLE at temperatures that are reachable using the Peltier effect for cooling. It also offers a stable routing magnitude at lower temperatures because the routing magnitude is mainly determined by the hole g-factor. The routing magnitude can be increased by decreasing the heavy-light-hole splitting Δ_{lh} in the QW. However, this will limit the operating range to lower temperatures. Similarly, a larger splitting extends the operating range of the effect to larger temperatures but at the cost of a lower achievable P_c and, consequently, directionality C. Furthermore, the grating parameters used in the simulation are not optimized. They can be tuned further for a large directionality of emission at certain angles or energies by moving the plasmonic resonance through the spectrum, making different parts overlap with the emitter spectrum.

Further tuning of the routing magnitude C is possible by varying the cap layer thickness d between the QW and the plasmonic grating, which changes the coupling between the two systems. A 30 nm cap was used most of the time for (Cd,Mn)Te/(Cd,Mg)Te as a good compromise between being as thin as possible while functioning well as QW barrier. A thicker 250 nm cap layer was used to disable the plasmonic enhancement of the TMRLE in Ref. [30]. In the (In,Ga)As/(In,Al)As model, the cap layer thickness can be changed to show its influence on the expected emission directionality. For these calculations, the photon energy is limited to $E = 0.8$ eV and the emission angle to 15°, but the cap thickness d is varied and P_c is scanned from 0 % to 100 %. Figure 9.10 shows the resulting calculated dependence of the directionality C on P_c for cap layer thicknesses d between 10 nm and 500 nm for the hybrid (In,Ga)As/(In,Al)As structure. In all cases, the directionality C increases linearly for $P_c < 20\,\%$. After that, a maximum directionality is reached for slightly larger P_c, and it decreases slowly for further increasing P_c. This shows that $C = 100\,\%$, i.e. full control over the light emission direction, can not be achieved by an ever-increasing external magnetic field. Regarding the distance d between the emitters in the QW and the semiconductor/metal interface, the model shows the largest achievable directionality for 30 nm and not for the thinner 10 nm cap. This can be attributed to the best match of the emitter polarization and that of the propagating SPPs. For

larger cap layers, though, the directionality decreases for all P_c as the interaction between the QW emission and the evanescent SPPs at their interface decreases and is almost 0 for $d = 500$ nm. This distance is about equal to the light wavelength in the structure with $n = 3.3$ [106, 107]. In general, the penetration depth of the SPP field into a dielectric is about half the light wavelength in the medium $\lambda/2$ [108]. This was also the case for the hybrid (Cd,Mn)Te/(Cd,Mg)Te QW structures in Ref. [30], where a 250 nm cap layer with $n \approx 2.7$ [50] did not show SPP enhancement of the TMRLE anymore for the ≈ 750 nm emission from the QW. Furthermore, the SPP propagation length along a flat gold/semiconductor interface is about one order of magnitude larger for (In,Al)As compared to (Cd,Mg)Te at the respective emission wavelengths of 1600 nm and 750 nm. This is useful for applications where the routing is supposed to happen directly on-chip and not for emitted light in the far-field. The propagation length can be estimated as $\delta_{SPP} = (2 \cdot \mathrm{Im}(k_{SPP}))^{-1}$ [108].

This section focussed on the (In,Ga)As/(In,Al)As QW system and showed its feasibility as a source of a temperature-independent TMRLE. However, every QW structure with a large enough intrinsic g-factor is a possible candidate for routing at large temperatures. Another possible candidate is an $In_{0.53}Ga_{0.47}As$ QW with InP barriers, which is also lattice-matched and well-studied [103]. The main differences to the system discussed here are the offsets of the valence and conduction bands forming the QW for the electrons and holes. In comparison, the valence band offset is larger for (In,Ga)As/InP, which creates a stronger confinement of the holes in the QW and possibly a larger hole g-factor. This needs to be verified and tested in experiments, though.

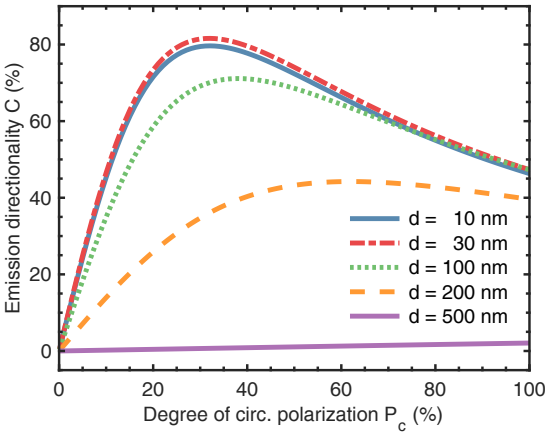

Figure 9.10 Dependence of the directionality C on the degree of circular polarization P_c for different cap layer thicknesses d from 10 nm to 500 nm in the hybrid (In,Ga)As/(In,Al)As QW structure for light emitted at 0.8 eV and 15°. Adapted from [48].

9.6 Summary

In this chapter, the temperature dependence of the transverse magnetic routing of light emission (TMRLE) from hybrid plasmonic-semiconductor QW structures was investigated, which show the largest routing magnitude due to the coupling of the QW emission with surface plasmon polaritons (SPPs) that possess spin-momentum locking. The key parameter determining the routing magnitude for a given structure is the degree of circular polarization of the interband optical transitions P_c in the plane perpendicular to the magnetic field in Voigt geometry. For both the emission from the light-hole and heavy-hole excitons, P_c grows linearly with the applied magnetic field due to its dependence on the Zeeman splitting of the light holes in the Voigt geometry $\Delta_{l,V}$, and it is inversely proportional to the splitting between the heavy- and light-hole subbands Δ_{lh}, see Eq. (5.1).

We showed with experimental data that the routing decreases with increasing temperatures in structures based on the diluted magnetic semiconductor (Cd,Mn)Te due to the reduced giant Zeeman splitting from the strong exchange interaction with the magnetic Mn-ions. It is proportional to

the polarization of the Mn spins and can be described well using a modified Brillouin function. At larger temperatures, the emission from light-hole excitons contributes to the directionality with the opposite sign compared to the main emission from the heavy-hole excitons. This proves the importance of the near-field interaction between the QW and the SPPs, as far-field effects would not lead to routing in opposite directions. It was further shown that the temperature dependence is similar for different periods of the plasmonic grating, and the comparison with an alternative, similar semiconductor structure revealed the possible influence of modulation doping and the resulting 2D-electron gas close to the QW on the cooling of the Mn-spin system and the TMRLE. Finally, a non-magnetic, narrow bandgap (In,Ga)As/(In,Al)As QW structure was proposed for temperature-independent TMRLE because its Zeeman splitting is based on the intrinsically large hole g-factor in the QW and does not originate from the exchange interaction with magnetic ions.

Chapter 10

Weak Coupling of Surface Plasmons and Exciton

Many magneto-optical intensity effects, like the TMOKE (Chapter 4) and the TMRLE (Chapter 5), can be enhanced significantly by combining magnetic and plasmonic materials into hybrid structures. For the TMRLE, the enhancement of the routing magnitude from about 0.1 % to more than 4 % by adding a plasmonic gold grating in close proximity to a (Cd,Mn)Te/(Cd,Mg)Te QW was first shown in Refs. [30, 52], with new structures reaching up to 15 % in Chapter 8. With a plasmonic grating, the QW emission is routed by first emitting into evanescent surface waves at the semiconductor-metal interface, like surface plasmon polaritons (SPPs), which possess strong spin-momentum locking [32]. This locking of their momentum direction to their polarization or transverse spin enables the translation of the polarization P_c of the exciton optical transition into a fixed propagation direction of the SPP along the metal-semiconductor interface, and consequent directional emission into the far-field via the periodic grating structure. For the TMOKE, an enhancement of at least one order of magnitude was shown, e.g., for a plasmonic grating on top of a bismuth iron garnet film [15, 17], or close to the exciton resonances of a DMS (Cd,Mn)Te/(Cd,Mg)Te QW structure [60], see also Section 4.4. Due to the large influence of the SPPs on the magneto-optical effects, the tuning of the grating parameters is of great interest for possible applications and further enhancement of magneto-optical effects, but also in revealing further insights into the magnetic environment close to the surface.

This chapter will show the influence of the grating period and the grating slit width on the SPP-enhanced directionality spectrum $\rho(E, \theta)$ and how the TMRLE can be used to probe the weak SPP-exciton coupling. First, Section 10.1 shows the grating parameter influence on the reflection and emission spectra, before Section 10.2 explains the TMRLE contributions of different surface waves using the directionality spectrum from the 230 nm grating period measured in a larger angular range. Next, Section 10.3 presents the grating period dependence of the TMRLE, and Section 10.4 the dependence on the slit width. Following that, Section 10.5 explains the origin of an unexpected hump-shaped deviation of the directionality that is connected to both the excitonic and plasmonic systems and can be used to precisely probe their weak coupling and the dielectric environment in general. Then, Section 10.6 shows the expansion of the existing theoretical model to reproduce this coupling, and Section 10.7 shows why the TMOKE is not suited to probe the weak coupling, although the excitons and SPPs clearly influence each others TMOKE contributions.

A publication about the data presented in this chapter is currently in preparation [109].

10.1 Grating Parameter Influence on Optical Spectra

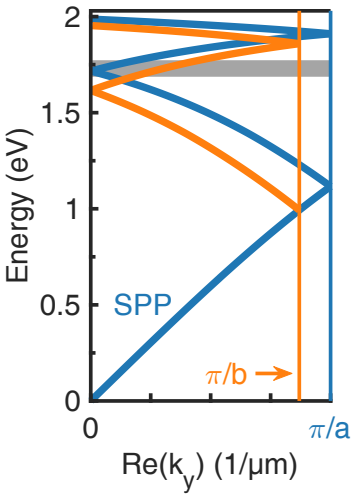

Figure 10.1 Schematic SPP dispersion in the reduced zone scheme for two grating periods $a < b$ (blue, orange) and exciton emission (gray).

As a quick reminder, it was shown in Chapter 3 that the interaction between SPPs and light in the far field is not possible for a flat metallic film due to the mismatch of their wavevectors k_y and k_{SPP}. This mismatch can be overcome by introducing a period metal structure like a periodic grating instead, which adds multiples of the reciprocal lattice vector $2\pi/a$ to the in-plane wavevector of the incoming light k_y [49]:

$$\frac{\omega}{c}\sin\theta = k_{\mathrm{SPP}} \pm m\frac{2\pi}{a}\,. \tag{10.1}$$

The left side is the in-plane component k_y of the light with wave vector $k = \omega/c$, and the right side comprises the plasmon wave vector k_{SPP} and the reciprocal grating vector with diffraction order $m = (0, 1, 2, \dots)$. This creates additional SPP branches originating from $\pm m2\pi/a$ that cross the light dispersion in the combined dispersion diagram. Changing the grating period a, therefore, changes the energy $E(k)$ of the diffracted SPP branches. This is shown schematically in the reduced zone scheme in Figure 10.1 for two different grating periods $a < b$ in blue and orange, respectively. For b, the SPP dispersion is folded back at smaller k_y, which movies the diffracted branches to lower energies, see also Eq. (10.1). The exciton emission at a constant energy is shown as a reference in gray. For the TMRLE, TMOKE, and other magneto-optical effects, this results in a modified spectral dependence of the resonant enhancement of their magnitude at the resonances, see e.g. Sections 4.4 and 5.4.

In the reflection and emission spectra $I(E, \theta)$ of the structures, this is visible as a changing $E(\theta)$ dependence of the SPP resonances. As an example, the top row of Figure 10.2 shows spectra of the light intensity reflected from four grating periods ranging from 230 nm to 260 nm. Here, the p-polarized reflection spectra containing the SPP resonances are normalized with the s-polarized spectra that do not contain the SPPs to reduce the influence of intensity oscillations from interference effects (compare Figure 8.2(b)). The SPP resonance at the gold/(Cd,Mg)Te interface is best visible for the 260 nm grating period as a minimum in the reflected light intensity that appears around 1.55 eV at large reflection angles and moves to smaller angles with increasing energy. For increasing (decreasing) grating periods a, the SPP resonance moves to lower (higher) energies in the reflected intensity spectrum. This matches the expected effect of the changing zone border $\pm\pi/a$, where larger a move the border to smaller values, decreasing the diffracted SPP energy, see Figure 10.1. The bottom row of Figure 10.2 shows the intensity spectra of the p-polarized QW emission for the same gratings, but in a narrower spectral range. It is highlighted by dashed lines in the reflection spectra above. The emission intensity is centered around 1.68 eV with a spectral width of about 10 meV for all grating periods a. However, the angular distribution of the emitted intensity is influenced by a: Following the shifting SPP dispersion sweeping across the exciton emission line, the emitted intensity is highest at large angles for $a = 230$ nm and shifts towards smaller angles with increasing grating periods. The s-polarized emission from the QW is not influenced by SPPs and has the same angular intensity distribution for all grating periods (not shown here).

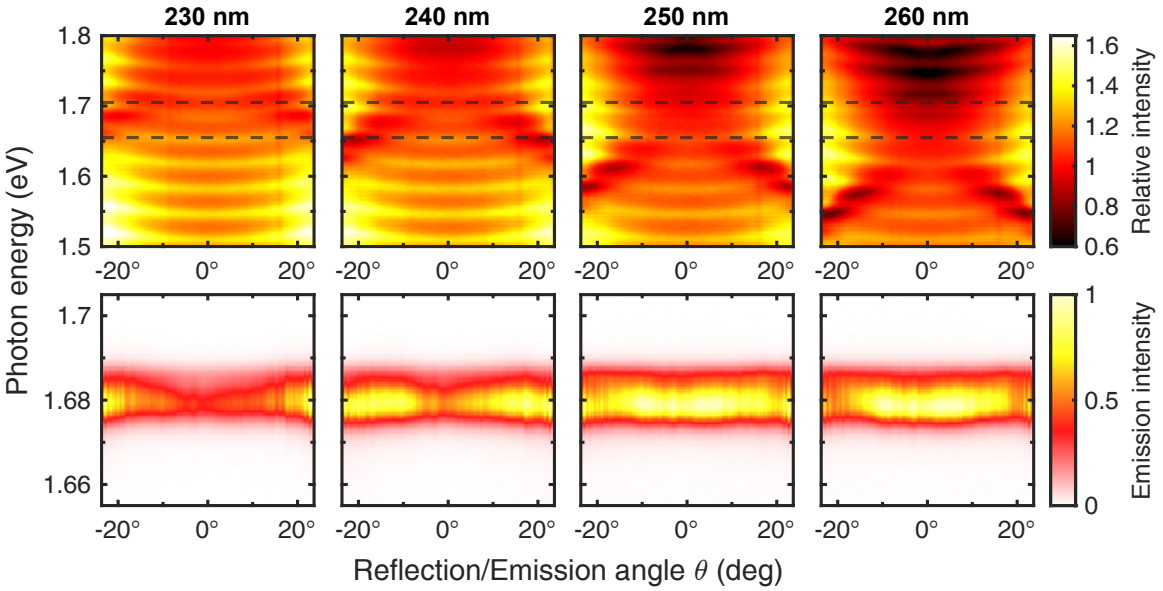

Figure 10.2 For grating periods from 230 nm to 260 nm of the hybrid structure: **Top row:** Relative intensity I_p/I_s of reflected p- and s-polarized light, highlighting the shift of the SPP dispersion towards lower energies for increasing grating periods. **Bottom row:** Intensity spectra (arb. units) of the QW emission in p-polarization. Dashed lines in top row correspond to narrower spectral range in the bottom row.

Similar behavior occurs for different slit widths w of the gold grating, which are generally kept small compared to the gold bar width to best support propagating SPPs and enable their far-field interaction through the periodicity. The influence of the slit width on the SPP dispersion $E(k)$ is less direct than that of the periodicity. The slits lead to the formation of energy gaps in the SPP dispersion at the borders of the reduced zone scheme at $k_y = 0$ and π/a, which shifts the folded SPP branches to higher energies. This is shown schematically in Figure 10.3. The red curve (dash-dotted) corresponds to negligibly small slits and energy gaps, and the green curve shows the case for larger slits, where the resulting bandgaps shift both diffracted SPP branches to higher energies. This energy gap formation between the plasmonic branches can be explained by the reduced translation symmetry of the grating for larger slits, which is, in a sense, similar to the energy gap between the acoustic and optical phonons branches in the classical model of a periodic crystal lattice. For phonons, the energy gap at the zone border is proportional to the mass difference in the two-atomic base of the periodic lattice, which corresponds to a reduction of the translation symmetry [110]. This basic explanation is supported by simulations of the SPP dispersion. The SPP resonances in the resulting spectra can be fitted well using the folded analytical SPP dispersion from Eqs. (3.3) and (3.5) with two additional fitting parameters that depend only on the slit width: the frequency

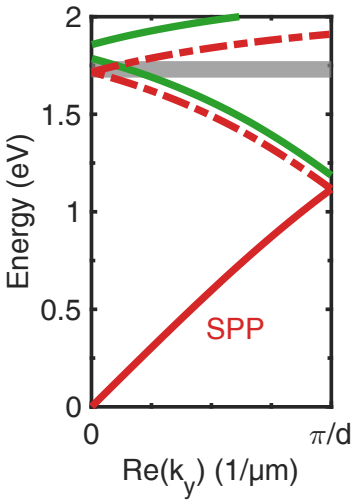

Figure 10.3 Schematic SPP dispersion in the reduced zone scheme for small (red) and larger grating slits w (green), and the exciton emission (gray).

shift and the coupling of the dispersion branches. Figure 10.4 shows supporting experimental data of the light intensity emitted from the QW for gratings with a 240 nm period but different slit widths w between 40 nm and 60 nm. For increasing slit widths, the emission maximum connected to the SPP resonance shifts to larger emission angles θ. This trend is also apparent in whitelight reflection spectra (not shown here), where an increase in slit width moves the SPP absorption curve to higher energies. Note that the slit width values have an uncertainty of a few nm due to the lift-off processing, as discussed in Section 6.1.

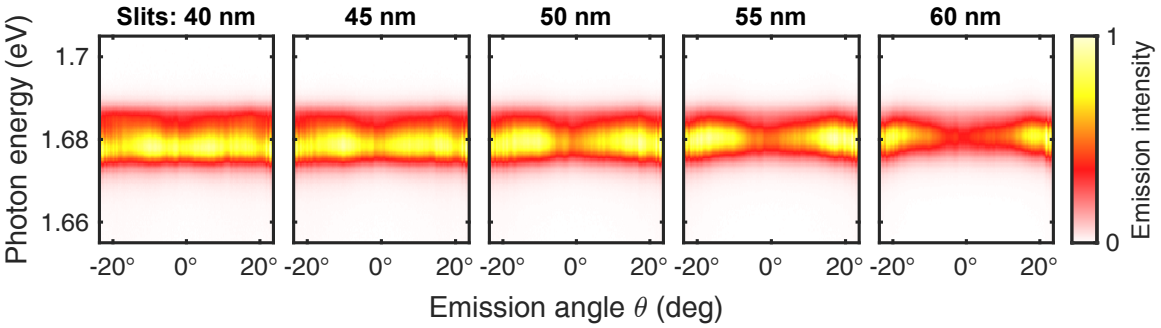

Figure 10.4 For 240 nm grating period: Intensity spectra (arb. units) of the QW emission in p-polarization for grating slit widths from 40 nm to 60 nm.

As a quick summary, both the grating period a and the slit width w have a noticeable impact on the position of the SPP resonance, and both should be considered for specifically tailored emission or reflection characteristics. Consequently, both parameters impact SPP-enhanced magneto-optical effects like the TMRLE and TMOKE, which will be discussed in the following sections. This chapter focuses mostly on the influence of the grating period, as it has a larger influence on the spectra and magneto-optical intensity effects. The slit width can, however, be used for finer tuning of the SPP dispersion or to reveal more or less of the semiconductor structure below, e.g. to allow for better excitation through the grating.

10.2 TMRLE Contributions of Different Surface Waves

In the previous Chapters 8 and 9, the directionality of the emission due to the TMRLE was mostly studied on hybrid plasmonic semiconductor structures comprising plasmonic gratings with a 250 nm grating period. It showed a significant enhancement of the emission routing compared to a bare (Cd,Mn)Te/(Cd,Mg)Te QW structure while also possessing a flat and easy-to-understand directionality spectrum $\rho(E, \theta)$ without any sharp features because of the advantageous position of the SPP resonance at small emission angles (see e.g. Figure 8.5). As shown in the previous Section 10.1, different grating periods a shift the SPP resonances through the spectrum and, therefore, also their resonant influence on the directionality spectra. This generally leads to more complex directionality spectra while also revealing further details about the SPP influence on the directionality and the interaction of the excitons in the QW with the SPPs. This section will first discuss the directionality spectrum measured on the hybrid structure with a 230 nm grating period and explain it in detail, also focussing on a resonant directionality feature at the intersection of the excitonic and plasmonic resonances, which indicates a coupling of the two systems. The following sections will then dive

deeper into the period and slit width dependence of the directionality to give further insight into this coupling.

The main (Cd,Mn)Te/(Cd,Mg)Te QW structure is covered in several spatially separated gold gratings with varying periods from 200 nm to 800 nm. Each grating period exists five times with different slit widths. For further information on the structure, see Section 6.1. For most of the following measurements, the sample was placed at an angle of about 22.5° with respect to the optical axis. This results in a larger detectable range of emission angles between $\theta = 0°$ and 45° instead of the usual symmetric ±23.5°. All measurements were performed at about $T = 4\,\mathrm{K}$ sample temperature and with an external magnetic field of $B = \pm 485\,\mathrm{mT}$.

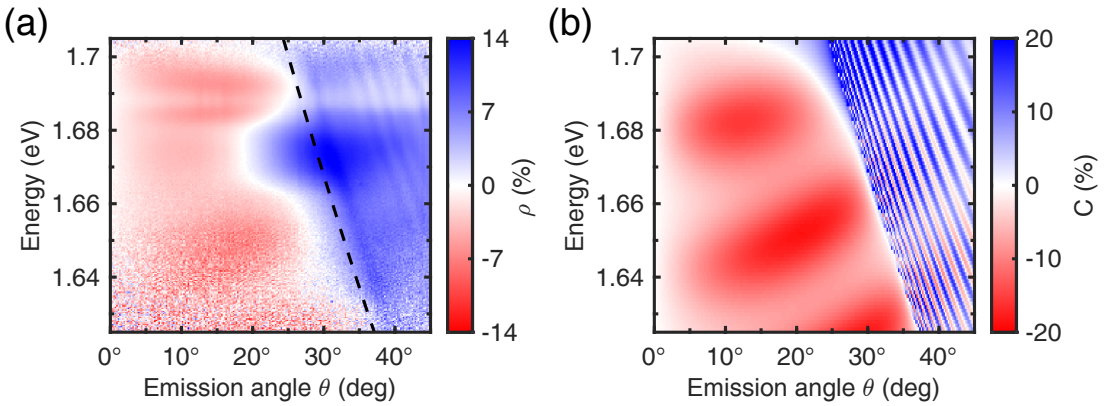

Figure 10.5 For the hybrid structure with 230 nm grating period: **(a)** Experimental directionality $\rho(E, \theta)$ at $T = 4\,\mathrm{K}$ and $B = 485\,\mathrm{mT}$ according to Eq. (8.5). Dashed line indicates the first-order diffracted beam, see Eq. (10.2). **(b)** Simulated directionality $C(E, \theta)$ using the theoretical model presented in Refs. [30, 48] with $P_c = 0.09$.

As an example the directionality $\rho(E, \theta)$ of the QW emission according to Eq. (8.5) for the 230 nm grating period is shown in Figure 10.5(a). The colors red and blue represent opposite signs of ρ and their saturation the magnitude. Therefore, blue (positive ρ) indicates that more light is emitted for positive than negative magnetic fields and vice versa for red. The directionality C as the antisymmetric part of ρ according to Eq. (8.6) can not be calculated in the larger, non-symmetric angular range. However, $\rho = C$ can be assumed here because the large-angle TMRLE measurements closely match those done in the smaller angular range on the same gratings, and ρ will be called directionality, like for all previous measurements. The SPP resonance of the 230 nm grating is located at larger angles than the 250 nm grating. Consequently, the directionality spectrum $\rho(E, \theta)$ in Figure 10.5(a) differs from those of the 250 nm grating. As shown in Chapter 9, those were mostly flat and uniform, and showed a positive directionality ρ (blue) for the whole positive angular range up to 23.5°. The directionality from the 230 nm grating, on the other hand, has the opposite sign at small angles (red) but prominently features a sign change (white line) around $\theta = 25°$. Therefore, the light emitted at small angles is routed in the opposite direction by the magnetic field than the light emitted at the same energy but large angles. The largest routing takes place close to the emission maximum around $E = 1.68\,\mathrm{eV}$ and $\theta = 30°$ with up to $\rho = 14\,\%$, which can be assigned to the optimal interaction between the QW and the SPPs with spin-momentum locking. Both the sign change of the directionality and the routing maximum are close to the SPP resonance, which is located around $\theta = 20°$ to 30° for the 230 nm grating according to the reflection spectra

in Figure 10.2. This sign change close to the SPP resonance is also in accordance with our model of the TMRLE described in Refs. [30, 48]: The large positive directionality (blue) originates from the strong routing contribution of the diffracted SPPs that was already discussed in the previous chapters for the 250 nm grating. The weaker negative directionality at small angles (red), on the other hand, can be attributed to evanescent photonic modes that exist for arbitrary k_y. They also propagate along the plasmonic interface but possess weaker electric fields, which leads to less directional emission [30]. The sign of the transverse spin of the SPPs and the photonic modes are energy-dependent and can be opposite or equal for a given k_y. Therefore, their contribution to the TMRLE can also be opposite or equal and thus compensate or enhance each other. These opposite directionality contributions are responsi igure 10.5(a).

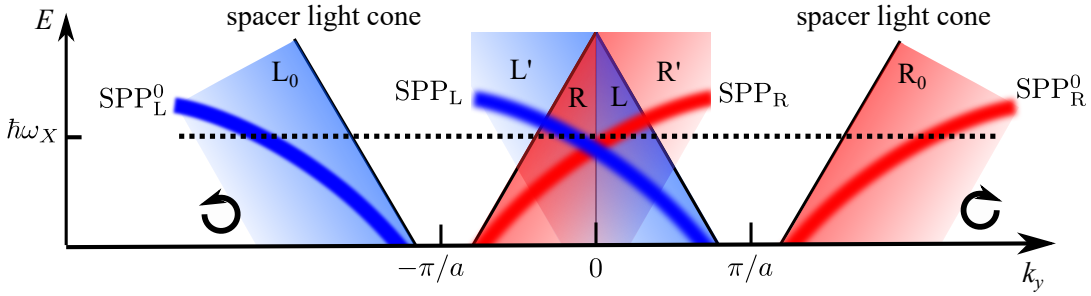

Figure 10.6 Schematic presentation of the relevant dispersion relations for the near-field enhanced TMRLE and their contribution to the directional emission in the far-field (red/blue). $SPP^0_{L/R}$ represent the SPP dispersions at a homogeneous metal film and $SPP_{L/R}$ the branches diffracted by the periodic grating. L_0/R_0 are the corresponding photonic modes at the homogeneous film, and R/R′, L/L′ those shifted by the periodicity. Reproduced with permission from [30].

A schematic presentation of these competing and enhancing contributions to the near-field TMRLE is depicted in the dispersion diagram of Figure 10.6. It shows the resonant SPPs as thick lines and the arbitrary photonic modes as colored patches, and the colors red and blue represent opposite transverse spins and, therefore, contributions to the emission directionality C. The two outer areas of the diagram at large $|k_y|$ represent the dispersion relations for a sample with a non-periodic, homogeneous metal film, namely $SPP^0_{L/R}$ of the SPPs and L_0/R_0 of the photonics modes close to the light dispersion line (black). Both route the emission in the same direction along the plain metal film, as indicated by the matching colors. The directionality contribution is strongest for the resonant SPP branches and for the photonic modes just below the light dispersion lines. There, the electric field $E \propto e^{-|k_z z|}$ is large due to small k_z.

We are, however, interested in the dispersion relations diffracted by the periodic grating, which enables the directional emission of the routed surface waves. Those modes are shown in the center of the diagram between $k_y = \pm\pi/a$, and each mode here was translated by the reciprocal grating vector $\pm 2\pi/a$. The SPPs are labeled $SPP_{L/R}$, and R, R′, L, and L′ mark different regions for the two photonic modes along the black lines. The different modes with opposite contributions (red/blue) overlap and can either enhance or reduce the directional emission. Most interesting are the regions R and L, where the photonic modes with opposite spins overlap with each other and with the folded SPP branches $SPP_{L/R}$ that possess the largest transverse spin. The region L, for example, is crossed by both SPP branches, with SPP_L enhancing the TMRLE and SPP_R reducing it due to opposite spins. Because of the overlap of the left- and right-propagating waves in the center, the sign of the transverse spin (and thus of the TMRLE contribution) changes at the borders L′-R

and R′-L. This corresponds to the sign change of the TMRLE in Figure 10.5(a), which is further enhanced by the presence of the SPP mode. The directionality is largest in R′ and L′ because the opposite contribution vanishes, and the SPPs and photonic modes enhance each other. By changing the grating period a, the origins of the diffracted modes change, and so does the overall routing spectrum that results from the overlap and interplay of all the different contributions. [30, 52]

Returning to the experimental TMRLE data in Figure 10.5(a), the step-like increase of the directionality to the right of the sign change due to the appearance of the first-order diffracted beam also occurs here. As a guide to the eye, the dashed black line shows the first-order diffracted beam according to

$$\theta = \arcsin\left(m\frac{\lambda}{a} - n_{\mathrm{d}}\right), \tag{10.2}$$

with the emission angle θ, light wavelength λ, grating period a, refractive index of the dielectric (Cd,Mg)Te n_{d} according to [50], and $m = 1$ for the first order in this case. It reproduces the step-like directionality increase well, albeit at slightly smaller angles. Thin lines of weakly oscillating directionality from the interference of waves reflected at the sample backside are also visible to the right of the dashed line, which was already discussed for Figure 8.5.

Finally, the most notable feature of the directionality $\rho(E, \theta)$ in Figure 10.5(a) is located close to the emission maximum at 1.681 eV. Here, the white line deviates from the expected monotonic trend set by the SPP dispersion, and a hump of positive directionality ρ (blue) is formed towards lower emission angles. This resonant feature is present for all other grating periods that feature the sign change of ρ at the SPP resonance. For comparison, Figure 10.5(b) shows the simulated directionality spectrum $C(E, \theta)$ based on the theoretical model presented in Refs. [30, 48] and briefly in Sections 8.5 and 9.5. It will be discussed in more detail later in this chapter. Compared to the experimental data in Figure 10.5(a), the off-resonant shape of the TMRLE signal is reproduced well. It features the same slope and position of the sign change, and the oscillating far-field effects are also present, although with a slightly overestimated contribution. Notably, though, the directionality hump close to the QW resonance is absent and can not be reproduced with different sets of simulation parameters either. This suggests a feature or an interaction taking place that is not yet included in the theoretical model and the corresponding simulations. Its position in the directionality spectrum close to both the semiconductor QW emission resonance and the sign change as a feature of the periodic grating and the SPPs hint at an interaction between the two systems that is worth investigating further. The remainder of this chapter will present the dependence of the directionality signal on several parameters of the hybrid structure, like the grating period or the QW resonance energy. In the process, the origin of the hump-shaped deviation will be revealed as a local contributions of the excitons to the dielectric environment of the semiconductor which, in turn, influences the plasmonic dispersion. This resonant influence in the TMRLE reveals the weak coupling between the excitons and SPPs.

10.3 Period Dependence of the Emission Routing

The directionality $\rho(E, \theta)$ was measured for different grating periods at $T = 4\,\mathrm{K}$ and with $B = 485\,\mathrm{mT}$. The directionality spectra for five grating periods a between 210 nm and 250 nm are shown in Figure 10.7 as an example. Here, the shift of the SPP resonance towards lower energies and thus

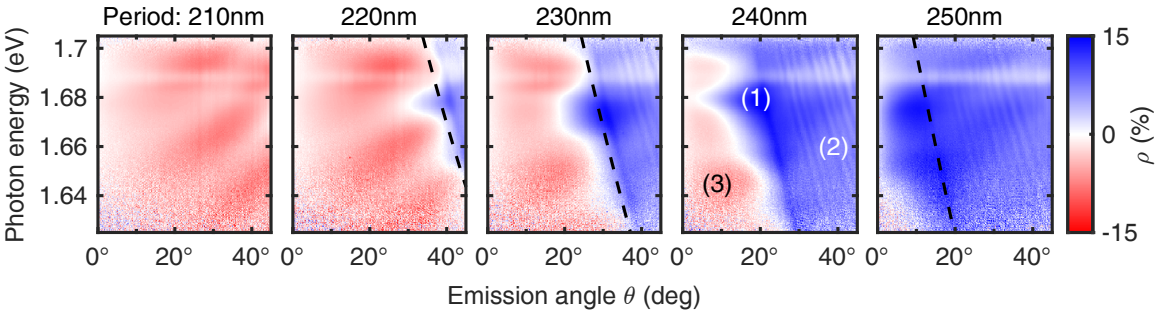

Figure 10.7 Directionality spectra $\rho(E, \theta)$ for different periods of the plasmonic grating from 210 nm to 250 nm in the larger angular range of 0° to 45° and at $T = 4\,\mathrm{K}$ with $B = 485\,\mathrm{mT}$. The grating slits are 50 nm wide. Dashed line indicates the first-order diffracted beam, see Eq. (10.2).

smaller angles for increasing grating periods a is directly visible in the directionality spectra, where the sign change (white line) shifts accordingly (see the reflection spectra in Figure 10.2 for comparison). For **210 nm**, the directionality is negative (red) and fairly flat for the depicted angular and spectral range. The SPP resonance has no influence on the directionality in this range, and the directionality is mainly facilitated by the photonic modes at the metal/semiconductor interface. Additionally, the weak oscillation of the signal along the diagonal axis (top left to bottom right), which originates from the interference of directly emitted and backside-reflected light, is well visible in this spectrum (see Section 5.2 for details). The routing magnitude ranges from around $\rho = -5\,\%$ in the valleys up to $-7.5\,\%$ in the maxima.

For **220 nm**, the dispersion relations of the diffracted optical modes are shifted, and the sign change of ρ appears at large emission angles. It also features the notable hump-shaped feature at the emission maximum around 1.68 eV. The appearance of the first-order diffracted beam according to Eq. (10.2) was added as a guide to the eye (dashed line), and also moves inwards with increasing grating periods. The part of the directionality spectrum shown in red remains largely unchanged, as it comprises the non-resonant photonic modes and the weak oscillations originating from reflections in the semiconductor part. The spectrum for **230 nm** was already shown in Figure 10.5. It continues the trend of the inwards-shifting diffracted modes, resulting in a larger portion of the measured range now colored blue (positive ρ). The directionality reaches up to 14 % close to the sign change due to the combined near-field contributions from the resonant SPPs and photonic modes with the same sign. The hump feature follows the inward moving sign change and sticks to the QW emission maximum. For $a =$ **240 nm**, the resonant SPP contribution moves further toward lower angles, and the directionality hump reaches 0°. Contributions from three different surface waves are present in the spectrum, marked (1)–(3): The maximum directionality at 20° follows the shifting SPP dispersion with up to $\rho = 14\,\%$ (1), assisted by the photonic mode with the same directional contribution. The directionality decreases for larger angles (e.g. 40°), where the influence of the SPP resonance diminishes and the photonic modes prevail (2). Lastly, the photonic modes with the opposite directionality sign are still present at low energies and angles (3). This spectrum demonstrates the competition and enhancement of the overlapping modes in the directionality spectrum well, which were discussed in Figure 10.6. Directionality spectra from the 240 nm grating featuring the hump were already shown in Section 9.3 on the TMRLE temperature dependence. Finally, the SPP dispersion moves further inwards in the **250 nm** spectrum, where ρ is now mostly positive (blue), and the SPP enhanced maximum of the directionality is located between

10° to 15°, as was seen in all previous measurements on the 250 nm grating, e.g. in Chapter 9. The directionality at large angles is dominated by the photonic modes. This case is similar to the 210 nm spectrum, which featured only photonic modes with the opposite sign. A further increase of the period leads to a lower maximum directionality as the SPP resonance reaches 0°.

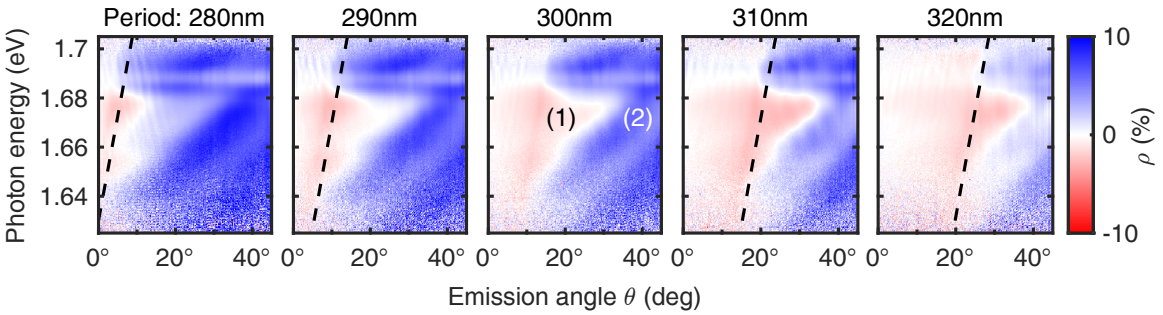

Figure 10.8 Directionality spectra $\rho(E, \theta)$ for grating periods between 280 nm and 320 nm in the larger angular range of 0° to 45° and at $T = 4\,\mathrm{K}$ with $B = 485\,\mathrm{mT}$. Note the lower colorbar limits than in Figure 10.7. The dashed line indicates the first-order diffracted beam, see Eq. (10.2).

Figure 10.8 shows the directionality spectra $\rho(E, \theta)$ for the larger periods from 280 nm to 320 nm. Starting at 280 nm, the opposite SPP branch appears at 0° and shifts towards larger angles. This SPP branch with the opposite propagation direction originates from $k_y = -2\pi/a$ instead of $2\pi/a$ and has the opposite directionality contribution. This branch enhanced the directionality at the negative emission angles for $a < 250\,\mathrm{nm}$ according to $\rho(\theta) = -\rho(-\theta)$. The SPP with negative directionality (red) shifts to larger angles for increasing a and is always accompanied by the directionality hump at the emission maximum at 1.68 eV. The directionality resulting from this SPP branch is notably smaller at only $\rho = -2.5\,\%$ (1) compared to 6 % in the blue regions (2), most likely due to opposite directionality contributions from the SPP and the photonic modes that compensate each other. This is best apparent for the 320 nm period, where the directionality at low angles almost vanishes with only non-resonant contributions with opposite signs remaining.

The resonant influence of the SPPs on the directionality spectrum repeats for larger grating periods a once the second and third-order SPPs (originating from $\pm 4\pi/a$ and $\pm 6\pi/a$) shift into the spectral and angular range of the experiment. Crucially, the directionality hump is also present for the higher-order SPP branches. This is shown in the directionality spectra of Figure 10.9(a) for the 440 nm and 640 nm gratings in comparison with the 230 nm grating. All three spectra show a similar directionality $\rho(E, \theta)$, with only the leading hump of the SPP-enhanced directionality visible at large angles. Overall, the directionality from the photonic and resonant SPP modes decreases for the increasing grating periods.

These two trends of repeating directionality spectra for larger grating periods but with decreasing overall magnitude are also evident in Figure 10.9(b). It shows the average directionality ρ of the light emitted in a 10 meV window around 1.68 eV and between $14° - 16°$ in dependence on the grating period a from 210 nm to 800 nm. The data are taken from two measurement series: those measured in the larger angular range for grating periods between 210 nm and 320 nm (blue circles) and those in the smaller, symmetric range for 320 nm – 800 nm (orange squares). Starting at 210 nm with $\rho = -4\,\%$, the directionality is negative until the SPP-enhanced directionality contribution crosses 15° and flips the sign at 240 nm. The maximum ρ at this angle is reached on the 250 nm grating and decreases afterward until it changes sign again for 290 nm when the opposite SPP

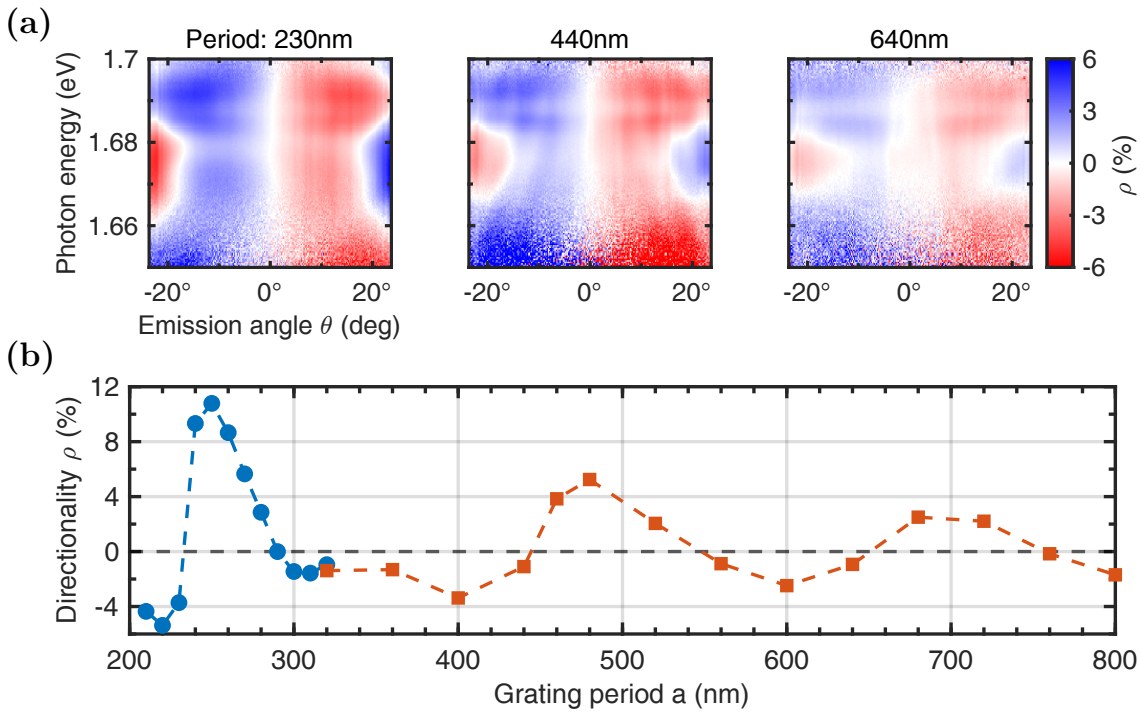

Figure 10.9 (a) Directionality spectra $\rho(E, \theta)$ for the grating periods 230 nm, 440 nm and 640 nm between $\theta = \pm 23.5^\circ$ and at $T = 4\,\mathrm{K}$ with $B = 485\,\mathrm{mT}$. **(b)** Directionality ρ of light emitted in a 10 meV windows around 1.68 eV and between $14^\circ - 16^\circ$ for grating periods a from 210 nm to 800 nm. Blue circles and orange squares mark data from two different measurement series.

appears. The next SPP branch crosses 15° at $a = 480\,\text{nm}$ with ρ up to 5 % and still 3 % for the third SPP branch at $a = 680\,\text{nm}$ ρ is negative between those maxima due to the SPP branches with opposite group velocity. This periodic repetition of the SPP influence on the directionality neatly fits the schematic depiction of the dispersion relations in Figure 10.6, where all left-propagating SPP branches (negative $\mathrm{d}\omega/\mathrm{d}k$, blue) have the same sign of directionality contribution and all right-propagating branches (positive $\mathrm{d}\omega/\mathrm{d}k$, red) the opposite sign. Note that the SPPs enhancing the directionality for the 200 nm − 300 nm range are the lowest possible order, as they originate from $\pm 2\pi/a$, and a further reduction of the grating period will not increase the routing magnitude further.

To quickly summarize, the sign change in the directionality spectra follows the SPP resonance for different grating periods. The hump-shaped feature is present for all grating periods with the sign change in the measured range and it sticks to the sign change. This suggests a connection to the SPPs. At the same time, it is always close to the energy of the QW exciton resonance at 1.68 eV, which suggests a connection to the semiconductor part of the hybrid structure.

10.4 Slit Width Dependence of the Emission Routing

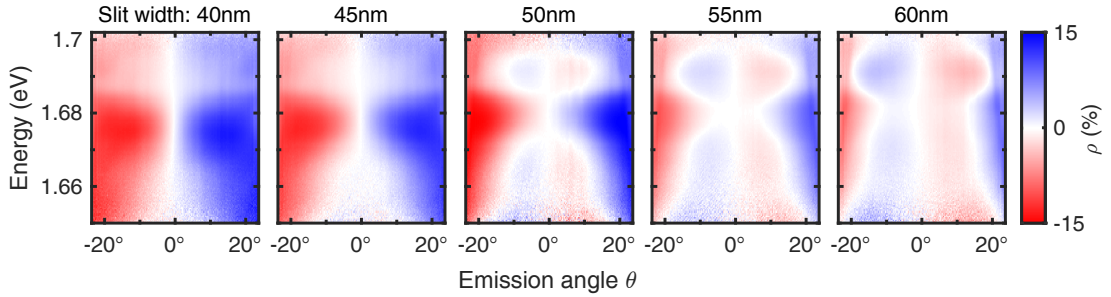

Figure 10.10 Directionality $\rho(E, \theta)$ for various widths of the grating slits from 40 nm to 60 nm with a 240 nm grating period, in the angular range between ±23.5°.

Another parameter of the plasmonic grating that influences the SPP dispersion is the width of the slits w. It can, therefore, be used to verify the plasmonic involvement in the hump-shaped directionality feature. In general, the slits in the metal film are kept small compared to the grating period. This keeps the interface similar to a planar metal film supporting propagating surface waves and enables the far-field interaction of the waves (e.g. SPPs) with photons due to the periodicity of the grating. The directionality $\rho(E, \theta)$ was measured on the five grating structures with varying slit widths w from 40 nm to 60 nm for the 240 nm grating period. Note that the actual slit width has an uncertainty of a few nm from the lift-off processing, according to Section 6.1. Their emission spectra were already presented in Figure 10.4 and showed a shift of the SPP-related emission maximum from larger to smaller angles θ for increasing slit widths. The corresponding $\rho(E, \theta)$ spectra are shown in Figure 10.10 in the smaller angular range between ±23.5°. Starting with the 240 nm/50 nm grating (period/slits) in the center, the sign change of ρ is depicted as a white line for low energies, and the hump-like directionality feature at 1.68 eV extends to smaller angles and reaches 0°. The maximum directionality of 15 % is reached near the hump. The same grating was also measured in the large angular range with similar results, see Figure 10.7 for comparison. Increasing the

slit width w up to 60 nm moves the diffracted SPP resonance to higher energies and shifts the directionality sign-change to larger angles. At the same time, the hump becomes less pronounced. The routing magnitude ρ decreases from a maximum of 14 % to about 8 %, although it is unclear if the overall routing magnitude decreases or if the routing maximum shifts to angles outside the measured range. Decreasing the slit width to 40 nm has the opposite effect and moves the SPP resonance towards lower energies and, therefore, the sign change of ρ further towards $\theta = 0°$. Consequently, the hump feature is no longer distinguishable, and the 240 nm/40 nm directionality spectrum looks similar to the usual 250 nm/50 nm spectrum shown in the previous chapters. The maximum directionality decreases to about $\rho = 10$ %.

These results suggest that the slit width can be used for further fine-tuning of the spectral and angular dependence of the TMRLE, or to reduce or increase the transmitted or reflected light intensity by changing the percentage of the surface that is covered in gold. However, the slits can not be made arbitrarily wide because they cease to support propagating SPPs. The hump-shaped directionality feature seems to be influenced slightly by the slit width and decreases in size for larger slit widths, but this small data sample does not allow for a general conclusion. It is possible that the SPP dispersion changes more than the other directionality contributions, e.g. the arbitrary photonic modes or the step-like increase of ρ linked to the appearance of the first-order diffracted beam (Eq. (10.2)). This would support the theory of a connection between the hump-like feature and the SPP resonances.

10.5 Probing the Weak Coupling

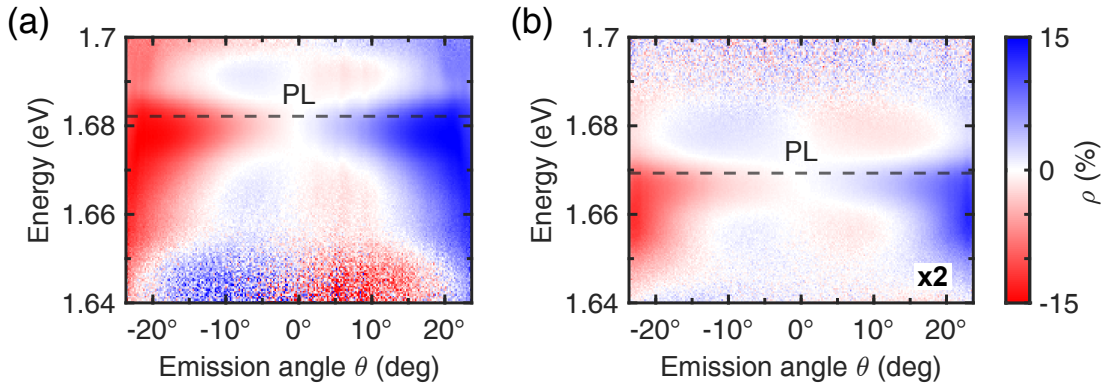

Figure 10.11 Comparison of the directionality spectra $\rho(E, \theta)$ from **(a)** the main sample (240 nm grating) and **(b)** the alternative sample (230 nm) with different QW emission energies (dashed lines). The routing magnitude ρ in (b) is doubled for a better comparison.

The measurements of the directionality $\rho(E, \theta)$ for the different grating periods in Section 10.3 link the hump-like deviation to both the semiconductor QW part of the hybrid structure, and the periodic grating and the SPPs. Regarding the connection to the QW, the hump always manifests close to the energy of the QW emission maximum at approximately 1.68 eV, independent of the grating period. To verify this, the directionality spectra of the main sample can be compared to those from the alternative sample, whose emission maximum is at lower energies of approximately 1.67 eV due to a slightly different QW composition. This comparison is shown in Figure 10.11

with the directionality spectra of (a) the main structure with a 240 nm grating period and (b) the alternative structure with a 230 nm grating period. The routing magnitude ρ in (b) is doubled for a better comparison, and the grating periods were chosen for their similar directionality spectra with a clearly visible hump. The directionality signal in (b) is noisy above 1.69 eV because no light was detected, and the same is true for the lower energies in (a). In both cases, the hump is located close to the respective emission maximum, which is highlighted by a dashed line. This confirms the connection between the hump-shaped feature and the QW emission energy and, thus, with the semiconductor QW structure.

At the same time, the hump-shaped directionality deviation is also connected to the periodic grating structure, as it follows the SPP resonance and its larger directionality through the spectra for changing grating parameters, see Sections 10.3 and 10.4. This is true for the first-order diffracted SPP in Figure 10.7 and the higher-order ones in Figures 10.8 and 10.9(a). Similarly, altering the slit width for a set grating period also shifts the SPP resonance, which in turn affects the directionality hump as seen in Figure 10.10. Because the hump is also pinned to the QW emission energy, it can not originate from the SPPs alone. In that case, it would need to shift up and down in energy together with the SPP dispersion. Instead, the grating parameters only influence the emission angle θ at which the hump appears. Furthermore, such a SPP dispersion feature would appear in the directionality simulations for the hybrid structure, which uses a more sophisticated model than the analytical approximation of the SPP dispersion for a flat metal film according to Eq. (3.3), even with the added influence of the periodic grating according to Eq. (3.5). Similarly, other optical resonances that are influenced by the periodicity of the grating are also ruled out as the sole origin of the feature for the same reason.

Therefore, the most obvious explanation for the hump-shaped deviation of the directionality, which is connected to the SPP dispersion and always located at the energy of the QW emission, is a local contribution of the excitons to the dielectric environment ε at the metal/semiconductor interface. This change of ε at the exciton resonance energy is felt by the SPPs and changes their dispersion relation (Eq. (3.3)) locally at that energy, which leads to the hump-shaped deviation of the plasmon-enhanced emission directionality ρ. This SPP dispersion change can not be seen in the whitelight reflection spectra in Figure 10.2, where the SPP resonance appears as a spectrally broad intensity dip. The induced deviations are small compared to the spectral width of the resonance and are, therefore, not noticeable. This is further exacerbated by the additional interference patterns in those reflection spectra. On the contrary, the sign change of the directionality ρ linked to the SPP resonance is sharp and well-defined in the TMRLE spectra due to the easy-to-follow white line of the sign change in the $\rho(E, \theta)$ spectra. Consequently, a small deviation of the otherwise monotonous SPP dispersion is clearly visible in the TMRLE spectra along the white line as the hump-shaped feature.

This sensibility of the TMRLE to small changes in the SPP dispersion can be used to reveal the coupling between the excitons in the QW and the SPPs at the nearby interface in detail. The coupling between the two elementary excitations in the hybrid plasmonic semiconductor structure is in the weak regime, because a strongly coupled system would show a splitting at the crossing of the two resonances. Strong coupling between excitons and SPPs is generally not easy to achieve. It has been established mostly in organic semiconductors and transition metal dichalcogenides (TMDCs), where resulting Rabi splittings in the order of hundreds of meV were reported [111–113]. This hybridized mode is also termed *plexciton* resonance [114]. In inorganic semiconductors

like (Cd,Mn)Te, strong coupling is difficult to achieve due to the low oscillator strength of the excitons [115]. Moreover, the typical assumption for weak coupling in such structures is that the plasmon energy spectrum remains unchanged while the exciton emission is accelerated due to the Purcell effect. However, the detection of the weak coupling in this way is difficult because the accelerated exciton lifetime can also originate from non-radiative mechanisms that are not connected to the coupling [111, 116]. Nevertheless, the inverse influence from the excitons on the SPPs via contributions to the dielectric environment are apparent and probed with high sensitivity in our hybrid structure via the TMRLE. These results can, e.g., be used for tuning the plasmonic dispersion in these materials, or to probe the weak interaction in more detail, which is usually difficult to achieve. Furthermore, due to its sensitivity to the dielectric environment, the TMRLE close to the SPP resonance could also be used as a sensor for changes in the dielectric environment in general, not just for those induced by the excitons.

10.6 Expanded Theoretical Model

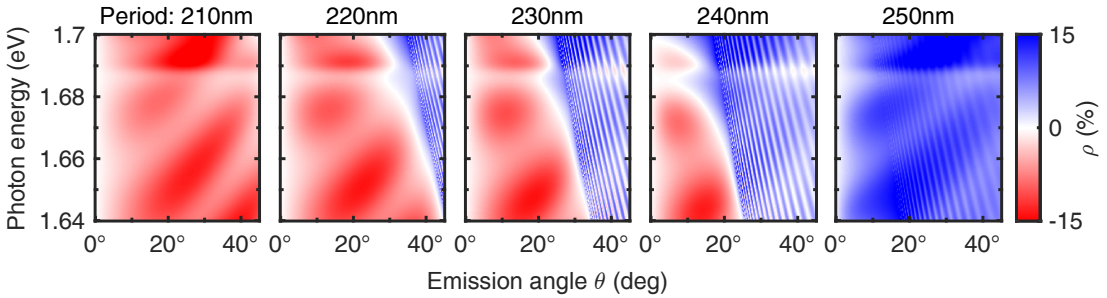

Figure 10.12 Simulated directionality spectra $\rho(E, \theta)$ for plasmonic grating periods from 210 nm to 250 nm with the extended model comprising the excitonic influence on the permittivity ε. The corresponding experimental data is shown in Figure 10.7.

The contribution of the excitons to the dielectric environment was not part of the theoretical model used to simulate the TMRLE in Refs. [30, 48, 52], based on the scattering matrix method. The modeled structure comprises a thick layer of non-magnetic (Cd,Mg)Te on top of a GaAs substrate, with the additional gold layer on top for the plasmonic resonance. Each layer is described via its dielectric function, which is not influenced by the magnetic field. Crucially, the thin magnetic (Cd,Mn)Te QW layer, from which the exciton emission originates, is not considered as a separate layer due to the similarity with the refractive index of the surrounding (Cd,Mg)Te layers. Instead, the excitons are described as circular dipole emitters placed 30 nm from the surface at the position of the magnetic QW, and their circular polarity $\pm P_c$ is inverted with the external magnetic field. Therefore, the exciton resonance does not have an influence on the dielectric functions of the structure, and consequently, on the SPP dispersion and its TMRLE contribution. This was shown in Figure 10.5 in the comparison of the experimental directionality data $\rho(E, \theta)$ with the simulated spectrum of this model, where the latter did not show the hump-shaped directionality feature.

To include this influence of the exciton resonance on the SPPs and their coupling, the model was expanded by A. N. Poddubny and V. Zakharov for the upcoming publication [109]. The expansion is based on the model of hybridized light-hole and heavy-hole states at weak magnetic

fields and their resonant influence on the permittivity ε introduced in Ref. [60] for a similar DMS (Cd,Mn)Te/(Cd,Mg)Te structure. There, it is used to describe the enhanced TMOKE from the bare QW structure in the vicinity of the QW exciton resonances, but it can be used equally well to improve the TMRLE simulations. The permittivity tensor of the semiconductor material is modified by resonant contributions from the heavy-hole (hh) and light-hole (lh) excitons in the form $\varepsilon = \varepsilon_\mathrm{b}(1 + \chi_\mathrm{hh} + \chi_\mathrm{lh})$ with the background permittivity ε_b, see Ref. [60] for details. Following the nomenclature from Ref. [60], the heavy-hole (hh) and light-hole (lh) energies are $E_\mathrm{hh} = 1.6870\,\mathrm{eV}$ and $E_\mathrm{lh} = 1.7050\,\mathrm{eV}$, the longitudinal-transverse splitting is $\hbar\omega_\mathrm{LT} = 1\,\mathrm{meV}$, the linewidths $\Delta_\mathrm{hh} = 2.3\,\mathrm{meV}$ and $\Delta_\mathrm{lh} = 5\,\mathrm{meV}$, the Zeeman splitting $\Delta_\mathrm{X,hh} = 1\,\mathrm{meV}$ and $\Delta_\mathrm{X,lh} = 4\,\mathrm{meV}$, and $Z = 0.2$ (see Ref. [109] for further details). These values were chosen based on experimentally determined properties of the structure and to best reproduce the spectra in Figure 10.7.

The result of the simulations using this extended model is shown in Figure 10.12 for the grating periods between 210 nm and 250 nm. In comparison to the experimental data in Figure 10.7, all features of the directionality spectra are now well reproduced by the updated model and it shows an excellent match. The different far-field effects are still overestimated compared to the near-field contributions from SPPs and photonic modes, but this was not intended to change with the modifications. Most importantly, the resonant changes to the dielectric permittivity lead to the same hump-shaped deviation of the sign change in the spectra, which confirms the theory of its origin and the coupling between the excitons and SPPs. From these simulated spectra we can see, that the feature is actually not just shaped like a hump sticking out, but includes two opposite deviations to the left and right in the spectra: The main hump towards smaller angles slightly below the resonance energy and an opposite contribution to larger angles slightly above the resonance energy. This S-shaped modification is in line with, e.g., typical TMOKE signals from optical resonances likes SPPs or excitons. It is important to note, that these changes are not a fundamental change of the model but rather an additional contribution that was not considered before. The directional emission still originates from the circular dipole emitters that are influenced by the magnetic field, while the added permittivity changes resonantly influence the final routing spectrum.

10.7 Comparison with TMOKE

Another magneto-optical effect that is strongly influenced by the presence of SPPs and other optical resonances is the transverse magneto-optical Kerr effect (TMOKE), which manifests as an intensity change of the light reflected from (or transmitted through) a magnetized medium in the Voigt geometry, see Section 4.3. Its geometry is, thus, similar to the TMRLE and both are magneto-optical intensity effects. The TMOKE is quantified by the parameter δ, which results from the comparison of the reflected light intensities $I(\pm B)$ for opposite magnetic fields $\pm B$ according to Eq. (4.5). Similar to the TMRLE, positive δ represent more light reflected for positive than negative magnetic fields and vice versa for negative δ. The non-resonant TMOKE magnitude is generally small at $\delta \approx 10^{-3}$, but it can be significantly enhanced near optical resonances with absorption, like SPPs, waveguide modes or excitons, see Section 4.4. The resonantly enhanced TMOKE usually manifests as an S-shaped signal with a sign change of δ, similar to the sign change close to the SPP resonance in the TMRLE spectra $\rho(E, \theta)$ above. Therefore, the optical resonances are clearly visible and easy-to-follow in the TMOKE spectra $\delta(E, \theta)$ and stand out against the negligible background effect.

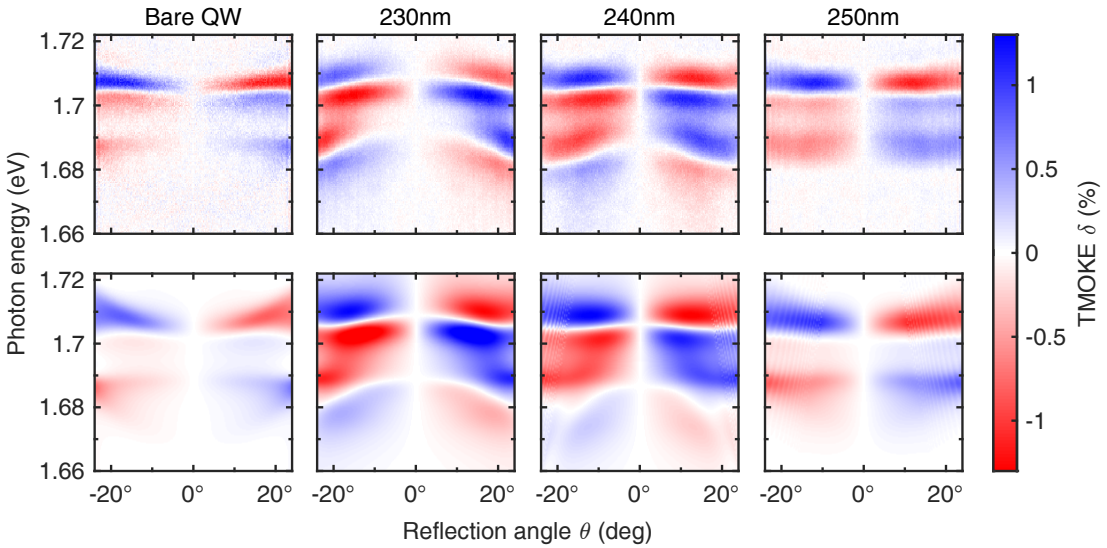

Figure 10.13 TMOKE $\delta(E, \theta)$ from the bare QW and from the hybrid structures with 230 nm, 240 nm and 250 nm grating periods. Comparison of experimental data (top row) and theoretical simulations (bottom row).

An example of the TMOKE at an optical resonance can be seen in the top-left panel of Figure 10.13, which shows the TMOKE δ measured on the bare (Cd,Mn)Te/(Cd,Mg)Te QW structure, i.e., without a plasmonic grating on top. Like for the TMRLE spectra, blue and red represent positive and negative values of δ and white for $\delta = 0$. The sample was illuminated with light from a thermal tungsten light source, and the reflected p-polarized intensity was measured for opposite magnetic fields $B = \pm 485$ mT and at $T = 4$ K, like for the TMRLE. The bare QW shows a strong TMOKE at the light-hole exciton resonance around 1.705 eV with up to $\delta = 1.1$ % and the typical sign change. As expected for the exciton dispersion, the TMOKE shows no angular dependence aside from an increasing δ for larger reflection angles. The heavy-hole exciton, which has the strongest TMRLE contribution, shows a weaker TMOKE of 0.5 % around 1.685 eV because the TMOKE magnitude depends on the Zeeman splitting, which is only enabled for the heavy-holes via the admixture of light-hole states and, thus, small at low magnetic fields [60]. The off-resonant TMOKE at, e.g., 1.66 eV is well below 0.1 %. The TMOKE spectrum can be reproduced well using the model established in Ref. [60], whose results are shown in the bottom row of Figure 10.13.

Samples featuring plasmonic resonances at a magnetic interface generally show a similarly clear TMOKE spectrum with an enhanced TMOKE response around the plasmonic resonance. It also manifests as a sign (and thus color) change, albeit diagonally through the $\delta(E, \theta)$ spectrum like the SPP resonance. This is shown, e.g., in Chapter 11 for magnetite-based samples or in Refs. [15, 17, 63]. The remaining panels of Figure 10.13 show the TMOKE $\delta(E, \theta)$ from the hybrid structure (with the plasmonic grating) for the grating periods 230 nm, 240 nm and 250 nm. In all three cases, the largest TMOKE δ still originates from the excitons in the QW. However, with the presence of the plasmonic grating, their TMOKE response is influenced by the SPPs at the interface, and the white lines corresponding to the exciton resonances are bent and become energy-dependent. The SPPs themselves only have a weak TMOKE response in comparison due to their non-magnetic interface and evanescent nature towards the magnetic QW 30 nm away. Nevertheless, their inward-shifting

influence for increasing grating periods can still be traced through the three spectra: The SPP resonance is located at smaller angles for larger energies, so that the higher-energy light-hole resonance is influenced the most for 230 nm and less for the larger periods, and the heavy-hole resonance at lower energies is strongly influenced for 230 nm and 240 nm but barely for 250 nm. Most directly, a small TMOKE contribution occurs at the energies below 1.68 eV for 230 nm and 240 nm. These TMOKE spectra can also be reproduced in great detail by the theoretical model based on the scattering matrix method, as is shown in the bottom row for comparison.

However, the TMOKE is not well suited for the detection and quantization of the coupling between the excitons and plasmons, even though the SPPs heavily influence the exciton TMOKE and despite the excellently matching theoretical model. This is evident in both the theoretical model and the experimental data. For the TMRLE, two magnetic-field dependent properties are modeled independently: First, the magnetic-field-controlled circular emitters are always present as light source for the routing effect. On the other hand, the interaction between the excitons and SPPs can be switched on and off, because their coupling is modeled via the resonant changes to the dielectric environment. In contrast, the TMOKE is solely described by the magnetic-field-dependence of the permittivity changes in the magnetic (Cd,Mn)Te QW layer. Therefore, it influences both the exciton and SPP resonances, and the interaction can not be switched off to see the differences like in the TMRLE model.

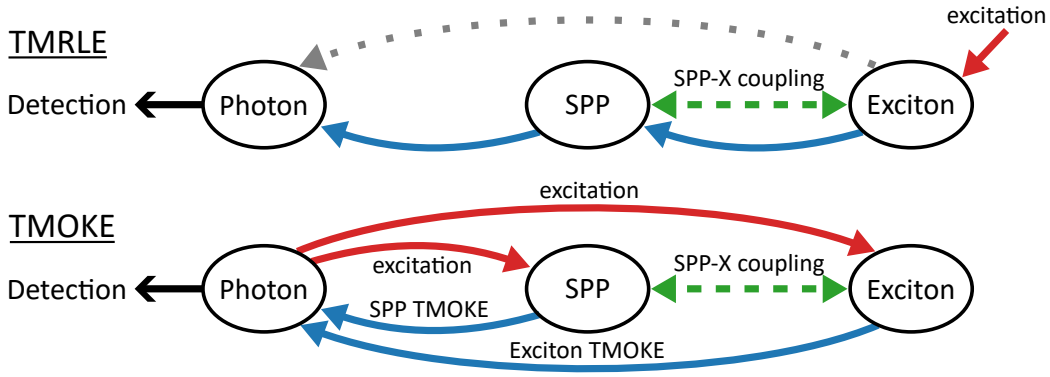

Figure 10.14 Schematic representation of the processes involved in the TMRLE and TMOKE between the excitons, SPPs and far-field photon radiation. The necessary interaction of excitons and SPPs for a strong TMRLE, without individual contributions from neither, enables the high sensitivity to the exciton-SPP coupling (green). The TMOKE involves a greater number of processes and interactions with individual, non-separable contributions to the overall TMOKE response, concealing the weak exciton-SPP coupling.

Furthermore, the magneto-optical response from the structure in TMOKE measurements is more complex than in TMRLE measurements. This is shown in Figure 10.14, which is a schematic representation of the processes involved in the two effects between the photonic, plasmonic, and excitonic systems. Excitations are shown as red arrows and magneto-optical responses in blue. The coupling between the SPPs and excitons is highlighted in green.
For the **TMRLE** (top), the structure are excited non-resonantly via a laser with energies above the band-gap, and the exciton ground-state is reached via relaxation processes. The excitons can directly emit from the structure as photons (gray dotted arrow), but this emission shows negligible directionality and is not relevant for the coupling. Beyond that, the excitons recombine and emit

into the SPPs, which then emit photons into the far-field for detection. This unidirectional and simple path from the excitons to SPPs and directional photons is the reason for the high sensitivity of the TMRLE spectra to the exciton-SPP coupling shown in green, as no individual directionality contributions from excitons or SPPs exist and only their coupling creates a meaningful contribution. On the other hand, a greater number of processes are involved in the **TMOKE** (bottom) in both directions (excitation and response). Here, the incoming spectrally broad whitelight resonantly excites both the plasmonic and excitonic systems, and the SPPs and excitons both have an individual, direct and comparatively strong contribution to the TMOKE spectrum of the reflected light. Furthermore, the systems heavily influence each others TMOKE response and interfere with each other. Therefore, the final TMOKE spectrum is not a simple superposition of the individual contributions from SPPs, excitons, and the bare surface, and their effects are not clearly distinguishable. Accordingly, the weak interaction between the excitons and SPPs can not be determined from the TMOKE spectra, because the individual contributions can not be separated, neither experimentally nor in the theoretical model.

10.8 Summary

This chapter has investigated the dependence of the TMRLE on the geometric parameters of the plasmonic grating structure, i.e. the grating period and width of the slits. The maximum TMRLE follows the plasmonic resonance through the directionality spectra, whose dispersion is shifted by the grating parameters. Here, the grating period a shifts the folded SPP resonances originating from $k_y = \pm m2\pi/a$, and the slit width w causes gaps of the SPP dispersion to appear at the borders of the reduced zone scheme, which both influence the SPP-enhanced directionality. Furthermore, the additional directionality effects of the arbitrary photonic modes at the plasmonic interface, which either enhance or compensate the strong SPP contribution, has been shown. Notably, the experimental directionality data showed a hump-shaped deviation from the expected monotonic dependence on the emission angle. On the one hand, its energy is fixed to the QW emission maximum, which is defined by the properties of the semiconductor materials comprising the QW. On the other hand, it is attached to the sign change of the strong SPP directionality contribution and shifts through the spectrum in unison for changing grating periods. This deviation was not reproduced by the initial theoretical model used to describe und simulate the TMRLE. Therefore, the model was expanded by a resonant contribution of the QW excitons to the dielectric environment, which locally alters the SPP dispersion and, thus, the resulting SPP-enhanced directionality spectrum. The simulations following the expanded model reproduce the experimental data in all aspects, including the unexpected hump-shaped deviation. This sensitivity of the TMRLE to the interaction between the excitons and SPPs close to the directionality sign change can be used to directly probe the weak coupling of the two systems, which is otherwise difficult to detect.

The TMOKE is a similar magneto-optical intensity effect that occurs for reflected rather than emitted light, and is enhanced at the excitonic and plasmonic resonances. However, the TMOKE is not suitable for detecting the weak coupling between excitons and SPPs because both systems contribute individually to the TMOKE and interfere with each other, and their contributions can not be separated.

Chapter 11

Enhanced TMOKE in Magnetite-Based Plasmonic Systems

This chapter will focus on a different magneto-plasmonic system, which comprises a thin film of the ferrimagnet magnetite (Fe_3O_4) and one-dimensional plasmonic gold gratings that are either placed on top of the magnetite film or embedded into it. The transverse magneto-optical Kerr effect (TMOKE), a magneto-optical effect defined by its influence on the reflected or transmitted light intensity, will be investigated in the reflection and transmission geometry. The TMOKE is sensitive to the magnetic properties at the interface of two materials, making it an interesting candidate for controlling light at the nanoscale [60]. It is weak in planar magnetic films with relative intensity changes in the order of only 0.1 %, but can be significantly enhanced close to optical resonances, e.g., up to 13 % in bismuth-substituted iron garnets [17, 63]. In our case, the addition of the period grating enables the excitation of plasmonic and waveguide modes that enhance the effect by more than one order of magnitude in the transmission geometry and in a broad spectral range. The placement of the grating either in or above the magnetite film has an influence on the optical resonances and their TMOKE signal due to the changed interfaces.
First, the plain magnetite film will be characterized in Section 11.1 using Faraday rotation and ellipticity measurements. It is non-uniform and comprises Fe_3O_4/α-Fe nanoparticle complexes compared to the typical monocrystalline or polycrystalline Fe_3O_4 films (see Section 6.2 for details). Then, the different magnetization behavior in the Voigt geometry compared to the Faraday geometry will be discussed in Section 11.2, including the strong magnetization hysteresis. Next, Section 11.3 shows the TMOKE at a fixed angle for a better quantitative understanding of the different geometries, followed by the full angular and spectrally resolved TMOKE spectra in Section 11.4, which reveal, among other things, the influence of the mode hybridization on the TMOKE spectra.

Most results presented in this chapter have already been published in Ref. [4], with additional theoretical work and simulations by Sergey Dyakov. This chapter closely follows that publication, and its content and figures are reproduced for this thesis with permission.

11.1 Magnetic Properties of the Synthesized Films

The Magnetite samples all comprise a 100 nm thin film of Magnetite (Fe_3O_4) on top of a SiO_2 substrate. The films are non-uniform and consist of Fe_3O_4/α-Fe nanoparticle complexes with an average size of 6−10 nm, see Section 6.2. Compared to usual polycrystalline Fe_3O_4 films, synthesized nanostructured films like these showed a larger coercive force and saturation magnetization of up

to 660 Oe and 520 emu/cm^3, respectively. It is, therefore, necessary to experimentally determine the optical properties of these particular films in an external magnetic field for our magneto-optical studies.
The dielectric permittivity tensor $\hat{\boldsymbol{\varepsilon}}$ with additional off-diagonal elements is used for the theoretical description of the optical properties of the bare magnetite films on a macroscopic level:

$$\hat{\boldsymbol{\varepsilon}} = \begin{pmatrix} \varepsilon & -ig_z & ig_y \\ ig_z & \varepsilon & -ig_x \\ -ig_y & ig_x & \varepsilon \end{pmatrix}. \tag{11.1}$$

Here, the diagonal elements ε are the dielectric permittivity of the non-magnetized material, which are equal due to the lack of anisotropy in the nanocrystalline films. It was determined from standard ellipsometry measurements and is shown in Figure 6.5. The measurements show a relatively large imaginary part Im(ε) and, therefore, rather large internal optical losses of the magnetite film in the visible range. The data of our non-uniform magnetite films are close to literature data for monocrystalline and epitaxial films [89, 90], and were used for the calculation of the eigenmodes of the system in Ref. [4]. The magnetic permeability μ is assumed to be unity. The complex gyration vector $\boldsymbol{g}$ in the off-diagonal elements of Eq. (11.1) is proportional to the magnetization $\boldsymbol{g} = \alpha \boldsymbol{M}$. Here, α is assumed equal for all directions of M and therefore $g_x = g_y = g_z = g$.

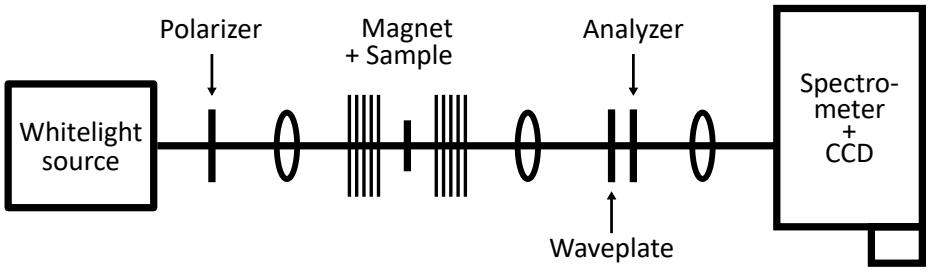

Figure 11.1 Schematic depiction of the measurement setup for the Faraday rotation angle ϑ and ellipticity ψ. The white light from the light source is linearly polarized and focussed onto the sample between the poles of an electromagnet in Faraday geometry. The transmitted light is collimated, passes through either a half- or quarter-wave plate followed by a second linear polarizer (analyzer) and is focussed onto the entrance slit of a spectrometer with a CCD-detector.

The gyration g of the magnetite film can be determined from the complex Faraday rotation, i.e. the ellipticity ψ and the rotation of the major axis of the ellipse ϑ for light transmitted through the sample, see Section 4.2. In short, for an absorbing medium with different absorption coefficients for the left and right circularly polarized light, this magnetic circular dichroism (MCD) leads to the change from linearly to elliptically polarized light after transmission with an additional rotation of the ellipse major axis due to the magnetic circular birefringence, i.e. different refractive indices for left and right circularly polarized light (Faraday effect). They were measured at room temperature using the setup shown schematically in Figure 11.1. The white-light source comprises a halogen lamp with a broad and flat emission spectrum, whose light is focussed onto a 100 µm pinhole by a lens and collimated using a second lens for a homogeneous spatial distribution of the light. The light is linearly polarized using a Glan-Thompson prism (polarizer) before it is focussed into a spot of about 1 mm on the sample using an achromatic lens. The sample is positioned between the poles of a water-cooled resistive electromagnet in the Faraday geometry, which is used to apply

bidirectional external magnetic fields of up to ±750 mT perpendicular to the magnetite film and along the direction of light propagation. The transmitted light is collected and collimated using a second lens before it passes through the combination of either a half- or quarter-wave plate followed by a Glan-Thompson prism (analyzer) for the Faraday rotation and ellipticity measurement, respectively. The polarizer and analyzer were set to the same polarization axis, and the main axis of the half- and quarter-wave plates was set to 22.5° and 45° regarding the analyzer axis, respectively. Finally, the light is focussed onto the entrance slit of a spectrometer, which separates the light into its spectral components and detects it using a CCD-detector with a spectral resolution of about 1.3 nm. Using this experimental configuration, the Faraday rotation angle ϑ and the ellipticity ψ can be determined in the small-angle approximation by measuring the light intensity I for opposite magnetic field directions $\pm B$ and comparing them [4]:

$$\vartheta = \frac{1}{2}\frac{I_l(+B) - I_l(-B)}{I_l(+B) + I_l(-B)} \quad \text{and} \tag{11.2}$$

$$\psi = \frac{1}{2}\frac{I_\sigma(+B) - I_\sigma(-B)}{I_\sigma(+B) + I_\sigma(-B)}. \tag{11.3}$$

With the half-wave plate set to 22.5° regarding the analyzer, the linearly polarized component I_l at 45° relative to the polarizer in front of the sample is detected. The rotation of the plane due to the Faraday effect is detected as an increase or decrease of the measured intensity, depending on the direction of the induced rotation $\pm\vartheta$ at opposite magnetic fields. For the ellipticity ψ, the circularly polarized component I_σ for one of the circular polarizations σ is detected instead due to the combination of the quarter-wave plate and the analyzer. These are equivalent to measuring opposite linear polarizations $I_{\pm 45°}$ or circular polarizations $I_{\sigma^\pm}$ at a constant magnetic field, i.e. $\vartheta = 1/2(I_{+45°} - I_{-45°})/(I_{+45°} + I_{-45°})$ and $\psi = 1/2(I_{\sigma^+} - I_{\sigma^-})/(I_{\sigma^+} + I_{\sigma^-})$.

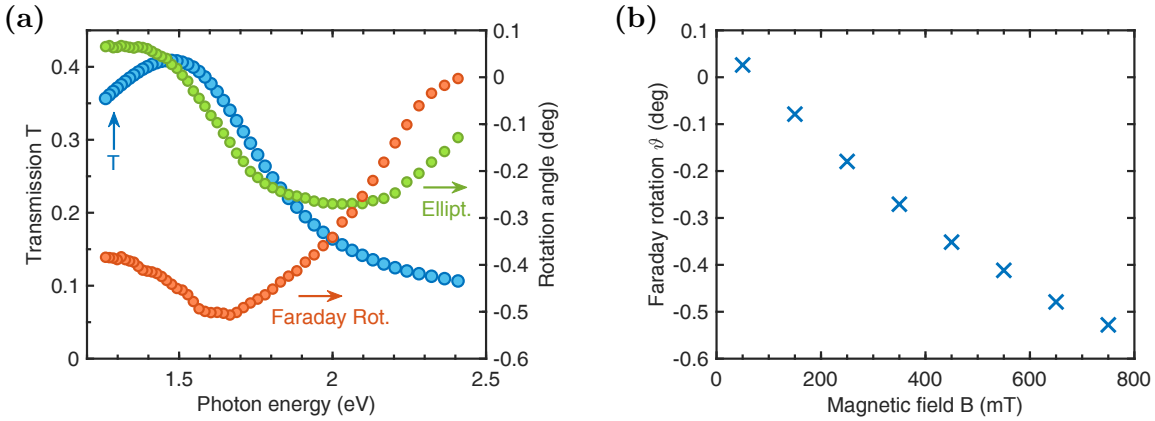

Figure 11.2 (a) Spectra of transmission (blue), Faraday rotation angle ϑ (orange) and ellipticity ψ (green) for light with energies between $E = 1.2$ eV and 2.5 eV through a 100 nm thin film of Fe_3O_4/α-Fe nanoparticle complexes at room temperature. The Faraday rotation and ellipticity were measured at $B = 750$ mT. **(b)** Magnetic field dependence of ϑ for light between 1.61 eV and 1.68 eV.

The results of these measurements are shown in Figure 11.2 for light with energies between 1.2 eV and 2.5 eV. First, Figure 11.2(a) shows the transmission spectrum $T(E)$ of the sample with the 100 nm thin bare magnetite film (blue points), where $T = I_s/I_0$ is the intensity transmitted through

the sample I_s in relation to the intensity measured without the sample I_0. It shows a flat spectral dependence without resonances, with a maximum of 0.4 around 1.5 eV and decreasing T towards 0.1 at the highest energies. Next, panel (a) also shows the Faraday rotation angle ϑ in orange and the ellipticity ψ in green according to Eqs. (11.2) and (11.3) in the same spectral range. Both have a similarly non-resonant spectrum, with the Faraday rotation reaching its largest value of $-0.5°$ at 1.65 eV and the ellipticity 0.25° between 2.0 eV and 2.1 eV. The number of data points was reduced for all three curves by averaging over equidistant ranges of the wavelength axis to reduce the noise. Figure 11.2(b) shows the magnetic field dependence of the Faraday Rotation ϑ between 1.61 eV and 1.68 eV and magnetic fields between 50 mT and 750 mT. For increasing magnetic fields, the rotation angle increases linearly at first and then increasingly flatter for the larger magnetic fields, indicating a saturation magnetization close to 750 mT. This was confirmed in measurements of the polar magneto-optical Kerr effect (PMOKE) for a larger range of magnetic fields (not shown here), which confirmed the saturation magnetization in the Faraday geometry between 600 mT to 800 mT, although at $T = 6$ K and not room temperature. The Faraday rotation shows the opposite sign at the lowest magnetic field of 50 mT, hinting at the hysteresis of magnetite.

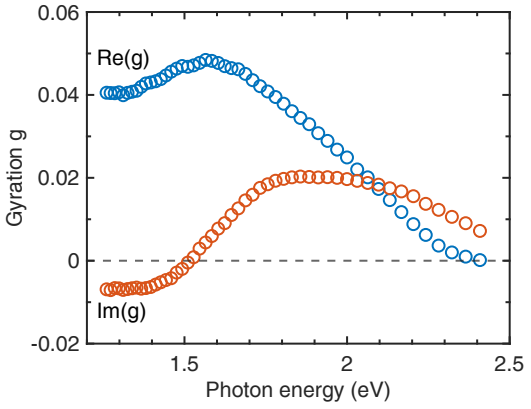

Figure 11.3 Real and imaginary parts of the gyration g derived from the Faraday rotation and ellipticity data using Eqs. (4.3) and (4.4).

The experimental Faraday rotation and ellipticity spectra $\vartheta(E)$ and $\psi(E)$ with the magnetic field in the z-direction can now be used to determine the complex gyration g, see Section 4.2 and Ref. [1]. For materials with cubic symmetry or crystals with a symmetry axis and for the light wave vector and magnetization oriented along that axis, the rotation ϑ and ellipticity ψ are connected to the complex gyration $g = g' + ig''$ via Eqs. (4.3) and (4.4). The thickness of the magnetic film is $d = 100$ nm, and n_0 is the real part of the refractive from the ellipsometry measurements shown in Figure 6.5. The resulting energy dependence of the real and imaginary parts $\mathrm{Re}(g)$ and $\mathrm{Im}(g)$ is shown in Figure 11.3 with blue and orange circles, respectively. Like the dielectric permittivity ε, the obtained gyration data of our synthesized magnetite film are close to literature data measured for monocrystalline and epitaxial magnetite films [89, 90]. These results were used for the theoretical modeling of the TMOKE response from the magnetite-based structures in Ref. [4].

11.2 Magnetization Hysteresis in Voigt Geometry

The measurements characterizing the isotropic magneto-optical parameters of the bare magnetite film were done in the Faraday geometry. However, the transverse magneto-optical Kerr effect (TMOKE) that is used to study the optical resonances of the hybrid plasmonic structures in detail occurs in the Voigt geometry, where the magnetic field is directed in the plane of the magnetite film and perpendicular to the plane of light incidence. The TMOKE is a prominent intensity effect, where the intensity of the reflected or transmitted light changes for opposite magnetic field directions $\pm B$. This differentiates it from, e.g., the Faraday effect and the other magneto-optical Kerr effects in

different geometries, which are mainly defined by their influence on the polarization of the light. The TMOKE is defined as the relative change δ of the reflected or transmitted light intensity I for the opposite in-plane magnetization M at the interface between two materials:

$$\delta = 2\frac{I(M) - I(-M)}{I(M) + I(-M)}. \tag{11.4}$$

For the TMOKE to occur in the transmission geometry, a lack of mirror symmetry needs to be present in the structure, which is given for our magnetite samples, either due to the substrate on one side of the bare magnetic film or by adding the plasmonic gold gratings on top of the magnetite film or embedded into it.

The dependence of the TMOKE magnitude δ on the external magnetic field B can be used to probe the magnetization curve $M(B)$ of the sample in the Voigt geometry. For this, the sample was mounted between the poles of an electromagnet and rotated around the axis of the magnetic field direction by 23°. An achromatic lens focussed the p-polarized light from a tungsten halogen lamp onto the magnetite sample with the plasmonic grating on top. A second lens collected the transmitted light and focussed it onto the spectrometer entrance slit to measure the spectrum of the transmitted light. The magnetic field was swept between ±105 mT in steps of 7 mT in both the forward and backward direction, as magnetite is known to show hysteresis behavior. The transmitted light intensity was detected at each step of the magnetic field. The TMOKE parameter δ was then calculated by comparing the transmitted intensities $I_i(\pm B)$ at the opposite magnetic field directions $\pm B$ of the same strength, based on Eq. (11.4). The subscript i indicates the direction of the magnetic field scan with f for the forward and b for the backward direction:

$$\delta(B) = 2\frac{I_f(+B) - I_b(-B)}{I_f(+B) + I_b(-B)}. \tag{11.5}$$

Switching the subscripts f and b completes the hysteresis loop.

The resulting magnetic field dependence of the TMOKE δ is shown in Figure 11.4 for three different energies of the light $E = 1.38$ eV, 1.43 eV, and 1.53 eV averaged in a 10 meV window and transmitted at an angle of $(23 \pm 1)°$. These three photon energies were chosen due to their different dependence on the magnetic field. The TMOKE δ according to Eq. (11.5) is shown as the solid line, and the dash-dotted line represents the switched subscripts. Focussing on the 1.38 eV case (blue) first, the TMOKE δ and thus the sample magnetization M already saturate at magnetic fields of ±100 mT with $\delta = \pm 0.4$ %. It shows a strong hysteresis behavior for lower fields, as $\delta = 0$ is only reached at ±42 mT, i.e. half the field strength needed to saturate the magnetization due to the strong coercive force. Next, the TMOKE signal at 1.53 eV (orange curve) has the same shape and magnitude but with the opposite sign. Generally, the shape of

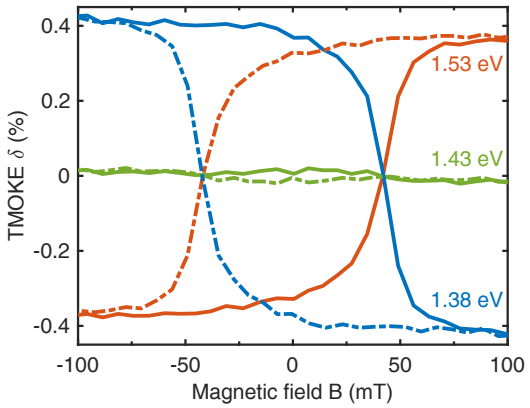

Figure 11.4 Magnetic field dependence of TMOKE δ at 23° transmission angle for three different photon energies. Solid lines correspond to Eq. (11.5), dashed lines to switched subscripts b and f.

the hysteresis curve is similar for all energies and always saturates at 100 mT, but the sign and magnitude of δ change in the vicinity of optical resonances introduced by the additional gold grating on top of the magnetite film, see Section 4.4. This is apparent for the TMOKE at 1.43 eV (green), i.e. between the two opposite maxima, which drops to $\delta = 0$ for all magnetic fields.

Notably, the magnetic field needed to saturate the sample magnetization for the TMOKE in the Voigt geometry is about one order of magnitude lower than in the Faraday geometry, as seen in Figure 11.2 for the Faraday rotation and, e.g., in Ref. [90] for the polar Kerr effect. In an applied external magnetic field, free poles form at the ends of the magnetic material, which produce a magnetic field directed in the opposite direction of the magnetization called the demagnetizing field. The strength of this demagnetizing field is proportional to the density of the free magnetic poles, which is small for a thin, long film magnetized along its long axis but large for the same film magnetized along the short axis, i.e., perpendicular to the plane of the film [117]. The latter is the case for the measurements in the Faraday geometry, where larger fields are needed to overcome the demagnetizing field, while the former describes the case of the TMOKE in the Voigt geometry, where weaker magnetic fields are needed to reach the saturation magnetization. All further measurements in the Voigt geometry were conducted at saturating magnetic fields above 100 mT at room temperature.

11.3 TMOKE in Reflection and Transmission

The focus of the studies on the magnetite-based plasmonic structures lies in the TMOKE, how it is influenced by the optical resonances of the structure, and how the TMOKE can be used for a better understanding of the modes and their hybridization. The transmission, reflection, and TMOKE spectra were measured using the Fourier imaging spectroscopy setup described in detail in Section 7.2. It enables the measurement of the reflected or transmitted light intensity $I(E, \theta)$ spectrally resolved and in a large range of reflection or transmission angles at the same time to visualize the complex angular and spectral dependence of the optical resonances. In short, the white light of a tungsten lamp is linearly polarized using a Glan-Thompson prism and a half-wave plate and focussed onto the sample using a microscope objective (MO). In the reflection geometry, the reflected light is collected by the same MO in the backscattering geometry in an angular range of $\pm 23.5^\circ$. In the transmission geometry, an identical MO on the backside of the sample collects the transmitted light in the same angular range. In both cases, the Fourier plane containing the angular information as offset from the optical axis is mapped onto the entrance slit of the imaging spectrometer by a telescope comprising two achromatic lenses. The resulting spectra have a spectral and angular resolution of about 1 nm and 0.4°. External magnetic fields in the Voigt geometry exceeding the saturation magnetization of the sample were applied using the water-cooled resistive electromagnet. All measurements were done at room temperature. To determine the TMOKE, the reflected or transmitted intensity $I(E, \theta)$ was measured for the two opposite magnetic field directions $\pm B$ with saturated sample magnetization. Each spectrum was taken with 3 s exposure time, and multiple spectra were accumulated to increase the signal-to-noise ratio for each magnetic field direction. Additionally, the magnetic field direction was switched back and forth multiple times with a measurement in between to eliminate fluctuations of the lamp intensity and other long-term influences on the measurement. For most measurements, the spectra were measured in three adjacent energy ranges to cover the spectral range from 1.2 eV to 2.0 eV.

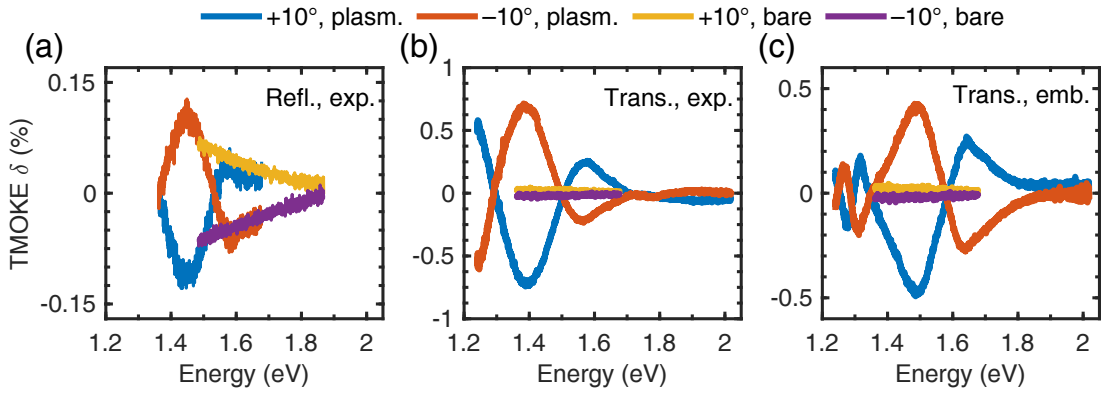

Figure 11.5 TMOKE spectra $\delta(E)$ at $\theta = \pm 10°$ for the sample with the exposed gold gratings in **(a)** reflection and **(b)** transmission, and **(c)** for the sample with embedded gold grating in transmission. Comparison between signal from the plasmonic structure (blue, orange) and signal from bare magnetite film (yellow, purple).

Before discussing the full spectrally and angular resolved spectra, though, Figure 11.5 shows spectrally resolved TMOKE signals at a fixed angle of ±10° to compare the reflection and transmission geometries. Panel (a) shows the TMOKE in reflection from the sample with the exposed (exp.) gold grating on top of the magnetite film, and (b) shows the TMOKE from the same sample in the transmission geometry. Panel (c) also shows TMOKE in transmission but from the sample with the gold grating embedded (emb.) into the magnetite film. Furthermore, each panel compares the effect from the plasmonic structure (blue and orange) to the effect from the bare magnetite film (yellow and purple) in the respective geometry. All data shown are extracted from the spectrally and angular resolved Fourier imaging spectra by averaging the reflected or transmitted intensity spectra $I(, \theta)$ in the angular range between $\theta = \pm 9°$ and $\pm 11°$ before using Eq. (11.4) to obtain the TMOKE parameter δ at saturated sample magnetization. The restriction to a small angular range allows for a better quantitative comparison of the different geometries and sample compositions. Starting with the TMOKE in reflection geometry in panel (a), the TMOKE on the bare magnetite film (yellow and purple) shows a monotonically decreasing magnitude for increasing energies without any resonant features, reaching up to $\delta = 0.07\,\%$ in this small spectral range. With the added plasmonic grating on top of the magnetite film (blue and orange curves), the TMOKE reaches up to $\delta = 0.1\,\%$ at 1.5 eV, but with a more complicated spectral dependence due to sign changes associated with the optical resonances introduced by the grating (see Section 4.4). Between 1.59 eV and 1.65 eV, the TMOKE has about the same magnitude and sign as the bare film, switching signs once at 1.55 eV and again below 1.4 eV, with the aforementioned maximum effect in between. As expected, the TMOKE is an odd effect regarding the angle and, therefore, $\delta(\theta) = -\delta(-\theta)$ holds true for the plasmonic and non-plasmonic case. Next, panel (b) shows the TMOKE from the same sample but in the transmission geometry and in a larger spectral range. The TMOKE δ from the hybrid structure (blue and orange) generally has the same shape as in reflection, but all features are shifted to slightly lower energies. For example, the two sign changes are now at 1.5 eV and 1.29 eV. Overall, the TMOKE magnitude in transmission is larger, with the maximum at 1.39 eV reaching 0.7 %. On the other hand, the TMOKE from the bare magnetite film is weaker and reaches only 0.03 % with the same monotonic spectrum. Finally, panel (c) shows the TMOKE in transmission from the sample with the plasmonic grating embedded into the magnetite film, i.e., at the interface

between magnetite and the substrate. Here, the resonances shift and the spectral dependence changes compared to panel (b), revealing more features. The maximum TMOKE magnitude is lower with 0.45 % at 1.49 eV and four sign changes occur around 1.25, 1.29, 1.35, and 1.58 eV, each indicating the presence of an optical resonance. The TMOKE from the bare film is the same as in panel (b).

The comparison of the plain magnetite film and the plasmonic structures shows that the addition of the period gold grating introduces resonances in the TMOKE signal. The plain magnetite film does not show any resonant behavior in the far-field transmission or reflection spectra because the eigenmodes of the system are all below the air light line and the momentum conservation law prohibits their interaction. In comparison, the periodicity of the grating enables the interaction between the eigenmodes of the structure with the light in the far field, i.e. the photon continuum. The sign changes of the signal are generally connected to an optical resonance of the structure with a large TMOKE response in the vicinity of that resonance, see Section 4.4. For these structures, the main resonances are SPPs at either interface of the gold grating and guided resonances in the magnetic magnetite film. However, all modes are hybrid modes with varying contributions from the constituents due to their close spacial proximity in the structure. The identification of the contributions needs additional theoretical modeling of the structures, which was done by Sergey Dyakov in Ref. [4].

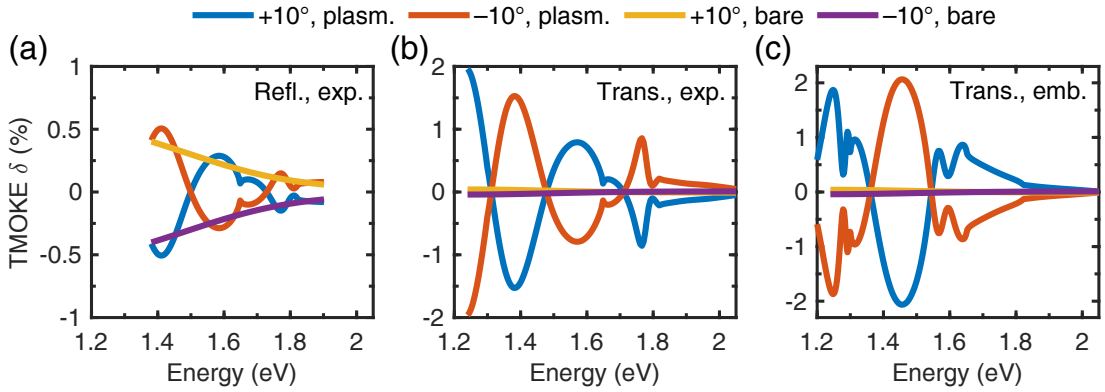

Figure 11.6 Theoretical TMOKE spectra $\delta(E)$ at $\theta = \pm 10°$ for the exposed gold gratings in **(a)** reflection and **(b)** transmission, and **(c)** for the embedded gold grating in transmission. Comparison between signal from the plasmonic structure (blue, orange) and signal from bare magnetite film (yellow, purple).

The comparison of the TMOKE measurements in reflection to those in transmission shows that the enhancement of the TMOKE signal due to the added periodic gold grating is only observed in the transmission geometry. While the TMOKE spectrum changes in reflection, the maximum $\delta = 0.1$ % is close to the 0.07 % measured on the bare magnetite film. However, in transmission, an enhancement of an order of magnitude occurs for both the exposed grating with 0.7 % and the embedded grating with 0.45 % compared to 0.03 % through the bare film. Based on the additional theoretical calculations in Ref. [4], we attribute this effect to the excitation of the hybrid modes discussed above, which appears to have a larger influence on the transmitted light than the reflected light. The spectral width of the TMOKE signal is broad and in the order of 100 to 200 meV (or around 100 nm peak to peak) for all three combinations of structures and geometries shown in Figure 11.5. This matches the spectral broadness of the plasmonic and waveguide resonances in the

full transmission and reflection spectra from the Fourier imaging setup, which will be shown next. Furthermore, the TMOKE spectra shown in Figure 11.5 can be reproduced well using theoretical modeling based on the rigorous coupled-wave analysis (RCWA), which is a Fourier modal method in the scattering matrix form. The theoretical background and results of the simulations are presented in Ref. [4] and summarized in Figure 11.6 on the same energy scale as Figure 11.5. The general shape of the main resonances is reproduced well but the magnitude of the TMOKE is overestimated in the simulations, and the simulated spectra comprise more features.

11.4 Fourier Imaging TMOKE Spectra

With the different geometries of measurement and grating position quantified, this section will present the full spectra from the Fourier imaging setup. The key advantage of the Fourier imaging spectroscopy (see Section 7.1) is the simultaneous measurement of the spectral and angular dependence of the transmitted or reflected light intensity $I(E, \theta)$, which allows for better tracking of the resonant optical modes through the spectra. The TMOKE spectra at $\theta = \pm 10°$ in Section 11.3 were created from the Fourier imaging spectra presented next. This section will follow the order of Section 11.3, which first addressed the sample with the gold grating on top of the magnetite film in the reflection geometry, then the same sample in transmission, and finally, the sample with the gold gratings embedded in the magnetite film in transmission.

11.4.1 Reflection Geometry - Exposed Grating

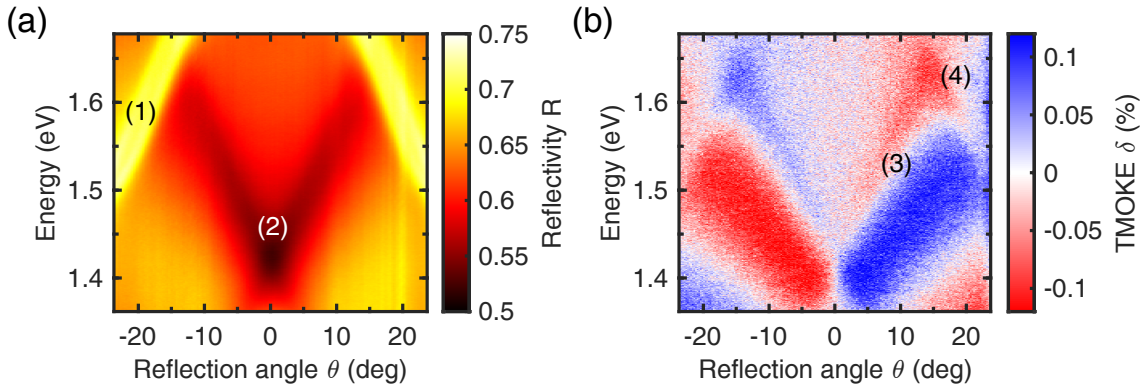

Figure 11.7 Reflection geometry, gold grating on top of the magnetite film:
(a) Reflectivity $R = I_{\text{grating}}/I_{\text{ref}}$ with the light intensity reflected from the structure with grating I_{grating} and from an unpatterned planar gold film I_{ref} as reference. **(b)** TMOKE δ according to Eq. (11.4) from the grating structure.

Starting in the reflection geometry with the sample comprising the exposed gold grating on top of the magnetite film, Figure 11.7(a) shows the reflectivity $R(E, \theta)$ and panel (b) the corresponding TMOKE spectrum $\delta(E, \theta)$, both for p-polarized light and between $1.36 - 1.68$ eV. The reflectivity R in (a) is defined as $R = I_{\text{grating}}/I_{\text{ref}}$, where I_{grating} is the light intensity reflected from the structure with the plasmonic gold grating and I_{ref} is the light reflected from a reference film of unpatterned

gold on top of the same magnetite film. The unpatterned gold film serves as a reference because it lacks the periodicity that enables the interaction of the plasmonic and waveguide modes of the structure with the far-field and therefore acts as a mirror. This definition of R highlights the optical modes enabled by the periodic grating in the reflectivity plot as regions of lower or higher reflected intensity than its surroundings, and removes influences of the optical elements or the light source spectrum. Two resonant features are clearly visible, one with an increased reflectivity compared to the reference film (1) and the other with a lower reflectivity (2). Both modes are symmetric regarding the reflection angle $R(\theta) = R(-\theta)$. The resonance labeled (1) is a plasmonic resonance because it does not appear in s-polarized spectra. With a grating period of 580 nm, it can be attributed to the plasmon at the air/gold interface. The plasmon at the interface of gold and the magnetic magnetite, which is expected to be influenced by the magnetic field and show an enhanced TMOKE, is located at higher energies outside the measured range because of the larger refractive index of magnetite compared to air. The other resonant feature (2) is visible in p- and s-polarized spectra but with slightly shifted resonance frequencies due to the polarization-dependent boundary conditions. Since it is not visible without the periodic grating structure, it can be identified as a waveguide mode inside the magnetite film with the larger refractive index $n_{\text{magn.}} > n_{\text{silica}}$, whose interaction with the incident light is enabled by the periodicity of the grating.

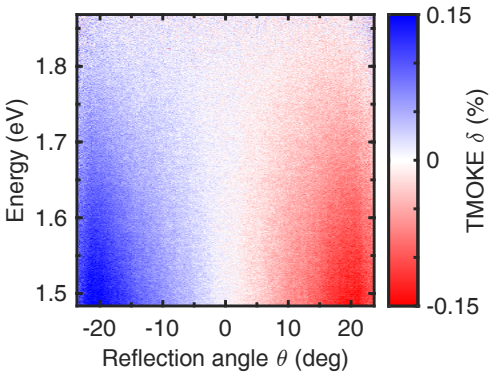

Figure 11.8 TMOKE $\delta(E, \theta)$ from the bare magnetite film in reflection.

Both optical resonances are also visible in the TMOKE spectrum in Figure 11.7(b). Here, the colors blue and red represent positive and negative values of the TMOKE δ, and the color saturation represents the magnitude. The color white represents $\delta = 0$, i.e. no change in the light intensity for opposite magnetic fields. As already seen in the cuts at $\pm 10^\circ$ in Figure 11.5, the TMOKE δ is an odd function of the incidence angle of the light θ and $\delta(\theta) = -\delta(-\theta)$. The waveguide resonance around (3) is clearly visible as a sign change (color change) of the TMOKE at the same energies and angles as the corresponding intensity dip (2) in (a). The largest TMOKE δ of up to ± 0.1 % at saturated magnetization is reached in a relatively large area of the spectrum below the waveguide mode. The opposite effect on the other side of the mode at higher energies reaches about ∓ 0.06 % in a smaller area and decreases with increasing distance from the resonance. The plasmonic resonance (1) from the reflection spectrum, on the other hand, is barely visible in the TMOKE spectrum. Most notably, it is not visible as the usual sign change (white line) of the TMOKE near an optical resonance but rather as the absence of a stronger TMOKE signal close to the waveguide effect (see around (4)). This confirms that this SPP is located at the interface of the exposed gold grating with air and not with the magnetic magnetite film. Therefore, it is only weakly influenced by the applied magnetic field through the proximity to the magnetite film and the hybridization of the SPP and waveguide modes at their crossing point. The hybridization can also be seen for the waveguide mode (3), which deviates from a straight white line close to the plasmon resonance at (4) towards lower energies due to the increasing hybridization. Studies on iron garnet films supporting plasmonic resonances showed a similar interaction in the TMOKE signal [17].

For comparison, the TMOKE spectrum $\delta(E, \theta)$ from the bare magnetite film is shown in Figure 11.8. As expected in the absence of the periodic grating structure, the TMOKE from the bare film does not show any optical resonances. The magnitude δ increases monotonously for increasing reflection angles and also towards lower energies in the measured spectral range. It reaches a maximum of close to 0.15 % for 20° and 1.5 eV at the edge of the measured range and is thus even larger than the plasmonic TMOKE. This confirms the findings of Figure 11.5 that the introduction of the plasmonic grating does not lead to an overall increase of the TMOKE magnitude in reflection for these structures. However, both measurements were done in a relatively small spectral range, and additional measurements are needed to compare the effect magnitudes in a larger spectral range.

To summarize, adding a plasmonic gold grating introduces several optical resonances into the reflection and TMOKE spectra. However, it fails to significantly increase the magnitude of the TMOKE δ in the measured spectral range, as was already seen in Figure 11.5. The two resonances can be identified by their polarization-dependent appearance and disappearance and the magnitude of their respective TMOKE signal. The hybridization of the two modes is visible in the TMOKE signal close to their crossing points, where the waveguide mode deviates from its expected straight path.

11.4.2 Transmission Geometry - Exposed Grating

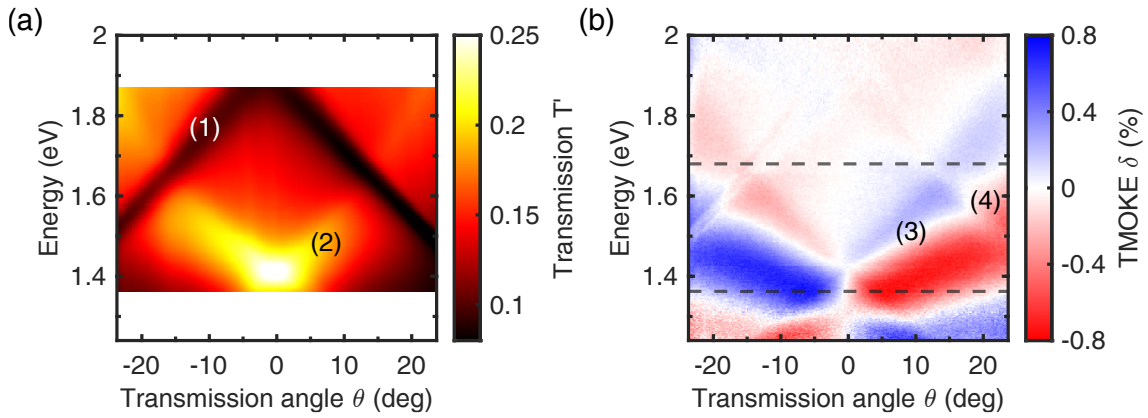

Figure 11.9 Transmission geometry, gold grating on top of the magnetite film:
(a) Transmission $T' = I_{\text{grating}}/I_{\text{bare}}$ with the light intensity transmitted through the structure with grating I_{grating} and through the bare magnetite film I_{bare}. **(b)** TMOKE δ according to Eq. (11.4) through the grating structure. Dashed lines indicate the spectral range measured in reflection in Figure 11.7.

The same sample with the exposed grating on top of the magnetite film was also measured in the transmission geometry. It already showed an increased TMOKE magnitude in Figure 11.5. The results are shown in Figure 11.9 with the transmission T' in (a) and the TMOKE δ in transmission in (b). Here, the transmission T' is defined as $T' = I_{\text{grating}}/I_{\text{bare}}$, i.e. the light intensity transmitted through the sample with the grating I_{grating} normalized to the intensity transmitted through the sample without the grating on top of the magnetite I_{bare}. This definition highlights the effect of the grating structure on the transmitted light and removes influences of the optical elements or the light source spectrum. A larger spectral range was measured here compared to the reflection

geometry by combining several subsequent measurements of the same sample in neighboring spectral ranges of the spectrometer: The transmission was measured between 1.36 eV and 1.87 eV by combining two measurements, and the TMOKE between 1.25 eV and 2 eV in three separate measurements. The transmission spectrum in (a) shows the same two resonances already seen in the reflection geometry, but with inverse effects on the spectrum. The plasmonic resonance at the gold/air interface (labeled (1)) shows a lower transmission (darker colors) in contrast to its higher reflected intensity in the reflection geometry in Figure 11.7(a), and the waveguide mode (2) can be identified by its increased transmission, while it showed a decreased reflection.

The TMOKE spectrum $\delta(E, \theta)$ in transmission in panel (b) looks similar to the TMOKE in reflection in Figure 11.7(b). The dashed lines indicate the smaller spectral range of the measurement in reflection. As seen before, all features of the TMOKE spectrum are moved to slightly lower energies in transmission, but the shape of the signal stays the same. Again, the resonance of the guided mode in the magnetic magnetite film is clearly visible around (3) as a sign change of the TMOKE (white line) with a large area of strong TMOKE response at lower energies and a smaller area of the opposite effect at higher energies. The TMOKE magnitude δ reaches up to $\pm 0.75\,\%$ at saturated magnetization in the large area below (3) and $\mp 0.25\,\%$ in the smaller area above the resonance. This is a significant enhancement compared to the TMOKE from the bare magnetite film in transmission, where only $\delta = 0.03\,\%$ is reached (see Figure 11.5) with a $\delta(E, \theta)$ spectrum like in reflection in Figure 11.8. It is also considerably larger than the TMOKE in reflection, where 0.1 % and 0.06 % were reached around the same resonance for the plasmonic structure and similar values from the bare structure. At small energies below 1.4 eV, areas of TMOKE with the opposite sign seem to appear again, likely linked to the continuing waveguide mode after the two branches cross around 1.4 eV. The plasmonic resonance at the non-magnetic air/gold interface is also vaguely visible from (4) towards lower angles for increasing energies. It is, again, best seen close to the crossing point with the magnetic waveguide mode next to (4) as a deviation of the white line (3) from its otherwise straight path due to the hybridization of the two modes. Other than that, no additional resonances are visible in the larger spectral range and the TMOKE magnitude quickly decreases for light above 1.7 eV, i.e. detuned from the waveguide mode. As expected for the TMOKE, measurements with s-polarized light show a negligible TMOKE magnitude of around 0.01 % for the resonant and non-resonant regions of the spectrum, which is around the detection limit of the setup (not shown here). The theoretical simulations of $T(E, \theta)$ and $\delta(E, \theta)$ presented in Ref. [4] reproduce the resonant features well and the same resonances in the transmission spectrum lead to the same TMOKE signal as in the experiments. The hybridization of the modes is better visible in the simulations, most notably of the plasmonic resonance at the non-magnetic gold interface. It has a comparably weak signal that is strongest at the crossing point with the waveguide mode in the magnetic film.

As a quick summary, the comparison of the TMOKE in the two measurement geometries shows a clear advantage of the transmission over the reflection geometry. Introducing the plasmonic grating does not significantly enhance the TMOKE magnitude in the reflection geometry. In contrast, a wide-band enhancement of the TMOKE magnitude δ is achieved in transmission compared to the bare magnetite film in reflection and transmission and compared to the TMOKE from the plasmonic structure in the reflection geometry. Due to the large absorption in magnetite, the measured spectra show spectrally broad resonances compared to, e.g., low-absorbing periodic slab waveguides and magneto-plasmonic crystals [15, 63, 118]. This results in the spectrally broad features in the TMOKE spectra and, thus, the wide-band enhancement of the TMOKE in transmission.

11.4.3 Transmission Geometry - Embedded Grating

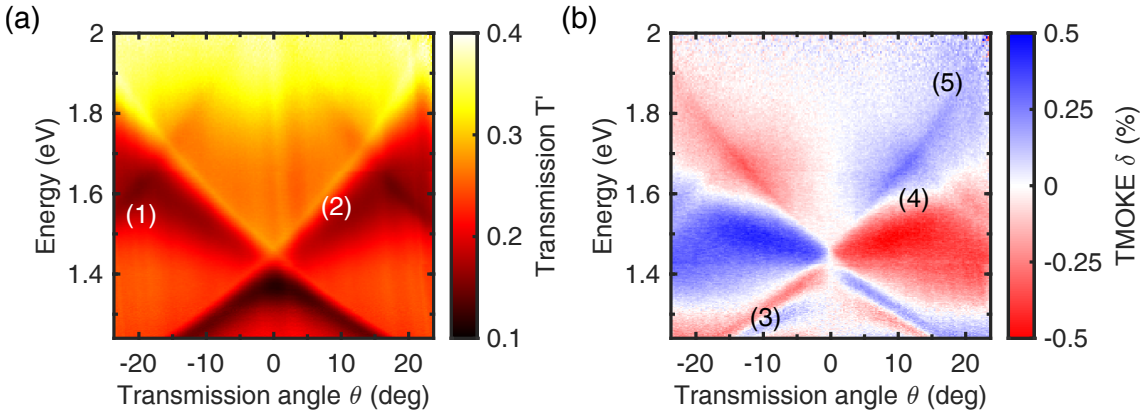

Figure 11.10 Transmission geometry, gold grating embedded in the magnetite film: **(a)** Transmission $T' = I_{\text{grating}}/I_{\text{bare}}$ with the light intensity transmitted through the structure with grating I_{grating} and through the bare magnetite film I_{bare}. **(b)** TMOKE δ according to Eq. (11.4) through the grating structure. Numbered labels are used for reference in the text.

Lastly, Figure 11.10 shows the data from the sample with the gold grating embedded in the magnetite film, with the transmission spectrum T' in panel (a) and the corresponding TMOKE spectrum δ in panel (b). Both are in the large spectral range between 1.25 eV and 2 eV, composed from three different spectral ranges. The transmission spectrum looks similar to the other sample with two modes visible at the same positions as in Figure 11.9(a): Here, the waveguide mode (2) is best visible and shows an X shape with the two opposite modes crossing around 1.4 eV. The lines of the X separate regions of higher and lower transmission T' in the spectrum, with the largest T' in the cone above the crossing point at high energies and the lowest T' in the cone below the crossing at small energies. The plasmonic resonance attributed to the air/gold interface (1) is, on the other hand, barely visible because the grating is no longer in direct contact with the air. The rather thin magnetite cover above the grating can explain the faint remnant. The plasmonic resonance at the new gold/silica interface is expected to become visible but is outside the measured spectral range. Next, Figure 11.10(b) shows the corresponding TMOKE spectrum in transmission. The X shape of the waveguide mode is also visible in the TMOKE spectrum, spanned by the characteristic white lines of $\delta = 0$ at (3) and (4) that separate areas of opposite TMOKE shown in red and blue. The lower part of the X (3) below 1.4 eV manifests as straight white lines that follow the path seen in the transmission spectrum. They are surrounded by comparatively small areas of TMOKE with up to $\delta = 0.25$ %. A larger portion of the lower part of the X is visible here due to the blue shift of the resonances compared to the previous sample. For energies above the crossing point at 1.4 eV, the white line of the TMOKE resonance does not perfectly follow the straight path of the waveguide mode and is bent towards lower energies instead. This deviation becomes stronger with increasing proximity to the remnant of the air/gold plasmon around (4), but the bending is less pronounced compared to the previous sample with the stronger plasmonic resonance. Their crossing around 1.65 eV can be seen as a dent in the white waveguide mode line next to (4) due to the hybridization of the mode. The TMOKE around this upper part of the X covers larger areas and reaches up to 0.45 % below the white line. Interestingly, a local maximum of $\delta = 0.35$ % is reached in a thin line (5) that follows the unbent waveguide mode from the transmission spectrum in (a). Lastly,

the plasmonic resonance of the air/gold interface is visible even less in the TMOKE spectrum of the embedded grating structure, aside from its influence on the waveguide mode discussed above. Therefore, embedding the periodic gold grating in the magnetite film instead of placing it on top of the film still allows the excitation of the magnetite waveguide mode but diminishes the influence of the non-magnetic plasmon resonance at the air/gold interface. However, it slightly reduces the TMOKE magnitude of the waveguide mode from about 0.75 % to 0.45 %, which is still several times larger than the effect seen in the reflection geometry. As for the previous case in transmission, the experimental spectra are reproduced well by the theoretical simulations in Ref. [4]. They show the suppressed plasmonic resonance and its weaker but still present influence on the strong magnetic waveguide mode in the transmission and TMOKE spectra.

11.4.4 Mode Hybridization

All modes seen in the reflection, transmission and TMOKE spectra are hybrid modes of surface plasmon polaritons (SPPs) at either interface of the gold grating with guided resonances of the magnetite film waveguide due to their close spatial proximity in the thin structure. Additional modes like localized surface plasmon modes at the individual gold stripes can also have an influence on the spectra, as well as other effects like the partial lifting of the mode degeneracy at high symmetry points of the period structure. All modes interact with each other in the thin structure, and the relative contributions towards the hybrid modes varies in each case. Therefore, additional theoretical modeling of the structures is necessary to predict and identify the variety of optical resonances, which has been done by Sergey Dyakov in Ref. [4] for these structures. A second mechanism of mode hybridization occurs due to the interaction of the already hybridized modes of the structure with the photon continuum in the far field, which is enabled by the periodic grating structure. This ultimately leads to the appearance of asymmetric Fano-type resonances in the optical transmission and reflection spectra, as the modes become quasi-guided or leaky and resonantly excitable via external light [119]. Theoretical calculations in Ref. [4] show that both hybridization mechanisms are necessary for the enhancement of the TMOKE compared to the case of the bare, planar magnetite film on the silica substrate.

11.5 Summary

In this chapter, we have studied the magneto-optical response of synthesized thin magnetite films with and without an additional plasmonic gold nanograting, and the grating was either placed on top of the magnetic magnetite film or embedded into the film. The magnetite film comprising Fe_3O_4/α-Fe nanoparticles was created using the laser electrodispersion technique, and its permittivity ε and gyration g are close to that of standard monocrystalline or epitaxial magnetite films. The periodic gold nanograting introduces optical resonances in the reflection, transmission and TMOKE spectra, which were identified as a guided mode in the magnetic magnetite film and a plasmonic resonance at the non-magnetic air/gold interface. The magnetic waveguide resonance is also clearly visible in the TMOKE spectra as a sign change of the TMOKE δ. It shows a multiple-wide-band enhancement of the TMOKE of up to $\delta = 0.75\,\%$ for the exposed grating close to the resonance, but only in the transmission geometry. In reflection, only about $\delta = 0.1\,\%$ were reached for both the plasmonic structure but also for the bare magnetite film. The plasmonic resonance of the non-magnetic

air/gold interface is also visible in the TMOKE spectra, albeit barely. It is best visible close to its crossing point with the waveguide mode, partly by its small TMOKE contribution but mostly by its influence on the waveguide mode, which bends towards lower energies close to the crossing. These are clear indicators for the hybridization of the two spatially close magnetic and non-magnetic modes, which seem to have a larger influence on the transmitted than the reflected light. For the embedded grating structure in transmission, the waveguide mode is still visible with up to $\delta = 0.45\,\%$, while the influence of the plasmonic resonance vanishes almost completely due to the different grating position.

In the Faraday geometry, large magnetic fields of up to 800 mT are needed to saturate the magnetization of the magnetite film. In the Voigt geometry, the magnetization and the TMOKE magnitude already saturate at small magnetic fields of 100 mT and show a clear hysteresis behavior. This can be used to switch the transmitted light intensity between two opposite states, with the effect being robust against changes of the energy or incidence angle of the light due to the spectrally broad TMOKE enhancement stemming from the large absorption in magnetite. Furthermore, the TMOKE can be used to extract more information about the different optical modes and their interactions at small magnetic fields. The spectral position of the modes and the wide-band TMOKE enhancement can be influenced by changing, e.g., the period of the grating or the width of the slits (as shown for the TMRLE in Chapter 10), and by changing the geometry of the structure, as shown for the plasmon resonance at the air/gold interface. The optical spectra can be reproduced well using theoretical simulations, which allows for an easy optimization of the plasmonic structure for various applications.

Chapter 12

Summary and Outlook

One of the main topics of this thesis is the transverse magnetic routing of light emission (TMRLE) from hybrid plasmonic-semiconductor structures, where the magnetic-field induced transverse circular polarization P_c of the exciton optical transitions in a diluted magnetic semiconductor (DMS) quantum well (QW) is translated into routed propagating surface plasmon polariton (SPP) waves due to their strong spin-momentum locking, and emitted directionally into the far-field. This thesis advances the understanding of the TMRLE from these hybrid structures in two key areas: First, the strong temperature dependence of the TMRLE from a DMS QW structure was investigated, which also revealed interesting influences like the emerging light-hole exciton emission at higher temperatures. Second, the influence of the plasmonic nanograting as the other constituent of the hybrid structure on the routing effect was shown. For this, different grating periods and slit widths were examined, uncovering the usually hard-to-detect weak coupling between the QW excitons and the SPPs as a large contributor to the emission directionality spectrum. Finally, another magneto-optical intensity effect was investigated, the transverse magneto-optical Kerr effect (TMOKE) for light reflected from or transmitted through a magnetite-based plasmonic waveguide structure. Here, the hybridization of the plasmonic and magnetic waveguide modes leads to a wide-band enhancement of the TMOKE in transmission.

Chapter 8 serves as an introductory chapter for the following TMRLE studies. It introduces reflection and emission spectra from the new main hybrid plasmonic-semiconductor structures comprising a (Cd,Mn)Te/(Cd,Mg)Te DMS QW and plasmonic gold nanogratings, characterizing the structures and its optical resonances. Next, the giant Zeeman splitting of the QW excitons due to the large exchange interaction with the magnetic Mn ions is determined, because it is the most important quantity for the TMRLE. Then, a typical spectrally and angularly resolved directionality spectrum $\rho(E, \theta)$ is explained in detail in Figure 8.5. For the exciton emission that is resonantly routed via SPPs, ρ reaches up to 15 % at $T = 4\,\mathrm{K}$ with controlling magnetic fields of $\pm 485\,\mathrm{mT}$. The emission routing from the QW and the other non-magnetic semiconductor layers is compared to a previously used alternative structure and to simulations based on our theory from Refs. [30, 48], showing good agreement.

In **Chapter 9**, the temperature dependence of the TMRLE from the hybrid structure is investigated. It is governed by the decreasing magnetic susceptibility of the DMS QW, i.e., the semiconductor light source of the hybrid structure, which leads to a smaller Zeeman splitting and transverse polarization degree P_c of the optical exciton transitions. This ultimately results in less directional emission at larger temperatures, which can be described well using the modified Brillouin function $B_{5/2}$ in Eq. (9.1) for the Mn spin polarization. Here, an additional temperature offset gets introduced

to address the strong heating of the Mn-spin system by continuous wave excitation. At larger temperatures, the emission from light-hole excitons begins to contribute to the directionality with the opposite sign compared to the main emission from the heavy-hole excitons. It was also shown that the plasmonic grating does not significantly influence the TMRLE temperature dependence. Furthermore, a non-magnetic (In,Ga)As/(In,Al)As QW structure was proposed for a temperature-independent TMRLE, because its Zeeman splitting is based on the intrinsically large hole g-factor and does not originate from the temperature-dependent exchange interaction of DMSs. Here, a directionality of 5 % is predicted up to 200 K for a 1 T magnetic field.

Chapter 10 investigates the dependence of the TMRLE on the geometric grating parameters, like the grating period and slit width, instead, and uncovers the influence of the weak exciton-SPP coupling on the directionality $\rho(E, \theta)$. The largest directionality is achieved due to the resonant near-field interaction between the QW excitons and the SPPs with strong spin-momentum locking at the grating surface. The grating parameters modify the plasmonic dispersion relation and, thus, their far-field emission characteristics. As expected, the maximum TMRLE follows the shifting plasmonic resonance through the directionality spectra. Crucially, a hump-shaped deviation from the expected monotonic SPP-enhanced directionality $\rho(E, \theta)$ is detected, that is locked to both the QW emission maximum and the strong SPP directionality contribution. Additionally, it was not part of our previous theoretical models. It is identified as the influence of the weak coupling between the QW excitons and the SPPs, which is usually difficult to detect, even by similar magneto-optical effects like the TMOKE. The existing theoretical model is expanded by a resonant contribution of the QW excitons to the dielectric environment, which locally alters the SPP dispersion and the resulting directionality, and reproduces the experimental spectra well.

Chapter 11 investigates the transverse magneto-optical Kerr effect (TMOKE), instead, a magneto-optical intensity effect in the same geometry as the TMRLE, but for reflected or transmitted light. The investigated structure is a plasmonic waveguide structure comprising a periodic gold grating either on top of or embedded into a synthesized thin magnetite waveguide film. The magnetite film comprising Fe_3O_4/α-Fe nanoparticles was created using the laser electrodispersion technique, and its permittivity ε and gyration g are close to that of standard monocrystalline or epitaxial magnetite films. The additional periodic grating introduces optical resonances of the magnetic waveguide structure and the plasmonic grating in the reflection, transmission and TMOKE spectra, which are hybrid in nature due to their spatial and spectral proximity. The TMOKE spectra show a richer picture of the optical modes than the usual intensity spectra and can be used to extract further information on the modes. For transmitted light, the guided modes in the thin magnetic film show a multiple-wide-band enhancement of the TMOKE compared to the case of the bare film. The plasmonic mode at the air/gold interface is also visible in the spectra but shows a negligible TMOKE due to its non-magnetic nature, except close to the magnetic waveguide mode due to the hybridization. The embedded grating shows a weaker TMOKE than the exposed grating, but the air/gold plasmonic resonance vanishes almost completely due to the different interfaces of the gold. All results are backed by theoretical simulations that reproduce the (magneto-)optical features well [4].

Outlook: The strong temperature dependence of the TMRLE from DMS QW structures limits its applicability beyond cryogenic temperatures, although the fit to the experimental data predicts a directionality of around 2 % at 200 K with magnetic fields of 1 T for our system. The proposed alternative structure based on a non-magnetic (In,Ga)As/(In,Al)As QW, where the Zeeman splitting

is governed by the large intrinsic hole g-factor instead of the strongly temperature-dependent exchange interaction, is predicted to show a lower routing magnitude than the DMS at low temperatures, but enables the stable application at a wider range of temperatures and, crucially, at higher temperatures. Similar structures with a large hole g-factor are also possible candidates for high-temperature routing, although this needs to be investigated experimentally. Ultimately, the TMRLE is a general concept and not limited to a magnetic semiconductor QW structure with a plasmonic nanograting. In general, it requires a light source whose selection rules are modifiable by a magnetic field, which is an intrinsic property of emitters in magnetic materials, and the emitter needs to have a non-zero transversal spin, i.e. $\boldsymbol{S} \parallel x \perp \boldsymbol{k}$, for routing along y and emission in the yz-plane. This is a feature of any structure with broken $z \rightarrow -z$ reflection symmetry, but the routing is significantly enhanced in the presence of subwavelength optical fields at an interface with strong spin-momentum locking, like SPPs [30]. Therefore, the novel two-dimensional materials emerging and attracting interest recently are another class of compelling candidates for the magnetic-field dependent light sources, for example the ferromagnetic monolayer CrI_3 [120]. Another interesting class of systems could be QW structures like ZnSe/(Cd,Zn)Se, where the light-hole state has the lowest energy and not the usual heavy-hole state. These systems are expected to show the same results, as was seen in the temperature-dependent measurements in Chapter 9, but light holes can be critical for other phenomena like optical orientation as the opposite effect to the TMRLE [43].

The TMRLE itself proves to be a versatile tool for a number of possible applications: Using the periodic grating structure to translate the routed SPPs into directional far-field emission enables the fine-tuning and optimization of the angular dependence of the resonant plasmonic contribution via the geometric grating parameters, and the emission energy can be varied using different QW structures or other novel light sources. For on-chip emission routing, the periodic structure can be substituted by a planar metal film which inhibits the SPP emission into the far-field without impeding the plasmon propagation. Since the TMRLE works for a single emitter just like for emitter ensembles, it can be used for the routing of quantum light source emission in novel optical devices like integrated photonic or optoelectronic circuits. Furthermore, the directionality of the routed emission can be controlled ultrafast up to the terahertz regime by optical or radiofrequency fields manipulating the magnetization of the magnetic ions [30].

Additionally, the TMRLE can serve as a flexible sensing tool for changes of the dielectric environment near the surface via modifications of the SPP dispersion. This was shown with the detection of the weak exciton-SPP coupling and can be used in that area for more detailed studies on different materials. More generally, though, it can be used to detect changes of the permittivity near the surface independent of their origin with a high sensitivity, e.g., due to the deposition of atoms or molecules on the surface. On the other hand, these results have a strong impact on the tuning of the SPP dispersion, because even the weak coupling already results in a quite noticeable change of the directionality spectra. Good candidates for a strong dispersion tuning could, therefore, be 2D transition-metal dichalcogenides (TMDCs) with generally strong exciton oscillator strengths even at room temperature [121]. Note, however, that strong coupling in TMDC layers has mostly been demonstrated for localized plasmons only, see e.g. Refs. [113, 122, 123]. Similarly, the TMRLE also depends on the magnetic environment near the emitter, so that a single emitter at the desired location could be used as a sensitive probe [30].

Lastly, the wide-band enhancement of the TMOKE in the magnetite-based waveguide structures proved robust against changes of the energy or incidence angle due to the large absorption, and only

low magnetic fields of 100 mT are needed to saturate the magnetization in the Voigt geometry with a clear hysteresis. Therefore, systems like this are candidates to switch the transmitted light intensity between two opposite states, and the rich TMOKE spectra at low magnetic fields allow for a better understanding of the optical resonances. Another interesting property of magnetite is a phase transition of its crystal structure from a pseudo-cubic to a monoclinic structure at 120 K, known as the Verwey transition, at which it also sharply transitions from a metal to an insulator [124]. The influence of this transition on the TMOKE spectra could provide further interesting insights into the plasmonic magnetite system, e.g., if the magnetooptical changes at the Verwey temperature are also rapid like the phase transition.

List of Acronyms

(Cd,Mg)Te	Cadmium Magnesium Telluride
(Cd,Mn)Te	Cadmium Manganese Telluride
(In,Al)As	Indium Aluminium Arsenide
(In,Ga)As	Indium Gallium Arsenide
Au	Gold
BIG	Bismuth Iron Garnet
BSC	Beam Splitter Cube
CB	Conduction Band
CBO	Conduction Band Offset
CCD	Charge-Coupled Device
CW	Continuous Wave
DMS	Diluted Magnetic Semiconductor
Fe_3O_4	Magnetite
FeO	Wüstite
FWHM	Full Width at Half Maximum
hh	heavy-hole
InP	Indium Phosphide
lh	light-hole
MBE	Molecular Beam Epitaxy
MCD	Magnetic Circular Dichroism
ML	Monolayer
Mn	Manganese
MO	Microscope Objective
MOKE	Magneto-Optical Kerr Effect
PID	Proportional Integral Derivative
PL	Photoluminescence
PMOKE	Polar Magneto-Optical Kerr Effect

QD	Quantum Dot
QW	Quantum Well
RCWA	Rigorous Coupled-Wave Analysis
SEM	Scanning Electron Microscopy
SiO_2	Silicon Dioxide
SPP	Surface Plasmon Polariton
TMDC	Transition Metal Dichalcogenide
TMOKE	Transverse Magneto-Optical Kerr Effect
TMRLE	Transverse Magnetic Routing of Light Emission
VB	Valence Band
VBO	Valence Band Offset
WL	White Light

Bibliography

[1] A. K. Zvezdin and V. A. Kotov. *Modern magnetooptics and magnetooptical materials*. Studies in condensed matter physics. Bristol: Philadelphia, Pa, 1997. 386 pp. ISBN: 978-0-7503-0362-0.

[2] M. Faraday. "Experimental researches in electricity. Nineteenth series". In: *Phil. Trans. R. Soc.* 136, 1846, pp. 1–20. ISSN: 0261-0523, 2053-9223. DOI: 10.1098/rstl.1846.0001.

[3] J. Kerr. "On rotation of the plane of polarization by reflection from the pole of a magnet". In: *Lond. Edinb. Dublin Philos. Mag. J. Sci.* 3.19, 1877, pp. 321–343. ISSN: 1941-5982. DOI: 10.1080/14786447708639245.

[4] S. A. Dyakov et al. "Wide-band enhancement of the transverse magneto-optical Kerr effect in magnetite-based plasmonic crystals". In: *Phys. Rev. B* 100.21, 2019, p. 214411. DOI: 10.1103/PhysRevB.100.214411.

[5] J. McCord. "Progress in magnetic domain observation by advanced magneto-optical microscopy". In: *J. Phys. D: Appl. Phys.* 48.33, 2015, p. 333001. ISSN: 0022-3727. DOI: 10.1088/0022-3727/48/33/333001.

[6] M. Mansuripur. *The Physical Principles of Magneto-optical Recording*. Cambridge, 1995. DOI: 10.1017/CBO9780511622472.

[7] D. Huang, D. Lattery, and X. Wang. "Materials Engineering Enabled by Time-Resolved Magneto-Optical Kerr Effect for Spintronic Applications". In: *ACS Appl. Electron. Mater.* 3.1, 2021, pp. 119–127. DOI: 10.1021/acsaelm.0c00961.

[8] T. Higo et al. "Large magneto-optical Kerr effect and imaging of magnetic octupole domains in an antiferromagnetic metal". In: *Nature Photon* 12.2, 2018, pp. 73–78. ISSN: 1749-4893. DOI: 10.1038/s41566-017-0086-z.

[9] M. D. Rotondaro, B. V. Zhdanov, and R. J. Knize. "Generalized treatment of magneto-optical transmission filters". In: *J. Opt. Soc. Am. B, JOSAB* 32.12, 2015, pp. 2507–2513. ISSN: 1520-8540. DOI: 10.1364/JOSAB.32.002507.

[10] J. Keaveney et al. "Optimized ultra-narrow atomic bandpass filters via magneto-optic rotation in an unconstrained geometry". In: *Opt. Lett., OL* 43.17, 2018, pp. 4272–4275. ISSN: 1539-4794. DOI: 10.1364/OL.43.004272.

[11] E. Ishida et al. "Amorphous-Si waveguide on a garnet magneto-optical isolator with a TE mode nonreciprocal phase shift". In: *Opt. Express, OE* 25.1, 2017, pp. 452–462. ISSN: 1094-4087. DOI: 10.1364/OE.25.000452.

[12] C. Rizal, H. Shimizu, and J. R. Mejía-Salazar. "Magneto-Optics Effects: New Trends and Future Prospects for Technological Developments". In: *Magnetochemistry* 8.9, 2022, p. 94. ISSN: 2312-7481. DOI: 10.3390/magnetochemistry8090094.

[13] V. I. Belotelov, A. N. Kalish, and A. K. Zvezdin. "Magneto-Optics of Plasmonic Crystals". In: *Magnetophotonics: From Theory to Applications*. Ed. by M. Inoue, M. Levy, and A. V. Baryshev. Springer Series in Materials Science. Berlin, Heidelberg, 2013, pp. 51–106. ISBN: 978-3-642-35509-7. DOI: 10.1007/978-3-642-35509-7_4.

[14] D. Kim et al. "Extreme anti-reflection enhanced magneto-optic Kerr effect microscopy". In: *Nat Commun* 11.1, 2020, p. 5937. ISSN: 2041-1723. DOI: 10.1038/s41467-020-19724-7.

[15] V. I. Belotelov et al. "Enhanced magneto-optical effects in magnetoplasmonic crystals". In: *Nature Nanotech* 6.6, 2011, pp. 370–376. ISSN: 1748-3395. DOI: 10.1038/nnano.2011.54.

[16] G. Armelles et al. "Magnetoplasmonics: Combining Magnetic and Plasmonic Functionalities". In: *Adv. Opt. Mater.* 1.1, 2013, pp. 10–35. ISSN: 2195-1071. DOI: 10.1002/adom.201200011.

[17] M. Pohl et al. "Tuning of the transverse magneto-optical Kerr effect in magneto-plasmonic crystals". In: *New J. Phys.* 15.7, 2013, p. 075024. ISSN: 1367-2630. DOI: 10.1088/1367-2630/15/7/075024.

[18] B. Caballero, A. García-Martín, and J. C. Cuevas. "Hybrid Magnetoplasmonic Crystals Boost the Performance of Nanohole Arrays as Plasmonic Sensors". In: *ACS Photonics* 3.2, 2016, pp. 203–208. DOI: 10.1021/acsphotonics.5b00658.

[19] N. Maccaferri et al. "Resonant Enhancement of Magneto-Optical Activity Induced by Surface Plasmon Polariton Modes Coupling in 2D Magnetoplasmonic Crystals". In: *ACS Photonics* 2.12, 2015, pp. 1769–1779. DOI: 10.1021/acsphotonics.5b00490.

[20] B. F. Diaz-Valencia et al. "Enhanced Transverse Magneto-Optical Kerr Effect in Magnetoplasmonic Crystals for the Design of Highly Sensitive Plasmonic (Bio)sensing Platforms". In: *ACS Omega* 2.11, 2017, pp. 7682–7685. DOI: 10.1021/acsomega.7b01458.

[21] M. G. Manera et al. "Magneto-Optical properties of noble-metal nanostructures: functional nanomaterials for bio sensing". In: *Sci Rep* 8.1, 2018, p. 12640. ISSN: 2045-2322. DOI: 10.1038/s41598-018-30862-3.

[22] D. O. Ignatyeva et al. "Magneto-optical plasmonic heterostructure with ultranarrow resonance for sensing applications". In: *Sci Rep* 6.1, 2016, p. 28077. ISSN: 2045-2322. DOI: 10.1038/srep28077.

[23] C. J. Firby and A. Y. Elezzabi. "High-speed nonreciprocal magnetoplasmonic waveguide phase shifter". In: *Optica, OPTICA* 2.7, 2015, pp. 598–606. ISSN: 2334-2536. DOI: 10.1364/OPTICA.2.000598.

[24] H. Shimizu and V. Zayets. "Plasmonic isolator for photonic integrated circuits". In: *MRS Bulletin* 43.6, 2018, pp. 425–429. ISSN: 1938-1425. DOI: 10.1557/mrs.2018.123.

[25] J. Wang et al. "Stopping surface magneto-plasmons by non-reciprocal graded waveguides". In: *Physics Letters A* 398, 2021, p. 127279. ISSN: 0375-9601. DOI: 10.1016/j.physleta.2021.127279.

[26] J. Qin et al. "Switching the Optical Chirality in Magnetoplasmonic Metasurfaces Using Applied Magnetic Fields". In: *ACS Nano* 14.3, 2020, pp. 2808–2816. ISSN: 1936-0851. DOI: 10.1021/acsnano.9b05062.

[27] X. Wu et al. "Chiromagnetic Plasmonic Nanoassemblies with Magnetic Field Modulated Chiral Activity". In: *Small* 16.3, 2020, p. 1905734. ISSN: 1613-6829. DOI: 10.1002/smll.201905734.

[28] O. H.-C. Cheng, D. H. Son, and M. Sheldon. "Light-induced magnetism in plasmonic gold nanoparticles". In: *Nat. Photonics* 14.6, 2020, pp. 365–368. ISSN: 1749-4893. DOI: 10.1038/s41566-020-0603-3.

[29] Y. Ding et al. "Second Harmonic Generation Covering the Entire Visible Range from a 2D Material–Plasmon Hybrid Metasurface". In: *Adv. Opt. Mater.* 9.16, 2021, p. 2100625. ISSN: 2195-1071. DOI: 10.1002/adom.202100625.

[30] F. Spitzer et al. "Routing the emission of a near-surface light source by a magnetic field". In: *Nature Phys* 14.10, 2018, pp. 1043–1048. ISSN: 1745-2481. DOI: 10.1038/s41567-018-0232-7.

[31] A. Aiello et al. "From transverse angular momentum to photonic wheels". In: *Nature Photon* 9.12, 2015, pp. 789–795. ISSN: 1749-4893. DOI: 10.1038/nphoton.2015.203.

[32] T. V. Mechelen and Z. Jacob. "Universal spin-momentum locking of evanescent waves". In: *Optica, OPTICA* 3.2, 2016, pp. 118–126. ISSN: 2334-2536. DOI: 10.1364/OPTICA.3.000118.

[33] K. Y. Bliokh and F. Nori. "Transverse spin of a surface polariton". In: *Phys. Rev. A* 85.6, 2012, p. 061801. DOI: 10.1103/PhysRevA.85.061801.

[34] J. Petersen, J. Volz, and A. Rauschenbeutel. "Chiral nanophotonic waveguide interface based on spin-orbit interaction of light". In: *Science* 346.6205, 2014, pp. 67–71. DOI: 10.1126/science.1257671.

[35] C. Junge et al. "Strong Coupling between Single Atoms and Nontransversal Photons". In: *Phys. Rev. Lett.* 110.21, 2013, p. 213604. DOI: 10.1103/PhysRevLett.110.213604.

[36] P. Banzer et al. "The photonic wheel - demonstration of a state of light with purely transverse angular momentum". In: *J. Eur. Opt. Soc. - Rapid Publ.* 8.0, 2013. ISSN: 1990-2573. DOI: 10.2971/jeos.2013.13032.

[37] H. Lin et al. "Directional emission of nanoscale chiral sources modified by gap plasmons". In: *Nanotechnology* 34.24, 2023, p. 245201. ISSN: 0957-4484. DOI: 10.1088/1361-6528/acc2c8.

[38] I. Söllner et al. "Deterministic photon–emitter coupling in chiral photonic circuits". In: *Nature Nanotech* 10.9, 2015, pp. 775–778. ISSN: 1748-3395. DOI: 10.1038/nnano.2015.159.

[39] R. J. Coles et al. "Chirality of nanophotonic waveguide with embedded quantum emitter for unidirectional spin transfer". In: *Nat Commun* 7.1, 2016, p. 11183. ISSN: 2041-1723. DOI: 10.1038/ncomms11183.

[40] I. J. Luxmoore et al. "Interfacing Spins in an InGaAs Quantum Dot to a Semiconductor Waveguide Circuit Using Emitted Photons". In: *Phys. Rev. Lett.* 110.3, 2013, p. 037402. DOI: 10.1103/PhysRevLett.110.037402.

[41] F. J. Rodríguez-Fortuño et al. "Near-Field Interference for the Unidirectional Excitation of Electromagnetic Guided Modes". In: *Science* 340.6130, 2013, pp. 328–330. DOI: 10.1126/science.1233739.

[42] P. Moroshkin et al. "Spin-momentum locking in optical rectification". In: *Phys. Rev. A* 106.2, 2022, p. 023521. DOI: 10.1103/PhysRevA.106.023521.

[43] I. A. Akimov et al. "Plasmon-to-exciton spin conversion in semiconductor-metal hybrid nanostructures". In: *Phys. Rev. B* 103.8, 2021, p. 085425. DOI: 10.1103/PhysRevB.103.085425.

[44] J. A. Gaj and J. Kossut, eds. *Introduction to the Physics of Diluted Magnetic Semiconductors*. Springer Series in Materials Science. Berlin Heidelberg, 2010. ISBN: 978-3-642-15855-1. DOI: 10.1007/978-3-642-15856-8.

[45] J. K. Furdyna. "Diluted magnetic semiconductors". In: *Journal of Applied Physics* 64.4, 1988, R29–R64. ISSN: 0021-8979. DOI: 10.1063/1.341700.

[46] B. Kuhn-Heinrich et al. "Zeeman pattern of semimagnetic (CdMn)Te/(CdMg)Te quantum wells in inplane magnetic fields". In: *Solid State Communications* 91.6, 1994, pp. 413–418. ISSN: 0038-1098. DOI: 10.1016/0038-1098(94)90776-5.

[47] D. J. Griffiths and D. F. Schroeter. *Introduction to quantum mechanics*. Third edition. Cambridge; New York, NY, 2018. 495 pp. ISBN: 978-1-107-18963-8.

[48] L. Klompmaker et al. "Transverse magnetic routing of light emission in hybrid plasmonic-semiconductor nanostructures: Towards operation at room temperature". In: *Phys. Rev. Research* 4.1, 2022, p. 013058. DOI: 10.1103/PhysRevResearch.4.013058.

[49] S. A. Maier. *Plasmonics: Fundamentals and Applications*. New York, 2007. ISBN: 978-0-387-33150-8 978-0-387-37825-1. DOI: 10.1007/0-387-37825-1.

[50] R. André and L. S. Dang. "Low-temperature refractive indices of $Cd_{1-x}Mn_xTe$ and $Cd_{1-y}Mg_yTe$". In: *Journal of Applied Physics* 82.10, 1997, pp. 5086–5089. ISSN: 0021-8979. DOI: 10.1063/1.366383.

[51] P. B. Johnson and R. W. Christy. "Optical constants of the noble metals". In: *Phys. Rev. B* 6.12, 1972, pp. 4370–4379. DOI: 10.1103/PhysRevB.6.4370.

[52] F. Spitzer. "Magneto-optical intensity effects in hybrid plasmonic structures". PhD diss. TU Dortmund University, 2019. DOI: 10.17877/DE290R-19898.

[53] A. E. Khramova et al. "Tuning the directionality of spin waves generated by femtosecond laser pulses in a garnet film by optically driven ferromagnetic resonance". In: *Phys. Rev. B* 107.6, 2023, p. 064415. DOI: 10.1103/PhysRevB.107.064415.

[54] I. V. Savochkin et al. "Generation of spin waves by a train of fs-laser pulses: a novel approach for tuning magnon wavelength". In: *Sci. Rep.* 7.1, 2017, p. 5668. ISSN: 2045-2322. DOI: 10.1038/s41598-017-05742-x.

[55] M. Jäckl et al. "Magnon Accumulation by Clocked Laser Excitation as Source of Long-Range Spin Waves in Transparent Magnetic Films". In: *Phys. Rev. X* 7.2, 2017, p. 021009. DOI: 10.1103/PhysRevX.7.021009.

[56] E. Betzig et al. "Near-field magneto-optics and high density data storage". In: *Appl. Phys. Lett.* 61.2, 1992, pp. 142–144. ISSN: 0003-6951. DOI: 10.1063/1.108198.

[57] D. Bossini et al. "Magnetoplasmonics and Femtosecond Optomagnetism at the Nanoscale". In: *ACS Photonics* 3.8, 2016, pp. 1385–1400. DOI: 10.1021/acsphotonics.6b00107.

[58] I. S. Maksymov, J. Hutomo, and M. Kostylev. "Transverse magneto-optical Kerr effect in subwavelength dielectric gratings". In: *Opt. Express, OE* 22.7, 2014, pp. 8720–8725. ISSN: 1094-4087. DOI: 10.1364/OE.22.008720.

[59] M. G. Barsukova et al. "Magneto-Optical Response Enhanced by Mie Resonances in Nanoantennas". In: *ACS Photonics* 4.10, 2017, pp. 2390–2395. DOI: 10.1021/acsphotonics.7b00783.

[60] O. V. Borovkova et al. “Transverse magneto-optical Kerr effect at narrow optical resonances”. In: *Nanophotonics* 8.2, 2019, pp. 287–296. ISSN: 2192-8614. DOI: 10.1515/nanoph-2018-0187.

[61] J. A. Gaj, R. R. Galazka, and M. Nawrocki. “Giant exciton Faraday rotation in $Cd_{1-x}Mn_xTe$ mixed crystals”. In: *Solid State Communications* 25.3, 1978, pp. 193–195. ISSN: 0038-1098. DOI: 10.1016/0038-1098(78)91477-1.

[62] A. L. Chekhov et al. “Wide tunability of magnetoplasmonic crystals due to excitation of multiple waveguide and plasmon modes”. In: *Opt. Express, OE* 22.15, 2014, pp. 17762–17768. ISSN: 1094-4087. DOI: 10.1364/OE.22.017762.

[63] L. E. Kreilkamp et al. “Waveguide-Plasmon Polaritons Enhance Transverse Magneto-Optical Kerr Effect”. In: *Phys. Rev. X* 3.4, 2013, p. 041019. DOI: 10.1103/PhysRevX.3.041019.

[64] A. V. Chetvertukhin et al. “Magneto-optical Kerr effect enhancement at the Wood’s anomaly in magnetoplasmonic crystals”. In: *Journal of Magnetism and Magnetic Materials*. Fifth Moscow international symposium on magnetism 324.21, 2012, pp. 3516–3518. ISSN: 0304-8853. DOI: 10.1016/j.jmmm.2012.02.079.

[65] D. Sylgacheva et al. “Transverse magnetic field impact on waveguide modes of photonic crystals”. In: *Opt. Lett., OL* 41.16, 2016, pp. 3813–3816. ISSN: 1539-4794. DOI: 10.1364/OL.41.003813.

[66] J. A. Girón-Sedas et al. “Giant enhancement of the transverse magneto-optical Kerr effect through the coupling of ε-near-zero and surface plasmon polariton modes”. In: *Phys. Rev. B* 96.7, 2017, p. 075415. DOI: 10.1103/PhysRevB.96.075415.

[67] A. Mukherjee et al. “Giant magneto-optical Kerr enhancement from films on SiC due to the optical properties of the substrate”. In: *Phys. Rev. B* 99.8, 2019, p. 085440. DOI: 10.1103/PhysRevB.99.085440.

[68] M. Amanollahi and M. Zamani. “Wide-angle giant transverse magneto-optical Kerr effect in a gyromagnetic superlens”. In: *Opt. Lett., OL* 43.19, 2018, pp. 4851–4854. ISSN: 1539-4794. DOI: 10.1364/OL.43.004851.

[69] V. I. Belotelov et al. “Extraordinary transmission and giant magneto-optical transverse Kerr effect in plasmonic nanostructured films”. In: *J. Opt. Soc. Am. B, JOSAB* 26.8, 2009, pp. 1594–1598. ISSN: 1520-8540. DOI: 10.1364/JOSAB.26.001594.

[70] V. I. Belotelov et al. “Intensity magnetooptical effect in magnetoplasmonic crystals”. In: *J. Phys.: Conf. Ser.* 303.1, 2011, p. 012038. ISSN: 1742-6596. DOI: 10.1088/1742-6596/303/1/012038.

[71] M. Peter et al. “Directional Emission from Dielectric Leaky-Wave Nanoantennas”. In: *Nano Lett.* 17.7, 2017, pp. 4178–4183. ISSN: 1530-6984. DOI: 10.1021/acs.nanolett.7b00966.

[72] H. Chen et al. “Enhanced Directional Emission from Monolayer WSe_2 Integrated onto a Multiresonant Silicon-Based Photonic Structure”. In: *ACS Photonics* 4.12, 2017, pp. 3031–3038. DOI: 10.1021/acsphotonics.7b00550.

[73] J. Fang et al. “Directional Modulation of Exciton Emission Using Single Dielectric Nanospheres”. In: *Adv. Mater.* 33.20, 2021, p. 2007236. ISSN: 1521-4095. DOI: 10.1002/adma.202007236.

[74] A. F. Cihan et al. "Silicon Mie resonators for highly directional light emission from monolayer MoS_2". In: *Nature Photon* 12.5, 2018, pp. 284–290. ISSN: 1749-4893. DOI: 10.1038/s41566-018-0155-y.

[75] Y. Kan et al. "Directional off-Normal Photon Streaming from Hybrid Plasmon-Emitter Coupled Metasurfaces". In: *ACS Photonics* 7.5, 2020, pp. 1111–1116. DOI: 10.1021/acsphotonics.0c00196.

[76] Y. Kan and S. I. Bozhevolnyi. "Molding Photon Emission with Hybrid Plasmon-Emitter Coupled Metasurfaces". In: *Adv. Opt. Mater.* 10.12, 2022, p. 2102697. ISSN: 2195-1071. DOI: 10.1002/adom.202102697.

[77] H. Aouani et al. "Plasmonic Antennas for Directional Sorting of Fluorescence Emission". In: *Nano Lett.* 11.6, 2011, pp. 2400–2406. ISSN: 1530-6984. DOI: 10.1021/nl200772d.

[78] K.-M. See et al. "Photoluminescence-Driven Broadband Transmitting Directional Optical Nanoantennas". In: *Nano Lett.* 18.9, 2018, pp. 6002–6008. ISSN: 1530-6984. DOI: 10.1021/acs.nanolett.8b02836.

[79] A. G. Lamprianidis et al. "Directional Coupling of Emitters into Waveguides: A Symmetry Perspective". In: *Laser Photonics Rev.* 16.1, 2022, p. 2000516. ISSN: 1863-8899. DOI: 10.1002/lpor.202000516.

[80] S. A. Dyakov et al. "Vertical Routing of Spinning-Dipole Radiation from a Chiral Metasurface". In: *Phys. Rev. Appl.* 14.2, 2020, p. 024090. DOI: 10.1103/PhysRevApplied.14.024090.

[81] J. R. Arthur. "Molecular beam epitaxy". In: *Surf. Sci.* 500.1, 2002, pp. 189–217. ISSN: 0039-6028. DOI: 10.1016/S0039-6028(01)01525-4.

[82] J. M. Hartmann et al. "CdTe/MgTe heterostructures: Growth by atomic layer epitaxy and determination of MgTe parameters". In: *Journal of Applied Physics* 80.11, 1996, pp. 6257–6265. ISSN: 0021-8979. DOI: 10.1063/1.363714.

[83] *Raith GmbH, 44263 Dortmund, Germany*. https://raith.com/. URL: https://raith.com/.

[84] W. J. Ossau and B. Kuhn-Heinrich. "Dimensional dependence of antiferromagnetism in diluted magnetic semiconductor heterostructures". In: *Physica B: Condensed Matter* 184.1, 1993, pp. 422–431. ISSN: 0921-4526. DOI: 10.1016/0921-4526(93)90392-J.

[85] K. H. Kim et al. "Energy-gap dependence on the Mn mole fraction and temperature in CdMnTe crystal". In: *Journal of Applied Physics* 106.2, 2009, p. 023706. ISSN: 0021-8979. DOI: 10.1063/1.3176955.

[86] W. Dickson, G. A. Wurtz, and A. V. Zayats. "Plasmonic Crystals: Controlling Light With Periodically Structured Metal Films". In: *Photonics*. 2015, pp. 107–167. ISBN: 978-1-119-01178-1. DOI: 10.1002/9781119011781.ch3.

[87] R. J. Harrison, R. E. Dunin-Borkowski, and A. Putnis. "Direct imaging of nanoscale magnetic interactions in minerals". In: *Proc. Natl. Acad. Sci.* 99.26, 2002, pp. 16556–16561. DOI: 10.1073/pnas.262514499.

[88] B. T. Melekh et al. "Nanostructured magnetic films of iron oxides fabricated by laser electrodispersion". In: *Tech. Phys. Lett.* 42.10, 2016, pp. 1005–1008. ISSN: 1090-6533. DOI: 10.1134/S1063785016100126.

[89] W. F. J. Fontijn et al. "Optical and magneto-optical polar Kerr spectra of Fe_3O_4 and Mg^{2+}- or Al^{3+}-substituted Fe_3O_4". In: *Phys. Rev. B* 56.9, 1997, pp. 5432–5442. DOI: 10.1103/PhysRevB.56.5432.

[90] J. F. Bobo et al. "Magnetic behavior and role of the antiphase boundaries in Fe_3O_4 epitaxial films sputtered on MgO (001)". In: *Eur. Phys. J. B* 24.1, 2001, pp. 43–49. ISSN: 1434-6036. DOI: 10.1007/s100510170020.

[91] B. E. A. Saleh and M. C. Teich. *Fundamentals of photonics*. Third edition. Wiley series in pure and applied optics. Hoboken, NJ, 2019. 2 pp. ISBN: 978-1-119-50687-4.

[92] W. J. Ossau and B. Kuhn-Heinrich. "Dimensional dependence of antiferromagnetism in diluted magnetic semiconductor heterostructures". In: *Physica B: Condensed Matter* 184.1, 1993, pp. 422–431. ISSN: 0921-4526. DOI: 10.1016/0921-4526(93)90392-J.

[93] J. A. Gaj, R. Planel, and G. Fishman. "Relation of magneto-optical properties of free excitons to spin alignment of Mn^{2+} ions in $Cd_{1-x}Mn_xTe$". In: *Solid State Communications* 29.5, 1979, pp. 435–438. ISSN: 0038-1098. DOI: 10.1016/0038-1098(79)91211-0.

[94] D. E. Aspnes et al. "Optical properties of $Al_xGa_{1-x}As$". In: *Journal of Applied Physics* 60.2, 1986, pp. 754–767. ISSN: 0021-8979. DOI: 10.1063/1.337426.

[95] D. Keller et al. "Heating of the magnetic ion system in (Zn,Mn)Se/(Zn,Be)Se semimagnetic quantum wells by means of photoexcitation". In: *Phys. Rev. B* 65.3, 2001, p. 035313. DOI: 10.1103/PhysRevB.65.035313.

[96] G. Bartsch et al. "Positively versus negatively charged excitons: A high magnetic field study of CdTe/$Cd_{1-x}Mg_xTe$ quantum wells". In: *Phys. Rev. B* 83.23, 2011, p. 235317. DOI: 10.1103/PhysRevB.83.235317.

[97] J. Debus et al. "Spin-flip Raman scattering of the neutral and charged excitons confined in a CdTe/(Cd,Mg)Te quantum well". In: *Phys. Rev. B* 87.20, 2013, p. 205316. DOI: 10.1103/PhysRevB.87.205316.

[98] Y. Hwang, Y. Um, and H. Park. "Photoluminescence characteristics of $Cd_{1-x}Mn_xTe$ single crystals grown by the vertical Bridgman method". In: *Nanoscale Res Lett* 7.1, 2012, p. 36. ISSN: 1556-276X. DOI: 10.1186/1556-276X-7-36.

[99] C. Weisbuch et al. "Intrinsic radiative recombination from quantum states in GaAs-$Al_xGa_{1-x}As$ multi-quantum well structures". In: *Solid State Communications* 37.3, 1981, pp. 219–222. ISSN: 0038-1098. DOI: 10.1016/0038-1098(81)91017-6.

[100] T. Dietl. "A ten-year perspective on dilute magnetic semiconductors and oxides". In: *Nat. Mater.* 9.12, 2010, pp. 965–974. ISSN: 1476-4660. DOI: 10.1038/nmat2898.

[101] V. F. Sapega et al. "Polarization of Valence Band Holes in the (Ga,Mn)As Diluted Magnetic Semiconductor". In: *Phys. Rev. Lett.* 94.13, 2005, p. 137401. DOI: 10.1103/PhysRevLett.94.137401.

[102] X. Cao, M. Zopf, and F. Ding. "Telecom wavelength single photon sources". In: *J. Semicond.* 40.7, 2019, p. 071901. ISSN: 1674-4926. DOI: 10.1088/1674-4926/40/7/071901.

[103] I. Vurgaftman, J. R. Meyer, and L. R. Ram-Mohan. "Band parameters for III–V compound semiconductors and their alloys". In: *Journal of Applied Physics* 89.11, 2001, pp. 5815–5875. ISSN: 0021-8979. DOI: 10.1063/1.1368156.

[104] V. V. Belykh et al. "Large anisotropy of electron and hole g factors in infrared-emitting InAs/InAlGaAs self-assembled quantum dots". In: *Phys. Rev. B* 93.12, 2016, p. 125302. DOI: 10.1103/PhysRevB.93.125302.

[105] Ya. V. Terent'ev et al. "Determination of hole g-factor in InAs/InGaAs/InAlAs quantum wells by magneto-photoluminescence studies". In: *Journal of Applied Physics* 121.5, 2017, p. 053904. ISSN: 0021-8979. DOI: 10.1063/1.4975353.

[106] M. Linnik and A. Christou. "Calculations of optical properties for quaternary III–V semiconductor alloys in the transparent region and above (0.2–4.0eV)". In: *Physica B* 318.2, 2002, pp. 140–161. ISSN: 0921-4526. DOI: 10.1016/S0921-4526(02)00467-2.

[107] H. W. Dinges et al. "Refractive indices of InAlAs and InGaAs/InP from 250 to 1900nm determined by spectroscopic ellipsometry". In: *Applied Surface Science* 54, 1992, pp. 477–481. ISSN: 0169-4332. DOI: 10.1016/0169-4332(92)90090-K.

[108] W. L. Barnes, A. Dereux, and T. W. Ebbesen. "Surface plasmon subwavelength optics". In: *Nature* 424.6950, 2003, pp. 824–830. ISSN: 1476-4687. DOI: 10.1038/nature01937.

[109] L. Klompmaker et al. "Magneto-optical spectroscopy of weak exciton-plasmon coupling". Manuscript in preparation, working title. 2023.

[110] C. Kittel. *Introduction to solid state physics*. 8th ed. Hoboken, NJ, 2005. 680 pp. ISBN: 978-0-471-41526-8.

[111] P. Vasa and C. Lienau. "Strong Light–Matter Interaction in Quantum Emitter/Metal Hybrid Nanostructures". In: *ACS Photonics* 5.1, 2018, pp. 2–23. DOI: 10.1021/acsphotonics.7b00650.

[112] P. Vasa. "Exciton-surface plasmon polariton interactions". In: *Adv. Phys. X* 5.1, 2020, p. 1749884. ISSN: null. DOI: 10.1080/23746149.2020.1749884.

[113] J. Sun et al. "Strong plasmon–exciton coupling in transition metal dichalcogenides and plasmonic nanostructures". In: *Nanoscale* 13.8, 2021, pp. 4408–4419. ISSN: 2040-3372. DOI: 10.1039/D0NR08592H.

[114] A. E. Schlather et al. "Near-Field Mediated Plexcitonic Coupling and Giant Rabi Splitting in Individual Metallic Dimers". In: *Nano Lett.* 13.7, 2013, pp. 3281–3286. ISSN: 1530-6984. DOI: 10.1021/nl4014887.

[115] F. Todisco et al. "Ultrastrong Plasmon–Exciton Coupling by Dynamic Molecular Aggregation". In: *ACS Photonics* 5.1, 2018, pp. 143–150. DOI: 10.1021/acsphotonics.7b00554.

[116] P. Vasa et al. "Coherent Exciton–Surface-Plasmon-Polariton Interaction in Hybrid Metal-Semiconductor Nanostructures". In: *Phys. Rev. Lett.* 101.11, 2008, p. 116801. DOI: 10.1103/PhysRevLett.101.116801.

[117] S. Chikazumi, C. D. Graham, and S. Chikazumi. *Physics of ferromagnetism*. 2nd ed. International series of monographs on physics 94. Oxford; New York, 2009. 655 pp. ISBN: 978-0-19-956481-1.

[118] S. G. Tikhodeev et al. "Waveguide-plasmon polaritons in photonic crystal slabs with metal nanowires". In: *Phys. Status Solidi C* 2.2, 2005, pp. 795–800. ISSN: 1610-1642. DOI: 10.1002/pssc.200460303.

[119] S. G. Tikhodeev et al. "Quasiguided modes and optical properties of photonic crystal slabs". In: *Phys. Rev. B* 66.4, 2002, p. 045102. DOI: 10.1103/PhysRevB.66.045102.

[120] K. L. Seyler et al. "Ligand-field helical luminescence in a 2D ferromagnetic insulator". In: *Nature Phys* 14.3, 2018, pp. 277–281. ISSN: 1745-2481. DOI: 10.1038/s41567-017-0006-7.

[121] P. Xie et al. "Coherent and incoherent coupling dynamics in a two-dimensional atomic crystal embedded in a plasmon-induced magnetic resonator". In: *Phys. Rev. B* 101.4, 2020, p. 045403. DOI: 10.1103/PhysRevB.101.045403.

[122] L. Liu et al. "Strong Plasmon–Exciton Interactions on Nanoantenna Array–Monolayer WS_2 Hybrid System". In: *Adv. Opt. Mater.* 8.5, 2020, p. 1901002. ISSN: 2195-1071. DOI: 10.1002/adom.201901002.

[123] W. Du et al. "Ultrafast Modulation of Exciton–Plasmon Coupling in a Monolayer WS_2–Ag Nanodisk Hybrid System". In: *ACS Photonics* 6.11, 2019, pp. 2832–2840. DOI: 10.1021/acsphotonics.9b00923.

[124] M. Alexe et al. "Ferroelectric Switching in Multiferroic Magnetite (Fe_3O_4) Thin Films". In: *Adv. Mater.* 21.44, 2009, pp. 4452–4455. ISSN: 1521-4095. DOI: 10.1002/adma.200901381.

List of Publications

[1] F. Spitzer, A. N. Poddubny, I. A. Akimov, V. F. Sapega, **L. Klompmaker**, L. E. Kreilkamp, L. V. Litvin, R. Jede, G. Karczewski, M. Wiater, T. Wojtowicz, D. R. Yakovlev, and M. Bayer. "Routing the emission of a near-surface light source by a magnetic field". In: *Nature Phys* 14.10, 2018, pp. 1043–1048. ISSN: 1745-2481. DOI: 10.1038/s41567-018-0232-7.

[2] S. A. Dyakov, I. M. Fradkin, N. A. Gippius, **L. Klompmaker**, F. Spitzer, E. Yalcin, I. A. Akimov, M. Bayer, D. A. Yavsin, S. I. Pavlov, A. B. Pevtsov, S. Y. Verbin, and S. G. Tikhodeev. "Wide-band enhancement of the transverse magneto-optical Kerr effect in magnetite-based plasmonic crystals". In: *Phys. Rev. B* 100.21, 2019, p. 214411. DOI: 10.1103/PhysRevB.100.214411.

[3] **L. Klompmaker**, A. N. Poddubny, E. Yalcin, L. V. Litvin, R. Jede, G. Karczewski, S. Chusnutdinow, T. Wojtowicz, D. R. Yakovlev, M. Bayer, and I. A. Akimov. "Transverse magnetic routing of light emission in hybrid plasmonic-semiconductor nanostructures: Towards operation at room temperature". In: *Phys. Rev. Research* 4.1, 2022, p. 013058. DOI: 10.1103/PhysRevResearch.4.013058.

[4] T. P. Lyons, D. J. Gillard, C. Leblanc, J. Puebla, D. D. Solnyshkov, **L. Klompmaker**, I. A. Akimov, C. Louca, P. Muduli, A. Genco, M. Bayer, Y. Otani, G. Malpuech, and A. I. Tartakovskii. "Giant effective Zeeman splitting in a monolayer semiconductor realized by spin-selective strong light–matter coupling". In: *Nat. Photon.* 16.9, 2022, pp. 632–636. ISSN: 1749-4893. DOI: 10.1038/s41566-022-01025-8.

[5] **L. Klompmaker**, A. N. Poddubny, V. A. Zakharov, L. V. Litvin, R. Jede, G. Karczewski, S. Chusnutdinow, T. Wojtowicz, D. R. Yakovlev, M. Bayer, and I. A. Akimov. "Magneto-optical spectroscopy of weak exciton-plasmon coupling". Manuscript in preparation, working title. 2023.

Acknowledgements

Finally, it is time to express my gratitude to all the people who made this thesis possible and supported me throughout my journey. First, I would like to thank Prof. Manfred Bayer for allowing me to write this thesis at his chair and in the International Collaborative Research Center TRR 160, and for providing such a friendly and modern working environment. Thank you also to Prof. Marc Aßmann for stepping in and seamlessly taking over the chair in the latter years with the same motivation and commitment.

I wish to extent a special thank you to Prof. Ilya Akimov for supervising not only this thesis but also my bachelor's and master's theses before, and for his guidance and mentorship throughout all those years. It is your openness, support and willingness to help at all times that made me come back for each step of my academic journey.

I also want to thank Prof. Alexander Poddubny, Vladimir Zakharov and Sergey Dyakov for their remarkable theoretical work and patient explanations, which breathed life into every detail of the experimental data, elevating its value beyond what it would have been on its own.

A heartfelt thank you needs to go to Felix Spitzer for introducing me to these fascinating research topics during my master's thesis and for continuing to mentor me at the beginning of this thesis. It has been a pleasure working with you every day and I could not have wished for a better office neighbor and friend.

I also want to sincerely thank Eyüp Yalcin, Carolin Harkort and Raphael Kaiser for choosing me to supervise their theses and helping me advance my own, and for creating a fun working environment in the lab even during the longest measurements. Each of you, in your own way, helped me become better by pushing me forward and always asking all the questions you had on your mind.

Furthermore, I could not have wished for better colleagues than those I met at E2 over the years. This includes my other office colleagues Alexander Kosarev, Jonas Vondran, Felix Godejohann and Mikhail Nestoklon, who both distracted and helped me a lot with talks about life and physics, my lab colleagues over the years, including Artur Trifonov and Stefan Grisard, but also Henning Moldenhauer, Erik Kirstein, Jan Mundry, Alexandr Kamenskii and all the other colleagues that created such a helpful and supporting environment and are just too plentiful for anybody to read. Thank you, all of you! This also includes Michaela Wäscher and Katharina Goldack for administrative support, Lars Wieschollek and Thomas Stöhr for technical assistance, and Daniel Tüttmann and Jonas Lichtenstein for providing the necessary liquid helium.

Lastly, I want to express my heartfelt gratitude to Ramona, my parents Gerrit and Janette, and my brother Steffen and sister Imke for their unwavering love and everlasting support throughout all the ups and downs of life, and to my friends for just being there and pushing everything else into the background.